ABSTRACT

Title of Document: EFFECT OF SWIRL ON THE CHOKING CRITERIA, SHOCK STRUCTURE, AND MIXING IN UNDER-EXPANDED SUPERSONIC NOZZLE AIRFLOWS

Ahmed Abdelhafez, Doctor of Philosophy, 2009

Directed by: Professor Ashwani K. Gupta
Department of Mechanical Engineering

Swirling flow in nozzles occurs in a number of important propulsion applications, including turbofans and turbojet engines, spin-stabilized rockets, and integral rocket/ramjets. This study examines the effect of imparting swirl to underexpanded supersonic nozzle airflow on the choking criteria, shock structure, and mixing. Fuel is injected coaxially along centerline at the nozzle throat. The nanosecond Schlieren and condensate-seeded Mie-scattering diagnostic techniques are utilized to visualize the shock structure and mixing within the free supersonic part of flowfield, while CFD numerical simulations are used to quantify the subsonic region inside nozzle. Thrust is measured experimentally to validate the numerical findings and assess the effect of swirl on nozzle choking criteria, primarily thrust and specific impulse.

It is found that the throat velocity itself (not any of its components) is choked in a swirling flowfield. Therefore, the limiting tangential Mach number is unity. Moreover, the application of swirl always results in a reduction in axial Mach number component. The mass flow rate through nozzle is found to be primarily a function of throat static pressure and axial Mach number. The reduction in the latter with swirl explains the observed reduction in mass flow. Greater reservoir pressures, on the other hand, result in higher throat static pressures, which

compensates for the reduced axial Mach number, and the mass flow rate can be kept constant at its non-swirling value. It is also found that the distribution of subsonic Mach number in a non-swirling flow is almost not affected with the application of swirl, i.e., non-swirling and swirling flows have the same subsonic Mach number profile. In terms of thrust and specific impulse, the application of swirl at matched nozzle reservoir pressure results in the expected reductions in discharge coefficient, thrust, and specific impulse. At matched mass flow, however, the application of swirl results in the enhancement of both thrust and specific impulse. This is attributed to the considerable degree of underexpansion associated with the swirling flow as a result of the higher nozzle reservoir pressure with swirl. In terms of shock strength, the application of swirl at matched reservoir pressure weakens the shock structure. Matching the mass flow, on the other hand, results in a stronger structure. Swirl is found to enhance supersonic mixing significantly, where swirl-induced vortices stir up and mix different regions of flowfield. High relative Mach numbers between air and fuel, combined with subsonic injection, are found to induce a negative-angled air/fuel shear layer, which results in mixing enhancement and a weaker shock structure.

EFFECT OF SWIRL ON THE CHOKING CRITERIA, SHOCK STRUCTURE, AND MIXING IN UNDEREXPANDED SUPERSONIC NOZZLE AIRFLOWS

By

Ahmed Abdelhafez

Dissertation submitted to the Faculty of the Graduate School of the
University of Maryland, College Park, in partial fulfillment
of the requirements for the degree of
Doctor of Philosophy
2009

Advisory Committee:

Professor Ashwani K. Gupta, Chair
Dr. Kenneth Yu, Associate Professor, Dean's Representative
Dr. Kenneth Kiger, Associate Professor
Dr. Bao Yang, Associate Professor
Dr. Peter Sunderland, Assistant Professor

Dedication

I would like to dedicate this thesis to my parents, Prof. Abdelhafez Hassanein and Mrs. Badiea El-Adawy. Without their continuing support and blessings I could not have ever made it this far in life. Because of their understanding and unconditional belief in my hopes and aspirations I have been able to excel in my career. Their contributions have been tremendous and wide-ranging in nature, and for that I will forever be indebted to them. It is for these reasons and countless more that this work is presented and dedicated in their honor.

Acknowledgments

The work presented below is the product of four years of effort, which have brought me into contact with a great many amazing people. My advisor, Dr. Ashwani Gupta, has opened my eyes to entirely new vistas of possibility, provided support even in the absence of funding, and steadfastly supported my efforts in every conceivable way. Dr. Kenneth Yu gave me valuable insights on optical diagnostic techniques and on proper experimental procedures.

My family has, of course, played a vital role in encouraging me and keeping me motivated. I would like to sincerely thank my father for his example and for being a spirit of wisdom in my life, giving me advice whenever I need it. Heartfelt thanks go to my mother for the love she has always shown me, and to my sister for always having faith in me.

Special thanks go to all my friends who got me out of the lab every once in a while and extended hands of help to make my life much easier, especially when I first moved to Maryland to join grad school. My thanks also go to all my brave compatriots in the Combustion Laboratory and to all the undergraduate students who did training on my project and helped significantly with the assembly and operation of the test facility and with data acquisition.

Finally, I would like to express my sincere gratitude to the Space Vehicle Technology Institute, who supported this work in joint funding by NASA, DoD, and USAF within the NASA Constellation University Institutes Project (CUIP). Special thanks go to Claudia Meyer, the Project Manager, for the financial support of the project. My thanks are also extended to the ESI-Group and CFDRC for providing the simulation package CFD-GEOM, CFD-FASTRAN, and CFD-VIEW used in all the numerical simulations of this study.

Table of Contents

List of Tables

List of Figures

Nomenclature

A	cross-sectional area
a	speed of sound
D	nozzle-exit diameter (11 mm)
DR	air-fuel density ratio at injection plane
F	nozzle thrust
I_{sp}	nozzle specific impulse
M	Mach number
M_c	convective Mach number
M_{rel}	relative Mach number between air and fuel at injection plane
$\dot{m}$	mass flow rate
p	pressure
R	specific gas constant
r	radial coordinate
S	swirl number
T	temperature
t	time
v	velocity
z	axial coordinate
γ	ratio of specific heats
δ_{pit}	Pitot thickness of air/fuel shear layer
ρ	density
$\vec{\omega}_{bc}$	Baroclinic vorticity vector

Subscripts

a	axial
t	tangential

I. MOTIVATION AND OBJECTIVES

Hypersonic vehicles, powered by scramjet engines, are pivotal for the future of high-speed flight. The critical science issues in hypersonic research under in-flight conditions have not been fully understood yet. These issues include mixing in supersonic airbreathing engines. It is desired to maintain supersonic flow through the combustor of a scramjet engine, in order to reduce the losses in total pressure and temperature inherent in decelerating the flow to subsonic speeds. Extensive investigations are still needed in order to achieve better understanding of the complicated flow dynamics and chemistry involved with the final goal of improved efficiency and performance. Successful operation of any air-breathing system depends primarily on efficient mixing of the injected fuel with airflow. The efficiency of an injection system is defined by the achievable degree of fuel/air mixing. Supersonic flows are compressible and resistant to fuel penetration and mixing. Therefore, the equivalence ratio of scramjet-engine operation has to be fuel-rich over a considerable part of the vehicle flight, in order to ensure that a flame is present to provide positive thrust. Any progress made on improving the engine efficiency must, therefore, be closely followed towards achieving efficient mixing between fuel and air. Scramjet flows have residence times of the order of only few milliseconds. In this short residence time, one must account for the mixing, ignition delay, and combustion time scales.

Swirl is one of the solutions of interest to the problem of poor supersonic mixing. The mixedness of a supersonic fuel jet injected into the supersonic airflow of a scramjet engine can be improved by imparting swirl to the fuel jet. This is achieved practically by tangential injection of fuel into its plenum and allowing the flow to accelerate through a nozzle. In other words, a subsonic swirling flow accelerates to supersonic speeds in a choked nozzle. Swirling compressible flows occur also in a variety of important practical applications, including

turbofans and turbojet engines, integral rocket/ramjets, fluidic vortex valves. In the first case, the tangential velocity component is induced by the motion of turbine blades. For ramjets, the swirl generated by fixed vanes located in the dump combustor inlet can lead to significantly improved combustor performance. Clearly, the generated swirl in each of those propulsion systems will persist at some level to the inlet of exhaust nozzle. The behavior of a transonic swirling flow is thus of practical importance, which motivated this current study to examine the effect of axisymmetric vorticity on nozzle flowfield, so that design parameters such as thrust and mass flow rate can be accurately determined.

Subsonic swirling flows have been examined extensively in the literature, but little of fundamental nature is known of the supersonic ones. Quasi-one-dimensional theory apply very well as a first approximation in non-swirling supersonic flowfields, but previous attempts to extend those theory to swirling supersonic flows have all failed, due to the intrinsic three-dimensionality of such flows. The most fundamental problem is the identification of choking criterion. One-dimensional theory without swirl prove that the throat Mach number is unity, implying that the mass flux through the throat of a fixed-geometry nozzle is maximum, and that the throat velocity is equal to the speed of sound. The first criterion of maximum mass flux can be carried over to the swirling flowfield with known stagnation conditions. It is still not clear, however, how the second criterion applies to choked swirling flows. Because of the non-uniform throat velocity distribution, it is difficult in the absence of CFD numerical simulations to predict which velocity or velocity component is equal to the local speed of sound.

The lack of comprehensive understanding of supersonic swirling flows has also led to a controversy in terms of the effect of swirl on nozzle thrust and specific impulse. While some studies showed that the discharge coefficient, thrust, and specific impulse decrease with swirl,

others reported that thrust can be increased with swirl. It is thus of fundamental as well as practical importance to determine how the nozzle propulsive characteristics are affected by the application of swirl.

All of the above motivations have shaped the objectives of this study. Answers are provided for key fundamental questions, such as: Is the throat velocity (or any of its components) equal to the local speed of sound in a swirling flowfield? If yes, then how does swirl affect the shape of sonic line? How does swirl affect the throat Mach number, pressure, and temperature? How does swirl affect nozzle thrust and specific impulse? The analysis is also extended beyond nozzle choking criteria to examine the effect of swirl on shock structure and mixing within the supersonic flowfield downstream of nozzle exit. An extensive investigation of the effects of flow compressibility and injection conditions on flowfield and mixing is also provided. This study contributes significantly to the understanding of the effect of swirl on nozzle performance and flowfield, while highlighting the similarities and differences of non-swirling and swirling flows. No idealized assumptions are made, which would limit the applicability of the attained findings in engine/nozzle design or numerical-model development.

II. LITERATURE REVIEW

This chapter comprises a survey of the available pertinent literature. The efforts and main conclusions of previous studies are summarized, compared, and discussed, in order to highlight the chronological progression of research and to point out the points of ambiguity and the aspects that require further substantiation. The main contribution of this current study lies in its attempt to clear such ambiguities and shed light on those aspects that still lack necessary quantification.

The following survey is subdivided into four sections. The first provides an introductory review of the application of swirl in subsonic flows. It is to be noted that this section is by no means comprehensive, as the examination of subsonic swirling flows is beyond the scope of this study. Nevertheless, a brief review is provided to aid the reader in comparing subsonic to supersonic swirling flows and to enrich the global picture behind this research by describing how swirl generally affects the flowfield in combustion and propulsion applications.

The second section of the survey is dedicated to discussing compressible shear layers, shock/shear-layer interaction, and shock-induced mixing in supersonic flows. This section gains its importance from the fact that the examined flowfield in this study comprises a complex shock structure, the presence of which significantly affects many flowfield parameters. The third section approaches the main objective of this study by addressing an important and heavily investigated application of swirling supersonic flows, namely swirling supersonic injected fuel jets in straight supersonic main airflows. The effect of swirl on fuel-jet penetration and mixedness is discussed, with the ultimate goal of enhancing scramjet-engine performance.

The fourth and final section of this survey addresses the main topic of this study by discussing the effect of imparting swirl to supersonic nozzle flows. Analytical and experimental previous studies are reviewed, highlighting the effect of swirl on shock structure, nozzle choking

criteria, discharge coefficient, thrust, and specific impulse. All positive and negative aspects of swirl are discussed, with emphasis on the points of uncertainty in previous studies, which motivated the research performed in this current study.

2.1 Swirling Subsonic Flows

Swirl-stabilized subsonic flames have been found to possess extremely useful characteristics, such as large turndown ratios and efficient mixing, thus allowing for the design of compact and stable combustion systems. Essential observations on the nature and characteristics of swirling flows have been presented by Gupta et al. (1984). In a swirling flowfield, the rotation of fluid plays a significant role in determining the flow structure and behavior; the centrifugal force created by the rotation of fluid forces the flow radially outwards.

The degree of flow rotation can be characterized by the swirl number, S, which is essentially a non-dimensionalized ratio of the mean axial and rotational momenta of the flow. In theory, the swirl number is a conserved quantity, and should be invariant with axial location in the flow. In practice, however, the swirl numbers calculated on the basis of available data are not generally conserved, and will vary somewhat, depending on the axial location at which they are obtained. Flows are generally compared in the literature on the basis of swirl numbers that are calculated at the exit plane of the duct or nozzle from which the rotating flow emerges.

Flows with high swirl numbers are found to display characteristics that have proven to be very useful in the field of combustion. If the swirl number of a simple subsonic flow is greater than 0.6, the flow displays vortex breakdown [Lefebvre (1983)]. In this situation, the pressure at the center of flow is reduced dramatically by the rotation. Fluid from the downstream region, which has a lower velocity and therefore a higher pressure, is forced back upstream, forming a

recirculation region in the flow. In a combustor, this feature is quite useful, since recirculation of hot product gases helps to ignite cool incoming reactants, which makes it possible to stabilize combustion in the combustor at much higher fuel and air flow rates than would otherwise be possible. The recirculating flow is quite turbulent, which provides a useful degree of mixing. In non-premixed combustors, where the fuel and oxidizer are injected separately, rapid and complete mixing is desirable, in order for high combustion efficiency to be achieved.

A very effective strategy in combustion has been to inject gaseous or liquid fuel directly into the recirculation zone. If the fuel is injected as a liquid, the fuel droplets evaporate rapidly in the hot recirculating gases. This approach is often employed in gas turbine applications [Cohen et al. (1996)]. However, since the recirculated fluid consists largely of product gases, the concentration of unburned oxidizer in the recirculation region is low. Ignition of fuel does not occur until the heated vaporized fuel is brought into contact with unburned oxidizer at the boundary of recirculation region. Turbulent distortions of the flow then mix the combusting material in order to promote rapid and complete combustion.

Experimental efforts have been made, in order to better understand the behavior of practical swirl combustors. Davis and Samuelsen (1996) presented observations on swirl-stabilized combustion in an atmospheric-pressure combustor, designed to incorporate components found in practical systems. The objective of their work was to optimize the combustor performance across a range of power settings and flow rates, providing stable and complete combustion under various conditions.

Li and Acharya (2001) presented work carried out using an optically-accessible swirl-stabilized combustor. The combustor was actively controlled, in order to reduce the effect of combustion instability in the system, thus allowing for examining the features of flame front.

Unstable combustion is a problem in certain combustion systems, particularly under lean premixed conditions, and develops when the Rayleigh criterion is met [Rayleigh (1945)]. This criterion predicts that unstable combustion, characterized by oscillatory fluctuations in combustor pressure and heat release, will be driven when some heat release mechanism is synchronized with an acoustic mode of the system. If the heat-release signature of the system is in phase with one or more of its acoustic modes, the locations of maximum local heat release coincide with those of maximum local pressure, and the instability will continue being amplified until the system breaks down or factors limiting further growth of instability are encountered.

The method by which swirl is imparted to a flow is also important. Two general strategies have been described and utilized in the literature. Tangential-entry systems generate swirling flows via the interaction of axial and tangential flows, which mix in an upstream mixing duct. These flows have been examined experimentally and can be characterized relatively easily [Gupta et al. (1984)]. The contours of mean velocity are smooth and radially-symmetric, which allows for calculating swirl numbers using relatively small amounts of experimental data.

Production combustion systems usually employ swirler assemblies, which consist of solid angled vanes, placed in the flow. The flow emerging from a swirler is more complex than that from a tangential-entry system, but this approach allows for imparting rotation to the flow in a much more compact geometry than is possible with tangential-entry systems. The open spaces between the vanes behave as separate ducts, and the flow emerging from each space interacts and mixes with the adjacent flows. Flows of this kind have been quite difficult to examine experimentally. However, new optical measurement techniques, particularly three-dimensional particle image velocimetry (3-D PIV), make it possible to examine complex rotational flows in an experimental context [Linck and Gupta (2003) and Gupta et al. (2004)].

2.2 Shock-Induced Mixing in Supersonic Flows

Hypersonic vehicles will play an important role in air transportation in the 21st century. Current orbital launch vehicles rely primarily on rocket engines that store both fuel and oxidizer on board, which greatly decreases payload capacity. Airbreathing vehicles, on the other hand, have the potential for larger relative payload capacities, because they use external air as oxidizer in the combustion process. Furthermore, airbreathing vehicles can be designed to employ horizontal landing and/or takeoff, resulting in much faster mission turnaround times.

Ramjets are often used for supersonic flight speeds below Mach 5. In these devices, the incoming airstream is slowed down to subsonic speeds before entering the combustor. Above Mach 5, however, the high static temperatures generated by that compression process cause the air to dissociate into atomic nitrogen and oxygen, with a significant amount of the flow energy used to break the molecular bonds. At such high Mach numbers it is thus necessary to employ a supersonic combustion ramjet (scramjet), where combustion takes place in the supersonic regime. Scramjets contain a number of complex flow features, including shock waves, expansion fans, boundary layers, shear layers, compressible turbulence, reaction fronts, and regions of both supersonic and subsonic flow. The understanding of interactions among these features is of key importance in the development of viable scramjet engines. Nevertheless, there are several aspects of high-speed combustion which are currently not well understood, i.e. mixing of reactants, mixing/combustion interaction, flame holding, and flame stability [Waltrup (1986) and Heiser et al. (1994)]. Oblique shock waves that form within a scramjet combustor are often unavoidable. In spite of the stagnation pressure losses they induce, they have the positive effects of enhancing fuel-air mixing and helping to stabilize the flame base.

Increased molecular mixing between fuel and oxidizer is essential for efficient combustion, which can be accomplished by increasing the turbulent mixing. It is now well known that large-scale coherent structures play an important role in incompressible turbulent mixing layers [Brown and Roshko (1974)]. These structures engulf surrounding unmixed fluid and carry it into the mixing layer. Furthermore, it is possible that two adjacent vortical structures roll up upon one another, creating one larger structure, which leads to spreading of the mixing layer [Winant and Browand (1974)]. These two processes are believed to be fundamental for turbulent mixing in incompressible mixing layers.

Studies of compressible shear layers have shown that large-scale structures are similarity important in compressible turbulent mixing, changing its nature with convective Mach number [Papamoschou and Roshko (1988), Clemens et al. (1990), Hermanson and Winter (1991), and Hall et al. (1991)]. It was found that the visual growth rate of a compressible shear layer with almost unity convective Mach number was only one-fourth the growth rate of an incompressible mixing layer having the same freestream velocity and density ratios, regardless of the values of these ratios [Papamoschou and Roshko (1988)]. Moreover, it is known that supersonic shear layers are highly stable [Miles (1958)], limiting the desired mixing of fuel and oxidizer. It was predicted that a supersonic shear layer will be completely stable, if the Mach number based on the relative speed exceeds 2.83, assuming an infinitely thin vortex sheet. This predicted stable nature of supersonic mixing layers has been later observed both in experiments [Papamoschou and Roshko (1988) and Chinzei et al. (1986)] and in numerical simulations [Menon (1988)].

Previous research has shown that flame holding in reacting supersonic flows is achieved by creating high-vorticity regions, where the fuel and air partially mix at lower velocities [Ben-Yakar (2000)]. In an experimental study Huh and Driscoll (1996a) successfully stabilized a

supersonic hydrogen/air flame, with coaxial injection, along the axis of a Mach-2.5 wind tunnel. Stabilization was achieved by using small-angled wedges mounted on the tunnel sidewalls to generate weak oblique shock waves that interact with the flame. It was found that these shock waves enhance fuel-air mixing to the extent that the flame length decreased by up to 30% for certain shock locations and strengths, which are optimum for the investigated geometry and operating conditions. The researchers reasoned that the enhanced mixing is partially attributed to radial inflows of air induced by the shocks into the fuel jet. It was concluded that optimizing the mixing and stability limits for any combustor geometry requires careful matching of shock strengths and locations of shock/flame interaction.

In continuation to the previous study Huh and Driscoll (1996b) aimed at quantifying and optimizing certain beneficial effects of oblique shock waves on a supersonic, non-premixed, jet-like flame, which was stabilized along the axis of a Mach-2.5 wind tunnel. A wedge was mounted on the sidewall, in order to generate an oblique shock wave that interacts with the flame. Schlieren was performed to show how the interaction occurs, and measurements were made to quantify how the flame length and flame blowout limits are affected by the shocks. An optimum shock-interaction location was investigated by adjusting the wedge position. It was found that shock waves enhance the fuel-air mixing to the extent that flame lengths decreased by 30% when optimum shock location and shock strength were chosen. The researchers reported that enhanced mixing resulted, in part, because the shocks turn flow and induce radial inflows of air into the fuel jet. The presence of a Mach disk splits the reaction zone into two parts and severely distorts the flame shape. Substantial improvements in flame stability (i.e., changes in blowout limits) were achieved by seeking proper interaction of shock waves with the flame-holding recirculation zone. The reason for significant improvement in flame stability is believed

to be the shock-induced adverse pressure gradient, which elongates the recirculation zone. Excessive shock strength or poor shock placement were observed to cause thermal choking, and the flame base moved upstream of fuel-tube exit, leading to dangerously high wall heat transfer rates. It was concluded that optimization of the mixing and stability limits requires careful matching of the shock-flame interaction location and the shock strength. The experimental results showed that best mixing and stability can be achieved when the primary shocks create radial inflow near the flame base and interact with the recirculation zone.

Roy and Edwards (2000) attempted to numerically simulate some of the complex-flame/shock-wave interaction experiments conducted by Huh and Driscoll (1996a, b). A three-dimensional Navier-Stokes solver for chemically reacting flows was used to study the structure of a supersonic hydrogen-air flame stabilized in a Mach-2.4 rectangular cross-section wind tunnel. The numerical model uses a 9-species, 21-reaction hydrogen oxidation mechanism and employs Menter's hybrid k-ω/k-ε turbulence model. An assumed probability density function was used to account for the effects of turbulent temperature fluctuations on the ensemble-averaged chemical reaction rates. Results were reported for a configuration in which the effects of wedge-generated shock waves on flame stability were determined. Computed Pitot and static pressure profiles were compared to the experimental measurements of Huh and Driscoll, and axial density gradient contour plots were compared to their experimental Schlieren photographs. The numerical results indicated that the computed flame is stabilized because of a synergistic interaction of a shock system created through volumetric expansion effects with the hot recirculation zone itself. Impinging shock waves on the recirculation zone result in intense mixing at near stoichiometric conditions on the outside of the recirculation zone—the resulting long particle residence times, higher fluid densities, and higher temperatures all promote flame

stabilization. The displacement of the hot recirculation zone out into the inviscid core flow actually generates the shock system that helps stabilize the flame.

Marble et al. (1990) demonstrated, both experimentally and computationally, the enhancement of mixing between hydrogen and air through the generation of strong streamwise vorticity introduced by the interaction of a weak shock with the unmixed medium of non-uniform density. The numerical computations indicated that the steady interaction between a weak shock wave in air with a coflowing hydrogen jet can be well approximated by the two-dimensional time-dependent interaction between a weak shock and an initially cylindrical region filled with hydrogen imbedded in air. The shock impinging process causes hydrogen cylinder to split into two parts. One of these mixes rapidly with air and the other forms a stably stratified vortex pair that mixes more slowly; about 60% of hydrogen mixes rapidly with air.

In a relevant experimental study Brummund and Nuding (1997) investigated the interaction between a shock wave and a supersonic shear layer to examine the shock-induced mixing enhancement effect. Hydrogen was injected into a Mach-2.0 air stream parallel to the combustion-chamber centerline through holes at the base of a symmetric wedge. The wedge was centered as a strut in the two-dimensional model chamber. A wedge located at the upper plate of the chamber was used to generate an oblique shock wave that impinges on the mixing layer. Schlieren, Pitot-tube measurements, Rayleigh scattering, and O_2 PLIF were applied. The results indicated that pronounced spreading of the shear layer occurs downstream of the shock/shear layer interaction region.

Yang et al. (1993) simulated shock-induced mixing numerically. Parallel flows of a heavy gas interspersed with other flows of a lighter one were overtaken by a normal shock wave. It was shown that vorticity is generated at each location of interaction of the density gradient

across each light/heavy interface with the shock-wave pressure gradient. Since the pressure and density gradient vectors are out of phase at these locations, their cross-product ($\nabla p \times \nabla \rho$) has non-zero values. This product defines the Baroclinic vorticity vector, $\partial_t \vec{\omega}_{bc} = (\nabla p \times \nabla \rho)/\rho^2$, which causes the light gas regions to roll up into one or more counter-rotating vortex pairs, stirring and mixing the light and heavy gases together. It was concluded that, whenever possible, multiple shock waves should be utilized.

Lu and Wu (1991) performed direct numerical simulations using a high-resolution total variation diminishing (TVD) scheme to study shock enhancement on two-dimensional confined (spatially growing) supersonic mixing flows. Several specially designed mixing enhancement schemes were examined with emphasis placed on the study of fundamental aspects involved in the shock-induced mixing enhancement process. The merits associated with these mixing enhancement schemes were evaluated based on a cost/effectiveness criterion, in which the cost paid for encountered total pressure loss and the improvement in mixing gained are considered together. The preliminary results showed that mixing enhancement using shock waves can only be effective if the stimulation begins from the very upstream. Being motivated by this observation, the researchers proposed and investigated the idea of using a wavy-wall configuration to generate the desirable periodic shock stimulation. The computed results showed that considerable improvement in mixing efficiency can be achieved (at the expense of slightly higher loss in total pressure) by appropriate manipulation of the parameters, including wall wavelength, relative phase shift between the top and bottom walls, as well as the amplitude of waviness. Several important findings associated with the shock-induced mixing enhancement in confined supersonic flows were reported by the researchers and are summarized as follows. (a) Shock waves induce substantial increase in turbulent intensities as well as energy extraction from

the mean flow. However, this effect is very local and is often accompanied by unfavorable downstream flow conditions that impede the growth of instability wave if no further shock stimulation is enforced. (b) Effective shock enhancement of supersonic mixing must be employed as early upstream as possible, and the application of shock waves ought to be spatially persistent; otherwise the use of shock waves will not necessarily yield the desirable mixing improvement. (c) The repeatedly occurring compression/expansion waves generated by wavy walls can effectively bring forward the improved flow mixedness to the upstream.

Shock waves of supersonic flows have significant positive effects on fuel-air mixing and flame stabilization, when they interact appropriately with the air/fuel shear layer. Some beneficial effects of this interaction are [Menon (1989)]: (a) directing the airflow locally towards fuel for increased entrainment rates, (b) creation of additional vorticity that enhances mixing, and (c) increasing the flow static pressure and temperature through a shock wave. The exact role of each effect needs further substantiation and quantification.

2.3 Swirling Supersonic Injected Jet in Supersonic Mainstreams

Previous studies have indicated that mixing of a supersonic jet injected into a supersonic duct flow is improved by imparting swirl to the injectant [Kraus and Cutler (1993 and 1995)]. These studies also indicated that a swirling jet acts as a vortex generator, generating an injectant-air plume that contains a single or dominant vortex. If the jet does act as a vortex generator, then there are several additional possibilities for further enhancement of fuel-jet mixing and penetration. Bushnell (1995) discussed many of these possibilities for application in the hypervelocity flight regime ($M \geq 10$), but they are equally relevant for the lower hypersonic flight numbers of $M \approx 6$-7, where flow speeds in the combustor are $M \approx 2$. The discussed

possibilities included the interaction of counter-rotating pairs of vortices (with common flow away from the wall) to increase penetration. Bushnell also noted that skewed wall jets act as vortex generators in subsonic flows and might also be effective in supersonic ones.

Swithenbank and Chigier (1968) were early pioneers of the idea of mixing enhancement in a supersonic flow by swirling the fuel jet. Swirl was generated by tangential injection into the plenum, and the swirling flow was accelerated in a nozzle. Vortex breakdown occurred in the jet, leading to increased entrainment of air. In their combustion tests, the combustion intensity was increased indicating a higher mixing efficiency. Although their tests were mainly subsonic, it was shown that a reverse flow zone can be found in a transonic swirling jet, which suggests that these effects could also be achieved in a supersonic jet.

The flow of supersonic swirling jets in a stagnant atmosphere was further investigated by Cutler et al. (1993), Cutler and Levey (1991), and Levey (1991). The swirling jets were created by tangential injection into a swirl chamber and accelerated through a convergent-divergent nozzle. The researchers observed higher peak helix angles than previous studies, as well as lower densities and pressures along the jet axis. They found that the growth rates of mixing layer increased considerably with swirl. Moreover, when the swirling jets were operated overexpanded, unstable shock interactions produced vortex breakdown.

Kraus and Cutler (1993 and 1995) and Kraus (1993) investigated the effects of swirl on mixing of a 30° flush-wall injector into a Mach-2 flow. Two swirling cases and a non-swirling case were investigated using the same convergent-divergent nozzle. Matching of exit pressures led to higher injectant total pressure and lower mass flow rate with swirl than without. An analysis was performed to bring the results to an equal-mass-flow-rate basis, and suggested that the addition of swirl results in better mixing. Note that the comparison was still based on unequal

injectant total pressures and mass flow rates. It is possible that if the total pressure of non-swirling case were to be raised to the value of swirling cases, then the penetration and mixing would be improved. In addition to mixing enhancement, the addition of swirl appeared to result in the generation of a dominant vortex, as evidenced by a lateral motion of the injectant plume.

Johnson (1996) investigated the possibility of increasing injectant penetration by injecting a pair of counter-rotating swirling jets into a Mach-2 airstream. Several injectors were considered, each of which injecting nominally the same mass flow rate when operated at the same supply pressure. Of primary interest were flush-wall and swept-ramp injectors utilizing counter-rotating pairs of swirling jets and pitched at 25° to the main flow. For comparison, flush-wall and swept-ramp injectors utilizing a single non-swirling jet at 25° as well as a surface-normal flush-wall injector were considered. It was found that for both ramp-injector cases, downstream penetration was nearly that of the normal injector. The addition of swept ramps had more influence on penetration than the addition of swirl, and the penetration was less than expected for the swirling jet pair. Mixing performance downstream of injector exit was also enhanced by the use of ramps, as compared to that of normal injector, and was best for the ramped swirling jet pair. In the case of flush-wall swirling jet pair, a vortex-interaction instability occurred, which led to the intermittent rotation (by ±180°) of the locations of vortex centers, such that their mutual interaction caused an intermittently reduced jet penetration.

Naughton et al. (1989) conducted an experimental study of the effect of streamwise vorticity on supersonic turbulent mixing. A Mach-3 streamwise vortex was generated using a strut-mounted swirl injector and injected into a Mach-3.5 freestream. The resulting flowfield was investigated using both five-hole and total-temperature probes. The results were compared to identical experiments with a baseline, swirl-free Mach-3 jet. Laser Light Sheet (LLS) images

were used to observe the mixing phenomena. The entrainment of energy and mass was used to evaluate mixedness for both the swirl and swirl-free cases. It was shown that streamwise vorticity does lead to a modest mixing enhancement of about 34% for the conditions tested. The researchers concluded that such enhancement might be small, but it is significant enough to encourage further examination of this topic.

Murugappan et al. (2004 and 2006) and Murugappan and Gutmark (2003) designed a swirling traverse injector that they tested in a cold Mach-2.0 cross flow and postulated is capable of controlling the spreading rate and mixing in high speed flows. The researchers referred to it as "The Controlled Supersonic Swirling Injector (CSSI)" and reported that it could be used to affect mixing both in the core and shear layer of the jet. The CSSI employed the superior mixing characteristics of swirl and an active control mechanism to manipulate the growth rate and spreading characteristics of the jet. Both Rayleigh/Mie scattering (from flowfield ice crystals) and NO PLIF were used to characterize penetration and mixing of the CSSI. Instantaneous images were used to study dynamic structures in the jet, whereas ensemble images provided information about jet trajectory. Standard-deviation images revealed information about the large-scale mixing/entrainment. PDFs were used to evaluate the probability and location of freestream, mixed, and jet fluids. They were also used to track the centerline as well as jet boundary on a dynamic scale. It was observed that the jet centerline, identified from PDF contours, does not match the time-averaged jet trajectory for several cases at different axial locations. This was attributed to the fact that the PDF marker considers jet unsteadiness, whereas the time-averaged marker could be smeared due to averaging. Near-field CSSI centerline trajectory agreed with low-speed scaling conventions. Streamwise images indicated that the injector was capable of providing high penetration, when compared to circular and swirling baseline injectors. An

increase of 16% in mixing was observed. Spanwise images showed a maximum of 78% increase in total area contained within the jet boundary. A higher spanwise extent of jet boundary was also observed with the control cases that provided more interfacial area for better mixing between jet and cross stream, when compared to their baseline counterparts.

Povinelli et al. (1969) investigated the penetration and spreading of helium injected into the vortex pattern generated by a delta wing in a Mach-2.0 airstream. Results were compared to a flat-plate injector with the same projected frontal area and angle of attack. It was concluded that the vortex motion generated by the delta wing injector led to substantial increases in the penetration and spreading rates of the injected fuel. In a subsequent study, Hersh and Povinelli (1970) obtained similar results for fuel injected into a counter-rotating vortex structure also generated by delta wings. Although these studies demonstrated the effects of swirl on penetration and spreading in supersonic flow, no experimental data confirming accelerated mixing rates had been produced. In fact, later studies conducted by Povinelli and Ehlers (1972) and Schetz and Swanson (1973) concluded that, for coaxial jets in supersonic flow, jets with swirl produced no discernible effect on mixing compared with non-swirling jets. However, it is suspected that the swirl number employed in those studies was too small to create radial and axial pressure gradients sufficient for mixing enhancement. The experimental investigation of Tillman et al. (1991) concluded that the axial vortex mechanism previously shown to be responsible for rapid mixing in low-speed, subsonic flows can be effective in the supersonic jet environment.

2.4 Swirling Supersonic Nozzle Flows

Swirling flow in nozzles occurs in a number of important propulsion applications, including turbofans and turbojet engines, spin-stabilized rockets, and integral rocket/ramjets. In the first two cases, the tangential velocity component is induced by the motion of turbine blades and by the rocket spin, respectively. For ramjets, recent experimental studies [Buckley (1983)] have demonstrated that swirl generated by fixed vanes located in the dump combustor inlet can lead to significantly improved combustor performance. Clearly, the generated swirl in each of those propulsion systems will persist at some level to the inlet of exhaust nozzle. Therefore, it is important to examine the effect of tangential velocity component on nozzle flowfield, so that design parameters such as thrust and mass flow rate can be accurately determined.

Of the infinite variety of possible families of swirl profiles, two cases have received particular attention, namely the free- and forced-vortex cases. The most fundamental problem has been the determination of a choking criterion. One-dimensional theory without swirl proves that the throat Mach number is unity, implying that (a) the mass flux through the throat of a fixed-geometry nozzle is maximum, and (b) the throat velocity is equal to the speed of sound. The first criterion of maximum mass flux can be carried over to the swirling flowfield with known stagnation conditions. It is not clear, however, how the second criterion applies to choked swirling flows. Because of the non-uniform throat velocity distribution, it is difficult in the absence of CFD numerical simulations to predict which velocity or velocity component is equal to the local speed of sound. The maximum-mass-flux criterion has been used by several investigators. It was originally introduced by Mager (1961) in his theoretical study of choked free-vortex flows with the ratio of specific heats $\gamma = 1.40$. His results were extended by

Swithenbank and Sotter (1964) to the case of $\gamma = 1.25$, while Glick and Kilgore (1967) presented results for γ in the range 1.10 – 1.28.

The analysis of the free-vortex case is simplified by the fact that it is a potential flow, whereas the forced-vortex flow is truly rotational. This may be the reason why there have been several unsuccessful attempts to derive analytical expressions for the output characteristics of nozzles with choked flows. Bastress (1965) tried to use the sonic velocity criterion by incorrectly assuming that the velocity magnitude was constant across each section and equal to the critical velocity at the throat. In addition, he assumed forced-vortex flow at all stations. Manda (1966a) used the constant-stagnation-enthalpy assumption to derive an equation for the axial velocity. Forced-vortex flow was again assumed at all stations, but this time the equality of velocity magnitude and critical velocity at throat was assumed to be satisfied only on the nozzle axis at the throat. King (1966) proposed another solution in which he pointed out that the assumption of forced-vortex flow cannot hold everywhere, as it renders the problem over-specified. Manda (1966b), however, showed that King's solution violated the radial momentum equation. Finally, all the preceding articles were summarized and discussed by Hsu (1971) who concluded that the basic reason behind the controversy lies in the fact that the one-dimensional approximation could not be applied to swirling flows.

Carpenter and Johannesen (1975) refuted Hsu's conclusions and attempted to extend one-dimensional theory to inviscid compressible swirling flow with the minimum of assumptions. They presented a method for predicting swirling compressible flow through a nozzle, given conditions at a reference section. The principal assumption they used is that changes in nozzle cross-sectional area are sufficiently gradual for the radial velocity component to be neglected at each section. This method was used to determine choked-flow conditions in the case of solid-

body rotation at the throat for different swirl intensities and values of the ratio of specific heats. An approximate analysis valid for low swirl intensities was developed. It was found that neither of the two aforementioned choking criteria gives correct results, although the maximum-mass-flux criterion proved to be a good approximation for moderate swirl. The main conclusion of practical importance was that the introduction of swirl to compressible nozzle flows need not lead to a significant reduction in specific thrust. It was also reported that for a fixed geometry the introduction of swirl is accompanied by a considerable reduction in both mass flux and thrust. However, if the mass flux is kept constant, the reduction in specific thrust is very moderate.

Lewellen et al. (1969) developed an approximation that can be used to determine how swirl affects the choking constraint on flow through the throat of a nozzle. It was found that the mass flow rate through a choked nozzle can be sharply reduced by introducing a tangential component of velocity into the flow. Moreover, the choking constraint imposes a limit on the maximum tangential Mach number that can be achieved in a vortex tube, even when an infinite pressure ratio is available. The theoretical choking constraint was used to speculate on the limiting tangential Mach number. It was concluded that this limiting value is 1.2, which is consistent with the experimental observations of Roschke and Pivirotto (1965) who reported a value of 1.05. Toomre (1963) achieved a value of 1.03, independent of mass flow rate, and Pinchak and Poplawski (1965) reported a value of 1.18 in a vortex chamber designed especially to circumvent the difficulties of end-wall dissipation.

The structure of highly underexpanded nozzle jets was investigated experimentally and analytically by Adamson and Nicholls (1959), who presented a method for calculating the position of the first Mach disk. In their calculation, the axial pressure distribution on flow centerline downstream of nozzle exit (calculated by method of characteristics) was used to define

a fictitious nozzle extension. The Mach disk was then assumed to exist at the point where atmospheric pressure would be attained upstream of the disk, i.e., the latter was assumed to exist at the end of fictitious nozzle extension. Physical arguments were employed to extend the analysis to nozzles with supersonic exit Mach numbers. An approximate method for computing the jet boundary, up to the point of maximum jet area, was also given. The analytical results compared favorably with experimental data at relatively low nozzle pressure ratios.

Lewis and Carlson (1964) experimentally determined the distance from nozzle exit plane to the first Mach disc in gas-only and gas-particle jets issuing from underexpanded supersonic nozzles. An empirical correlation of the data was presented which is valid for both jet types and incorporates the effect of gas specific-heat ratio. In a relevant experimental investigation Crist et al. (1966) studied the structure of underexpanded jets with stagnation pressures up to 15,000 psia, ambient pressures down to 100 μHg, and stagnation temperatures up to 4200 K. The location of first Mach disk was found to be insensitive to the ratio of specific heats, nozzle-lip geometry, and absolute pressure. For over-all pressure ratios up to about 300,000 the location of Mach disk was found to vary as the square root of overall pressure ratio. The diameters of Mach disk, jet boundary, and intercepting shock were found to increase with decrease in specific-heat ratio and to decrease at high stagnation density, where intermolecular forces become important. At high-pressure ratios, the ratio of Mach-disk diameter to Mach-disk position appeared to be constant for a given gas. It was also found that the properties along jet axis can be approximated by the properties of a flow through a hypothetical conical nozzle whose half-angle is given as a function of specific heat ratio. A simplified expression for the distribution of Mach number along the jet axis was given to good approximation as a function of specific-heat ratio.

Gostintsev et al. (1969) studied an underexpanded supersonic swirling gas jet issuing from a convergent nozzle. They showed that the effect of rotation on the wave structure of axisymmetric jet is qualitatively analogous to the effect of reduction in overpressure ratio. Using formulas for spiral isentropic flow, an approximate expression was obtained for estimating the location of first Mach disc in the swirling flow downstream of nozzle exit. Batson and Sforzini (1970) also studied the structure of swirling flow through a convergent nozzle with emphasis on the effect of swirl on flowfield, thrust, and mass flow produced by nozzled devices, such as jet engines and spin-stabilized rockets. It was reported that the axial velocity component increases, whereas the tangential one decreases, as the flow passes through nozzle throat.

In another study, which has application in ramjets and turbojets, Kornblum et al. (1986) presented an analytical performance prediction methodology for annular propulsive nozzles, with swirl introduced in the combustor upstream of nozzle. This methodology was applied to a specific nozzle design for a free-vortex swirl distribution. The results showed that the discharge coefficient, thrust, and specific impulse decrease as the amount of swirl is increased. However, for the values of swirl often encountered in ramjets and turbojets, the effect of swirl on nozzle performance is small and can be neglected in preliminary design and performance calculations. Application of the prediction methodology to swirl distributions other than free vortex was recommended for future work. Hoffman et al. (1987) followed this recommendation by applying the same methodology to investigate the effects of swirler design on nozzle performance. Four types of swirlers were investigated, namely free-vortex, constant-angle, forced-vortex, and Rankine-vortex swirlers. The computed results indicated again that swirl decreases the discharge coefficient, thrust, and vacuum specific impulse. The decrease in discharge coefficient correlates with the mass-averaged swirl for all four types of swirlers. The decrease in vacuum specific

impulse is, on the other hand, a function of swirler design. Forced-vortex swirlers induce the least reduction in specific impulse, whereas free-vortex ones induce the greatest reduction.

Naumova and Shmyglevskii (1967) demonstrated with a simple example that avoidance of flow rotation is a limitation that might reduce the thrust of supersonic nozzles. Maximum thrust can be achieved with a nozzle length that permits obtaining uniform flow at the exit. If the length limitation does not permit this, then the use of freedom in gas rotation might increase the nozzle thrust. Dutton (1987) investigated swirling flow in supersonic propulsion nozzles both numerically and experimentally. Computations were performed for a range of nozzle geometries, inlet swirl profiles, and swirl strengths. A time-dependent finite-difference technique was developed. The numerical results demonstrated, in agreement with the experimental data, that swirl has a minor effect on the specific impulse efficiency. However, relatively large reductions in nozzle discharge coefficient were computed with swirl. It was also reported that for conventional converging and converging-diverging nozzles, the major effect of swirl on flowfield is confined to the core region, with much less pronounced effect at the walls.

Vortex enhancement of supersonic mixing was studied experimentally by Settles (1991). Swirl was utilized to enhance shear layer growth and mixing. It was concluded that swirl enhances compressible mixing; the degree of enhancement increases with increasing swirl. Settles also reported that the effects of convective Mach number and density ratio on the enhancement effect of swirl are still unknown and were thus recommended for future work.

In an experimental investigation, which is very pertinent to this current study, Lee et al. (2004) examined the near-field flow structure of underexpanded coaxial swirl jets. Swirl streams were issued from a secondary annular nozzle, while a primary inner nozzle provided the underexpanded free jets. The interactions between the annular swirl and the underexpanded core

jets were examined, in order to quantify the effects of the former on the latter. It was shown that the presence of an annular swirl stream causes the core-flow Mach disc to move further downstream, with an increased diameter. In another pertinent study Lee et al. (2006) investigated the effect of nozzle-inlet configuration on underexpanded swirling jets, which were generated by a convergent nozzle with four tangential inlets at the supply chamber. The nozzle-inlet configuration was modified by using different plugs, holes, and needles, which were also utilized for measuring the flow properties at nozzle inlet. The experimental results showed that the presence of a coaxial needle inside the nozzle supply chamber controls the properties of generated underexpanded swirling jets. The structures of these jet flows are highly dependent on the detailed configuration of nozzle supply chamber.

Murakami and Papamoschou (2001) examined flow structure and mixing enhancement in 2D and axisymmetric supersonic jets surrounded by secondary annular subsonic coaxial ones. The supersonic jets were issued from a convergent-divergent nozzle operated at off-design conditions. It was shown that the mixing enhancement using secondary parallel injection (referred to as MESPI by the researchers) halves the length of potential core in both round and 2D jets. A short distance past the potential core, mixing enhancement caused a reduction in centerline Mach number by 30% in round jets and 20% in 2D ones. The corresponding reduction in peak molar concentration of a scalar injected in the primary flow was 65% in round jets and around 40% in 2D ones.

Knowles (1992) examined the practical possibility of reducing shock-associated noise and controlling mass flow in a supersonic jet by means of swirl. It was found that nozzle performance does not degrade by the introduction of swirl; on the contrary, specific thrust can be increased with swirl. However, the swirl velocity profile needs to be carefully controlled. It was

recommended that specific case studies be made to consider swirl in variable engine cycles. Carpenter (1985) developed a linearized theory for underexpanded inviscid supersonic jets with arbitrary initial swirl. Estimates were made of the effect of swirl on the total radiated sound power of shock-associated noise. It was found that this noise can be greatly reduced, or even eliminated, at sufficiently high swirl levels, which can be achieved at the expense of a very small thrust loss. Noise elimination was believed to be due to enhanced mixing that leads to the disappearance of some initial shock cells.

In another study more pertinent to mixing in free supersonic flows Yu et al. (1998) experimentally examined mode-switching phenomena of supersonic jets with swirl. They observed that the shock-cell spacing of swirling jets is smaller than that of non-swirling ones, which suggests enhanced mixing. In non-swirling compressible jets, the typical two-dimensional vortex roll-up is believed to be suppressed, and mixing and entrainment are reduced, as compared to incompressible jets. Therefore, to counter the adverse effects of compressibility on mixing, adding swirl to a supersonic jet is favorable. The enhanced entrainment and mixing in swirling supersonic jets is thought to be due to the inherent three-dimensionality associated with the axial component of turbulent vorticity in swirling jets. Yu (1997) studied underexpanded supersonic jets to determine the effect of swirl on mixing efficiency. The screech tones, which result from the interaction of shock waves with unstable jet boundaries, were examined at different degrees of swirl for their effect on mixing. Implication of enhanced mixing was discussed. It was also reported that swirl did not eliminate shock cells, nor did it affect their quasi-periodic nature, in spite of the generation of a recirculation zone in strongly swirling jets.

The investigation described in the present work contributes significantly to the understanding of the effect of imparting swirl to supersonic-nozzle airflow on flow structure and

mixing. Such effect has not been fully quantified in the literature yet, due to the inherent three-dimensionality of the problem. Some questions remain unanswered in past research, particularly regarding the nozzle choking criteria with swirl. Non-reacting conditions are considered here, wherein inert gases are used to simulate gaseous hydrogen fuel injected coaxially in underexpanded shock-rich nozzle airflow. The focus is to quantify the effects of swirl, as well as relative Mach number and air-fuel density ratio on flow structure and mixing. An analysis of the effect of convective Mach number across air/fuel shear layer is also conducted.

III. EXPERIMENTAL SETUP AND NUMERICAL SIMULATION ASSUMPTIONS

3.1 Swirling Supersonic Nozzle

The nozzle used to carry out the present investigations is shown schematically in Figure III-1. It can be seen that the nozzle is of the convergent type, which means that the examined supersonic airflow is always underexpanded. The nozzle has inlet and throat diameters of 50 and 11 mm, respectively. Linear reduction of diameter occurs over an axial distance of 100 mm, which results in a 22° included angle. The reservoir section of the nozzle extends axially for 60 mm upstream of the nozzle. The tangential-axial-entry technique is used for swirl generation with four equally-spaced circular tangential entries, each 12.7 mm (0.5 in) in diameter. This technique was proven in previous research to be an efficient method for generating supersonic

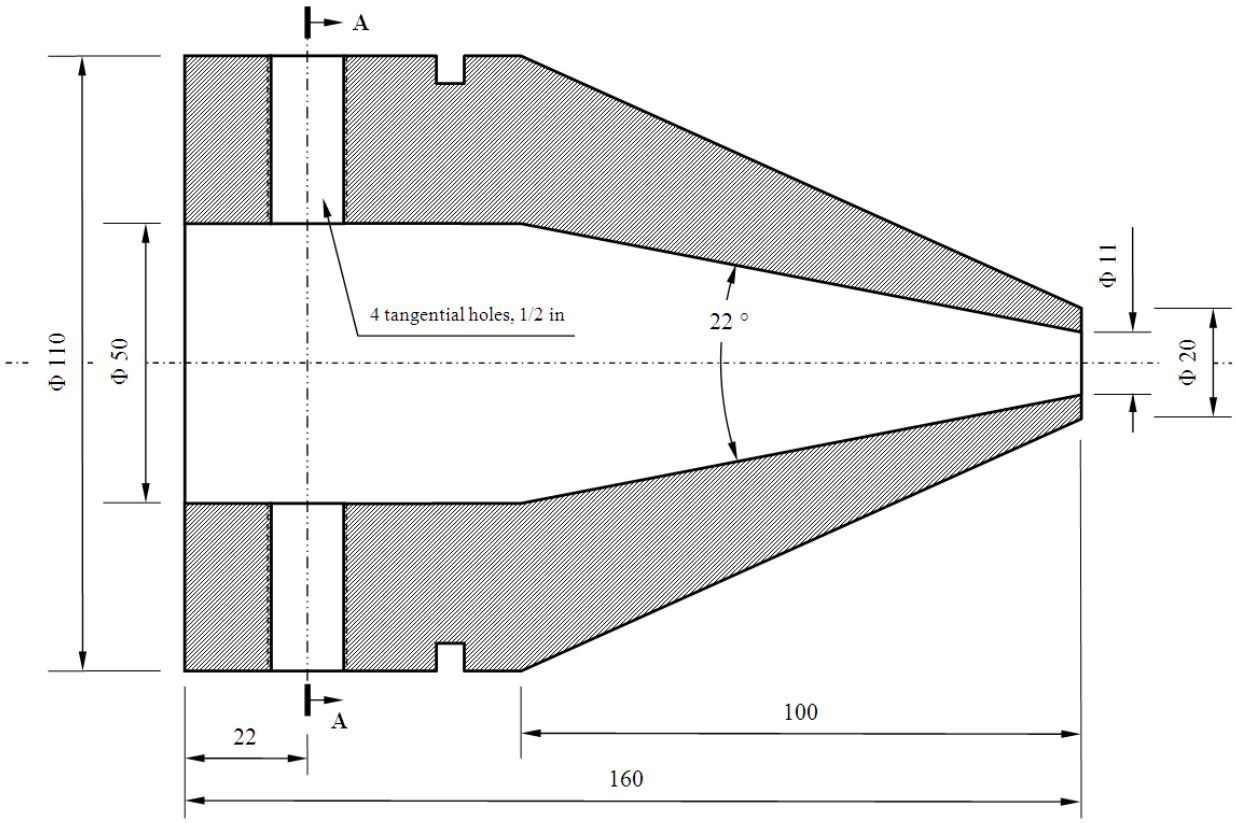

All dimensions are in mm

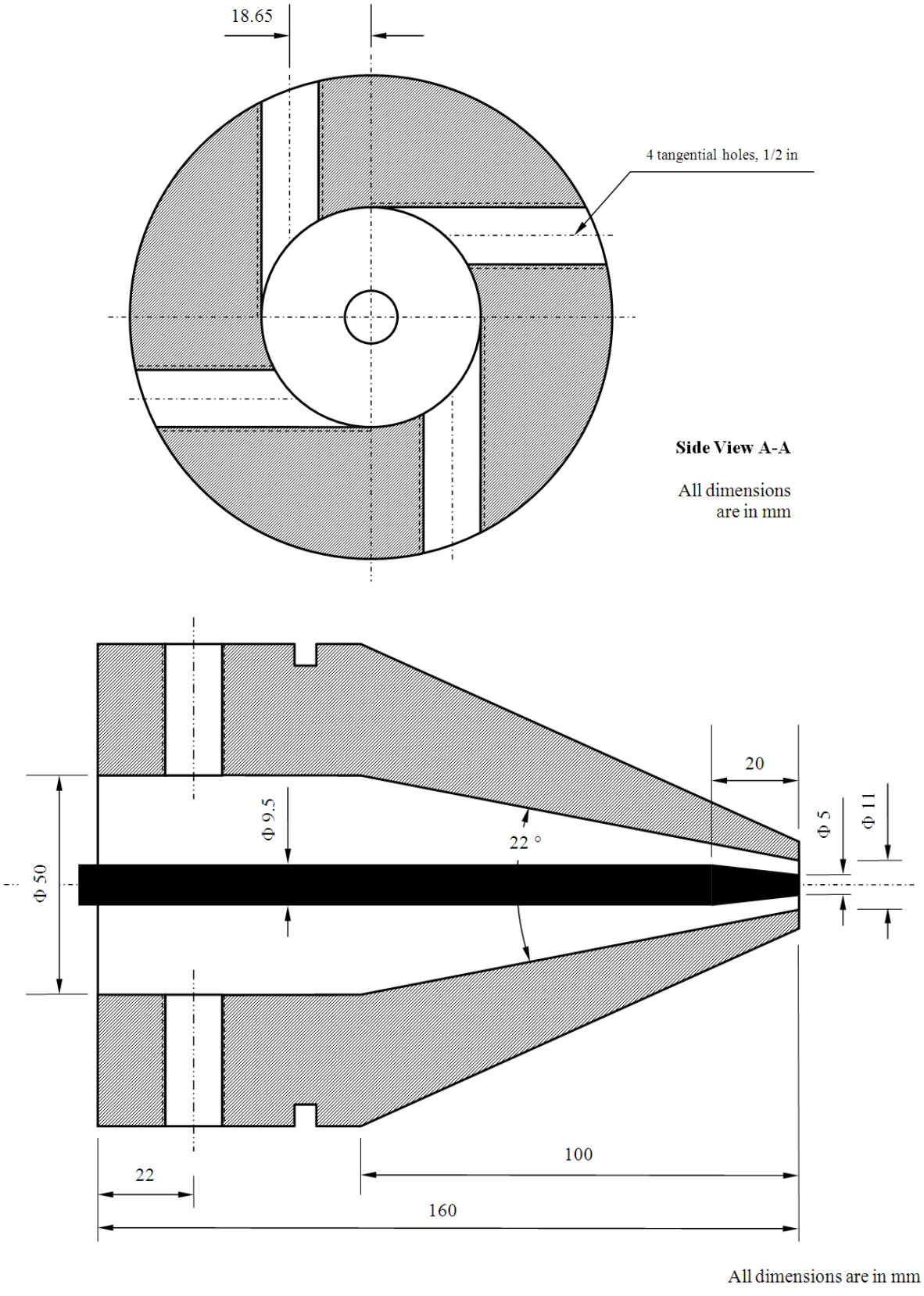

Figure III-1. Supersonic nozzle with swirling capabilities

swirling jets [Cutler et al. (1995) and Linck (2006)]. All four tangential entries are located at the same axial location within the reservoir section, namely 38 mm upstream of the nozzle. The axis of each entry is located 18.65 mm away from the corresponding parallel nozzle center-plane (see side view A-A), which ensures that the entry is tangent to the inner wall of reservoir section. This geometry allows for attaining the greatest possible degree of swirl (for the aforementioned dimensions) and the smoothest admission of swirl air into the nozzle.

Coaxial injection of fuel is implemented. A non-recessed stainless-steel system injects fuel at nozzle throat. The injection system has outer and inner diameters of 9.5 mm (3/8 in) and 4.0 mm, respectively. In order to avoid excessive blockage of nozzle throat by the injection system, its tip is tapered to an outer diameter of 5.0 mm over an axial distance of 20 mm. The presence of this non-recessed injection system alters the dimensions of available air passage and consequently the nozzle choking characteristics. Its effective inlet and throat areas are now 1892 and 75.4 mm^2, respectively, which results in an effective area ratio of 25.

The nozzle was machined out of a single aluminum rod 110 mm in diameter. Aluminum was preferred to stainless steel because the former has a higher thermal conductivity, which prevents overheating of nozzle walls during combustion experiments. The higher conductivity allows radiated heat to be dissipated effectively through the thick nozzle walls that act as a heat sink. The dissipated heat is removed by forced convection of the entrained ambient cold air through the large surface area of nozzle external walls. Preliminary calculations were carried out to optimize the thickness of nozzle lip for structural rigidity and maximum entrained ambient air. A 4.5-mm lip thickness at the exit plane allowed for significant entrainment as well as adequate rigidity for machining the nozzle exit to the desired surface finish and dimensional tolerance.

3.2 Air Delivery and Control Systems

Figure III-2 shows a schematic of the air delivery and control systems upstream of the nozzle. Compressed air is provided by main building compressor at 160 psig stagnation pressure through a 2-in line. A main mechanical gate valve allows for gradual increase of pressure and flow rate inside the delivery and control systems. This is dictated by the manufacturer of utilized thermal airflow controllers, in order to avoid damaging the seals of their control valves. See Table III-1 for the specs of these thermal controllers. After the gate valve the air line splits into two 1-in lines that convey the axial and tangential components of airflow. Each component is metered and controlled by a thermal controller of 1000 SLPM full scale. Such controllers can be operated in either of two modes, namely control flow rate or control exit pressure. The first mode allows for controlling the volume flow rate, independent of exit pressure (within linearity range),

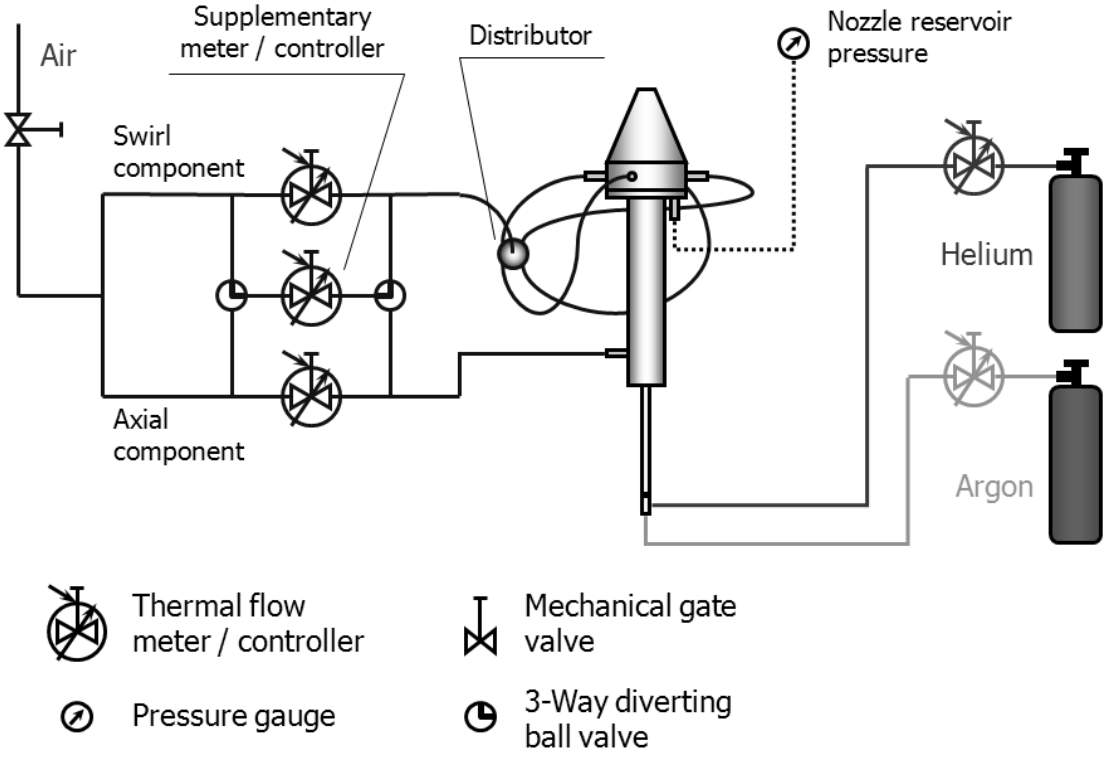

Figure III-2. Schematic of air delivery and control system

Table III-1. Specifications of thermal flow controllers

Property	**Value**
Make and model	Aalborg, GFC mass flow meters / controllers
Accuracy	±1.5% of full scale, including linearity for gas temperatures 15 – 45 °C and pressures 0.35 – 10.1 bar
Repeatability	±0.5% of full scale
Temperature coefficient	0.15% of full scale /°C
Pressure coefficient	0.15% of full scale /bar
Response time	Time constant = 800 ms Approximately 2 seconds to within ±2% of set flow rate for 25% to 100% of full scale flow rate
Set point	Remote, 0 – 5 V (≡ 0 – 100% of full scale)
Mode of operation	Control flow rate, or control exit pressure
Principle of operation	▪ Stream of gas entering the flow controller is split by shunting a small portion of the flow through a capillary stainless steel sensor tube. Remainder of gas flows through the primary flow conduit ▪ Geometries of primary conduit and sensor tube are designed to ensure laminar flow in each branch ▪ According to principles of fluid dynamics, both volume flow rates are proportional to one another. Therefore, flow rate measured in sensor tube is directly proportional to the total flow through the controller ▪ Heat flux is introduced at two sections of the sensor tube by means of precision wound heater-sensor coils. Heat is transferred through the thin wall of sensor tube to the gas flowing inside. This heat is carried by the gas stream from the upstream to the downstream coil windings ▪ The resultant temperature-dependent resistance differential is detected by an electronic control circuit. The measured gradient at sensor windings is linearly proportional to instantaneous volume flow rate

whereas the second mode allows for controlling the exit pressure while the flow rate is just metered. Since the nozzle choking criteria dictate the mass flow rate (for a given reservoir pressure), the controllers were operated in the second mode to allow for controlling the nozzle reservoir pressure while metering the flow rate that is conveyed to the nozzle. Two important remarks are to be made here. First, the controllers give a volume-flow-rate reading in SLPM. This reading is corrected manually for the exit pressure and converted to a mass-flow-rate value before it is used in any further analyses. Second, due to the friction losses inherent in the air lines between controllers and nozzle, both controller-exit pressure and nozzle-reservoir pressure are monitored, and only the latter is used in the analysis of nozzle choking criteria.

In the case that the desired flow rate of either axial or tangential components exceeds the full scale of its controller, a third supplementary controller is connected in parallel to the "choked" one via two 3-way diverting ball valves, in order to provide the required complementary flow rate (see Figure III-2). The following example explains this situation. All analyses of this study have been conducted at an air flow rate of 175 g/s. Under swirling conditions the entire airflow was directed to nozzle tangential entries with no axial component. The necessary reservoir pressure to achieve that air flow rate is 8.82 bar, which corresponds to controller-exit pressure and density of 9.05 bar and 10.51 kg/m^3, respectively. The resulting volume flow rate is 999 SLPM, i.e., the swirl-air controller is sufficient. Under non-swirling conditions, on the other hand, the necessary reservoir pressure to achieve the same air flow rate is 7.91 bar. (The need for higher reservoir pressures with swirl will be explained in detail in the next chapter.) The corresponding controller-exit pressure and density are 8.16 bar and 9.48 kg/m^3, respectively, which results in a volume flow rate of 1108 SLPM. The supplementary

controller is thus activated, and 1000 SLPM (≡ 90.25% of flow rate) are conveyed through axial-air controller, while the rest is conveyed through supplementary controller.

After the axial component has been controlled, it is forwarded to a conditioning chamber upstream of the nozzle. See Figure III-3 for a schematic of this chamber. It was designed to fulfill two tasks, adjust the axial air component before conveying it to the nozzle and provide support for the coaxial 3/8”-tube of fuel-injection system. Air enters radially at the bottom of chamber, where it turns to the axial direction. A flow straightener is incorporated to ensure an axisymmetric velocity profile at nozzle inlet. The tangential component, on the other hand, is forwarded to a distributor that splits the flow equally among four lines. This distributor is simply a small cylindrical chamber with one axial inlet and four identical 90°-spaced radial outlets. To ensure equal distribution of swirl air, the lines connecting the distributor outlets to the four tangential entries of the nozzle are of equal length. All four lines have a 1/2” internal diameter.

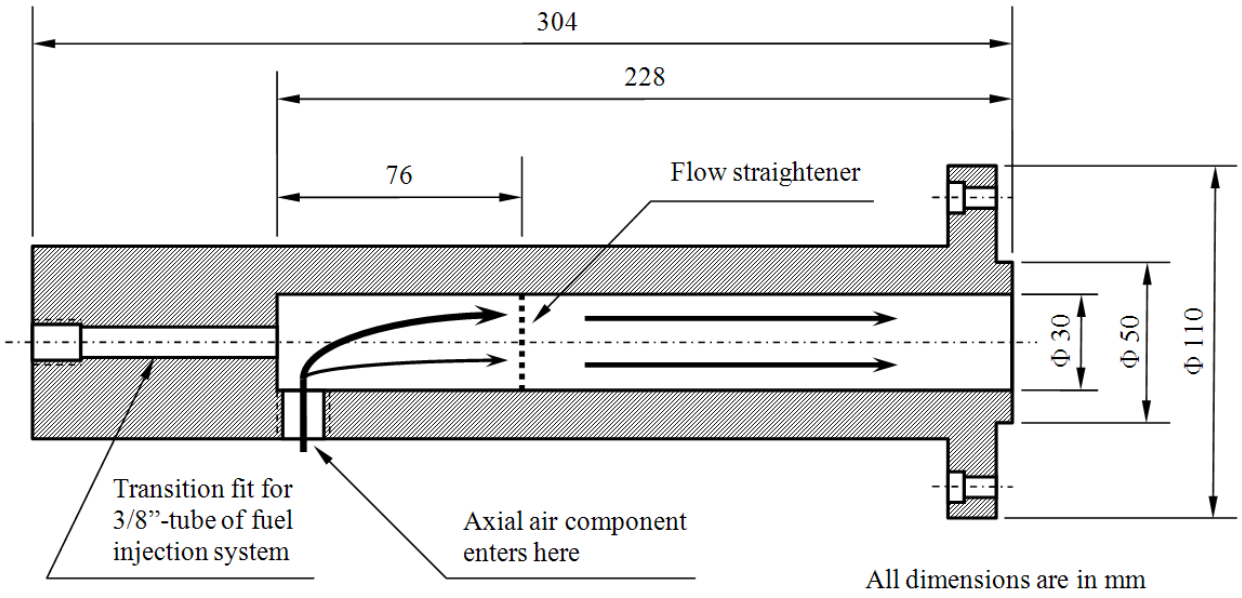

Figure III-3. Conditioning chamber for axial air component

As mentioned earlier and seen from Figure III-3, the conditioning chamber provides means for supporting the 3/8”-tube of fuel-injection system through the 76-mm transition-fit hole at the end. It should be noticed, however, that downstream of this hole the injection system is not supported for 228 mm inside the conditioning chamber and another 155 mm inside the nozzle. This 383-mm cantilever section of fuel-injection system was found to vibrate violently during experiments, especially with swirl. Therefore, a support flange (Figure III-4) was designed and installed between conditioning chamber and nozzle to provide the missing support close to the exit of injection system and maintain its concentricity with respect to the nozzle. This flange comprises a conical sleeve that embraces the injection system. The sleeve outer diameter decreases in the direction of flow from 19.7 to 9.6 mm over an axial distance of 100 mm, in order to provide streamlined performance and prevent any blockage close to the nozzle exit. The sleeve is held in place by three spokes extending to the support flange. The spokes are distributed evenly at 120° along the tangential direction. Their 5-mm thickness has been optimized to provide structural rigidity yet minimum blockage to the incoming axial component of airflow.

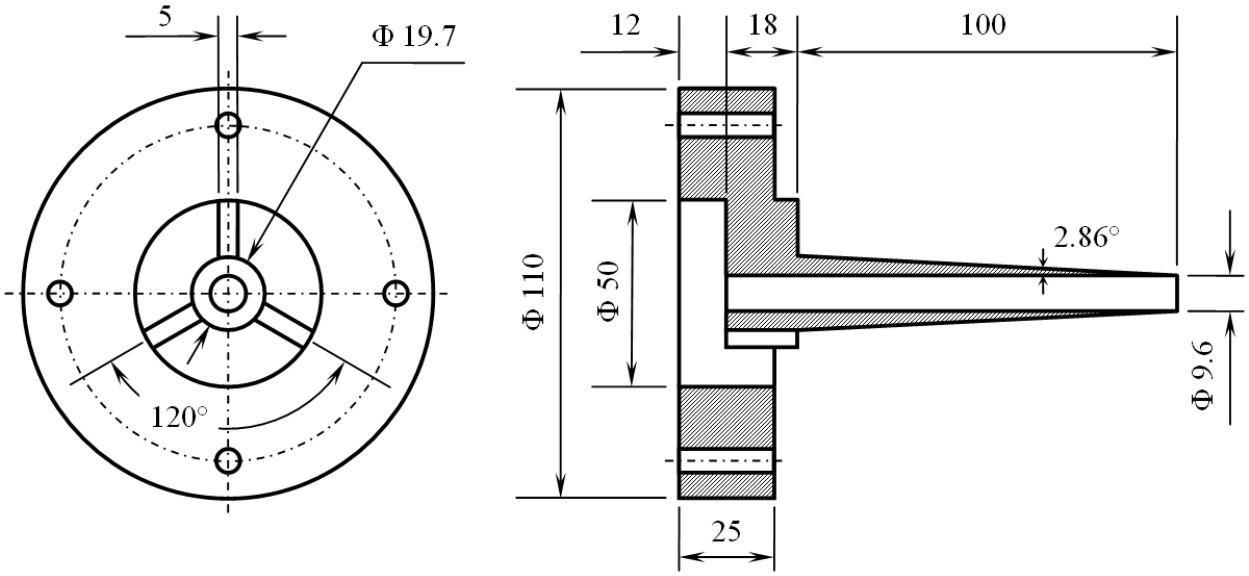

Figure III-4. Support flange for fuel-injection system

To get a better understanding of how the support flange fits between the conditioning chamber and nozzle, Figure III-5 shows the assembly of all three. It should be noted here that the spokes of support flange are located axially upstream of the nozzle tangential entries and do not affect the flowfield of tangential air component. Some wakes might exist in the flowfield of axial component behind the spokes, but the supersonic flow exiting the nozzle was found to be fully axisymmetric under both non-swirling and swirling conditions. It should also be noted that the conical sleeve of support flange ends 55 mm upstream of nozzle exit, which further ensures no blockage close to the throat.

3.3 Nanosecond Schlieren Setup

The primary experimental means of shock-structure visualization in this study is the nanosecond Schlieren diagnostic technique. Schlieren imaging yields the first derivative of refractive index in the test region, thus giving an estimate of the density gradients within flowfield. The intensity of captured light can be further processed using image-processing techniques to obtain more quantitative information of the shock structure.

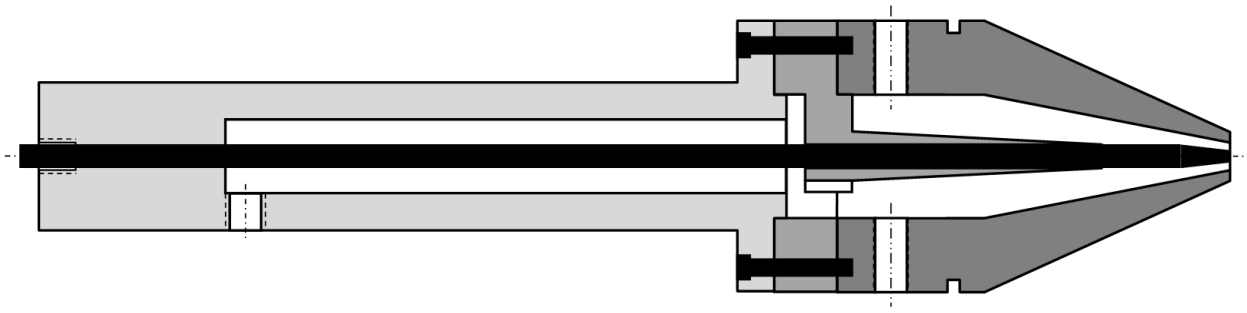

Figure III-5. Assembly of nozzle, support flange, and conditioning chamber

Figure III-6 shows a schematic of the utilized setup. The light source is a 532-nm Q-switched Nd:YAG laser with pulse duration of only 5 ns, which explains the term "nanosecond Schlieren" and makes this setup unique, compared to conventional Schlieren setups. The nanosecond light duration allows for capturing instantaneous images of the flowfield. No fluctuations are thus accumulated or averaged on the image, which allows for accurate visualization of the shock structure. See Table III-2 for the laser specifications.

Due to the fact that the intensity of laser light is too high for safe camera operation, the laser was equipped with neutral-density filters that reduce its light intensity. The divergence of the collimated beam is then increased by means of a plano-concave lens of 4-ft focal length. The divergent beam fully illuminates a 6-in concave mirror that has a 4-ft focal length as well. This mirror reflects the light in a collimated fashion through the test section, which is essential for avoiding skewed perspective of flowfield. After penetrating the flow, the light is focused by another 6-in concave mirror of 2-ft focal length. A knife-edge aperture intercepts the light at the focal point of second mirror to fulfill the Schlieren principles. The resulting images are then captured at a resolution of 1024 x 1024 pixels using a high-speed camera that is synchronized with the laser. See Table III-3 for the specifications of this camera.

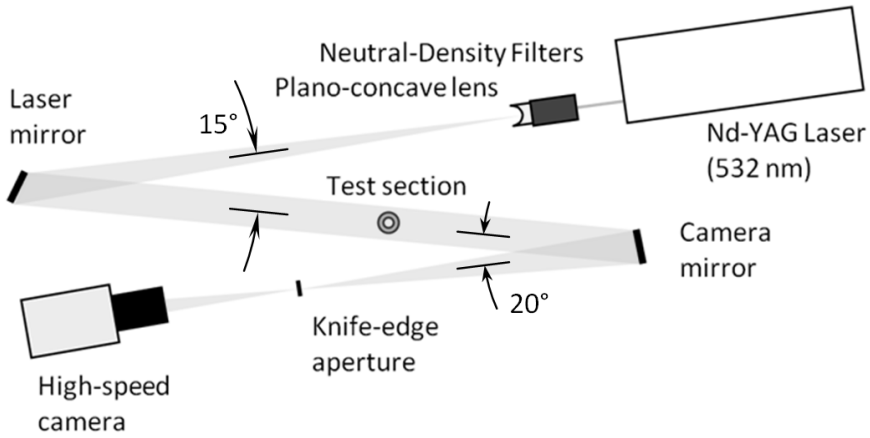

Figure III-6. Schematic top-view of nanosecond Schlieren setup

Table III-2. Specifications of Nd:YAG laser

Property	**Value**
Make and model	Quantel Laser, Brilliant b
Type	Nd:YAG, Q-switched
Wavelength used in experiments	532 nm
Energy per pulse	400 mJ
Repetition rate	10 Hz
Energy stability - shot to shot (%)	±4 (1.3)
Power drift	±5%
Pulse duration	5 ns
Linewidth standard	1.4 cm^{-1}
Pointing stability	< 50 μrad
Divergence	0.5 mrad
Beam diameter	6 mm

Table III-3. Specifications of high-speed camera

Property	**Value**
Make and model	Photron, ultima 1024
Resolution	1024 x 1024 at 1000 fps
Frame rates	60 – 16000 fps
Shutter type, speed	Global electronic shutter, 2 ms – 7.8 μs
Sensor	CMOS with 12-μm square pixels
Memory / record time	512 MB / 1.0 s (at 1000 fps)

Two important points are to be highlighted here. First, the axes of light beam remain within one horizontal plane throughout the whole setup, which is again essential for avoiding skewed perspective of flowfield. Second, a small amount of inevitable skew is induced by the finite 15° and 20° angles between the axes of light beam (see Figure III-6). This skew is evident in form of an oval-shaped captured image, where the vertical length scales are not distorted but the horizontal ones appear smaller than they actually are. In other words, the image has a horizontal diameter smaller than the vertical one. To minimize this type of skew the angles between light axes should be kept as small as possible. However, the aforementioned values of mirror diameters and focal lengths prevent the use of smaller angles, because otherwise the light would pass more than once through the test section, resulting in multiple appearances of flowfield on the captured image. A non-optical solution was devised for this problem, where the skew was treated digitally by stretching the image horizontally by a certain factor that recovers the image circularity.

3.4 Condensate-Seeded Mie-Scattering Setup

Since Schlieren is incapable of providing solid direct quantification of the variation of mixedness within the flowfield, a nanosecond condensate-seeded Mie-scattering diagnostic technique was developed and utilized to achieve this goal. The basic principle of this technique is to saturate either the air or fuel flow with the vapor of a volatile material upstream of nozzle. As the temperature decreases during expansion, some vapor has to condensate back to form a fog or mist of submicron seed particles that are small enough to follow the flow faithfully. When illuminated, these particles emit a Mie-scattering signal that is used for mixedness quantification. An ideal condensate-seeding material would have the following properties:

- High vapor pressure and evaporation rate, i.e., high volatility, in order to easily vaporize the liquid and saturate main flow with its vapor
- Boiling point close to the temperature of main flow (300 K in this case)
- Low latent of vaporization to prevent inducing great changes in flow temperature during evaporation or condensation
- Low liquid density, which results in a smaller mass of the condensate particle (for a certain particle size or volume). A lighter particle has lower inertia and can follow the local flow more faithfully
- Ratio of specific heats of vapor close to that of main flow, in order to minimize the changes in flow properties due to the use of condensate-seeding material
- Low liquid surface tension and low viscosity, if liquid vaporization is induced through solid atomization. Lower surface tension results in spray droplets of larger surface to volume ratio, which aids in droplet evaporation
- Low melting point to prevent freezing of seeding particles in cold supersonic flowfield during or after expansion

In search for the condensate-seeding material that best meets the above requirements and can be used to visualize the airflows examined here, four materials were considered, namely diethyl ether (C_2H_5–O–C_2H_5), n-pentane (C_5H_{12}), acetone (CH_3–CO–CH_3), and water. Table III-4 lists the physical properties of all four materials. The following observations can be made.

a) Diethyl ether has higher vapor pressure and evaporation rate and lower latent heat of vaporization, viscosity and melting point.

b) n-pentane has a lower liquid density.

c) Both diethyl ether and n-pentane have similar molecular weights, boiling points (close to 300 K), and ratios of vapor specific heats. Even the values of liquid surface tension are almost the same, keeping in mind that the 15.5-dyn/cm value of n-pentane is at 25 °C, which means that it will be slightly higher at 20 °C.

d) Diethyl ether is a dipolar molecule, whereas n-pentane is not.

Table III-4. Physical properties of potential liquids for use as condensate-seeders

Property	**Diethyl ether**	**n-Pentane**	**Acetone**	**Water**
Chemical formula	$C_2H_5–O–C_2H_5$	C_5H_{12}	$CH_3–CO–CH_3$	H_2O
Molecular weight [g/mol]	74	72	58	18
Vapor pressure [mmHg] (at 293 K)	440	426	400	27
Specific evaporation rate (relative to butyl acetate)	37.5	28.6	7.7	*(N/A)*
Boiling point [K] (at 1 atm)	308	308	330	373
Latent heat of vaporization [J/g] (at 300 K)	355	360	518	2257
Molecular dipole moment [D]	1.15	0	2.91	1.85
Liquid density [kg/m^3] (at 300 K)	713	626	790	996
Ratio of specific heats of vapor	1.081	1.070	1.11	1.31
Liquid surface tension [dyn/cm] (at 20 °C)	17.0	15.5 (25 °C)	23.3	72.8
Viscosity [cP] (at 300 K)	0.224	0.240	0.320	1.000
Melting point [K] (at 1 atm)	157	143	178	273

References for table data:

http://www.jtbaker.com
http://cameochemicals.noaa.gov
http://macro.lsu.edu
http://www.wikipedia.org
Griffiths, E. and Awbery, J. H., "The Latent Heat of some Refrigerants," Proceedings of the Physical Society, Vol. 44, No. 2, 1932, pp. 121-131.

Based on the aforementioned discussion of ideal condensate-seeding material, it can be concluded that diethyl ether is the best candidate. Besides, both diethyl ether and n-pentane were tested experimentally, and molecular dipolarity turned out to be of critical importance. Dipolar materials are known for having higher attraction forces between their molecules, which is not to be confused with the surface-tension force of a droplet in air. It was noticed experimentally that the droplets of diethyl ether formed by condensation are larger in size than those of n-pentane. Moreover, a much stronger light-scattering signal was observed with diethyl ether, which implies that the size of ether droplets allows for inducing a Mie-scattering signal, whereas n-pentane droplets are too small and thus reflect a much weaker Rayleigh-scattering signal. It should be noted here that no actual measurements of particle size were made to concur this statement. Nevertheless, these observations agree well with the work of Brummund and Mesnier (1999), where planar Mie- and Rayleigh-scattering were used for direct visualization of the shear/mixing layer between hydrogen fuel and Mach-2.0 airflow in a scramjet chamber. The evolution of this layer downstream of injector was visualized by Rayleigh-scattering directly from the gas molecules and by Mie-scattering from TiO_2 seed particles.

In conclusion of the analysis of optimum condensate-seeding material, diethyl ether was selected. See Figure III-7a for a schematic of the nanosecond Mie-scattering setup. Two metered streams of liquid diethyl ether (one for each air component) are solid-atomized through 0.02-in orifices, and the resulting spray jets are injected into the lines of high-pressure airflow supplied to nozzle. The spray droplets evaporate rapidly upon injection, and the vapor mixes thoroughly with air saturating it. The axial component is injected two feet upstream of conditioning chamber, while the tangential component is injected two feet upstream of four-way distributor. Controlled flow rates are injected, in order to provide adequate visualization of flowfield while

preventing over-saturation of airflow, which can result in the formation of a liquid diethyl-ether film on the internal walls of nozzle or air delivery system.

The supersonic flowfield is illuminated along a centerline plane using the same 532-nm Q-switched pulse laser of Schlieren setup. The nanosecond light duration prevents the seeding particles from creating light streaks on the captured images. Since the laser beam is too large (6 mm diameter) to be converted into a thin light sheet, an aperture is used to block the annular area of beam cross-section, allowing for a 1-mm core to propagate. A cylindrical lens of 2-mm diameter is then used to convert the 1-mm light beam into a sheet. The lens is located 2.5 ft away from the nozzle, as shown in Figures III-7b and III-8. This long distance is necessary to ensure almost uniform thickness and light intensity of the laser sheet within the region of interest inside flowfield (55 mm ≡ five nozzle diameters). Note that both thickness and light intensity decrease in the vertical direction away from the horizontal center plane of the sheet.

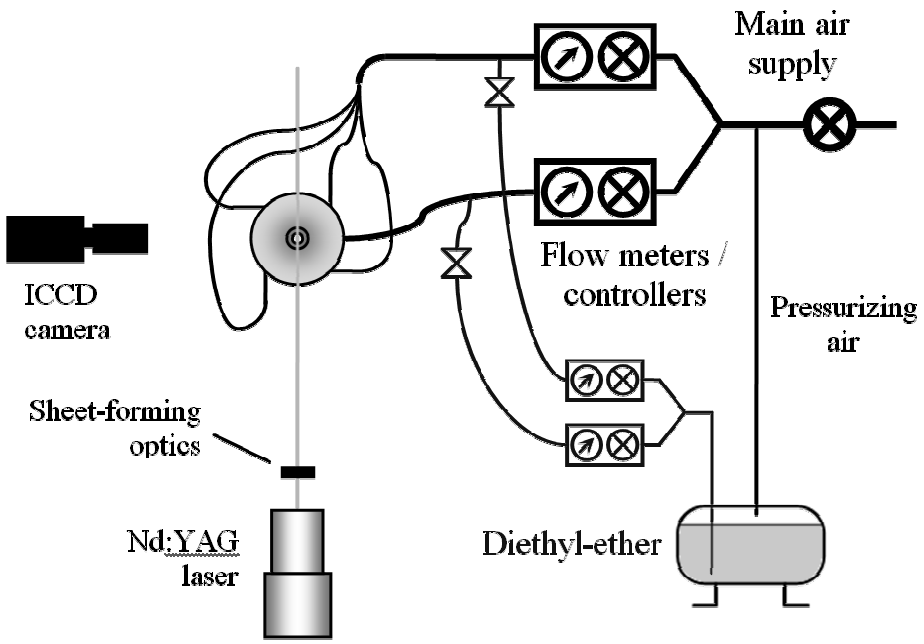

Figure III-7a. Schematic of condensate-seeded Mie-scattering setup

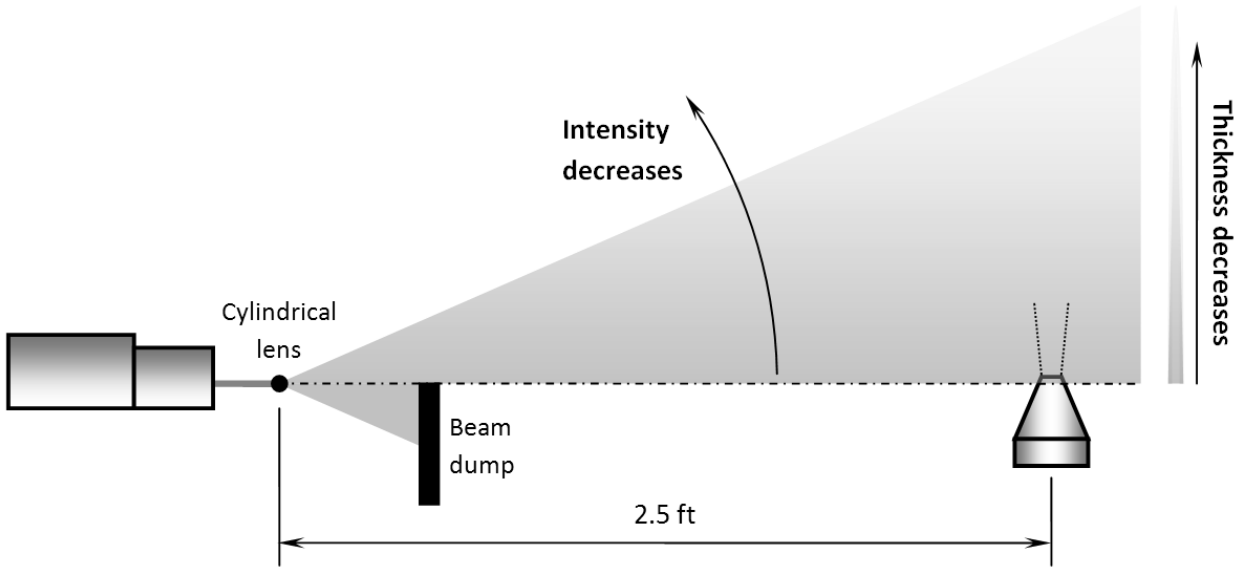

Figure III-7b. Schematic presentation of light sheet

Figure III-8. Photos of Mie-scattering setup

The Mie-scattering signal is captured using a Princeton Instruments PI-MAX2:1003 UNIGEN2 digital ICCD camera operated in synchronization with the laser and aligned at right angles to the light sheet. See Table III-5 for the specifications of this camera. Although the right-angle alignment does not allow for capturing the greater intensity of forward scattering, it was used to provide a non-skewed perspective of flowfield. A resolution of 1024 x 1024 pixels and a

Table III-5. Specifications of ICCD camera

Property	**Value**
Make and model	Princeton Instruments, PI-MAX2:1003
CCD	
Image sensor	Kodak KAI-1003; scientific grade; interline CCD
CCD format	1024 x 1024 imaging pixels Pixel size = 12.8 x 12.8-µm Detector dimensions = 13.1 x 13.1 mm (18.5 mm diagonal)
Pixel Full Well	150 ke-
Dark current	0.5 e-/pixel/s @ -20 °C
Deepest cooling temperature	-20 °C (air cooled)
Vertical shift rate	4 µsec/row
Intensifier	
Type	Unigen II
Method of coupling to the CCD	1:1 fiber optic
Intensifier input window	Fiber
Wavelength range / Quantum efficiency	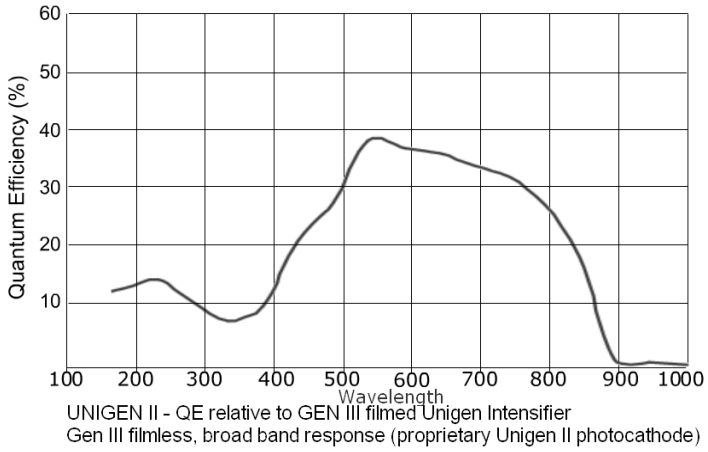
Minimum Gate Speed (optical FWHM)	< 2 ns
Maximum repetition rate (sustained/burst)	50/500 kHz
Resolution limit	64 lp/mm
Phosphor type	P46

gain of 125 were set for all images presented here. This value of gain was found sufficient for boosting the intensity of scattering signal while avoiding magnification of background noise. The intensity distribution on captured images was used to highlight the mixedness distribution, shock structure, shear layers, and slip lines within the flowfield. More details on the use of intensity distribution for flowfield quantification are provided in the next chapter.

3.5 Thrust measurement

Since nozzle thrust and specific impulse are key performance parameters that are affected by the application of swirl, thrust was measured to assess the effect of swirl. The experimental values were also used to validate the numerically obtained ones. In order to measure the thrust, the nozzle assembly (Figure III-5) was connected to a compression load cell (transducer). See Table III-6 for the specifications of the load cell.

3.6 Numerical Simulation Type and Assumptions

The ESI-Group CFD-FASTRAN 2008 LES-based code was used for all the simulations conducted in this study. A variable-size grid was generated for the examined geometry. Tighter meshing was implemented near and at the critical geometry locations, e.g., exits of nozzle and fuel-injection system. Special emphasis was placed on cell skewness. The geometry was sub-divided into individual volumes, each meshed separately, in order to keep the skewness level of the most skewed cell below 0.5. Mesh dependence was carefully examined through testing multiple levels of mesh tightness. A total of 7,166,860 nodes were found sufficient. Higher tightness levels did not yield any significant changes in the obtained profiles and were thus not considered, in order to optimize the computational time.

Table III-6. Specifications of compression load cell

Property	**Value**
Make and model	Omega, LCM302-200N
Capacity	200 N (45 lb)
Excitation	10 Vdc
Output	1 mV/V
Accuracy	±0.5% FSO (linearity, hysteresis, repeatability combined)
Zero balance	±2% FSO
Deflection	0.025 to 0.075 mm
Thermal effects	Zero: 0.009% FSO/°C Span: 0.036% FSO/°C

The Baldwin-Lomax turbulence model was implemented [Baldwin and Lomax (1978)]. Calculation of viscosity and conductivity was based on the kinetic theory of gases. The mass diffusivity was calculated based on Fick's law with a Schmidt number of 0.5. A turbulent Prandtl number of 0.9 was used for calculating the turbulent conductivity. Similar to the experimental conditions, the total temperature at air inlets was kept fixed at 300 K, while the total pressure was maintained at 7.91 bar for the non-swirling cases and 8.82 bar for the swirling ones. It should be recalled here, that the 8.82-bar value was carefully chosen to ensure that all analyses of this study have the same air flow rate of 175 g/s. The total pressure and temperature at air inlets were preserved throughout the iteration process in each examined case until convergence was attained. Owing to the relatively large cross-sectional areas of the air inlets, the entrance velocity of air was only 9.7 m/s, resulting in almost identical inlet stagnation and static conditions.

The nozzle walls were set to be isothermal at 280 K, based on multiple temperature measurements of the nozzle interior and exterior walls. This is attributed to the aforementioned fact that the nozzle is made of aluminum, which has a high thermal conductivity and thus allows the nozzle to act as a near-isothermal body. The walls of fuel-injection system, on the other hand, were set to be adiabatic, because the injection system is immersed almost totally into the nozzle and conditioning chamber, which allows for negligible amounts of heat to be conducted axially upstream through the thin walls of fuel system. Moreover, it is made of stainless steel that has a much lower thermal conductivity (relative to aluminum).

Since the simulation involves a free supersonic flow, special emphasis was placed on the choice of boundary conditions that represent the flow surroundings. The entire nozzle assembly was surrounded by a cylindrical enclosure of (40 D) diameter and (70 D) length, where D is the nozzle exit diameter (11 mm) — a good representative of jet size. The 40-D enclosure diameter assures that the side boundaries are far enough from the jet, in order to eliminate any interference of both and to maintain constant near-stagnation atmospheric properties at the boundaries. Consequently, the bottom and side enclosure surfaces were assigned the fixed-pressure boundary condition, which matches the constant actual atmospheric ambient pressure. The top side of enclosure, on the other hand, is an outlet located 55 D away from the nozzle exit (≈ 78% of the 70-D enclosure length). This guarantees that the flow leaves the simulated geometry shock-wave-free, since it was observed experimentally that complete transition to subsonic speeds occurs about 30 D downstream of nozzle exit.

The initial conditions of simulation were set for all cases at 1-atm static pressure, 300-K static temperature, 9.7-m/s axial velocity, and zero radial and tangential velocities. Consequently, the simulation incorporated the transient flow behavior as the high-pressure air expands and

"marches" from geometry inlet to exit. An initial CFL number of 0.1 was chosen that increases to unity as convergence is approached. Time integration is implicit, where the Point Jacobi (fully implicit) scheme was used. Backward Euler discretization was implemented. Each iteration included 20000 sub-iterations. Convergence was usually attained after 18500 – 19500 iterations.

IV. RESULTS AND DISCUSSION

The findings of this study are presented and discussed in this chapter, preceded by a description of test matrix. Multiple test conditions have been examined. The discussion starts by describing the simple shock structure of underexpanded nozzle flows, followed by shock-structure changes induced by the presence of a non-recessed coaxial fuel-injection system. An analysis of the swirling subsonic flowfield inside nozzle in the presence of injection system is made next. The effects of injection-system presence on air total and static pressures as well as subsonic swirl number are examined.

A discussion of the nozzle choking criteria with swirl follows, with the injection system present but in the absence of fuel injection. Answers are provided for the following questions, as they have not been fully quantified in the literature yet (see chapter II). (a) Is the throat velocity (or any of its components) equal to the local speed of sound in a swirling flowfield? If yes, then how does swirl affect the shape of sonic line? (b) How does swirl affect the throat Mach number, pressure, and temperature? (c) How does swirl affect the shock structure and nozzle thrust and specific impulse?

After examining the nozzle choking criteria with swirl, analyses are made of the effects of relative Mach number and density ratio across the air/fuel shear layer. The effects of these parameters on shock structure and mixing are investigated under both non-swirling and swirling conditions. Select cases were chosen for a further analysis of the effect of convective Mach number on shear layer growth. The attained findings are compared to those of previous research where applicable. The chapter concludes with the examination of one hydrogen-fueled reactive case, in order to highlight the challenges associated with stabilizing a free supersonic flame.

4.1 Test Matrix

The effect of swirl is investigated here by forwarding the entire airflow to nozzle tangential entries. This allows for examining a single degree of swirl, namely the maximum attainable one. Following a definition used for incompressible swirling jets [Gupta et al. (1984) and Claypole and Syred (1981)], a nozzle-based geometrical swirl number S_g is defined for air as

$$S_g = \left(\frac{\pi r_o R_o}{A_t} \right) \frac{m_t}{m_a + m_t} \qquad \text{(IV-1)}$$

where $\left(\pi r_o R_o / A_t \right) = 0.68$, for the geometry of used nozzle and its tangential entries, and m_a and m_t are the axial and tangential components of airflow, respectively. Consequently, all swirling cases of this study have a common nozzle-based geometrical swirl number of 0.68. The term "nozzle-based" refers to nozzle operation in the absence of coaxial injection system, as it will be shown later that the presence of this system reduces the geometrical swirl number down to 0.36. This significant reduction made the examination of the effect of swirl feasible only at its maximum attainable degree.

In addition to an extensive examination of the effect of swirl on shock structure, mixing, nozzle choking criteria, thrust, and specific impulse, the effects of two flow parameters are investigated here under both non-swirling and swirling conditions, namely the relative Mach number (M_{rel}) and air-fuel density ratio (DR). The former is defined here as:

$$M_{rel} = \frac{v_{air} - v_{fuel}}{0.5(a_{air} + a_{fuel})} \qquad \text{(IV-2)}$$

This definition relates the difference in freestream velocities between fuel and air to the average speed of sound. It should be noted that the fuel simulant is injected here at velocities smaller than those of transonic airflow in most examined cases. Therefore, v_{fuel} is subtracted from v_{air} in the above definition, in order for M_{rel} to have positive values. Nevertheless, in a few extreme cases

the fuel simulant is injected at velocities greater than those of airflow, and the corresponding values of M_{rel} are indicated here without neglecting their negative signs, in order to highlight the unique nature of those cases, i.e., $v_{fuel} > v_{air}$.

Each examined case in this study has a nominal value of M_{rel} that describes the injection conditions within that case. Since all cases to be presented here utilize no recess, i.e., fuel is injected at the throat of air nozzle, the nominal value of M_{rel} was calculated for each case using the fuel injection velocity and the sonic (throat) value of v_{air}. A comparison based on nominal M_{rel} thus allows for examining the effect of fuel-injection conditions on the global features of flowfield, including shock structure and mixing. Such analysis should not be confused with the shear-layer-specific analysis of the effect of convective Mach number (M_c) on shear-layer properties (to be discussed at the end of this chapter). Under non-swirling conditions, sonic v_{air} was found to be 323 m/s, based on isentropic ideal-gas relations. No similar simple calculations of v_{air} could be carried out for the swirling cases, due to the intrinsic three-dimensionality of swirling flows. Nevertheless, the results of numerical simulations revealed that the magnitude of sonic v_{air} is 329 m/s with swirl, which is almost equal to the non-swirling value. This fact allowed for examining the same nominal values of M_{rel} under both non-swirling and swirling conditions in this study.

The shock structure and all properties of airflow, including the aforementioned values of v_{air}, depend on air total pressure and temperature. Both were kept constant at 7.91 bar and 300 K, respectively, for all non-swirling cases presented in this study, which resulted in a fixed air flow rate of 175 g/s. It was noticed, however, that imparting swirl to airflow at the same nozzle reservoir pressure of 7.91 bar results in reduced mass flow rate through the nozzle. This observation agrees with the findings of many previous studies (see chapter II), where it was

proven that imparting swirl to the airflow results in "additional choking" of the nozzle, i.e., a lower mass flow rate compared to the corresponding non-swirling conditions at the same reservoir pressure. A theoretical limit of no flow was even predicted at an infinitely large swirl number. Therefore, a higher reservoir pressure is necessary to maintain the same flow rate through the nozzle. It was found in this study that a value of 8.82 bar yields identical air flow rates of 175 g/s in the non-swirling and swirling cases.

Table IV-1 lists the test matrix for the results presented here. A total of 48 cases are examined (24 non-swirling cases plus their swirling counterparts). Case pair 0 utilizes no fuel injection and serves for performing the following analyses:

(a) Effect of presence of coaxial injection system on the variations of subsonic swirl number,

(b) Effect of swirl on nozzle choking criteria, i.e., sonic line, throat Mach-number components, pressure and temperature, and

(c) Effect of swirl on supersonic flowfield, shock strength, shock positions, and jet diameter.

Case pairs 1 – 13 study the effect of M_{rel}, wherein the injectant is helium. The injection velocity of helium is changed to induce different values of nominal M_{rel}. The effect of DR is studied through case pairs 14 – 23, wherein the injectant comprises different inert-gas mixtures. The mixture composition is varied to change mixture density and consequently DR. In order to maintain constant M_{rel} throughout the DR analysis, the injection velocity was adjusted to account for the changes in a_{fuel} due to the varying injectant composition. The values to be examined in both analyses of M_{rel} and DR were carefully selected according to the following criteria:

- The experimentally attainable ranges are spanned with narrow intervals, in order to quantify the examined effects accurately. For example, M_{rel} is examined over the range 0.44 – 0.26 with 8 intervals, while DR is covered in the range 12.68 – 4.33 with 6 intervals

Table IV-1. Test Matrix

Constant parameters:
Air total temperature at inlet = 300 K
Nozzle reservoir pressure = 7.91 bar (non-swirling), 8.82 bar (swirling)
Geometrical swirl number for swirling cases, $S_g = 0.68$

Case	Injected Gas	M_{rel}	DR	Experimental	Numerical
0 & 0s	Air only; no fuel injection				
Effect of Relative Mach Number					
1 & 1s	Helium	0.44	35.50	✓	✓
2 & 2s		0.41		✓	
3 & 3s		0.39		✓	
4 & 4s		0.37		✓	
5 & 5s		0.35		✓	✓
6 & 6s		0.32		✓	
7 & 7s		0.30		✓	
8 & 8s		0.28		✓	
9 & 9s		0.26		✓	✓
10 & 10s		*0.21*			✓
11 & 11s		0.00			✓
12 & 12s		-0.21			✓
13 & 13s		-0.48			✓
Effect of Density Ratio					
14 & 14s	*100% Helium*	0.21	*35.50*		✓
15 & 15s	80% Helium / 20% Argon		12.68	✓	✓
16 & 16s	70% Helium / 30% Argon		9.60	✓	
17 & 17s	60% Helium / 40% Argon		7.72	✓	
18 & 18s	50% Helium / 50% Argon		6.46	✓	✓
19 & 19s	40% Helium / 60% Argon		5.55	✓	
20 & 20s	30% Helium / 70% Argon		4.86	✓	
21 & 21s	20% Helium / 80% Argon		4.33	✓	✓
22 & 22s	50% Helium / 50% Krypton		3.24		✓
23 & 23s	50% Argon / 50% Krypton		2.29		✓

- The numerical simulations span the experimental ranges with wide intervals, i.e., one simulation at the beginning of range, one in the middle, and one at the end. Case pairs 1, 5, and 9 within the M_{rel} analysis, for example, were examined both experimentally and numerically. The same applies for case pairs 15, 18, and 21 within the DR analysis. The duplicate examination of a few case pairs provides means of code validation and percentage-error assessment through direct comparison of the experimental and numerical results. It should be noted, however, that only the experimental data were considered when quantifying the effects of M_{rel} and DR on flowfield parameters, since the experimental results require no further validation, unlike the numerical ones
- The numerical simulations extend beyond the experimental ranges to broaden the scope of analysis and qualitatively examine how accurate the experimental trends would be when extrapolated beyond the ranges they were obtained in. No accurate assessments of the extrapolation errors could be made, since the extended numerical simulations involve some error themselves and thus cannot be considered as accurate reference for the extrapolated experimental trends. Nevertheless, good agreement was observed, and estimates of the extrapolation errors are given here, which will support the findings of future studies

Note that case pairs 10 and 14 (highlighted in *italics* in Table IV-1) are identical, as they have the same fuel simulant (helium), M_{rel}, and DR. These two case pairs link the analyses of M_{rel} and DR. Also note that a letter "s" next to a case number denotes a swirling case.

4.2 Shock Structure (Non-Swirling, No Fuel Injection)

The shock structure of simple underexpanded supersonic flow is shown schematically in Figure IV-1. As can be seen, the structure comprises a shock-cell unit that gets repeated periodically to form a shock-cell train. This unit can be described as follows. Axial under-expanded flow undergoes an expansion fan and turns outwards. The free-jet boundary adapts accordingly and turns outwards as well. Passing again through the expansion fan, the outward flow turns back to axial. As the expansion fan meets the boundary, it reflects into a compression fan that coalesces later into the intercepting shock wave. The annular flow adjacent to boundary turns inwards through the compression fan, and the boundary again adapts by turning inwards as well. For slightly underexpanded nozzles, this intercepting shock reflects directly into a reflected shock at the centerline, forming the familiar diamond configuration. However, as the pressure ratio across the nozzle is increased, this reflection no more takes place at the centerline, and a Mach disk is formed. The reflected shock turns the inward annular flow back to the axial direction. Since the Mach disk maintains the axial direction of core flow, the entire flow is now axial again. As the reflected shock impinges on the flow free boundary, it reflects into an expansion fan, starting another shock-cell unit. The repetition of units is continued until viscous effects become predominant, and this structure is no longer observed.

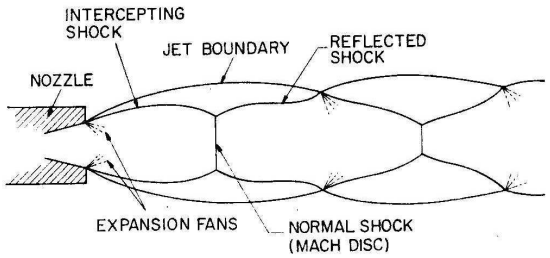

Figure IV-1. Schematic of shock structure of highly underexpanded nozzle flow
[from Adamson and Nicholls (1959)]

In presence of a coaxial injection system, the shock structure differs significantly from the simple one described above. Figure IV-2 shows a Schlieren image as well as a schematic of the shock structure of free nozzle flow in the presence of a non-recessed coaxial injection system with no fuel injection. Two distinct sub-structures are identifiable from Schlieren image and highlighted in the schematic. The first sub-structure is the simple nozzle-rim structure discussed above. A new sub-structure is generated due to the existence of coaxial injection system. It should be noted here that both sub-structures are not fully independent of each other. The presence of each affects the other. This interaction is, however, not indicated on the schematic in Figure IV-2, for easier understanding of the newly introduced sub-structure off injection system. Indicated here is how each structure would propagate if fully independent of the other. From this point forward, the nozzle-rim and injection-system sub-structures will be denoted "primary" and "secondary" shock structures, respectively, in this study.

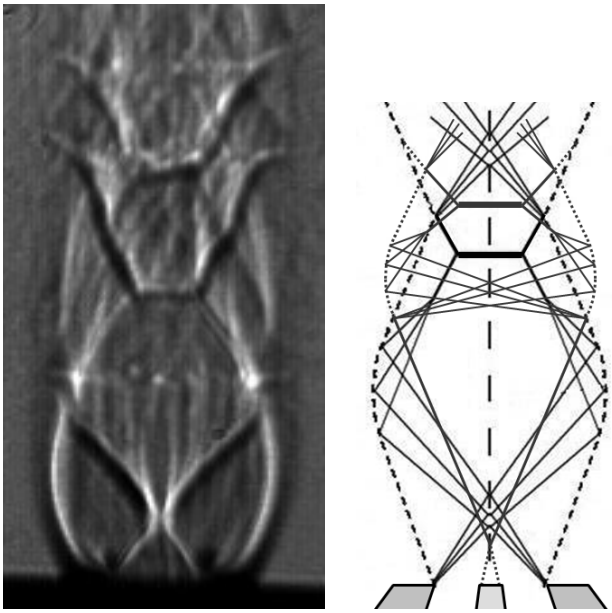

Figure IV-2. Shock structure of non-swirling (case 0) underexpanded nozzle airflow in presence of non-recessed coaxial injection system with no fuel injection

The secondary structure starts with the airflow generating an inner conical boundary that completes the cone-frustum shape of fuel system tip. At the centerline, the flow collapses into itself, generating a conical shock wave that turns the flow back to parallel. This shock wave impinges on the outer flow boundaries shortly downstream of the impingement location of nozzle-rim expansion fan. The outer boundaries are altered by the impingement of that conical shock as observed from Figure IV-2. The shock reflects into an expansion fan that creates its own compression fan, intercepting shock, Mach disk, and reflected shock, similar to the primary structure. Both Mach disks of primary and secondary structures appear distinctly in Figure IV-2.

The effect of coaxial fuel injection is shown in Figure IV-3. Helium is used as fuel stimulant. As observed, the secondary shock structure is altered slightly. A shear layer develops in place of the former inner conical boundaries of airflow. Due to the presence of helium, the shear layer does not converge to a sharp point at the centerline. Moreover, due to the curved shape of this shear layer, the airflow undergoes gradual compression through a compression fan, which collapses later into a shock wave that generates the secondary shock sub-structure.

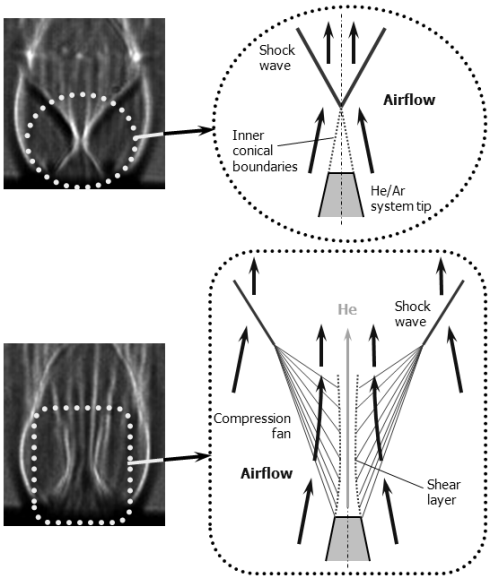

Figure IV-3. Effect of fuel injection on shock structure of underexpanded nozzle flow

4.3 Validation of Numerical Code

Numerical simulations of the flowfield have been performed in this study, in addition to the experimental investigation, to broaden the scope of analysis of the latter and provide the desired quantification of certain flowfield parameters. For example, the Schlieren and Mie-scattering techniques are incapable of visualizing the helical motion of a swirling flow or quantifying the different components of Mach number. Therefore, the numerical results are used to provide the missing data needed for examining the nozzle choking criteria, air/fuel shear layer, and propagation of swirl throughout flowfield.

Before presenting any of the numerical results, code validation is demonstrated here by comparing the experimentally measured thrust values to the numerically computed ones. As will be seen later in the discussion of nozzle thrust and specific impulse, the computed and experimental thrusts differ by only 0.6 – 3.2%, which shows very good agreement and confirms the capability of numerical code to quantify the subsonic and throat flows with high accuracy. When the experimental and numerical visualizations of supersonic flowfield are, however, compared side by side in Figure IV-4, the incompetence of numerical code in capturing the details of shock structure can be observed. Shown in Figure IV-4 are a Schlieren image and the corresponding numerically-obtained center-plane Mach number profile of case 0 (non-swirling airflow without fuel injection) from Table IV-1. The Mach number has been particularly chosen amongst other physical flow parameters, as it gives the clearest visualization of shock structure; shock waves are identifiable at regions of steep gradients of Mach number. Such steep gradients are not observed in Figure IV-4. Therefore, the analysis of supersonic flowfield will be based primarily on experimental data. It should be noted here that this numerical code has been utilized in previous studies by the author [Abdelhafez and Gupta (2008) and Abdelhafez et al. (2007)] to

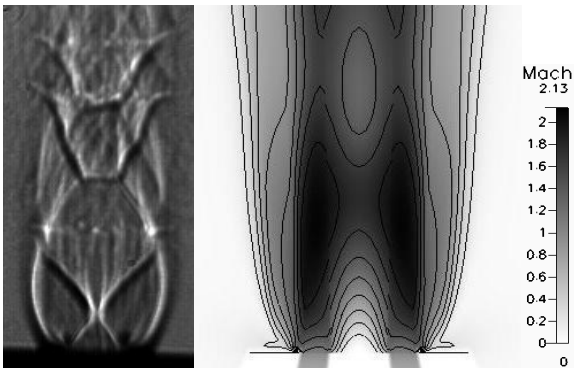

Figure IV-4. Comparison of experimental (Schlieren, left) and numerical (Mach number profile, right) visualizations of shock structure. Air only, no swirl (case 0)

quantify the effect of fuel-injection parameters on shock-induced mixing in confined supersonic airflows. The shock trains of such duct flows were captured successfully by the code, which infers that the deficiency observed in this study is attributed to the unconfined nature of the examined supersonic flowfield.

4.4 Effect of Injection-System Presence

As mentioned earlier, the effect of swirl is investigated here by introducing the entire airflow through nozzle tangential inlets. Based on aforementioned definition, the resulting geometrical swirl number should be 0.68 in the absence of coaxial injection system. However, since the geometry at hand involves one, the effect of its presence on nozzle performance is analyzed first. It was shown in earlier research [Lee et al. (2006)] that the presence of a coaxial needle inside nozzle affects the airflow properties. Figure IV-5 shows the axial variation of subsonic swirl number inside nozzle in the absence as well as presence of the coaxial injection system. Using the same conditions of case 0s in Table IV-1 (injection system present, no fuel injection), another case was simulated with the injection system absent. The swirl number was computed at select sections inside the nozzle using the correlation [Gupta (1984)]

$$S = \frac{\int_{R_i}^{R_o} v_a \, v_t \, r^2 \, dr}{R_o \int_{R_i}^{R_o} v_a^2 \, r \, dr} \qquad \text{(IV-3)}$$

where v_a and v_t are the numerically-obtained axial and tangential velocity components, respectively. Multiple observations can be made from Figure IV-5. The most obvious and expected one is that the swirl number decreases, as flow progresses towards nozzle throat. This agrees with the findings of Linck (2006) and can be attributed to two facts: (a) v_a increases substantially due to flow expansion and acceleration, and (b) v_t was observed to decrease slightly due to viscous losses, as the flow passage narrows and boundary layers develop at the walls. It is worth noting that the swirl number can be roughly approximated as being proportional to the ratio of average tangential to axial components (neglecting the effect of nozzle geometry), which explains the trends depicted in Figure IV-5.

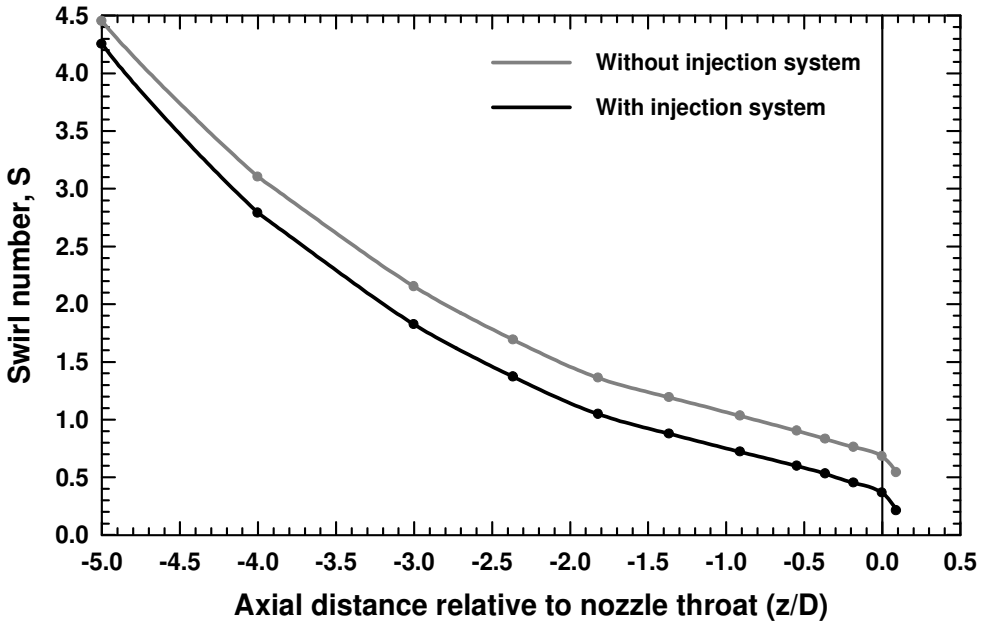

Figure IV-5. Axial variation of subsonic swirl number inside nozzle in the absence and presence (case 0s) of coaxial injection system. Nozzle throat at z/D = 0

Figure IV-5 also reveals that the presence of injection system induces an additional reduction in swirl number throughout the entire nozzle. This is attributed to the development of a second boundary layer along the injection-system walls. Close to the plane of tangential inlets, the relative reduction is small but keeps increasing as the flow progresses through nozzle. This statement is concurred by Figure IV-6, where the relative reduction in swirl number is plotted. While the upstream sections experience minor reductions, a 47% reduction from 0.68 to 0.36 exists at the nozzle throat due to the presence of injection system, which blocks 17% of throat area. The significant reduction in throat swirl number is further explained in Figure IV-7. Shown is the radial variation of tangential Mach number at z/D = –0.1 in the absence and presence of injection system. It can be clearly observed that a considerable percentage of angular momentum is lost, simply due to the physical existence of injection system up to r/D of 0.25. Even at 0.25 < r/D < 0.28 some angular momentum is lost within the injection-system boundary layer.

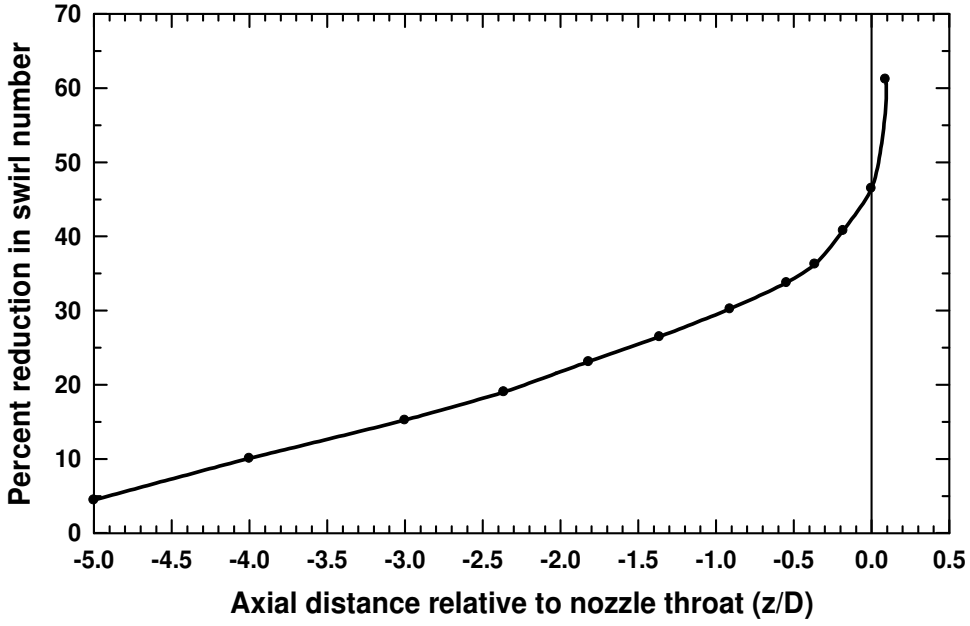

Figure IV-6. Axial variation of relative reduction in subsonic swirl number inside nozzle due to the presence of coaxial injection system (case 0s). Nozzle throat at z/D = 0

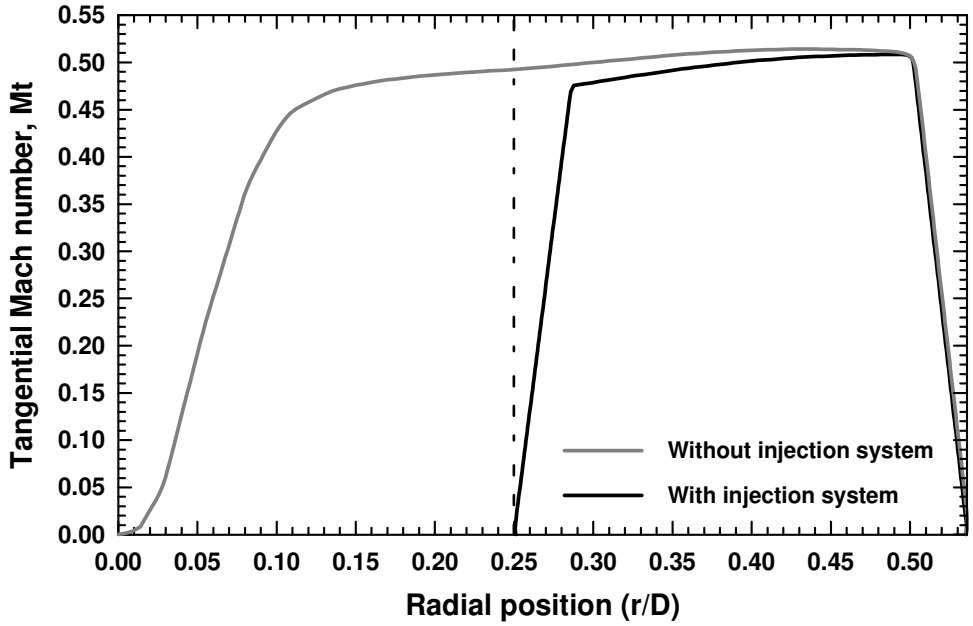

Figure IV-7. Radial variation of tangential Mach number at z/D = –0.1 in the absence and presence (case 0s) of injection system. Dotted line at r/D = 0.25 represents radius of coaxial injection system at tip

The combination of three facts is expected to induce these common observations of Figures IV-5 to IV-7. First, the angular momentum dominates the flow at upstream sections but loses this domination to the axial momentum progressively along the nozzle. Second, the angular momentum experiences higher losses, as the ratio of boundary-layer thickness to flow-passage height increases along the axial direction. Third, the injection system blocks higher percentages of nozzle cross-sectional area at downstream locations.

4.5 Nozzle Choking Criteria

4.5.1. Nozzle Flowfield

Another interesting observation to be made from Figures IV-5 and IV-6 is the considerable reduction in trans-throat swirl number on both absolute and relative scales. Figure

IV-8 explains this behavior by comparing the flow sections about nozzle throat (z/D = –0.1) and (z/D = +0.1). The radial variations of axial and tangential Mach number components (M_a and M_t) are shown in Figures IV-8a and IV-8b, respectively. A significant increase in trans-throat axial momentum is observed, which incorporates both jet acceleration and expansion. Significant radial expansion occurs in the absence of the restricting walls of nozzle and injection-system. On the other hand, a reduction in the magnitude of trans-throat M_t is observed, which agrees with the findings of Batson and Sforzini (1970). Careful inspection of Figure IV-8b, however, reveals that radial expansion results in an increase in angular momentum, which is undermined by the decrease associated with the reduction in magnitude of M_t. Therefore, the main conclusion to be made here is that the noticeable reduction in trans-throat swirl number (observed in Figures IV-5 and IV-7) is attributed mainly to the considerable increase in trans-throat axial momentum. Recall that the swirl number is proportional to the ratio of tangential to axial momenta.

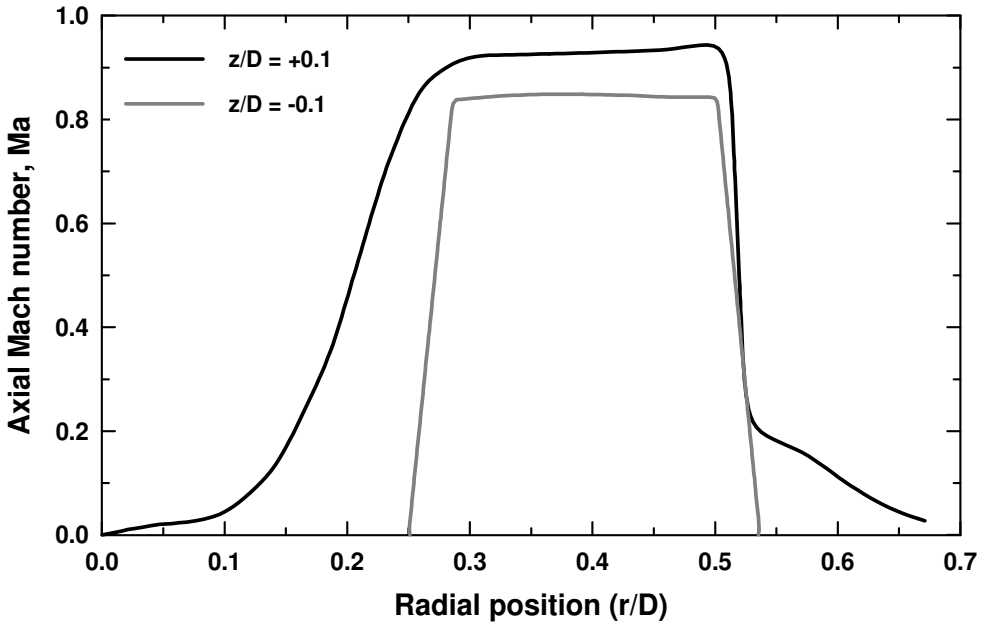

Figure IV-8a. Radial variation of trans-throat axial Mach-number component in case 0s

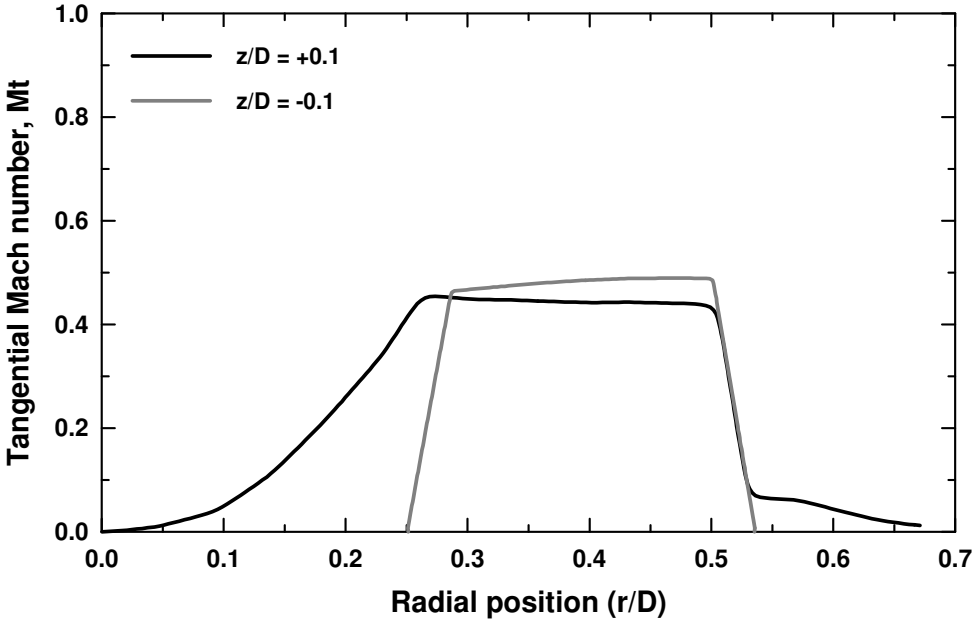

Figure IV-8b. Radial variation of trans-throat tangential Mach-number component in case 0s

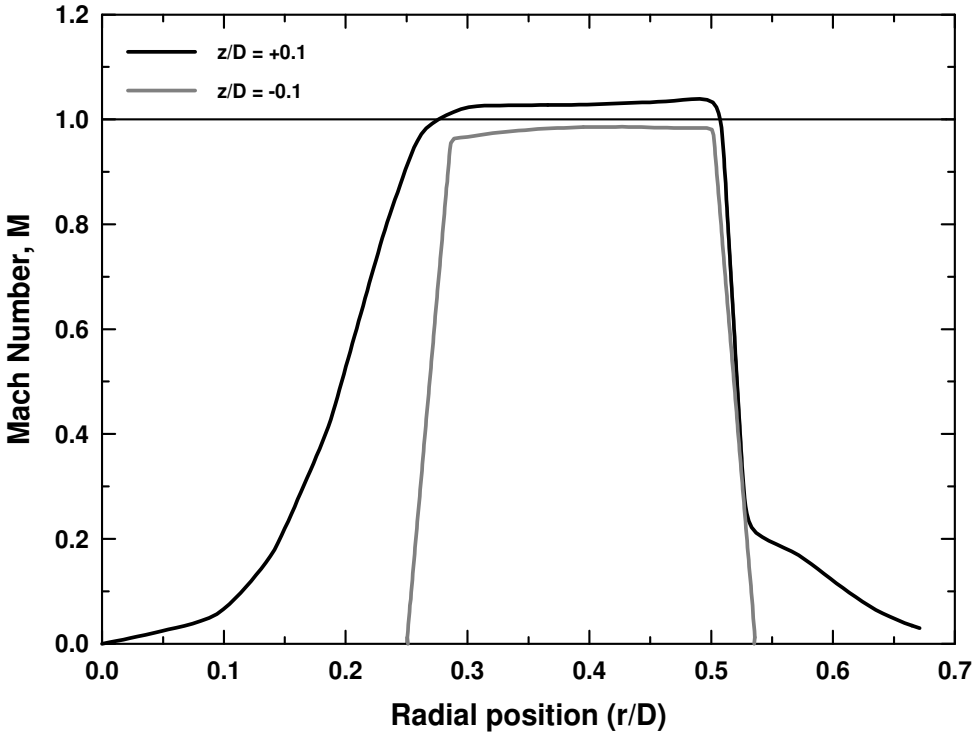

Figure IV-8c. Radial variation of trans-throat Mach number in case 0s

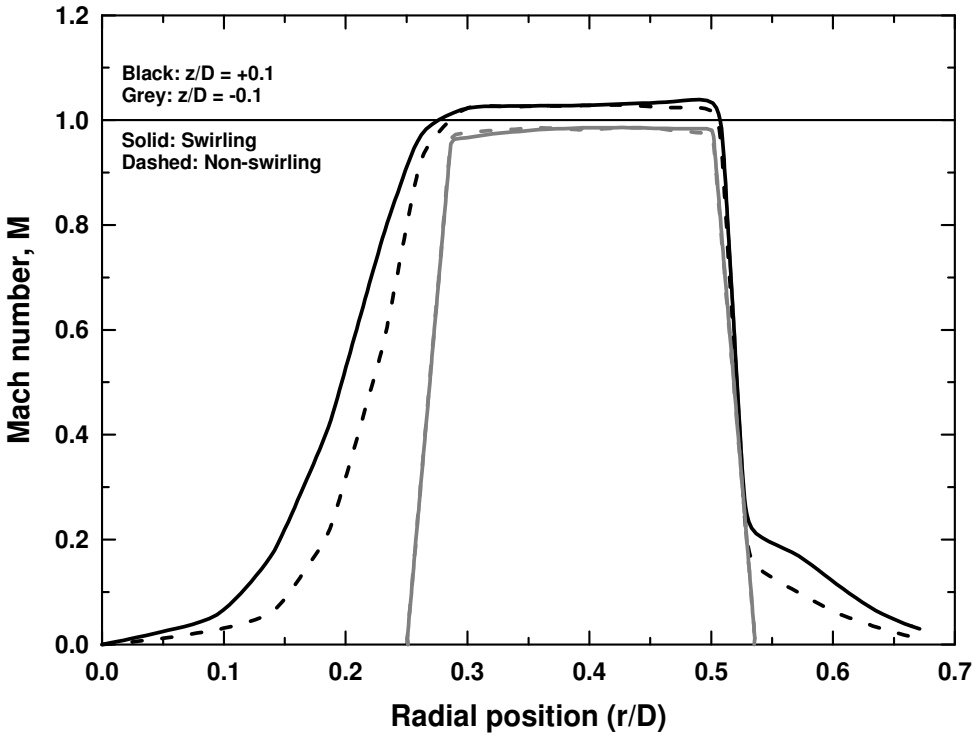

Figure IV-8d. Comparison of the radial variations of trans-throat Mach number in cases 0 (non-swirling, dashed) and 0s (swirling, solid)

A notable observation to be made from Figure IV-8a is that the trans-throat magnitudes of M_a are subsonic in the swirling flowfield. This is distinctly different from the behavior of non-swirling flow, where M_a transitions to supersonic values through the throat. Figure IV-8c explains such unusual behavior under swirling conditions. Shown is the radiation variation of overall trans-throat Mach number (M) within the swirling flowfield. The expected transition to supersonic propagation through nozzle throat is observed, which yields the main conclusion that both non-swirling and swirling flowfields behave similarly in terms of M, and not M_a. Such similarity exists on both the qualitative and quantitative scales, which is concurred by Figure IV-8d, where the radial distributions of non-swirling and swirling trans-throat Mach number are compared. The values of M within the jet ($0.26 < r/D < 0.47$) are very similar. Figure IV-9 further proves this fact by comparing the non-swirling and swirling sonic lines, which appear to

be almost identical except at greater radii, where the sonic line is reached earlier in the swirling flowfield. This agrees with the findings of Batson and Sforzini (1970), where it was reported that the flow velocity near the wall increases with swirl, due to Coriolis effects and area choking. The boundary layers are also identifiable in Figure IV-9 beyond the radial range $0.26 < r/D < 0.47$.

The remarkable similarity of trans-throat non-swirling and swirling flows can even be traced back to the subsonic flowfield inside nozzle. Figure IV-10 shows the axial variations of cross-section-averaged subsonic Mach number. It is clearly noticeable how the non-swirling and swirling behaviors are almost identical, which strengthens the findings of Figure IV-8d and also partially explains the aforementioned fact that the swirling value of sonic v_{air} (329 m/s) is close to the non-swirling value (323 m/s). The static temperature completes the picture, as the velocity is function of both Mach number and static temperature. Figure IV-11 shows the axial variations of non-swirling and swirling, total and static temperatures inside nozzle. Notice that the throat static temperature increases by about 10 degrees with the introduction of swirl, which further proves the close similarity of non-swirling and swirling flowfields; a behavior that extends from subsonic Mach number to static temperature and consequently velocity magnitude.

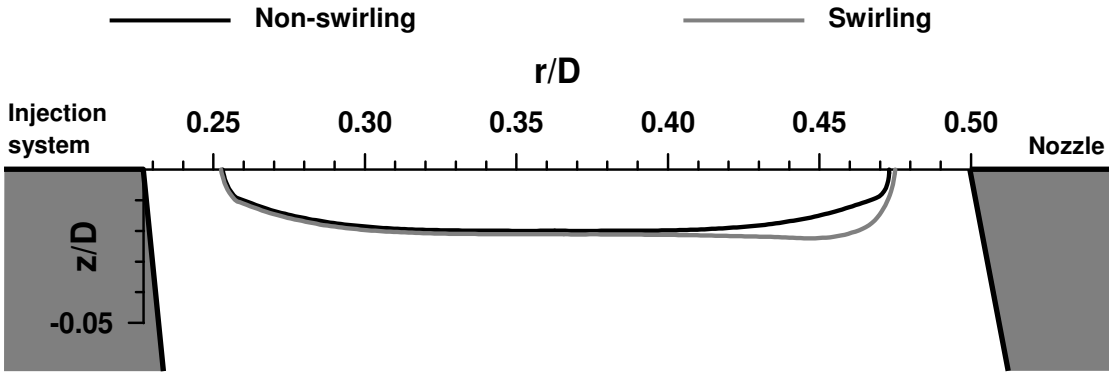

Figure IV-9. Sonic lines in cases 0 (non-swirling) and 0s (swirling)

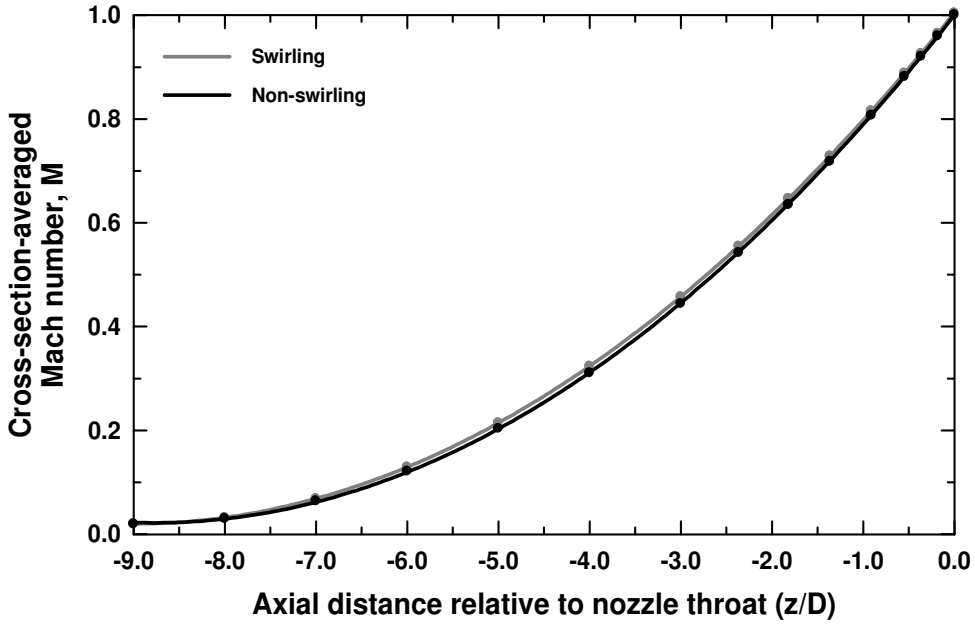

Figure IV-10. Axial variations of cross-section-averaged subsonic Mach number in cases 0 (non-swirling) and 0s (swirling)

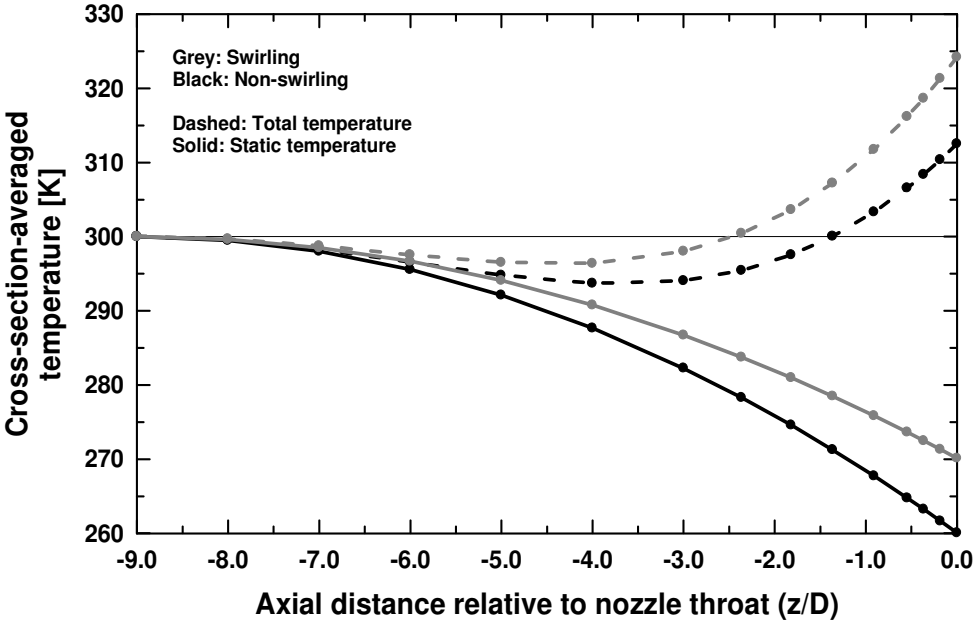

Figure IV-11. Axial variations of cross-section-averaged total and static temperatures inside nozzle in cases 0 (non-swirling, black) and 0s (swirling, grey)

It should be noted at this point that the observed throat values of static temperature are considerably higher than what would be expected in isentropic flows. The isentropic value of sonic static temperature is 250 K in airflow of 300 K total temperature. This behavior can be explained by recalling that the nozzle examined here is made of aluminum. As mentioned earlier, the high thermal conductivity of aluminum allows the nozzle to be almost isothermal at a temperature of about 280 K. The relatively warmer entrained ambient air loses heat to the external nozzle walls, which is conducted to the inner walls and convected to the flow within. The fact that the airflow inside nozzle is gaining heat energy (i.e., not isentropic) is evident in Figure IV-11, where it can be clearly observed that the throat total temperature is considerably higher than its 300-K inlet value. If the flow were isentropic, it would have a constant total temperature throughout.

Further careful inspection of Figure IV-11 reveals that the total temperature initially decreases below 300 K by about 5 degrees in the upstream sections of nozzle before recovering and increasing beyond 300 K. This peculiar behavior can be explained by observing Figure IV-12, where a schematic representation of heat flow and static-temperature distribution is depicted. Notice that the static temperature of nozzle flow decreases from 300 K at inlet to about 265 K at throat. Meanwhile, the stagnation temperature of ambient air is 300 K, and the temperature of nozzle walls was found experimentally to be almost constant at 280 K. It is expected to observe heat transfer from the ambient air to nozzle flow at the downstream sections. The heat flux is expected to increase as the flow approaches nozzle throat, because (a) the temperature difference between ambient air and nozzle flow increases, and (b) the thickness of nozzle wall decreases. In other words, the potential for heat transfer increases, while the resistance decreases. This explains the greater rates of total-temperature increase in Figure IV-11 as the throat is

approached. The peculiar observation, however, is that the 280-K nozzle walls are surrounded by warmer media on both sides at the upstream sections. This allows heat to be conducted axially downstream through the walls from both the ambient air and nozzle flow. The heat lost from the latter at the upstream sections explains the initial decrease in flow total temperature below 300 K, before recovery occurs at the downstream sections.

It might be argued here that these examined conditions do not compare directly to the fundamental *isentropic* quasi-1D flow through nozzles, so how does the current analysis contribute to the understanding of the effect of swirl on such basic flow? The answer to this question is twofold. First, it was proven in the literature (see chapter II) that one-dimensional approximation cannot be applied to swirling flows without either violating some conservation equations or enforcing assumptions that are too ideal for actual flows. Three-dimensional viscous numerical simulations, on the other hand, can now be implemented to study the behavior of such actual flows. Second, non-isentropic nozzle flows with heat transfer through nozzle walls occur in a number of important practical propulsion applications, including turbofans and turbojet engines, spin-stabilized rockets, and integral rocket/ramjets. Heat transfer is essential for cooling the nozzle walls, especially near the throat section. The presented distributions of Mach number, pressure, and temperature might be specific to the examined geometry and flow conditions, which is also the case in many previous studies. Nevertheless, this study contributes significantly to the understanding of the effect of swirl on nozzle performance and flowfield, while highlighting the similarities and differences of non-swirling and swirling flows. No idealized assumptions are made, which would limit the applicability of the attained findings in engine/ nozzle design or numerical-model development.

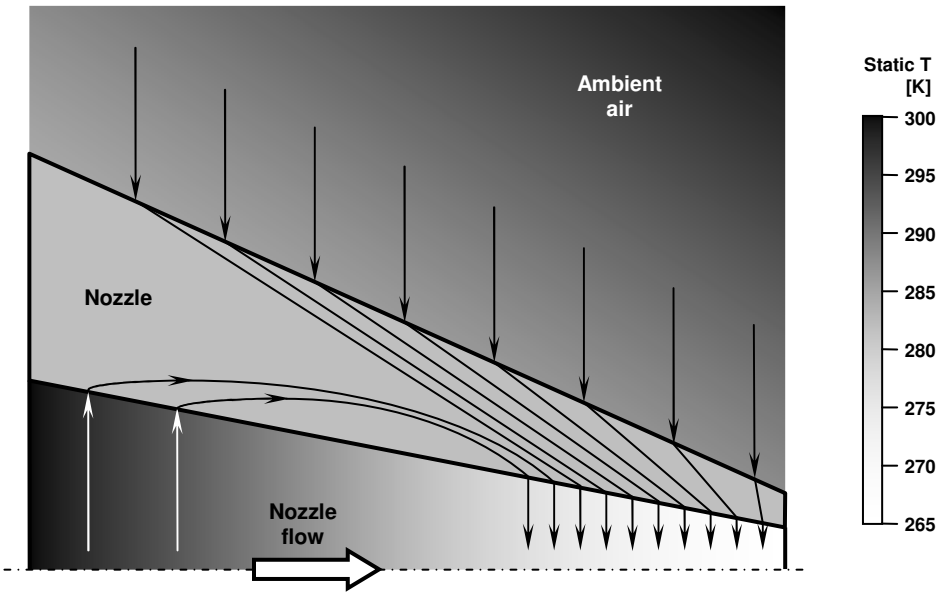

Figure IV-12. Schematic representation of heat flow and static-temperature distribution

Having observed that the throat static temperature increases by 10 K with application of swirl, the question that arises here is whether this is the actual effect of swirl or the result of the swirling flow taking a longer path through the nozzle and thus getting heated up by the relatively warmer 280-K nozzle walls. The answer to this question is discussed as follows. Consider a new case, to be called 0's, which is a swirling case like 0s but has the lower reservoir pressure of case 0. All three cases have the same inlet total temperature of 300 K. A side argument might be made here that the aforementioned Mach-number similarity of non-swirling and swirling flows is attributed to the higher nozzle reservoir pressure with swirl, which leads to a common air flow rate. Figure IV-13, however, refutes this argument. Shown are the axial variations of Mach number inside nozzle for cases 0, 0's, and 0s. It is clearly evident that non-swirling and swirling flows are unconditionally similar in terms of Mach number, regardless of inlet conditions.

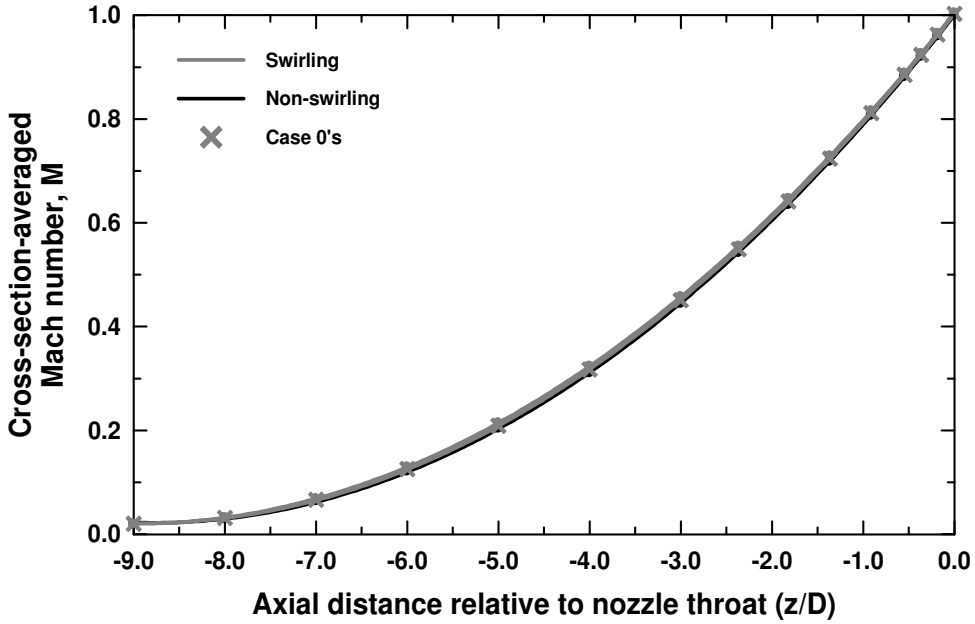

Figure IV-13. Axial variations of cross-section-averaged Mach number inside nozzle in cases 0 (non-swirling, reservoir pressure = 7.91 bar), 0's (swirling, reservoir pressure = 7.91 bar), and 0s (swirling, reservoir pressure = 8.82 bar)

In terms of temperature, on the other hand, it is expected here that only cases 0s and 0's will behave identically. Both are swirling, and the airflow takes the same longer path through nozzle in both. Figure IV-14, however, shows that the resemblance is only qualitative. Depicted are the axial variations of total and static temperatures inside nozzle for cases 0, 0's, and 0s. It can be distinctly seen that case 0's is identical to neither 0 nor 0s. These differences are believed to be partially attributed to an implicit effect of total pressure. It is known that pressure is a form of energy, i.e., the higher the flow pressure is, the greater is its energy potential. This extra energy can be transformed to other forms within the flow, e.g., viscous heating. If case 0's is compared to 0s from this point of view, it can be deduced that the latter simply has more energy. Cases 0 and 0's, on the other hand, start off with the same energy level (same inlet total

temperature and pressure). The difference in static temperature between 0 and 0's can thus be mainly attributed to more heat gained by the latter from nozzle walls along its longer path inside nozzle. Consequently, since cases 0's and 0s share the same longer path, the difference in static temperature between them cannot be attributed to heat transfer from nozzle walls. Part of the extra pressure energy stored within the 0s-flow is believed to be consumed in viscous heating, since 175 g/s of air are forced through the nozzle, whereas case 0's has a lower flow rate of only 150 g/s. Therefore, the overall increase in total temperature from case 0 to 0s incorporates both external heating through nozzle walls (≈ 60%) and internal viscous heating through the transformation of some pressure energy into heat (≈ 40%).

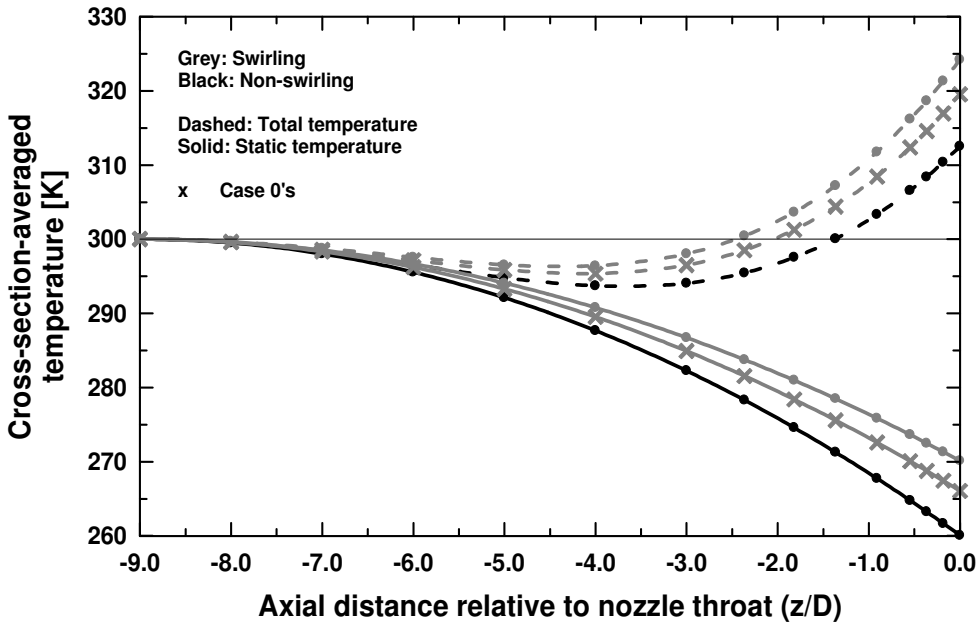

Figure IV-14. Axial variations of cross-section-averaged total and static temperatures inside nozzle in cases 0 (non-swirling, reservoir pressure = 7.91 bar), 0's (swirling, reservoir pressure = 7.91 bar), and 0s (swirling, reservoir pressure = 8.82 bar)

Having analyzed the Mach number and total and static temperatures, the discussion proceeds to analyzing the effect of swirl on the total and static pressures. Figure IV-15 shows the subsonic axial variations of total and static pressures for cases 0, 0's, and 0s. The first important observation to be made is that no significant pressure energy is consumed in additional viscous heating when case 0 is swirled to become 0's. This confirms the aforementioned argument that the difference in static temperature between 0 and 0's is attributed mainly to more heat gained by the latter from nozzle walls. A fundamental question arises at this point: If the application of swirl at the same nozzle reservoir pressure (i.e., cases 0 and 0's) results in very minor changes in throat static pressure and temperature, then what causes the significant reduction in flow rate with swirl? Recall that the mass flow rate is the product of throat density, cross-sectional area, and *axial* velocity component, i.e.,

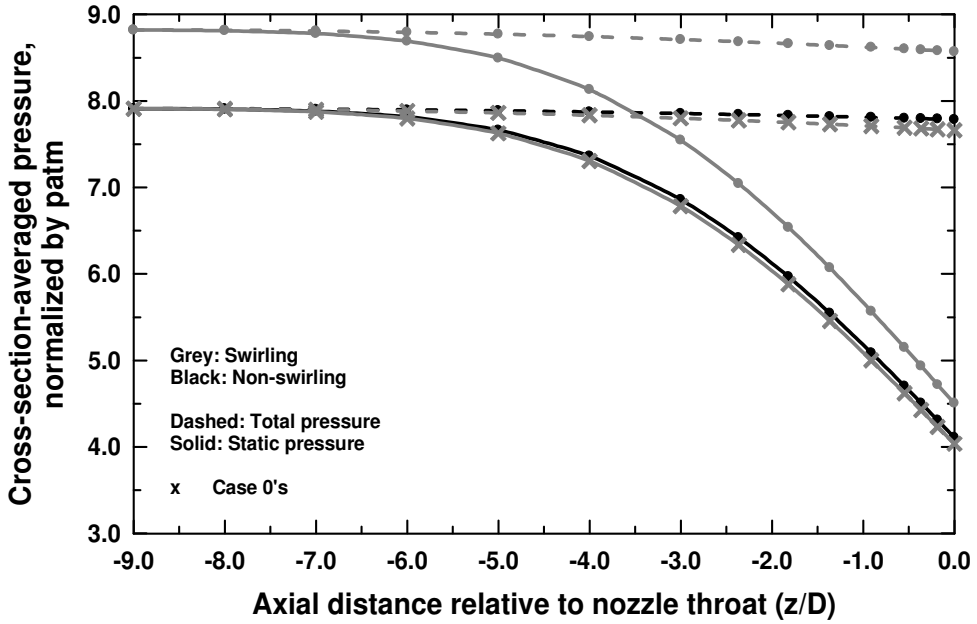

Figure IV-15. Axial variations of cross-section-averaged total and static pressures inside nozzle in cases 0 (non-swirling, reservoir pressure = 7.91 bar), 0's (swirling, reservoir pressure = 7.91 bar), and 0s (swirling, reservoir pressure = 8.82 bar)

$$\dot{m} = \left(\rho A v_a\right)_{throat} = \left(\frac{p}{RT} A M_a \sqrt{\gamma R T}\right)_{throat}$$

If the minor changes in throat static temperature are neglected, the above equation reduces to

$$\dot{m} \propto \left(p M_a\right)_{throat} \tag{IV-3}$$

Recall from the analyses of Figures IV-8a, IV-8d, and IV-13 that non-swirling and swirling flows are similar in terms of overall Mach number (M) and not axial Mach number component (M_a). At the throat, $M_a = M = 1$ in non-swirling flows, but $M_a < M = 1$ in the swirling ones. Therefore, the application of swirl results in a reduction in axial Mach number component. If no measures are taken towards increasing the nozzle reservoir pressure (cases 0 and 0's), the throat static pressure remains almost unchanged (Figure IV-15), and Equation IV-3 dictates that the mass flow rate will decrease. The greater reservoir pressure of case 0s, on the other hand, results in a higher throat static pressure, which compensates for the reduced axial Mach number component with swirl, and the mass flow rate can thus be kept constant at its non-swirling value. This explains the need for higher nozzle reservoir pressure with swirl to avoid reduction in mass flow rate.

The analysis of nozzle flowfield is concluded here by a remark that pertains to the tangential component of Mach number, M_t. It has been observed that the limiting Mach number in a swirling flowfield is the overall Mach number. It reaches its sonic value at the throat, independent of flow rate and inlet conditions, which means that all three components of Mach number are intrinsically subsonic. At extremely high degrees of swirl the value of tangential component approaches that of overall Mach number, which is believed to remain sonic at the throat. It should be noted here that this could not be examined experimentally in this study. No numerical simulations were conducted either in this regard, as they would not be considered a solid reference in the absence of experimental validation. Nevertheless, the current findings of

this study support those of Toomre (1963) and Roschke and Pivirotto (1965), where it was reported that the limiting tangential Mach number is almost unity. The findings of Lewellen et al. (1969) and Pinchak and Poplawski (1965), who reported values of 1.2 and 1.18, respectively, are, however, questioned here but not refuted.

4.5.2. Thrust and Specific Impulse

In light of the analysis of nozzle flowfield, the effect of swirl on nozzle thrust (F) and specific impulse (I_{sp}) can now be quantified. The former is calculated here as follows. From the integral form of momentum equation:

$$\int \rho \vec{v} \left(\vec{v} \bullet \hat{n}\right) dA \quad = \quad -\int p \hat{n}\, dA \quad + \quad \vec{F}$$

If the entire nozzle assembly (i.e., nozzle, support flange, and conditioning chamber; see Figure III-5) is taken as the control volume, the axial component of the above equation simplifies to

$$F = \left(p A\right)_{throat} + \dot{m} v_{a,throat} \tag{IV-4}$$

Note that the axial component of airflow enters the conditioning chamber radially. Thus, the terms $(pA)_{inlet}$ and $(\dot{m} v_a)_{inlet}$ are excluded from the axial momentum equation. The same applies for the tangential entries as well. The specific impulse is defined as

$$I_{sp} = \frac{F}{\dot{m} g} \tag{IV-5}$$

Applying Equations IV-4 and IV-5 to cases 0, 0's, and 0s, the following results are obtained

Case	$p_{reservoir}$ [bar]	p_{throat} [Pa]	$\dot{m}$ [kg/s]	$v_{a,\,throat}$ [m/s]	F_{num} [N]	**F_{exp} [N]**
0	7.91	4.11×10^5	0.175	323.26	87.6	**87.0**
0's	7.91	4.04×10^5	0.150	326.96	79.5	**77.0**
0s	8.82	4.51×10^5	0.175	329.44	91.6	**89.0**

Note that wall friction losses $\left(\int \tau_w \, dA\right)$ were not accounted for in the calculation of thrust, which explains why the numerically obtained values are higher than the experimentally measured ones. Also note that the listed thrust values serve only for validation of numerical code, where very good agreement can be observed. However, before any assessment can be made of the effect of swirl on nozzle thrust and specific impulse, the flows of cases 0, 0's, and 0s have to be optimized by eliminating any degree of underexpansion. This can be achieved by considering a convergent-divergent (CD) nozzle that has the following characteristics: (a) the convergent section is identical to the nozzle examined here, and (b) the exit-to-throat area ratio of the divergent section allows the flow to expand exactly to the atmospheric back pressure, which eliminates any degree of under- or overexpansion and results in shock-free supersonic flow outside the CD nozzle within near-field region. For the non-swirling flow of case 0 the necessary divergent section has an exit-to-throat area ratio of 1.685, which corresponds to an exit diameter of about 1.3 D. Since cases 0's and 0s cannot be fully optimized by the same divergent section, as they do not have the same throat static pressure of case 0, only the latter is optimized here, and any remaining degrees of over- or underexpansion in the swirling cases are tolerated. This optimization procedure was conducted numerically in three more simulations of cases 0, 0's, and 0s, where a CD nozzle was considered with an exit diameter of 1.3 D. The nozzle divergent section was designed using the method of characteristics. The following results were obtained.

Case	$p_{reservoir}$ [bar]	$\dot{m}$ [kg/s]	F [N]	I_{sp} [s]
0	7.91	0.175	99.2	57.8
0's	7.91	0.150	84.0	57.1
0s	8.82	0.175	106.1	61.8

Comparing cases 0 and 0's after optimization it can be clearly seen that the application of swirl at constant nozzle reservoir pressure results in reductions in the discharge coefficient, thrust, and specific impulse, which is in direct agreement with the findings of Carpenter and Johannesen (1975), Kornblum et al. (1986), and Hoffman et al. (1987). Partial agreement also exists with the results of Carpenter (1985) who reported that high swirl levels can be achieved at the expense of a very small thrust loss.

The effect of increasing nozzle reservoir pressure from case 0's to 0s results in the expected thrust enhancement. The relative increase in mass flow is overtaken by a greater relative enhancement in thrust, and the specific impulse is thus increased as a result of increasing the nozzle reservoir pressure. If cases 0 and 0s are finally compared, it is clearly evident that the application of swirl at constant mass flux in a fixed-geometry nozzle results in the enhancement of thrust as well as specific impulse. This is mainly attributed to the considerable degree of underexpansion associated with the flow of case 0s at nozzle exit as a result of the higher nozzle reservoir pressure. These results agree completely with those of Knowles (1992) who examined the use of swirl to reduce screech noise in supersonic jets. Controlled mass flow rates were used, and it was reported that specific impulse can be increased with swirl.

4.6 Supersonic Flowfield

4.6.1. Shock structure

The above analysis of nozzle choking criteria with swirl provided answers for almost all the objective questions of this study. One question, yet to be answered, is how swirl affects the supersonic flowfield, shock strength, shock positions, and jet diameter. Before answering this question an important fact should be recalled here, pertaining to the flowfield inside nozzle. This flow is blind to the atmospheric back pressure outside, due to the sonic barrier at the throat. In

other words, the subsonic flow does not adapt to the back pressure by fixing the throat static pressure at a certain value, regardless of nozzle reservoir pressure. Figure IV-15 is a direct manifestation of this fact, where it is clearly evident that the higher reservoir pressure of case 0s results in a higher throat static pressure. However, once the flow exits nozzle, it is highly sensitive to the back pressure. If the flow pressure is different from that back pressure, the former has to be matched to the latter, which results in the formation of a shock structure in the supersonic flowfield outside nozzle. Convergent nozzles always generate underexpanded jets, if the back pressure is atmospheric. The super-atmospheric throat static pressure dictates how much expansion is still needed and consequently controls the geometry and strength of the formed shock structure, as explained earlier in the analysis of Figure IV-1.

Based on the findings of Adamson and Nicholls (1959), Lewis and Carlson (1964), and Crist et al. (1966), the axial position of first Mach disk (relative to nozzle exit) increases with reservoir pressure. In light of the present analysis, this statement should be corrected to say that the axial position of first Mach disk is affected by both throat static pressure and degree of swirl. Figure IV-16 explains why this correction is necessary. Shown are the flowfield images of cases 0, 0's, and 0s. The horizontal white lines highlight the differences in positions of first Mach disk in cases 0's and 0s relative to case 0. It can be observed that the reservoir pressure is not the sole parameter that controls the position of first Mach disk. Although cases 0 and 0's have the same reservoir pressure, the later has an axially compact shock structure. This does not apply for cases 0 and 0s, which have different reservoir pressures yet similar positions of first Mach disk. Only the comparison of 0's and 0s reveals the expected trend, where increasing reservoir pressure results in axial stretching of shock structure. The effect of swirl explains those unexpected behaviors. Swirling flowfields have two unique features that are absent in non- swirling ones.

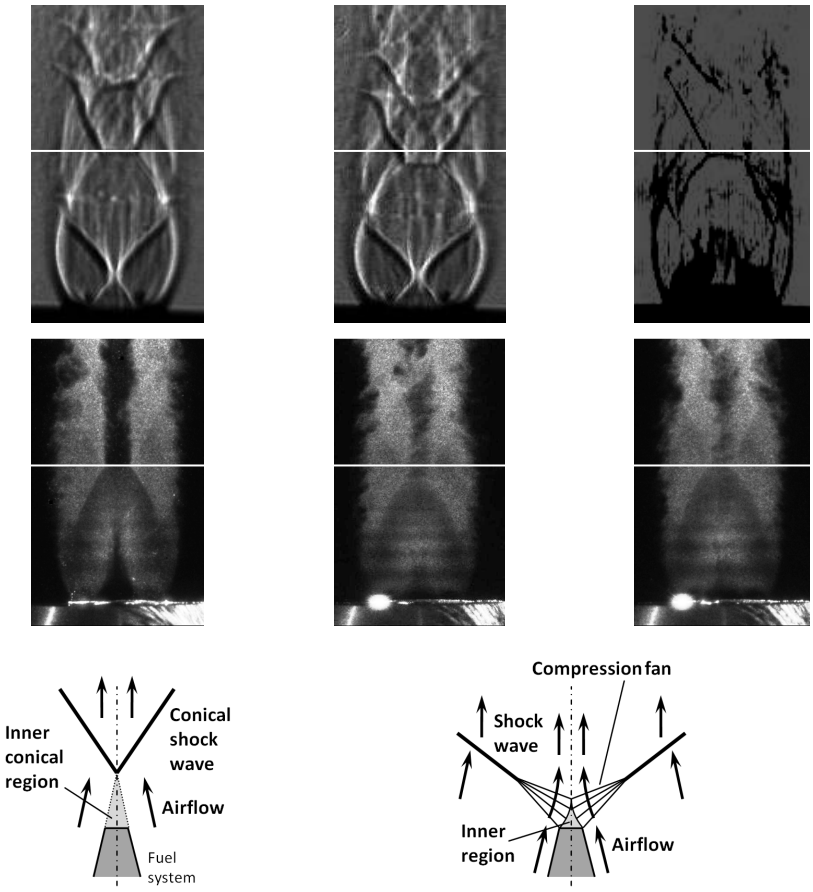

Figure IV-16. Images of non-swirling underexpanded nozzle airflow with no fuel injection. Top: Schlieren; Bottom: Mie-scattering. Left: case 0 (non-swirling, reservoir pressure = 7.91 bar); Middle: 0's (swirling, reservoir pressure = 7.91 bar); Right: 0s (swirling, reservoir pressure = 8.82 bar)

First, the flow is pushed radially outwards by the Coriolis effect. Second, a swirling jet has two velocity gradients (axial and tangential) across its shear layer with the ambient air, which contributes to increasing the jet diameter, as compared to a non-swirling jet with an axial velocity gradient only. The fact that swirl increases jet diameter is concurred in Figure IV-16, where is can be observed that the jet diameter within first shock cell is slightly larger in case 0's than it is in case 0. The larger diameter is accompanied by an axially compact shock structure,

which appears to be a common feature of supersonic and subsonic swirling jets. Thus, it can be concluded here that the effects of swirl and nozzle reservoir pressure interfere destructively from the point of view of shock-structure axial compactness. Increasing reservoir pressure stretches the shock structure axially (case 0's to 0s), whereas swirl shrinks it (case 0 to 0's). This explains why the axial positions of first Mach disk in cases 0 and 0s are almost identical. It should be noted here that the effects of swirl and nozzle reservoir pressure interfere constructively from the point of view of jet radial expansion. Note from Figure IV-16 that the flowfield of case 0s has a slightly larger diameter than that of case 0's. Also note from Figure IV-8d that the combination of swirl and higher reservoir pressure results in the considerably greater radial expansion in case 0s, compared to case 0.

To quantify the effects of swirl and nozzle reservoir pressure in more detail, Figure IV-17 shows the axial distributions of centerline static pressure in the supersonic flowfields of cases 0, 0's, and 0s. Multiple observations can be made from Figure IV-17. The flat segments of nearly constant static pressure immediately downstream of nozzle exit represent the confined inner region observed in Figure IV-16 and discussed in the analysis of Figure IV-1. Very low subsonic Mach numbers exist inside this region, which explains why its centerline static pressure is almost equal to the total pressure of surrounding supersonic airflow. Swirl results in axial shrinking of this region, as observed from Figure IV-16 as well. The presence of nozzle-rim expansion fan is noticed downstream of the inner region. Sub-atmospheric pressures are reached, as the flow passes through expansion fan twice (refer back to the analysis of Figure IV-1 for more details). Note that case 0s expands from 4.4 to 0.4 atm, whereas case 0 expands only from 4.0 to 0.5 atm. This confirms that the combination of swirl and higher reservoir pressure results in a greater expansion fan in case 0s, which was concluded earlier in Figure IV-16. The considerably larger

dark region observed immediately downstream of nozzle exit in the Schlieren image of case 0s is in fact a greater nozzle-rim expansion fan.

The realm of first primary and secondary shock cups is identified in Figure IV-17 as the region of recovery from the minimum sub-atmospheric pressure to a local maximum of super-atmospheric pressure. It can be seen that the first primary shock cup is approached at z/D ≈ 1.45 in case 0, ≈1.4 in case 0s, and ≈1.25 in case 0's. This agrees with the qualitative analysis made earlier in Figure IV-16. The effect of swirl is evident in the upstream shift from 1.45 to 1.25, while the effect of nozzle reservoir pressure is obvious in the downstream shift from 1.25 to 1.4. Both effects interfere destructively, yielding almost the same axial compactness of shock structure in cases 0 and 0s.

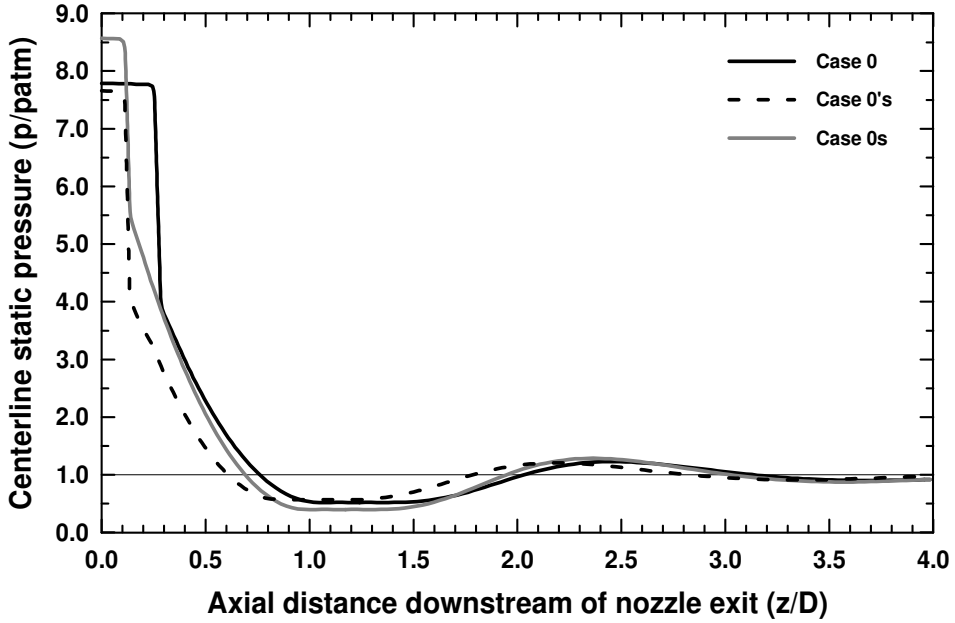

Figure IV-17. Axial variation of centerline static pressure within first two shock cells in cases 0 (non-swirling, reservoir pressure = 7.91 bar), 0's (swirling, reservoir pressure = 7.91 bar), and 0s (swirling, reservoir pressure = 8.82 bar)

The strength of shock structure can also be quantified from Figure IV-17. While the structure of case 0 recovers 0.70 atm, that of case 0's recovers only 0.64 atm. The structure of case 0s, on the other hand, recovers 0.89 atm. Thus, it can be concluded here that the application of swirl at matched nozzle reservoir pressure weakens the shock structure as expected. Both non-swirling and swirling flowfields start off with the same level of energy, but the latter dissipates more pressure energy than the former in friction losses inside nozzle. Consequently, the swirling throat flow has a smaller potential of pressure energy to dissipate through shock structure. The application of swirl at matched mass flow, on the other hand, results in a stronger structure, because of the greater potential of pressure energy at the throat.

Having analyzed the effect of swirl on shock structure, the analysis extends now to examine the supersonic swirl number. Figure IV-18 shows the axial variation of supersonic swirl number within the first two shock cells of case 0s. Similar to the transonic behavior (observed earlier in Figures IV-5 and IV-6), the supersonic swirl number decreases in the axial direction, which is again attributed to substantial increase in axial momentum, as the flow expands and accelerates. A minimum swirl number of 0.07 is observed at z/D of about 1.4, before the swirl number experiences a slight local increase between z/D of 1.4 and 2.7. Recall from Figure IV-17 that the realm of first primary and secondary shock cups in case 0s starts at z/D $\approx$ 1.4. To understand why the supersonic swirl number experiences a slight local increase within the shock cups, it should be noted that the axial and tangential velocity components behave very differently through shock cups. Figure IV-19 helps explain this statement. Depicted is a three-dimensional schematic of shock structure, showing the orientation of v_a and v_t with respect to the main features, i.e., Mach disk, intercepting, and reflected shocks. It can be easily visualized how v_a is always perpendicular to the Mach disk. Moreover, both intercepting and reflected shocks are

oblique with respect to v_a. For these two reasons, the axial Mach number and momentum undergo significant reductions through shock structure. The tangential velocity component, on the other hand, is always parallel to all features of shock structure. According to the fundamentals of gas dynamics, the velocity component parallel to the plane of a shock wave is preserved through the shock and experiences no change. Combining the behaviors of v_a and v_t through shock structure, one can easily explain the small local increase in swirl number within realm of shock cups, especially when one recalls that the swirl number is proportional to the ratio of average tangential to axial momenta.

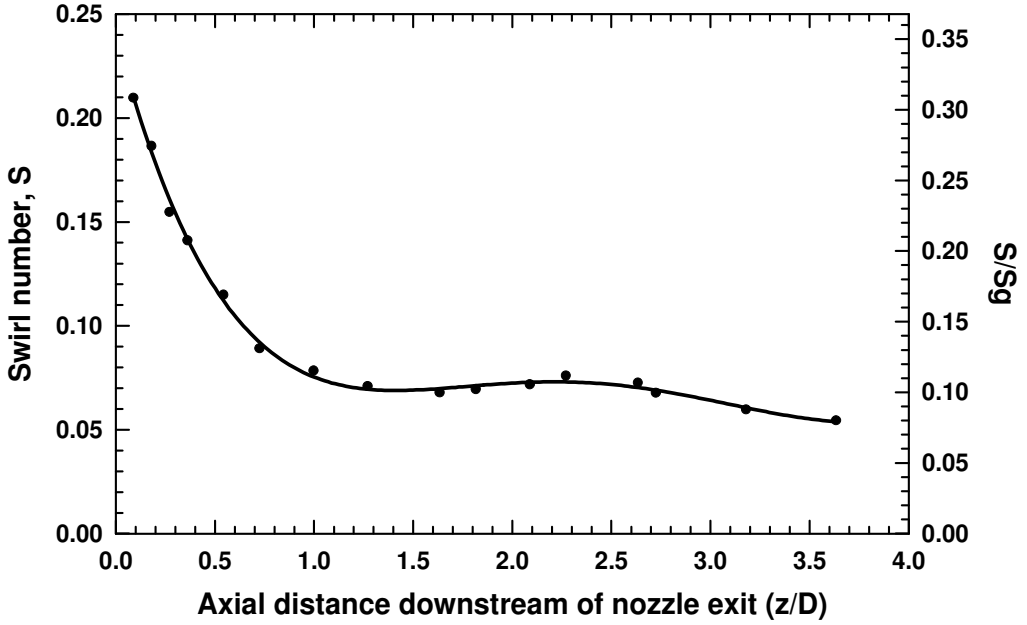

Figure IV-18. Axial variation of supersonic swirl number within first two shock cells in case 0s

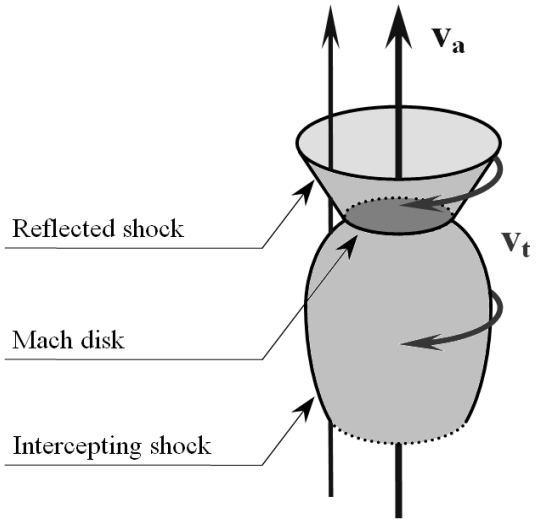

Figure IV-19. 3-D schematic of shock structure showing orientation of axial and tangential velocity components with respect to Mach disk and intercepting and reflected shocks

4.6.2. Mixing

Up to this point, the analysis of supersonic flowfield has been dedicated to quantifying the effect of swirl on shock structure. This section completes the picture by examining how swirl affects supersonic mixing. Vortex enhancement of supersonic mixing was investigated in numerous previous studies, e.g., Settles (1991), Murakami and Papamoschou (2001), Carpenter (1985), Yu et al. (1998), and Yu (1997). It was unanimously reported that the streamwise vorticity counters the adverse effects of compressibility, which results in enhanced supersonic mixing and shear-layer growth with swirl.

Supersonic mixing is examined experimentally in this study by means of the Mie-scattering technique. Air is saturated with the vapor of diethyl ether upstream of the nozzle. As air temperature decreases during expansion, some vapor condenses back to form a fog or mist of submicron seed particles that are small enough to follow the flow faithfully. When illuminated, these particles emit a Mie-scattering signal that is used for mixedness quantification. Figure IV-

16 shows the Mie-scattering images of cases 0, 0's, and 0s. Several important observations can be made from these Mie-scattering images. First, the dark core region downstream of nozzle exit has almost no diethyl-ether seeding particles, hence its dark appearance. It is believed to comprise toroidal vortices of subsonic flow, where kinetic energy is dissipated in viscous heating. Moreover, the static pressure and temperature within this region are equal to the corresponding stagnation values of the surrounding supersonic flow. Diethyl ether particles are thus heated up and re-evaporated, which explains the dark appearance of the core region. It should be noticed here that swirl strongly affects the size of this region. It is forced by the greater nozzle-rim expansion fan of swirling flowfield to take a smaller size with curved boundaries, which explains the schematic to the right in Figure IV-16.

The conical shock wave of secondary shock structure is also identifiable in the Mie-scattering images; so are all the other major shocks of flowfield, such as intercepting shock, Mach disk, and reflected shock. The second important observation to be made here is that the intensity of Mie-scattered light increases after the flow passes through each shock. This is attributed to flow compression. The dense fog of seeding particles downstream of a shock wave scatters more light. Based on this observation it can be concluded which shocks are stronger than others. The intercepting shock, for example, is distinctly stronger than the reflected one. The Mach disk is an exception of this rule. Being a normal shock, it decelerates the incoming core flow to subsonic speeds, thus raising its temperature significantly. The higher temperature is believed to cause re-evaporation of the liquid diethyl-ether seeding particles. Their absence explains the dark appearance of subsonic core flow downstream of Mach disk. This subsonic core is separated by slip lines from supersonic annular flow. The considerably lower temperature of this annular flow preserves the existence of liquid seeding particles.

The most remarkable observation to be made from the Mie-scattering images in Figure IV-16 is that swirl enhances mixing significantly, which agrees with the findings of all studies in the aforementioned literature review. A clear proof is evident in the smeared slip lines and narrower subsonic core downstream of first primary Mach disk in the swirling flowfield. Enhanced mixing occurs between the supersonic and subsonic sides of slip lines, which is absent across the sharp slip lines of non-swirling flowfield. Note that the presence of visible seeding particles inside the warmer subsonic core means that (a) the annular supersonic flow is the source of these particles, and (b) swirl-induced vortices stir up the core and annular flows across slip lines, thus lowering the temperature of core flow down to the level where it can sustain the presence of liquid seeding particles.

It should be noted here that the analysis of Mie-scattering images cannot be extended to a quantitative level, i.e., the intensity scale of scattered light cannot be converted to a mixture fraction scale, even when fuel is injected into the airflow. This is attributed to the nature of condensate seeding, where the local temperature and pressure strongly affect the size, concentration, and even presence of seeding particles. The obtained light-intensity scale is thus a complicated function of pressure, temperature, and air mixture fraction. Decoupling the three individual effects is a very intricate process.

4.7 Effect of Relative Mach Number (M_{rel})

Having attained thorough understanding of the goal objectives of this study, i.e., the effect of swirl on nozzle choking criteria and supersonic flowfield, the analysis proceeds to examine the effect of fuel injection at different relative Mach numbers. Recall that M_{rel} is defined here as the ratio of ($v_{air} - v_{fuel}$) to the average speed of sound, where v_{air} is the throat velocity of

air, and v_{fuel} is the injection velocity of fuel, since fuel is injected coaxially at nozzle throat (i.e., no recess) in all the following analyses. Also recall that the close values of sonic air velocity under non-swirling and swirling conditions allowed for examining the same values of relative Mach number and air-fuel density ratio (DR) with and without swirl. Another very important detail to be pointed out here is that swirl is imparted to air at matched mass flow from this point forward, i.e., all swirling cases have the same mass flow rate of the non-swirling ones (175 g/s). This implies that the swirling cases have the elevated nozzle reservoir pressure of 8.82 bar. Matching of air mass flow ensures a fair comparison between the different case-pairs based on mixture fractions and mixedness.

The effect of M_{rel} is examined in case-pairs 1 – 13 given in Table IV-1. Case-pairs 1 – 9 span the M_{rel} range 0.44 – 0.26 experimentally. Case-pairs 1 (range begin), 5 (range middle), and 9 (range end) were selected to be examined both experimentally and numerically, in order to optimize the parameters of numerical code for best agreement with the experimental results. It should be noted, however, that only the experimental data was considered when quantifying the effects of M_{rel} and DR on flowfield parameters, since it requires no further validation. The experimental range is extended numerically to -0.48 in case-pairs 10 – 13. Case-pair 11 represents a unique condition, where fuel is injected at the throat velocity of air, resulting in M_{rel} of zero. Case-pairs 12 and 13 represent the extreme situations, where fuel is injected at velocities higher than the throat velocity of air. The corresponding values of M_{rel} are indicated here without neglecting their negative signs, in order to highlight the unique nature of those two case-pairs.

Keeping all airflow properties constant, the flow rate of fuel (simulated by helium) was changed to induce different fuel velocities and thus multiple values of M_{rel}. The injection Mach number of helium was kept below 0.3 (except in case-pairs 12 and 13), in order to maintain a

constant helium density and to avoid compressibility effects on the helium-side of air/helium shear layer. The resulting DR was about 35.5 for most cases. The supply pressure of helium was carefully selected for each case-pair to match the total pressures of helium and air at injection.

Figure IV-20 shows the effect of M_{rel} at constant DR. The experimental results, i.e., Schlieren and Mie-scattering images, are depicted in Figures IV-20a and IV-20b, respectively, while Figure IV-20c shows the numerical results in form of center-plane Mach number and fuel mixture fraction profiles. The non-swirling cases are depicted in the top row of each figure, while the bottom one contains the swirling cases. The values of M_{rel} and injection Mach number of each case-pair are indicated at the top of its column.

The most remarkable observation to be made from the Schlieren and Mie-scattering images, as well as the fuel mass fraction profiles, in Figure IV-20 is that the air/fuel shear layer initiates with a negative angle that transforms later to positive. In other words, the cross-sectional area of core flow converges initially to a minimum value before propagating divergently as expected. Figure IV-21 helps explain this observation. Shown are the axial variations of computed centerline Mach number and fuel mass fraction for different values of M_{rel} under non-swirling conditions. Note that subsonic injection is implemented throughout the analysis of M_{rel}. However, the centerline Mach numbers are observed to increase from the subsonic injection values to supersonic maxima of 1.75 – 2.10. The only possible way for the subsonic core flow to expand to supersonic speeds is to resemble a convergent-divergent nozzle. This can only be achieved if the cross-sectional area of core flow initially converges to a throat before diverging again. The creation of a throat allows the core flow to transition from subsonic to supersonic speeds. To attain further understanding of the location of core-flow throat within flowfield, Figure IV-22 shows how the axial position of this throat varies with M_{rel}. Notice that at high M_{rel}

M_{rel}	**0.44**	**0.41**	**0.39**	**0.37**	**0.35**	**0.32**	**0.30**	**0.28**	**0.26**
M_{He}	0.03	0.04	0.06	0.07	0.09	0.10	0.12	0.13	0.15
					Non-Swirling				
Case	**(1)**	**(2)**	**(3)**	**(4)**	**(5)**	**(6)**	**(7)**	**(8)**	**(9)**
	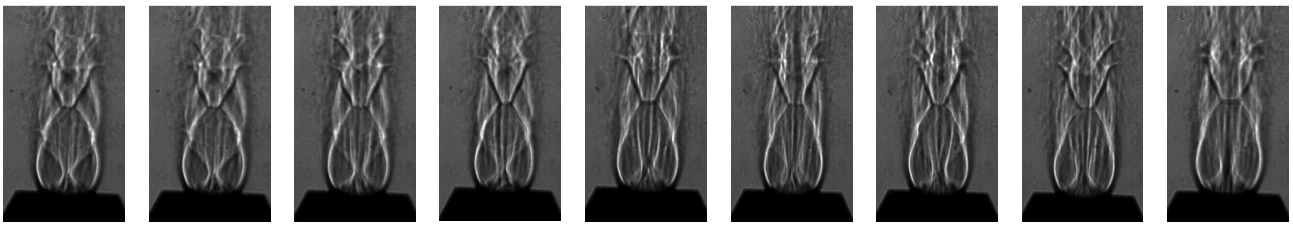								
					Swirling				
Case	**(1s)**	**(2s)**	**(3s)**	**(4s)**	**(5s)**	**(6s)**	**(7s)**	**(8s)**	**(9s)**
	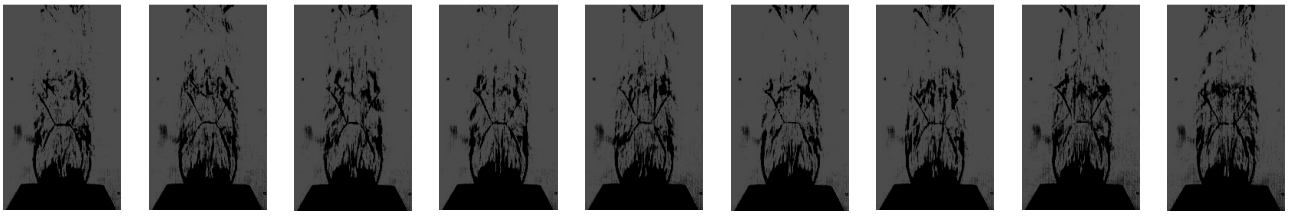								

Figure IV-20a. Effect of M_{rel}; Schlieren images (constant DR = 35.50)

M_{rel}	**1.91**	**1.81**	**1.72**	**1.63**	**1.53**
M_{fuel}	M_{He} = 0.03	M_{He} = 0.06	M_{He} = 0.09	M_{He} = 0.12	M_{He} = 0.15
			Non-Swirling		
Case	**(1)**	**(3)**	**(5)**	**(7)**	**(9)**
	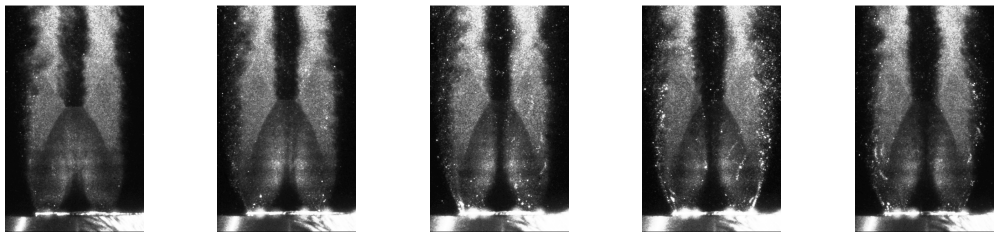				
			Swirling		
Case	**(1s)**	**(3s)**	**(5s)**	**(7s)**	**(9s)**
	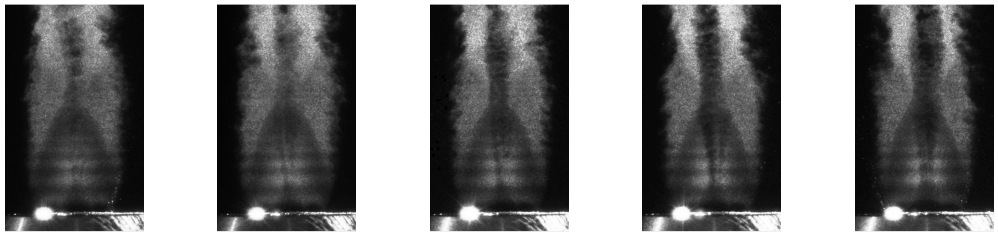				

Figure IV-20b. Effect of M_{rel}; Mie-scattering images (constant DR = 35.50)

M_{rel}	**0.44**	**0.35**	**0.26**	**0.21**	**0.00**	**-0.21**	**-0.48**
M_{fuel}	M_{He} = 0.03	M_{He} = 0.09	M_{He} = 0.15	M_{He} = 0.18	M_{He} = 0.32	M_{He} = 0.46	M_{He} = 0.63

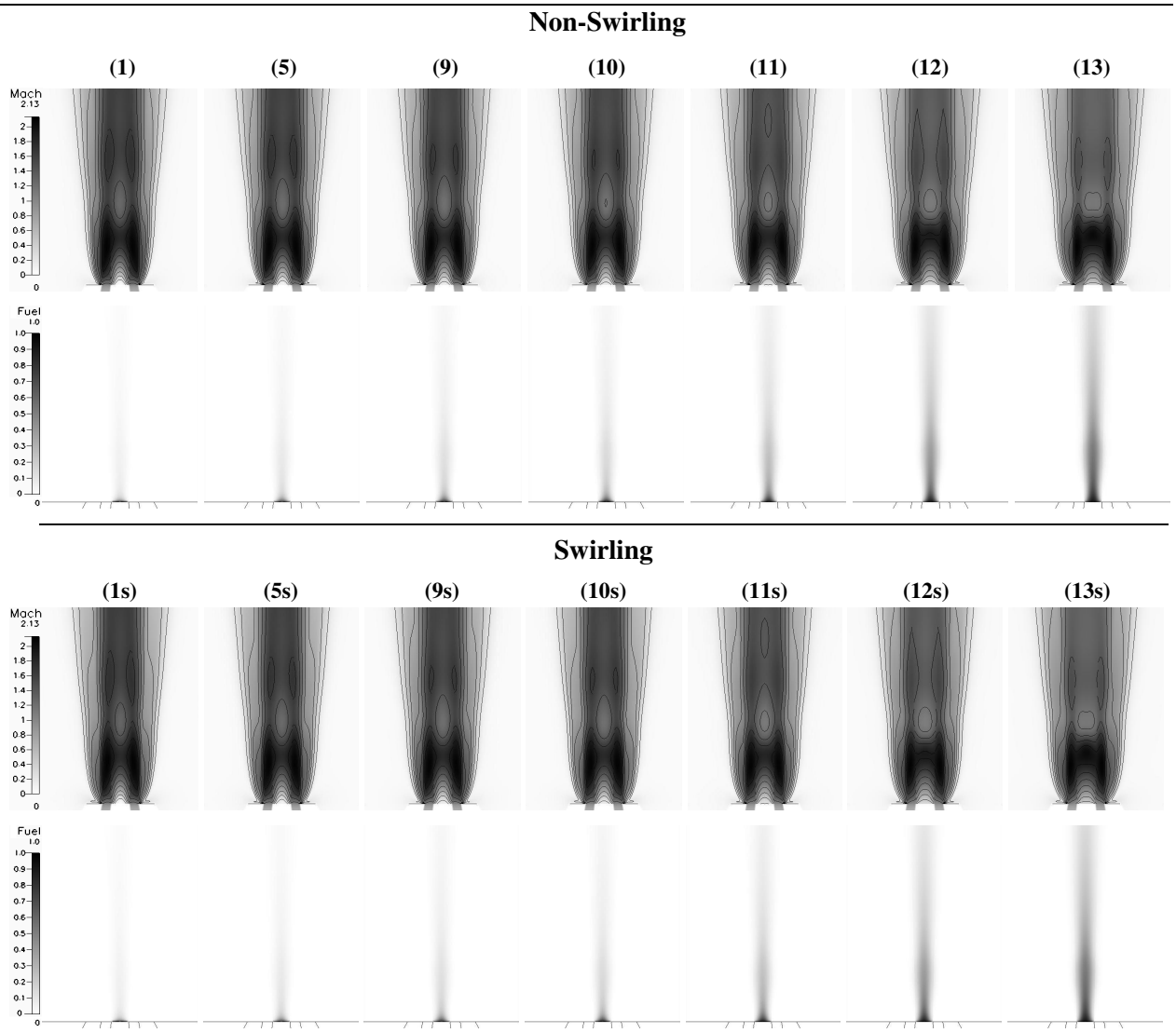

Figure IV-20c. Effect of M_{rel}; numerical results (constant DR = 35.50)
Mach number and fuel mass fraction profiles

(i.e., low injection velocities) the core flow propagates axially for about 0.5 D with a negative shear angle. The throat of core flow, however, approaches nozzle exit at low M_{rel} (high injection velocities), and negative-shear-angle propagation is confined to an axial distance of 0.25 D only.

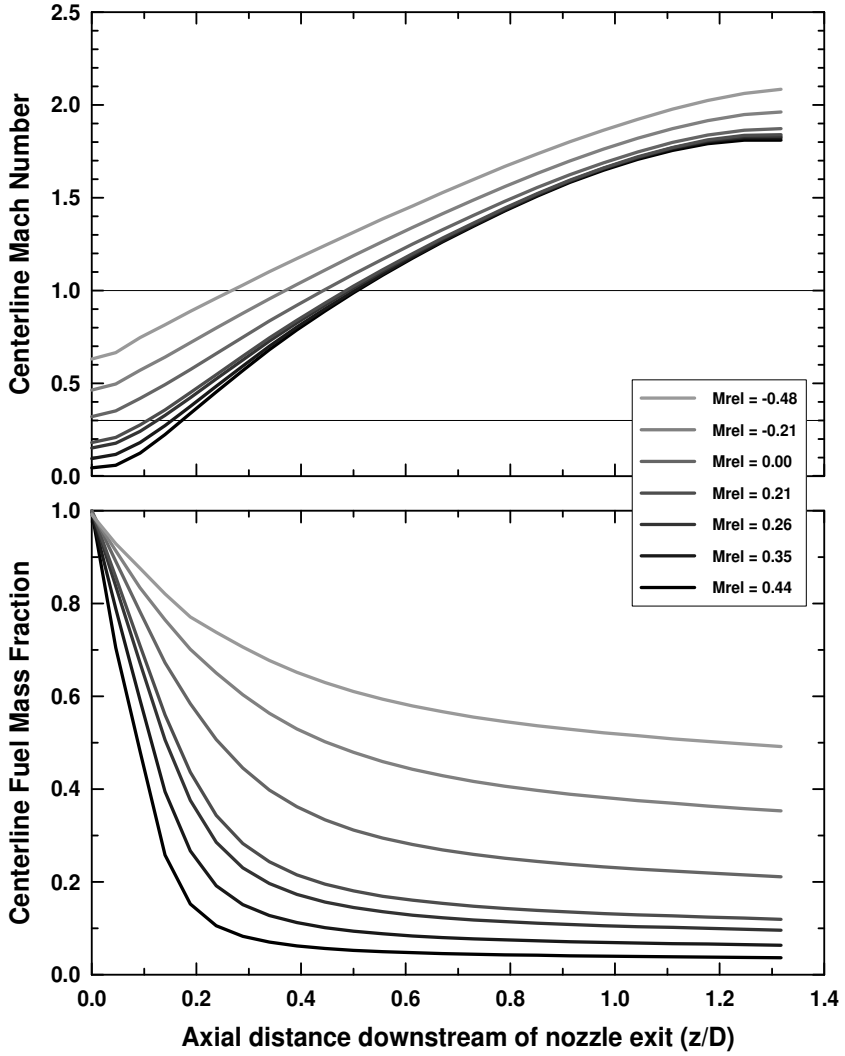

Figure IV-21. Axial variations of centerline Mach number and fuel mass fraction for different values of M_{rel} under non-swirling conditions

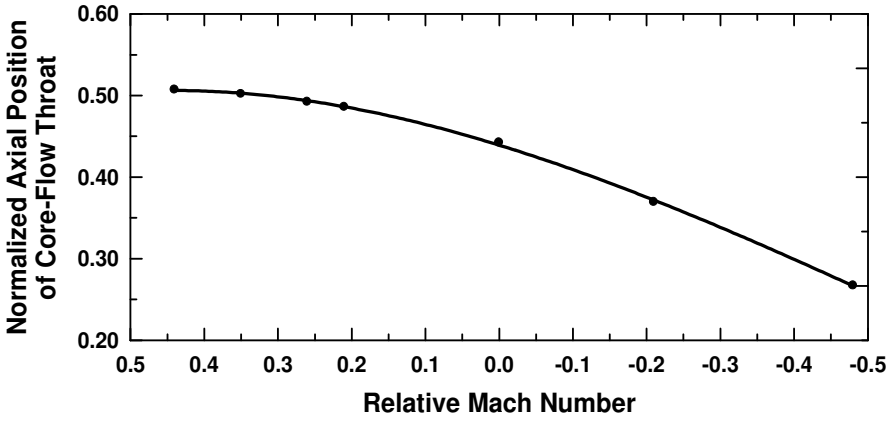

Figure IV-22. Variation of axial position of core-flow throat with M_{rel}

Another important observation to be made from Figure IV-21 is that the initial mixing rate up to z/D of about 0.2 is observed to be affected significantly by the compressibility of fuel injection. Note that incompressible injection is implemented up to M_{rel} of 0.21, whereas case-pairs 11 – 13 (0.00 to -0.48) utilize compressible injection. Higher M_{rel} demonstrate superior mixing. The mixture fraction of fuel drops to centerline values as low as 0.13, which demonstrates how short the potential core of fuel is at high M_{rel}.

Combining the analyses of core-flow throat and initial mixing rate, it can be concluded here that fuel injected at low subsonic Mach numbers (high M_{rel}) has to propagate for longer axial distances with a negative shear angle, before the fuel-rich core flow reaches a throat after which it propagates supersonically. This is advantageous from two aspects. First, increasing the distance between core throat and injection point allows for more mixing to take place across a supersonic/subsonic shear layer, which is significantly more effective than the fully supersonic one downstream of core throat. This is evident in the rates of decay in centerline fuel mass fraction in Figure IV-21. Notice that the decay rates are significantly higher upstream of core throat, which indicates better mixing quality. The second advantage of low injection Mach numbers is that a negative-angled shear layer propagates with a radially inwards component, which allows it to confine the fuel-rich core flow more effectively. This core is thus consumed more rapidly by the growing shear layer, which results in superior mixing at high M_{rel}. The Mie-scattering images in Figure IV-20b confirm this discussion. It can be clearly observed that the high M_{rel} of case-pair 1 results in near-complete mixing of the helium jet with surrounding airflow. Mixing deteriorates gradually as M_{rel} is decreased, which is evidenced in the increasing darkness and size of the unseeded helium-rich core flow.

Another notable advantage of the presence of a negative shear angle downstream of injection point can be observed in the strength of shock structure. As shown schematically in Figure IV-23, the inner conical boundaries and conical shock wave, which initiate the secondary shock sub-structure in the absence of fuel injection, are replaced by a compression fan that is generated off the curved profile of a negative shear angle at subsonic injection Mach numbers. This fan allows for gradual compression of the airflow. Although the fan eventually collapses into a shock wave, the strength of this wave is significantly lower than the conical one at no fuel injection. If M_{rel} is decreased (by increasing injection Mach number), the throat of core flow approaches the injection point, as mentioned earlier. Consequently, the negative shear angle and its compression fan diminish gradually. At the extreme of sonic injection a positive shear angle exists right from the start, accompanied by a strong shock at the injection point. This results in a stronger shock structure. Figure IV-20c confirms this discussion. Notice that the average Mach number within second shock cell is significantly reduced, as the injection Mach number increases and M_{rel} decreases.

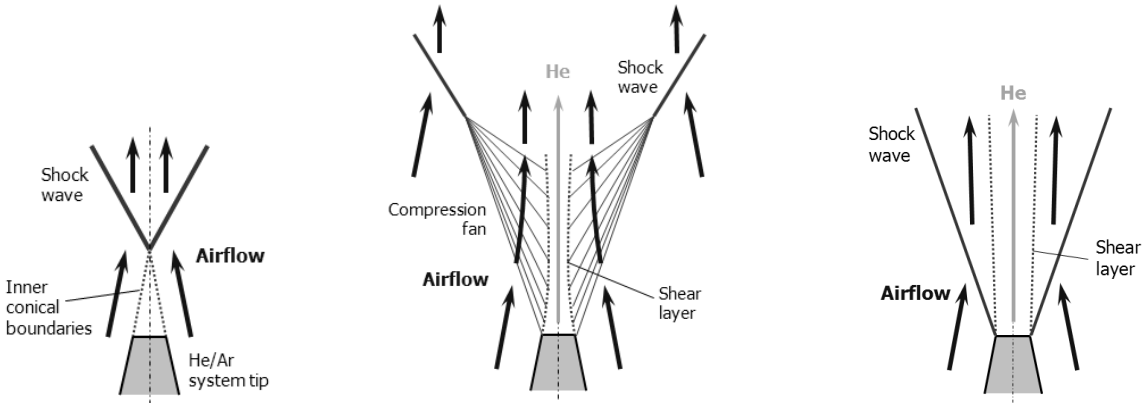

Figure IV-23. Schematic presentation of how the secondary shock sub-structure initiates. Left: no fuel injection; Middle: high M_{rel}; Right: Low M_{rel}

The analysis of M_{rel} is concluded by highlighting the effect of swirl. The first outcome of applying swirl is significant mixing enhancement. This has been expected and can be clearly observed from the Mie-scattering images in Figure IV-20b. Notice that the unseeded core flow in all swirling cases has considerably brighter shades and smaller sizes. Enhanced mixing with the surrounding supersonic airflow explains the presence of seeding particles inside the core flow of swirling cases, whereas the helium-rich core flows of non-swirling cases are particle-free.

4.8 Effect of Air-Fuel Density Ratio (DR)

Having analyzed the effect of relative Mach number, the analysis proceeds to examine the effect of air-fuel density ratio (DR) at constant M_{rel}. DR is defined here as the ratio of throat density of air to injection density of fuel. Also recall that the close values of sonic air velocity under non-swirling and swirling conditions allowed for examining the same values of DR with and without swirl. Another very important detail to be pointed out again here is that swirl is imparted to air at matched mass flow, i.e., all swirling cases have the same mass flow rate of the non-swirling ones (175 g/s). This implies that the swirling cases have the elevated nozzle reservoir pressure of 8.82 bar. Matching of air mass flow ensures a fair comparison between the different case-pairs based on mixture fractions and mixedness.

The effect of DR is examined in case-pairs 14 – 23 given in Table IV-1. Case-pairs 15 – 21 span the DR range 12.68 – 4.33 experimentally. Case-pairs 15 (range begin), 18 (range middle), and 21 (range end) were selected to be examined both experimentally and numerically, in order to optimize the parameters of numerical code for best agreement with the experimental results. It should be noted again here that only the experimental data was considered when quantifying the effect of DR on flowfield parameters, since it requires no further validation. The

experimental range is extended numerically from both sides. Case 14 examines a DR of 35.5, while case-pairs 22 and 23 have DR of 3.24 and 2.29, respectively. Note that case pairs 10 (from M_{rel} analysis) and 14 are identical, as they have the same fuel simulant (helium), M_{rel}, and DR.

Keeping all airflow properties constant, fuel was simulated by different inert-gas mixtures (helium, argon, and krypton). The mixture composition is varied to change mixture density and consequently DR. In order to maintain a constant M_{rel} of 0.21 throughout this analysis, the injection velocity was adjusted to account for the changes in a_{fuel} due to the varying injectant composition. The supply pressure of fuel was carefully selected for each case-pair to match the total pressures of fuel and air at injection. Compressible injection is utilized throughout this analysis, except for case-pair 14, which is copied over from M_{rel} analysis. Case-pair 23 represents the extreme conditions, where fuel is injected at its sonic velocity, i.e., the injection system is choked.

Figure IV-24 shows the effect of DR at constant M_{rel}. The experimental results, i.e., Schlieren and Mie-scattering images, are depicted in Figures IV-24a and IV-24b, respectively, while Figure IV-24c shows the numerical center-plane Mach number and fuel mixture fraction profiles. The non-swirling cases are depicted in the top row of each figure, while the bottom one contains the swirling cases. The values of DR and injection Mach number of each case-pair are indicated at the top of its column, together with the composition of fuel simulant.

In light of the comprehensive M_{rel} analysis, the effect of DR will be analyzed here in a concise fashion. It can be observed from the Schlieren and Mie-scattering images, as well as the fuel mass fraction profiles, in Figure IV-24 that the air/fuel shear layer again initiates with a negative angle that transforms later to positive. Consequently, the cross-sectional area of core flow converges initially to a throat before propagating divergently. This allows the core flow to

DR	12.68	9.60	7.72	6.46	5.55	4.86	4.33
M_{fuel}	0.37	0.44	0.50	0.56	0.61	0.66	0.70
	80% He / 20% Ar	70% He / 30% Ar	60% He / 40% Ar	50% He / 50% Ar	40% He / 60% Ar	30% He / 70% Ar	20% He / 80% Ar
Non-Swirling							
Case	**(15)**	**(16)**	**(17)**	**(18)**	**(19)**	**(20)**	**(21)**
	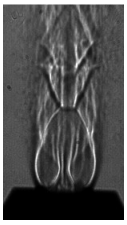	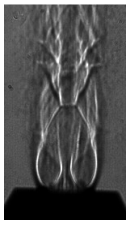		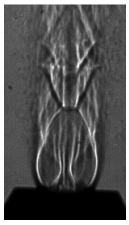	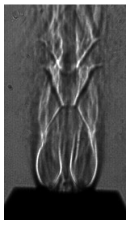	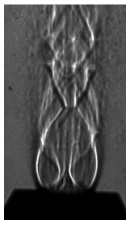	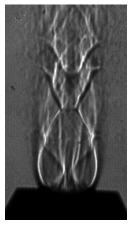
Swirling							
Case	**(15s)**	**(16s)**	**(17s)**	**(18s)**	**(19s)**	**(20s)**	**(21s)**
			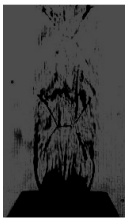				

Figure IV-24a. Effect of DR; Schlieren images (constant M_{rel} = 0.21)

DR	12.68	7.72	5.55	4.33
M_{fuel}	0.37	0.50	0.61	0.70
	80% He / 20% Ar	60% He / 40% Ar	40% He / 60% Ar	20% He / 80% Ar
Non-Swirling				
Case	**(15)**	**(17)**	**(19)**	**(21)**
	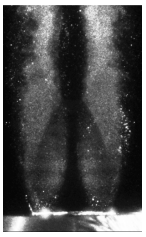	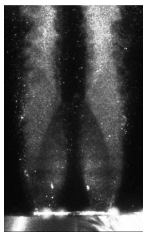	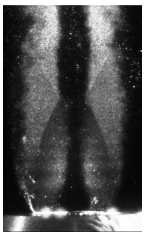	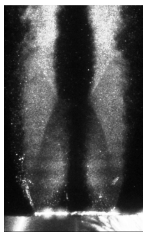
Swirling				
Case	**(15s)**	**(17s)**	**(19s)**	**(21s)**
	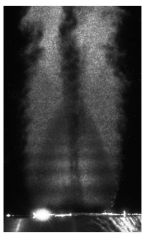	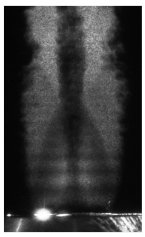	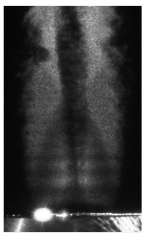	

Figure IV-24b. Effect of DR; Mie-scattering images (constant M_{rel} = 0.21)

DR	**35.50**	**12.68**	**6.46**	**4.33**	**3.24**	**2.29**
M_{fuel}	0.18	0.37	0.56	0.70	0.83	1.00
	100% He	80% He / 20% Ar	50% He / 50% Ar	20% He / 80% Ar	50% He / 50% Kr	50% Ar / 50% Kr

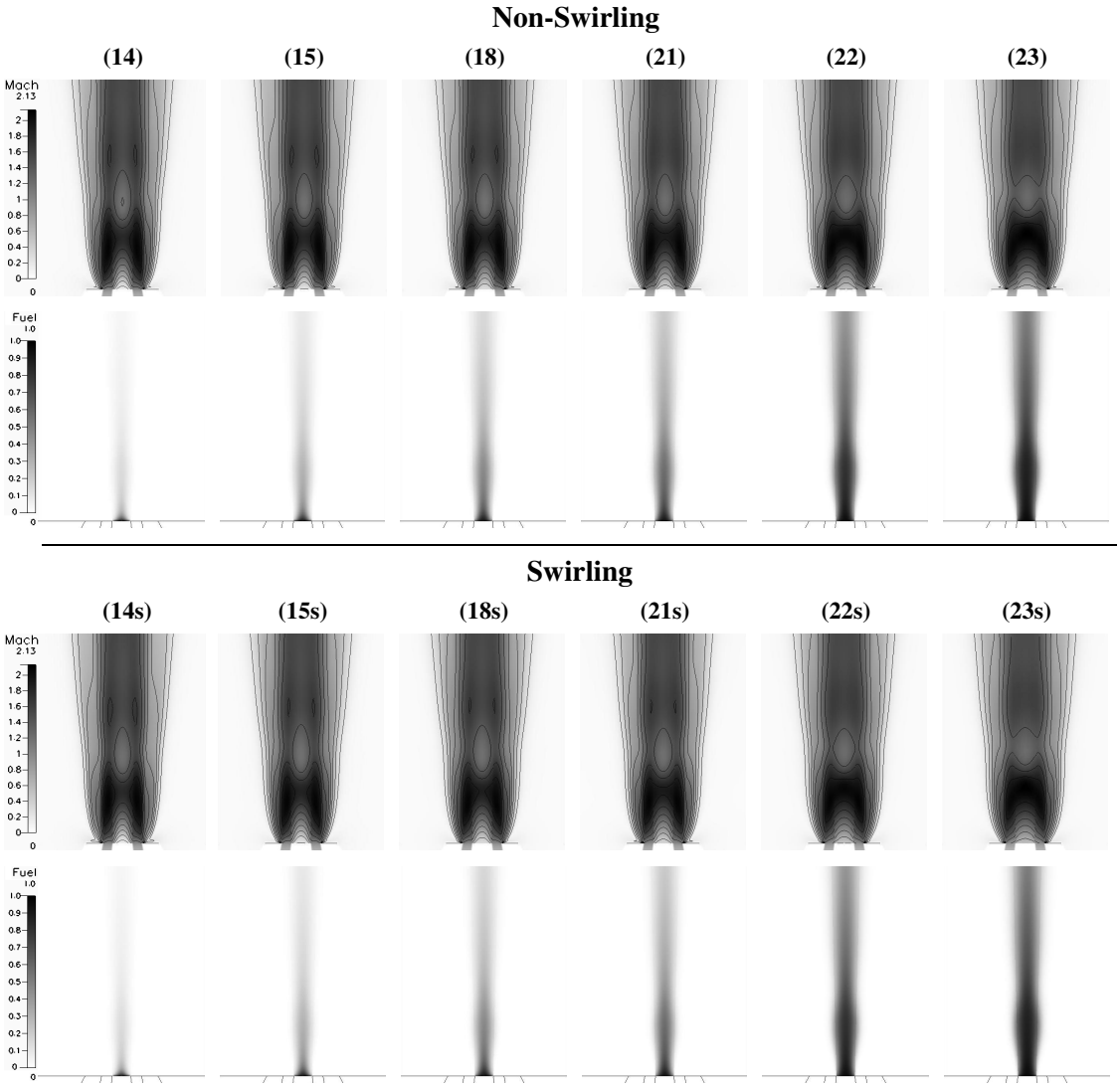

Figure IV-24c. Effect of DR; numerical results (constant M_{rel} = 0.21)
Mach number and fuel mass fraction profiles

accelerate from the subsonic Mach numbers of injection to supersonic maxima of 1.84 – 2.13 in Figure IV-25. The variation of axial position of core throat with DR is shown in Figure IV-26. Notice that at high DR the core flow propagates axially for about 0.5 D with a negative shear angle. However, at a DR of 2.29 the throat of core flow is exactly at the nozzle exit, and

negative-shear-angle propagation is completely absent. Also notice from the rate of decay in centerline fuel mass fraction in Figure IV-25 that a fully supersonic, positive-angled shear layer (DR = 2.29) yields deteriorated mixedness, compared to the supersonic/subsonic negative-angled shear layer at DR = 35.50. The findings of Figures IV-25 and IV-26 are confirmed in the Mie-scattering images of Figure IV-24, where mixing is observed to deteriorate gradually as DR is decreased, as evidenced in the increasing size of unseeded fuel-rich core flow.

The effect of DR on shock-structure strength is observed in Figure IV-24c. Notice again that the transition from negative to positive shear angles results in stronger shock structure at low DR, as evidenced in the decreasing average Mach number within second shock cell. The axial position of first primary Mach disk is observed to be once more almost constant (1.32 – 1.46) for the range of examined DR in Figure IV-25, which is confirmed in the Schlieren and Mie-scattering images of Figure IV-24.

The analysis of DR is concluded here by highlighting the effect of swirl. The first outcome of applying swirl is again significant mixing enhancement, which can be clearly observed from the Mie-scattering images in Figure IV-24b. Notice that the unseeded core flow in all swirling cases has considerably brighter shades and smaller sizes. Enhanced mixing with the surrounding supersonic airflow explains the presence of seeding particles inside the core flow of swirling cases, whereas the fuel-rich core flows of non-swirling cases are particle-free.

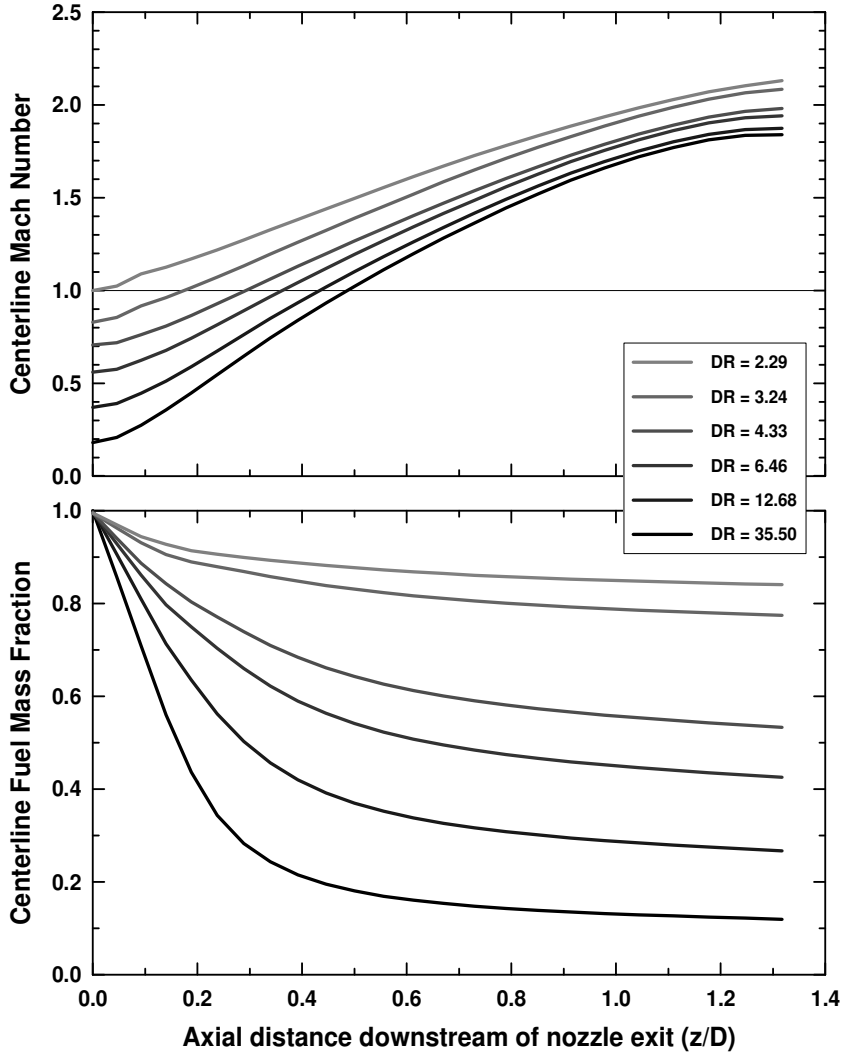

Figure IV-25. Axial variations of centerline Mach number and fuel mass fraction for different values of DR under non-swirling conditions

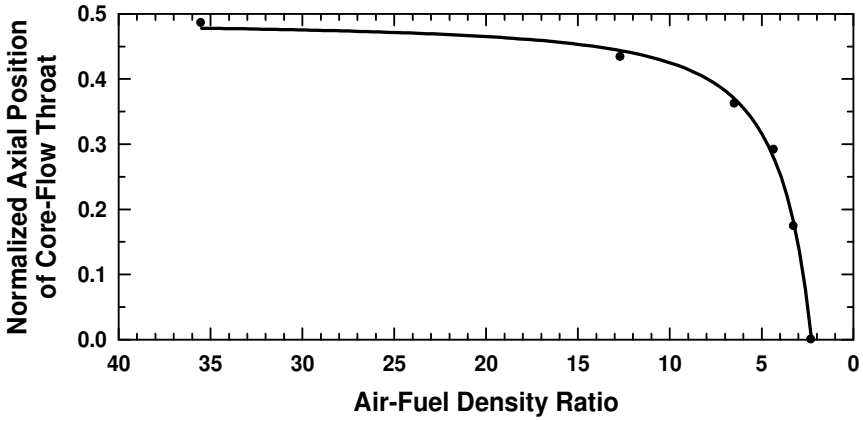

Figure IV-26. Variation of axial position of core-flow throat with DR

4.9 Shear Layer Growth

The analyses of M_{rel} and DR revealed how the angle of air/fuel shear layer critically affects both shock structure and mixing. This section is thus dedicated to attaining better understanding of shear-layer growth, which is another very important parameter. An analysis of shear-layer thickness is conducted here, following the same roadmap of Papamoschou and Roshko (1988). They defined a convective frame of reference that incorporates the effect of flow compressibility and accounts for different speeds of sound on both sides of the shear layer. Figure IV-27 compares this convective frame of reference to the stationary (traditional) one. Notice that the former moves with the flow at the convective wave velocity (v_c). The mainstream Mach numbers on both sides of shear layer transform to this new frame of reference as follows

$$M_{c_{air}} = \frac{v_{air} - v_c}{a_{air}} \quad \text{and} \quad M_{c_{fuel}} = \frac{v_c - v_{fuel}}{a_{fuel}} \tag{IV-6}$$

where M_c stands for convective Mach number. Both values are considerably close, and they always have the same sign, since v_c always lies somewhere between v_{air} and v_{fuel}. If a streamline is traced across the shear layer, as seen in Figure IV-27, a point has to be met, where the local velocity is v_c on an absolute scale but zero (stagnation) on the convective one. This stagnation point forces the equilibrium of total pressures on both sides of shear layer, i.e.,

$$p_{air}\left(1 + \frac{\gamma_{air} - 1}{2} M_{c_{air}}^2\right)^{\frac{\gamma_{air}}{\gamma_{air} - 1}} = p_{fuel}\left(1 + \frac{\gamma_{fuel} - 1}{2} M_{c_{fuel}}^2\right)^{\frac{\gamma_{fuel}}{\gamma_{fuel} - 1}} \tag{IV-7}$$

Substituting from Equation IV-6 into IV-7, the convective wave velocity can be solved for by trial and error. Back-substitution in Equation IV-6 then yields the individual convective Mach numbers of air and fuel. The effect of convective Mach number on shear-layer thickness can thus be quantified, which is a direct indication of how the degrees of compressibility of mainstreams

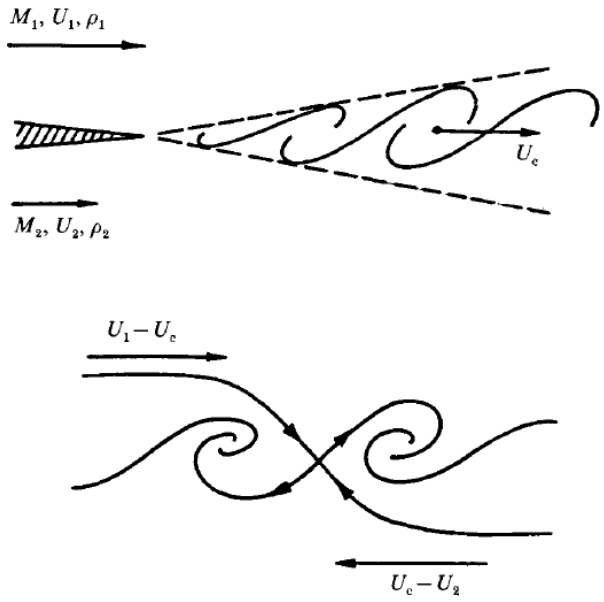

Figure IV-27. Schematic presentation of the stationary (top) and convective (bottom) frames of reference with sketches of streamlines; Papamoschou and Roshko (1988)

on both sides of the shear layer affect its growth rate. Shear-layer thickness is determined as follows. Consider the shear layer shown schematically in Figure IV-28. A *Pitot thickness*, δ_{pit}, is defined after Papamoschou and Roshko (1988) as the width of total-pressure profile from 5% to 95% of the difference of mainstream values. The parameters (p, γ, v, and a) of air and fuel mainstreams are thus calculated at the end points of δ_{pit}.

The analysis of shear-layer thickness is carried out here on all the numerical cases given in Table IV-1, since their simulations contain all the necessary data. The axial positions z/D = 0.1 and 1.0 were selected in each case. Before constructing the final plot of δ_{pit} versus M_c, twenty-four additional simulations were conducted to replicate the 12 numerical case-pairs of Table IV-1 under incompressible conditions, while maintaining their individual velocity and density ratios. The analysis of shear-layer thickness was applied to the attained incompressible flowfields at z/D = 0.1 and 1.0 as well. The ratio of compressible to incompressible shear-layer thicknesses was finally calculated for all the 24 numerical cases at hand. Figure IV-29 is the fruit

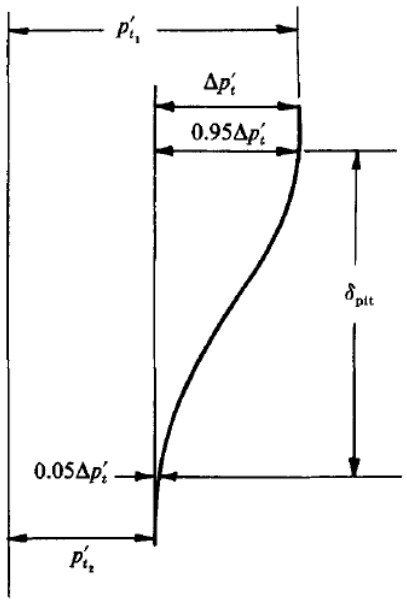

Figure IV-28. Definition of shear-layer Pitot thickness; Papamoschou and Roshko (1988)

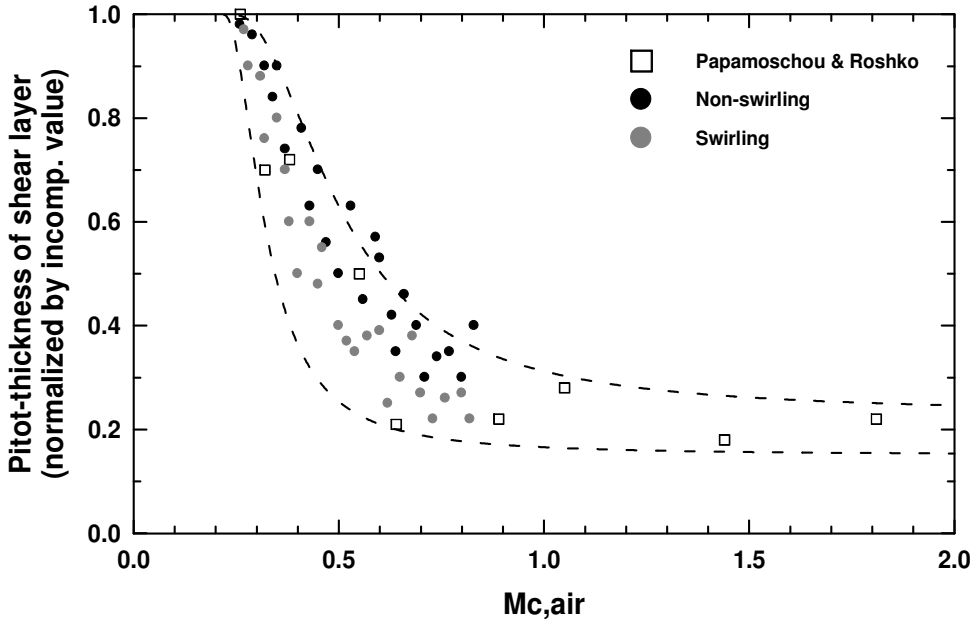

Figure IV-29. Normalized Pitot thickness of shear layer versus $M_{c,air}$

of this effort. The normalized Pitot thickness of shear layer is plotted versus air convective Mach number. All data points fall in the Mach-number range 0.25 – 0.83. The findings of Papamoschou and Roshko (1988) are also included. Good qualitative agreement is observed, since most data points of this current study fall within the dashed lines that represent bounding envelopes of the results of Papamoschou and Roshko. A very important conclusion to be made from Figure IV-29 is that the normalized shear-layer Pitot thickness decreases with the application of swirl. It should be noted, however, that this reduction occurs in the normalized thickness and not the absolute one. As a matter of fact, it was noticed throughout the computations of Figure IV-29 that the absolute value of shear-layer thickness increases slightly with swirl, which agrees with findings of Cutler et al. (1993), Cutler and Levey (1991), and Levey (1991). The controversy is caused here by the fact that the thickness of an incompressible shear layer was found to increase more with swirl than that of a compressible shear layer.

4.10 Effect of Heat Release

Although the objectives of this study focus on examining the effect of swirl on nozzle performance and supersonic flowfield under non-reacting conditions only, a preliminary concluding analysis is conducted here to introduce to the effect of combustion, i.e., heat release. The additional challenge of flame stability is also briefly discussed.

The effect of combustion gives rise to a whole new family of additional parameters that require detailed individual substantiation. For instance, the chemical reactions of combustion release heat that significantly affects the profiles of pressure and temperatures within flowfield. Moreover, turbulence-chemistry interaction becomes a critical parameter that affects most of flowfield properties. Ignition delay emerges as a new important parameter as well, especially at

the high flow speeds within supersonic flames. Some of the parameters of interest, such as thrust and specific impulse, are also affected significantly by heat release.

The absence of combustion throughout all the previous analyses of this study explains why the term "equivalence ratio" has not been encountered. This is understood, of course, since the ratio of mass flow rates of air and fuel-simulant is far less meaningful than other parameters (e.g., swirl, M_{rel}, DR, and M_c) in the previous analyses. From the point of view of combustion, however, the equivalence ratio is a key parameter. Note here, however, that this ratio can be defined in multiple ways. In terms of supply flow rates, i.e., mass flow rates fed to the nozzle, a supply equivalence ratio is defined. The variation of mixedness within flowfield yields the so-called local equivalence ratio. A third definition, termed overall equivalence ratio, accounts for the mass flow rate of the ambient air that gets entrained into the free flame.

The reacting case to be presented here was tested experimentally under the conditions listed in Table IV-2. Successful stabilization of a supersonic flame could not be achieved without the use of a bluff body. This is attributed mainly to the following reasons:

(a) The high supersonic speeds at hand,

(b) No recess was utilized, in order to match the conditions of non-reacting analyses as closely as possible. Negative recess might help by allowing for some subsonic partial-premixing to take place upstream of nozzle throat,

(c) The low temperature of supersonic air jet (in the absence of any preheating) does not allow for sustained ignition, and

(d) The strength of airflow shock structure is simply not sufficient to sustain the flame.

Table IV-2. Test conditions of the reacting case

Parameter	**Value**
Nozzle reservoir pressure	7.0 bar
Air total temperature at nozzle inlet	300 K
Geometrical swirl number	0.36
Air flow rate	140 g/s
Fuel type	Gaseous hydrogen
Fuel flow rate	6.9 g/s
Supply equivalence ratio	1.7
Flame stabilization	Cylindrical bluff body in cross-flow; Cylinder diameter = 0.1 in; Cylinder axial location, z/D = 1.3

The bluff body is a 0.1-in stainless-steel cylinder placed in cross-flow at an axial location z/D of 1.3. This location is upstream of the first primary Mach disk, which ensures that the bluff body is placed in supersonic flow; the Mach number is estimated to be about 1.6 at that location. See Figure IV-30 for a photo that explains how the bluff body is supported. Note that the fuel flow rate has been the main limitation during testing, since the maximum attainable value is only 6.9 g/s. The nozzle reservoir pressure could not thus be increased beyond 7.0 bar without blowing off the flame. Also note that the supply equivalence ratio is fuel-rich, which means that complete combustion cannot be attained without the entrainment of ambient air into the reaction zone. Swirl was utilized to benefit from its aforementioned advantageous effects on mixing.

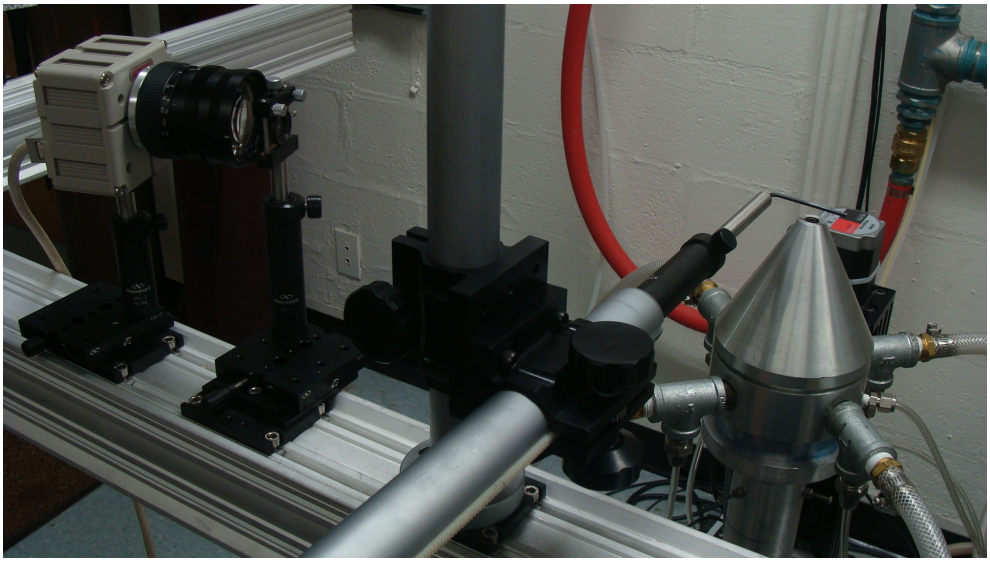

Figure IV-30. Support and alignment of bluff body

Figure IV-31 shows a photo of the obtained supersonic flame. Shown are also a Schlieren image of the corresponding non-reacting flowfield and a simplified schematic that explains the Schlieren image. It can be seen that the presence of blunt bluff body in the supersonic flowfield creates a bow shock. Downstream of this shock the flow splits around the bluff body into two separate streams, which explains the observed V-shape. The flow remains supersonic within the two streams, which is evident in the presence of three successive shock cups within each stream, as observed from the Schlieren images as well as the schematic. Both supersonic streams embrace a subsonic core downstream of the bluff body. It can be clearly observed by comparing the flame photograph to Schlieren image that the flame is confined to that subsonic core immediately downstream of bluff body. The supersonic Mach numbers within the side streams are still high enough downstream of bow shock, which does not allow for flame stabilization. Nevertheless, it should be noticed that a supersonic flame is successfully stabilized downstream

of the first shock cups. This is evident in the sudden enlargement in the size of reacting region as the supersonic side flows pass through their first set of shock cups. The bright high-intensity regions are supersonic flames that extend over the second and third sets of shock cups. These flames are stabilized by the shock structures within, as well as by the reacting subsonic core flow, which is in agreement with the findings of previous studies (see chapter II) on flame stabilization in supersonic flowfields. It has been shown that flame holding in reacting supersonic flows is achieved by creating high-vorticity regions, where the fuel and air partially mix at lower velocities. Such regions of high vorticity exist here with the shock structure as well as the boundaries that separate the supersonic side streams from the subsonic core flow.

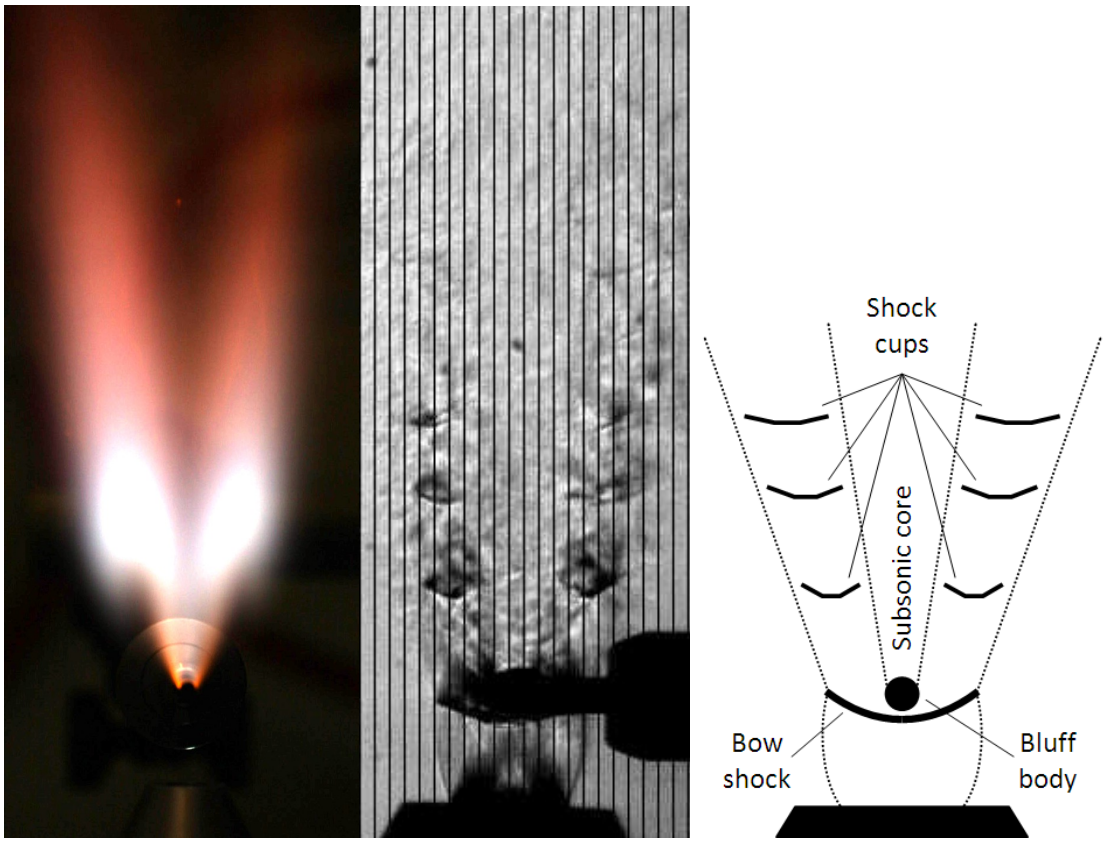

Figure IV-31. Supersonic flame

V. CONCLUSIONS

This study examined the effect of swirl on the choking criteria, shock structure, and mixing in underexpanded supersonic nozzle airflow with coaxial fuel injection. A convergent nozzle was used to generate the underexpanded air jet. The nozzle has swirling capabilities, wherein the axial-tangential-entry technique is used to control the degree of swirl imparted to airflow. Non-reacting conditions were considered; fuel was simulated by mixtures of helium, argon, and krypton inert gases. Injection was performed at the throat of air nozzle. The shock structure and mixing within supersonic flowfield outside nozzle were visualized experimentally using the nanosecond Schlieren and Mie-scattering diagnostic techniques, respectively. CFD numerical simulations were performed on the entire flowfield to quantify the profiles of all properties of interest, such as pressure, temperature, and velocity and Mach number components. In addition to the effect of swirl, different injection conditions were examined as well. The air-fuel relative Mach number and density ratio were changed to study how the air/fuel shear layer is affected. The subsequent changes in shock structure and mixing were also studied. A separate study of the effect of flow compressibility on shear-layer thickness was finally conducted. The following conclusions were obtained.

5.1 Nozzle Choking Criteria

The Mach number itself was found to be choked at nozzle throat in a swirling flowfield, i.e., all of its components (axial, tangential, and radial) remain subsonic through throat. This conclusion resolves the controversy of choking criterion in the literature and rules out the earlier assumption that the axial Mach number component is choked in a swirling flowfield, similar to non-swirling flows. The application of swirl always results in a reduction in axial Mach number

component, which explains the fact that mass flow through nozzle is reduced with swirl (at matched reservoir pressure); an observation that was termed “additional choking” in the literature. The throat mass flux is proportional to the product of throat density and axial Mach number component. Since the latter always decreases with swirl, the reduction in mass flow can be reversed by increasing throat density through the use of higher nozzle reservoir pressure.

The fact that the Mach number itself is choked in a swirling flowfield was backed up with the observation that Mach number distributions in subsonic non-swirling and swirling flows are very similar and almost independent of inlet conditions. Two different reservoir pressures were examined under swirling conditions, and both flowfields showed almost identical subsonic Mach number distributions. The novel conclusion can thus be made that the Mach number of swirling flow is solely dependent on cross-sectional area, similar to non-swirling flows. It is again to be noted here that the similarity is in terms of Mach number itself and not any of its components.

Another conclusion to be made from the choked Mach number in swirling flowfields is that the limiting tangential Mach number is unity, unlike what was reported in some earlier studies that a value of 1.2 can be achieved. If the tangential Mach number is greater than unity, then the Mach number itself would be even greater, which is impossible to achieve within the nozzle convergent section, according to the findings of this study. In fact, the tangential momentum was found not to be conserved throughout the subsonic swirling flowfield, as some earlier studies assumed. It decays gradually due to viscous effects, as the flows progresses axially. This explains why the swirl number always decreases in the axial direction, regardless whether fixed swirl vanes or the axial-tangential-entry technique are used for generating swirl.

In terms of thrust and specific impulse, the application of swirl at matched nozzle reservoir pressure results in the expected reductions in discharge coefficient, thrust, and specific

impulse. At matched mass flow, however, the application of swirl results in the enhancement of both thrust and specific impulse. This is mainly attributed to the considerable degree of underexpansion associated with the flow of case 0s at nozzle exit as a result of the higher nozzle reservoir pressure.

5.2 Shock Structure and Mixing

The presence of a coaxial injection system was found to affect the geometrical swirl number, which decreased from 0.68 down 0.36. The shock structure was also found to differ significantly from that of simple underexpanded flow. Two distinct shock sub-structures can be identified within flowfield. The first one is the simple nozzle-rim structure that also exists in the absence of injection system. Its presence, however, generates a new sub-structure that starts with the airflow creating an inner conical boundary, which completes the cone-frustum shape of fuel-system tip. At the centerline, the airflow collapses into itself, generating a conical shock wave that propagates within flowfield to create its own shock train.

The effects of swirl and nozzle reservoir pressure were found to interfere destructively from the point of view of shock-structure axial compactness. Increasing reservoir pressure stretches the shock structure axially, whereas swirl shrinks it. On the other hand, both effects were found to interfere constructively from the point of view of radial jet expansion; both result in greater jet diameter. The application of swirl at matched reservoir pressure was found to weaken the shock structure as expected. Both non-swirling and swirling flowfields start off with the same total pressure, but the latter dissipates more pressure energy than the former in friction losses inside nozzle. Consequently, the swirling throat flow has a smaller potential of pressure energy to dissipate through shock structure. The application of swirl at matched mass flow, on

the other hand, was found to result in a stronger structure, because of the greater potential of pressure energy at the throat.

Swirl was found to enhance supersonic mixing significantly, which agrees with the findings of all previous studies. A nanosecond condensate-seeded Mie-scattering diagnostic technique was uniquely developed in this study to visualize the variation of mixedness within the supersonic flowfield. To the knowledge of the author, condensate-seeding was never used before for experimental visualization of mixedness in supersonic flows, and this is where the current study contributes significantly to the development of diagnostic techniques. It should be noted, however, that the obtained profiles of Mie-scattering signal can be analyzed only qualitatively, i.e., the intensity scale of scattered light cannot be converted directly to a mixture fraction scale, even when fuel is injected into the airflow. This is attributed to the nature of condensate seeding, where the local temperature and pressure strongly affect the size, concentration, and even presence of seeding particles. The obtained light-intensity scale is thus a complicated function of pressure, temperature, and mixture fraction. Decoupling the three individual effects becomes a very intricate process.

5.3 Effect of Injection Conditions

The effect of injection conditions was examined here at a variety of injection Mach numbers, as well as air-fuel relative Mach numbers and density ratios. It was found that fuel injected at low subsonic Mach numbers has to propagate initially with a negative shear angle. In other words, the cross-sectional area of fuel-rich core flow converges first, before this core flow reaches a throat after which it propagates supersonically. This behavior was found advantageous from multiple aspects. First, increasing the distance between core throat and injection point

allows for more mixing to take place across a supersonic/subsonic shear layer, which is significantly more effective than the fully supersonic one downstream of core throat. Second, a negative-angled shear layer propagates with a radially inwards component, which allows it to confine the fuel-rich core flow more effectively. This core is thus consumed more rapidly by the growing shear layer, which results in superior mixing. Finally, the presence of a negative-angled shear layer was found to allow for gradual compression of airflow along the curved surface of shear layer, which significantly reduces the strength of shock structure.

The analysis of the effect of flow compressibility on shear-layer thickness was conducted using the approach of an earlier study, where a convective frame of reference was defined, which moves with the flow at the local convective wave velocity. This frame incorporates the effect of flow compressibility and accounts for different speeds of sound on both sides of the shear layer. The obtained results were found in good agreement with those of the earlier study. Flow compressibility results in significant reduction in shear-layer thickness. When normalized by its incompressible value, the thickness of shear layer was found to decrease with the application of swirl. It should be noted, however, that this reduction was observed only on the normalized scale and not the absolute one. The absolute value of shear-layer thickness was found to increase slightly with swirl, which agrees with the findings of multiple previous studies. The controversy is caused here by the fact that the thickness of an incompressible shear layer was found to increase more with swirl than that of a compressible shear layer.

VI. RECOMMENDATIONS FOR FUTURE WORK

This study of the effect of swirl on underexpanded supersonic nozzle airflow has analyzed multiple aspects and parameters of the flowfield and yielded many conclusions that contribute significantly to the understanding of the problem and answer a lot of open questions from the literature. Nevertheless, some details still require further substantiation and are thus recommended for future work, as summarized below.

- All the analyses of this study have been conducted at no recess, i.e., fuel was injected at nozzle throat. Recessing the injection system negatively inside nozzle or positively into the supersonic flowfield is expected to yield substantial changes in shock structure and mixing. Negative recess allows for injection in a subsonic environment, whereas positive recess extends the ranges of relative and convective Mach numbers beyond the extents of the current study. The analysis of recess is thus recommended for future work. As a matter of fact, the author has already started efforts to update the test facility for examining the effect of recess.

- A single value of inlet total temperature was examined here, namely 300 K. The effect of changing this temperature is thus recommended for future work. A wide range of temperatures can be examined from the high values of combustion-generated exhaust gases down to cryogenic values. The effect of inlet total temperature might have been already examined in earlier studies, but only under non-swirling conditions, which should motivate future studies to examine that effect under swirling conditions as well.

- Non-reacting conditions have been mainly considered here. The examination of reacting conditions, on the other hand, provides several new avenues for analysis. The effect of combustion gives rise to a whole new family of additional parameters that require detailed individual substantiation. For instance, the chemical reactions of combustion release heat that significantly affects the profiles of pressure and temperatures within flowfield. Moreover, turbulence-chemistry interaction becomes a critical parameter that affects most of flowfield properties. Ignition delay emerges as a new important parameter as well, especially at the high flow speeds within supersonic flames. Some of the parameters of interest, such as thrust and specific impulse, are also affected by heat release. Flame stabilization becomes an extra challenge to be understood and overcome, as was seen in the preliminary analysis conducted here.

- A convergent nozzle was used here to generate an underexpanded airflow. Convergent nozzles are easy to design and operate, as they always generate a supersonic flowfield (provided that the reservoir pressure is high enough, of course). However, convergent nozzles always create underexpanded flows. Convergent-divergent (CD) nozzles, on the other hand, are capable of generating both under- and overexpanded flows, which is an added advantage. Overexpanded flows start with a shock wave, instead of an expansion fan, at the nozzle rim. Consequently, the near-field shock structure is significantly different, which is also worth examining. CD nozzles, however, have the disadvantage that the nature of generated flow is controlled primarily by the nozzle reservoir pressure, i.e., under- and overexpanded flows can never be created by the same nozzle at the same reservoir pressure. An interesting, yet practically impossible, comparison of those flows at the same inlet total pressure is thus ruled out, unless multiple nozzles of different exit-

throat area ratios are used. Another challenge to be overcome is that an overexpanded flow requires significantly higher reservoir pressures to be generated, than does an underexpanded flow. A more powerful air compressor or the use of a vacuum exhaust chamber thus becomes necessary.

- Nanosecond Schlieren and Mie-scattering were used here to visualize shock structure and mixedness, respectively. CFD numerical simulations were thus necessary to quantify the different velocity components. An additional validation of the presented numerical results can thus be made in future studies by performing 3-D particle image velocimetry on the supersonic flowfield. 3-D PIV is already complicated enough when performed on subsonic swirling flows, and it comes even more complicated at supersonic speeds. Some of the challenges to be expected are: (a) The twin shots must have nanosecond exposure as well as nanosecond time difference, in order to freeze the seeding particles in space and be able to capture the same particles on both images, for the cross-correlation software to yield significant results. (b) The laser sheet is expected to be considerably thick to be able to capture the third component of velocity that is perpendicular to the sheet. Increasing the sheet thickness results in reduced accuracy of particle detection through cross-correlation and consequently less accurate quantification of velocity components. (c) The seeding particles have to be small enough to follow the flow faithfully, which requires the use of high-resolution cameras.

APPENDIX A. LIST OF PUBLICATIONS

A.1 Journal Publications

Abdelhafez, A. and Gupta, A. K., "Swirling Underexpanded Supersonic Airflow, Part I: Shock Structure," submitted to the Journal of Propulsion and Power.

Abdelhafez, A. and Gupta, A. K., "Swirling Underexpanded Supersonic Airflow, Part II: Mixing," submitted to the Journal of Propulsion and Power.

Abdelhafez, A. and Gupta, A. K., "Effect of Swirl on the Choking Criteria of Fixed-Geometry Nozzles," submitted to the Journal of Energy.

A.2 Publications in Conference Proceedings

Abdelhafez, A., Kareem, A., and Gupta, A. K., "Swirl Effects on Mixing in Free Underexpanded Supersonic-Nozzle Airflow," 47th AIAA Aerospace Sciences Meeting and Exhibit, Orlando, FL, Jan. 5-8, 2009, AIAA-2009-1419.

Abdelhafez, A. and Gupta, A. K., "Swirl Effects on Free Underexpanded Supersonic Airflow," 47th AIAA Aerospace Sciences Meeting and Exhibit, Orlando, FL, Jan. 5-8, 2009, AIAA-2009-1557.

Abdelhafez, A. and Gupta, A. K., "Advanced Mixing in High-Speed Flows for Efficient Combustion," 2nd Intl. Energy 2030 Conference, Abu Dhabi, UAE, Nov 4-5, 2008.

Abdelhafez, A. and Gupta, A. K., "Swirl Effects on Shock Structure in Free Under-Expanded Supersonic-Nozzle Airflow," 44th AIAA/ASME/SAE/ASEE Joint Propulsion Conference & Exhibit, Hartford, CT, July 21-23, 2008, AIAA-2008-4502.

Abdelhafez, A. and Gupta, A. K., "Numerical Investigation of Oblique Fuel Injection in Supersonic Combustors," 46th AIAA Aerospace Sciences Meeting and Exhibit, Reno, NV, Jan. 7-10, 2008, AIAA-2008-0068.

Abdelhafez, A., Gupta, A. K., Balar, R., and Yu, K., "Evaluation of Oblique and Traverse Fuel Injection in a Supersonic Combustor," 43rd AIAA/ASME/SAE/ASEE Joint Propulsion Conference & Exhibit, Cincinnati, OH, July 8-11, 2007, AIAA-2007-5026.

Abdelhafez, A., Yu, K., and Gupta, A. K., "Interaction of a Gaseous Fuel Jet with Shock-Wave-Rich Airflow," 45th AIAA Aerospace Sciences Meeting and Exhibit, Reno, NV, Jan. 8-11, 2007, AIAA-2007-0390.

APPENDIX B.

SOME OF THE RELEVANT PUBLICATIONS OF THE AUTHOR

Swirling Underexpanded Supersonic Airflow, Part I: Shock Structure

A. Abdelhafez[1] and A. K. Gupta[2]
University of Maryland, College Park, MD 20742

This study is the first of two studies that examine the effect of imparting swirl to underexpanded supersonic nozzle airflow on nozzle choking criteria, thrust, and specific impulse, as well as jet shock structure and mixing. The effects of swirl are examined at matched nozzle reservoir pressure as well as matched mass flow. A convergent nozzle is used to generate the underexpanded airflow. It was found that the throat velocity itself (and not any of its components) is choked in a swirling flowfield. Therefore, the limiting tangential Mach number is unity. Moreover, the application of swirl always results in a reduction in axial Mach number component. The mass flow rate through nozzle was found to be primarily a function of throat density and axial Mach number. The reduction in the latter with swirl explains the observed reduction in mass flow. Greater reservoir pressures, on the other hand, result in higher throat densities, which compensates for the reduced axial Mach number, and the mass flow rate can be kept constant at its non-swirling value. It was also found that the distribution of subsonic Mach number (and not any of its components) in a swirling flow is solely dependent on cross-sectional area, similar to non-swirling flows, i.e., non-swirling and swirling flows have the same subsonic Mach number profile. In terms of thrust and specific impulse, the application of swirl at matched nozzle reservoir pressure results in loss of thrust, which is attributed to reductions in both mass flow rate and throat static pressure. The specific impulse, on the other hand, increases, since the percentage reduction in mass flow is greater than that of thrust. At matched mass flow, however, the application of swirl results in the enhancement of both thrust and specific impulse.

[1] Graduate Student, Dept. of Mechanical Engineering, 2181 Glenn Martin Hall, AIAA Student Member.
[2] Distinguished University Professor, Dept. of Mechanical Engineering, 2181 Glenn Martin Hall, AIAA Fellow.

Nomenclature

A = cross-sectional area

a = speed of sound

D = nozzle-exit diameter (11 mm)

F = nozzle thrust

I_{sp} = nozzle specific impulse

M = Mach number

$\dot{m}$ = mass flow rate

p = pressure

R = specific gas constant

r = radial coordinate

S = swirl number

T = temperature

t = time

v = velocity

z = axial coordinate

γ = ratio of specific heats

ρ = density

$\vec{\omega}_{bc}$ = Baroclinic vorticity vector

Subscripts

a = axial

t = tangential

I. Introduction

Swirling flow in nozzles occurs in a number of important propulsion applications, including turbofans and turbojet engines, spin-stabilized rockets, and integral rocket/ramjets. In the first two cases, the tangential velocity component is induced by the motion of turbine blades and by the rocket spin, respectively. For ramjets, recent experimental studies [1] have demonstrated that swirl generated by fixed vanes located in the dump combustor inlet can lead to significantly improved combustor performance. Clearly, the generated swirl in each of those propulsion

systems will persist at some level to the inlet of exhaust nozzle. Therefore, it is important to examine the effect of tangential velocity component on nozzle flowfield, so that design parameters such as thrust and mass flow rate can be accurately determined.

Of the infinite variety of possible families of swirl profiles, two cases have received particular attention, namely the free- and forced-vortex cases. The most fundamental problem has been the determination of a choking criterion. One-dimensional theory without swirl proves that the throat Mach number is unity, implying that (a) the mass flux through a fixed-geometry nozzle is a maximum, and (b) the throat velocity is equal to the speed of sound. The first criterion of maximum mass flux can be carried over to the swirling flowfield with known stagnation conditions. It is not clear, however, how the second criterion applies to choked swirling flows. Because of the non-uniform throat velocity distribution, it is difficult in the absence of CFD numerical simulations to predict which velocity or velocity component is equal to the local speed of sound. The maximum-mass-flux criterion has been used by several investigators. It was originally introduced by Mager [2] in his theoretical study of choked free-vortex flows with the ratio of specific heats $\gamma = 1.40$. His results were extended by Swithenbank and Sotter [3] to the case of $\gamma = 1.25$, while Glick and Kilgore [4] presented results for γ in the range 1.10 – 1.28.

The analysis of the free-vortex case is simplified by the fact that it is a potential flow, whereas the forced-vortex flow is truly rotational. This may be the reason why there have been several unsuccessful attempts to derive analytical expressions for the output characteristics of nozzles with choked flows. Bastress [5] tried to use the sonic velocity criterion by incorrectly assuming that the velocity magnitude was constant across each section and equal to the critical velocity at the throat. In addition, he assumed forced-vortex flow at all stations. Manda [6] used the constant-stagnation-enthalpy assumption to derive an equation for the axial velocity. Forced-vortex flow was again assumed at all stations, but this time the equality of velocity magnitude and critical velocity at throat was assumed to be satisfied only on the nozzle axis at the throat. King [7] proposed another solution in which he pointed out that the assumption of forced-vortex flow cannot hold everywhere, as it renders the problem over-specified. Manda [8], however, showed that King's solution violated the radial momentum equation. Finally, all the preceding articles were summarized and discussed by Hsu [9] who concluded that the basic reason behind the controversy lies in the fact that the one-dimensional approximation could not be applied to swirling flows.

Carpenter and Johannesen [10] refuted Hsu's conclusions and attempted to extend one-dimensional theory to inviscid compressible swirling flow with the minimum of assumptions. They presented a method for predicting

swirling compressible flow through a nozzle, given conditions at a reference section. The principal assumption they used is that changes in nozzle cross-sectional area are sufficiently gradual for the radial velocity component to be neglected at each section. This method was used to determine choked-flow conditions in the case of solid-body rotation at the throat for different swirl intensities and values of the ratio of specific heats. An approximate analysis valid for low swirl intensities was developed. It was found that neither of the two aforementioned choking criteria gives correct results, although the maximum-mass-flux criterion proved to be a good approximation for moderate swirl. The main conclusion of practical importance was that the introduction of swirl to compressible nozzle flows need not lead to a significant reduction in specific thrust. It was also reported that for a fixed geometry the introduction of swirl is accompanied by a considerable reduction in both mass flux and thrust. However, if the mass flux is kept constant, the reduction in specific thrust is very moderate.

Lewellen et al. [11] developed an approximation that can be used to determine how swirl affects the choking constraint on flow through the throat of a nozzle. It was found that the mass flow rate through a choked nozzle can be sharply reduced by introducing a tangential component of velocity into the flow. Moreover, the choking constraint imposes a limit on the maximum tangential Mach number that can be achieved in a vortex tube, even when an infinite pressure ratio is available. The theoretical choking constraint was used to speculate on the limiting tangential Mach number. It was concluded that this limiting value is 1.2, which is consistent with the experimental observations of Roschke and Pivirotto [12] who reported a value of 1.05. Toomre [13] achieved a value of 1.03, independent of mass flow rate, and Pinchak and Poplawski [14] reported a value of 1.18 in a vortex chamber designed especially to circumvent the difficulties of end-wall dissipation.

The structure of highly underexpanded nozzle jets was investigated experimentally and analytically by Adamson and Nicholls [15], who presented a method for calculating the position of the first Mach disk. In their calculation, the axial pressure distribution on flow centerline downstream of nozzle exit (calculated by method of characteristics) was used to define a fictitious nozzle extension. The Mach disk was then assumed to exist at the point where atmospheric pressure would be attained upstream of the disk, i.e., the latter was assumed to exist at the end of fictitious nozzle extension. Physical arguments were employed to extend the analysis to nozzles with supersonic exit Mach numbers. An approximate method for computing the jet boundary, up to the point of maximum jet area, was also given. The analytical results compared favorably with experimental data at relatively low nozzle pressure ratios.

Lewis and Carlson [16] experimentally determined the distance from nozzle exit plane to the first Mach disc in gas-only and gas-particle jets issuing from underexpanded supersonic nozzles. An empirical correlation of the data was presented which is valid for both jet types and incorporates the effect of gas specific-heat ratio. In a relevant experimental investigation Crist et al. [17] studied the structure of underexpanded jets with stagnation pressures up to 15,000 psia, ambient pressures down to 100 μHg, and stagnation temperatures up to 4200 K. The location of first Mach disk was found to be insensitive to the ratio of specific heats, nozzle-lip geometry, and absolute pressure. For over-all pressure ratios up to about 300,000 the location of Mach disk was found to vary as the square root of overall pressure ratio. The diameters of Mach disk, jet boundary, and intercepting shock were found to increase with decrease in specific-heat ratio and to decrease at high stagnation density, where intermolecular forces become important. At high-pressure ratios, the ratio of Mach-disk diameter to Mach-disk position appeared to be constant for a given gas. It was also found that the properties along jet axis can be approximated by the properties of a flow through a hypothetical conical nozzle whose half-angle is given as a function of specific heat ratio. A simplified expression for the distribution of Mach number along the jet axis was given to good approximation as a function of specific-heat ratio.

Gostintsev et al. [18] studied an underexpanded supersonic swirling gas jet issuing from a convergent nozzle. They showed that the effect of rotation on the wave structure of axisymmetric jet is qualitatively analogous to the effect of reduction in overpressure ratio. Using formulas for spiral isentropic flow, an approximate expression was obtained for estimating the location of first Mach disc in the swirling flow downstream of nozzle exit. Batson and Sforzini [19] also studied the structure of swirling flow through a convergent nozzle with emphasis on the effect of swirl on flowfield, thrust, and mass flow produced by nozzled devices, such as jet engines and spin-stabilized rockets. It was reported that the axial velocity component increases, whereas the tangential one decreases, as the flow passes through nozzle throat.

In another study, which has application in ramjets and turbojets, Kornblum et al. [20] presented an analytical performance prediction methodology for annular propulsive nozzles, with swirl introduced in the combustor upstream of nozzle. This methodology was applied to a specific nozzle design for a free-vortex swirl distribution. The results showed that the discharge coefficient, thrust, and specific impulse decrease as the amount of swirl is increased. However, for the values of swirl often encountered in ramjets and turbojets, the effect of swirl on nozzle performance is small and can be neglected in preliminary design and performance calculations. Application of the

prediction methodology to swirl distributions other than free vortex was recommended for future work. Hoffman et al. [21] followed this recommendation by applying the same methodology to investigate the effects of swirler design on nozzle performance. Four types of swirlers were investigated, namely free-vortex, constant-angle, forced-vortex, and Rankine-vortex swirlers. The computed results indicated again that swirl decreases the discharge coefficient, thrust, and vacuum specific impulse. The decrease in discharge coefficient correlates with the mass-averaged swirl for all four types of swirlers. The decrease in vacuum specific impulse is, on the other hand, a function of swirler design. Forced-vortex swirlers induce the least reduction in specific impulse, whereas free-vortex ones induce the greatest reduction.

Naumova and Shmyglevskii [22] demonstrated with a simple example that avoidance of flow rotation is a limitation that might reduce the thrust of supersonic nozzles. Maximum thrust can be achieved with a nozzle length that permits obtaining uniform flow at the exit. If the length limitation does not permit this, then the use of freedom in gas rotation might increase the nozzle thrust. Dutton [23] investigated swirling flow in supersonic propulsion nozzles both numerically and experimentally. Computations were performed for a range of nozzle geometries, inlet swirl profiles, and swirl strengths. A time-dependent finite-difference technique was developed. The numerical results demonstrated, in agreement with the experimental data, that swirl has a minor effect on the specific impulse efficiency. However, relatively large reductions in nozzle discharge coefficient were computed with swirl. It was also reported that for conventional converging and converging-diverging nozzles, the major effect of swirl on flowfield is confined to the core region, with much less pronounced effect at the walls.

Vortex enhancement of supersonic mixing was studied experimentally by Settles [24]. Swirl was utilized to enhance shear layer growth and mixing. It was concluded that swirl enhances compressible mixing; the degree of enhancement increases with increasing swirl. Settles also reported that the effects of convective Mach number and density ratio on the enhancement effect of swirl are still unknown and were thus recommended for future work.

In an experimental investigation, which is very pertinent to this current study, Lee et al. [25] examined the near-field flow structure of underexpanded coaxial swirl jets. Swirl streams were issued from a secondary annular nozzle, while a primary inner nozzle provided the underexpanded free jets. The interactions between the annular swirl and the underexpanded core jets were examined, in order to quantify the effects of the former on the latter. It was shown that the presence of an annular swirl stream causes the core-flow Mach disc to move further downstream, with an increased diameter. In another pertinent study Lee et al. [26] investigated the effect of nozzle-inlet configuration on

underexpanded swirling jets, which were generated by a convergent nozzle with four tangential inlets at the supply chamber. The nozzle-inlet configuration was modified by using different plugs, holes, and needles, which were also utilized for measuring the flow properties at nozzle inlet. The experimental results showed that the presence of a coaxial needle inside the nozzle supply chamber controls the properties of generated underexpanded swirling jets. The structures of these jet flows are highly dependent on the detailed configuration of nozzle supply chamber.

Murakami and Papamoschou [27] examined flow structure and mixing enhancement in 2D and axisymmetric supersonic jets surrounded by secondary annular subsonic coaxial ones. The supersonic jets were issued from a convergent-divergent nozzle operated at off-design conditions. It was shown that the mixing enhancement using secondary parallel injection (referred to as MESPI by the researchers) halves the length of potential core in both round and 2D jets. A short distance past the potential core, mixing enhancement caused a reduction in centerline Mach number by 30% in round jets and 20% in 2D ones. The corresponding reduction in peak molar concentration of a scalar injected in the primary flow was 65% in round jets and around 40% in 2D ones.

Knowles [28] examined the practical possibility of reducing shock-associated noise and controlling mass flow in a supersonic jet by means of swirl. It was found that nozzle performance does not degrade by the introduction of swirl; on the contrary, specific thrust can be increased with swirl. However, the swirl velocity profile needs to be carefully controlled. It was recommended that specific case studies be made to consider swirl in variable engine cycles. Carpenter [29] developed a linearized theory for underexpanded inviscid supersonic jets with arbitrary initial swirl. Estimates were made of the effect of swirl on the total radiated sound power of shock-associated noise. It was found that this noise can be greatly reduced, or even eliminated, at sufficiently high swirl levels, which can be achieved at the expense of a very small thrust loss. Noise elimination was believed to be due to enhanced mixing that leads to the disappearance of some initial shock cells.

In another study more pertinent to mixing in free supersonic flows Yu et al. [30] experimentally examined mode-switching phenomena of supersonic jets with swirl. They observed that the shock-cell spacing of swirling jets is smaller than that of non-swirling ones, which suggests enhanced mixing. In non-swirling compressible jets, the typical two-dimensional vortex roll-up is believed to be suppressed, and mixing and entrainment are reduced, as compared to incompressible jets. Therefore, to counter the adverse effects of compressibility on mixing, adding swirl to a supersonic jet is favorable. The enhanced entrainment and mixing in swirling supersonic jets is thought to be due to the inherent three-dimensionality associated with the axial component of turbulent vorticity in swirling

jets. Yu [31] studied underexpanded supersonic jets to determine the effect of swirl on mixing efficiency. The screech tones, which result from the interaction of shock waves with unstable jet boundaries, were examined at different degrees of swirl for their effect on mixing. Implication of enhanced mixing was discussed. It was also reported that swirl did not eliminate shock cells, nor did it affect their quasi-periodic nature, in spite of the generation of a recirculation zone in strongly swirling jets.

The present work provides an experimental/numerical investigation of the effect of imparting swirl to underexpanded supersonic nozzle airflow on nozzle choking criteria, thrust, and specific impulse, as well as jet shock structure. Such effect has not been fully quantified in the literature yet, due to the inherent three-dimensionality of the problem. Some questions remain unanswered in past research and will be quantified and discussed here. For example, is the throat velocity (or any of its components) equal to the local speed of sound in a swirling flowfield? If yes, then how does swirl affect the shape of sonic line? How does swirl affect the throat Mach number, pressure, and temperature? How are the shock structure and nozzle thrust and specific impulse affected?

II. Experimental Setup

The experimental investigation of this present work has been performed on the UMD supersonic facility. The utilized supersonic-nozzle assembly is shown schematically in Figure 1. A convergent nozzle of inlet-to-exit area ratio of 25 is used to generate an underexpanded supersonic airflow. Reservoir pressures of up to about 9 atm (abs) are available, yielding near-field Mach numbers of up to 2.2 under non-swirling conditions. The nozzle has swirling capabilities, wherein the axial-tangential-entry technique with four tangential inlets is utilized to accurately control the degree of swirl imparted to airflow. This technique has been proven in previous research to be an efficient method for generating supersonic swirling jets [32 – 34]. Thermal flow meters/controllers are used to meter the flow rates of axial and tangential air components with an accuracy of ±1.5% full-scale.

The nozzle was machined out of a single aluminum rod. Aluminum was preferred to stainless steel because the former has higher thermal conductivity, which prevents overheating of nozzle walls during combustion experiments. The higher conductivity allows radiated heat to be dissipated effectively through the thick nozzle walls. The dissipated heat is removed by forced convection of the entrained ambient cold air through the large surface area of nozzle external walls. The thickness of nozzle lip was optimized to allow for significant entrainment of ambient air while having adequate rigidity for machining the exit section to the desired surface finish and dimensional tolerance.

A coaxial fuel-injection system can be used to inject fuel along the axis of air nozzle. A support flange upstream of nozzle ensures and maintains concentricity of the fuel injection system with respect to air nozzle, especially under swirling conditions. This flange comprises a conical sleeve that embraces the injection system. The sleeve wall-thickness decreases in the direction of flow to provide streamlined performance and prevent any blockage close to the nozzle exit. The sleeve is held in place by three spokes extending to the support flange. Their thickness has been optimized to provide rigidity with minimum blockage to incoming axial component of airflow. It should be noted here that those spokes are located physically upstream of air tangential inlets and do not affect the flowfield of tangential air component. Some wakes are expected to exist in axial-component flowfield behind the spokes, but the supersonic flow exiting the nozzle was found to be fully axisymmetric with and without swirl.

Since nozzle thrust and specific impulse are key performance parameters that are affected by the application of swirl, thrust was measured to assess the effect of swirl. The experimental values were also used to validate the numerically obtained ones. In order to measure the thrust, the nozzle assembly was connected to a compression load cell (transducer) of 200-N capacity and ±0.5% FSO accuracy.

The nanosecond Schlieren diagnostic technique was used to visualize the shock-structure in this study. Schlieren imaging yields the first derivative of refractive index in the test region, thus giving an estimate of the density gradients within flowfield. The intensity of captured light can be further processed using image-processing techniques to obtain more quantitative information of the shock structure. Figure 2 shows a schematic of the utilized setup. The light source is a 532-nm Q-switched Nd:YAG laser with pulse duration of only 5 ns, which explains the term “nanosecond Schlieren” and makes this setup unique, compared to conventional Schlieren setups. The nanosecond light duration allows for capturing instantaneous images of the flowfield. No fluctuations are thus accumulated or averaged on the image, which allows for accurate visualization of shock structure.

Due to the fact that the intensity of laser light is too high for safe camera operation, the laser was equipped with neutral-density filters that reduce its light intensity. The divergence of the collimated beam is then increased by means of a plano-concave lens. The divergent beam fully illuminates a concave mirror, which reflects the light in a collimated fashion through the test section. This is essential for avoiding skewed perspective of flowfield. After penetrating the flow, the light is focused by another concave mirror. A knife-edge aperture intercepts the light at the focal point of second mirror to fulfill the Schlieren principles. The resulting images are then captured at a resolution of 1024 x 1024 pixels using a high-speed camera that is synchronized with the laser.

III. Numerical Simulation Type and Assumptions

The ESI-Group CFD-FASTRAN 2008 LES-based code was used for all the simulations conducted in this study. A variable-size grid was generated for the examined geometry. Tighter meshing was implemented near and at the critical geometry locations, e.g., the exits of nozzle and fuel-injection system. Special emphasis was placed on the level of cell skewness. The geometry was sub-divided into individual volumes, each meshed separately, in order to keep the skewness level of the most skewed cell below 0.5. Mesh dependence was carefully examined through testing multiple levels of mesh tightness. A total of 7,166,860 nodes were found sufficient. Higher tightness levels did not yield any significant changes in the obtained profiles and were thus not considered, in order to optimize the computational time.

The Baldwin-Lomax turbulence model was implemented [35]. Calculation of viscosity and conductivity was based on the kinetic theory of gases. The mass diffusivity was calculated based on Fick's law with a Schmidt number of 0.5. A turbulent Prandtl number of 0.9 was used for calculating the turbulent conductivity. Similar to the experimental conditions, the total temperature at air inlets was kept fixed at 300 K, while the total pressure was maintained at 7.91 bar for the non-swirling case and 8.82 bar for the swirling one. The 8.82-bar value was carefully chosen to ensure a common air flow rate of 175 g/s. (The need for higher nozzle reservoir pressure with swirl is explained in detail in the 'Results and Discussion' section.) The total pressure and temperature at air inlets were preserved throughout the iteration process in each examined case until convergence was attained. Owing to the relatively large cross-sectional areas of the air inlets, the entrance velocity of air was only 9.7 m/s, resulting in almost identical inlet stagnation and static conditions.

The nozzle walls were set to be isothermal at 280 K, based on multiple temperature measurements of the nozzle interior and exterior walls. This is attributed to the aforementioned fact that the nozzle is made of aluminum, which has a high thermal conductivity and thus allows the nozzle to act as a near-isothermal body. The walls of fuel-injection system, on the other hand, were set to be adiabatic, because the injection system is immersed almost totally into the nozzle and conditioning chamber, which allows for negligible amounts of heat to be conducted axially upstream through the thin walls of fuel system. Moreover, it is made of stainless steel that has a much lower thermal conductivity (relative to aluminum).

Since the simulation involves a free supersonic flow, special emphasis was placed on the choice of boundary conditions that represent the flow surroundings. The entire nozzle assembly was surrounded by a cylindrical

enclosure of (40 D) diameter and (70 D) length, where D is the nozzle exit diameter (11 mm) — a good representative of jet size. The 40-D enclosure diameter assures that the side boundaries are far enough from the jet, in order to eliminate any interference of both and to maintain constant near-stagnation atmospheric properties at the boundaries. Consequently, the bottom and side enclosure surfaces were assigned the fixed-pressure boundary condition, which matches the constant actual atmospheric ambient pressure. The top side of enclosure, on the other hand, is an outlet located 55 D away from the nozzle exit (≈ 78% of the 70-D enclosure length). This guarantees that the flow leaves the simulated geometry shock-wave-free, since it was observed experimentally that complete transition to subsonic speeds occurs about 30 D downstream of nozzle exit.

The initial conditions of simulation were set for all cases at 1-atm static pressure, 300-K static temperature, 9.7-m/s axial velocity, and zero radial and tangential velocities. Consequently, the simulation incorporated the transient flow behavior as the high-pressure air expands and "marches" from geometry inlet to exit. An initial CFL number of 0.1 was chosen that increases to unity as convergence is approached. Time integration is implicit, where the Point Jacobi (fully implicit) scheme was used. Backward Euler discretization was implemented. Each iteration included 20 sub-iterations. Convergence was usually attained after 18500 – 19500 iterations.

IV. Test Matrix

The effect of swirl is investigated here by forwarding the entire airflow to nozzle tangential entries. This allows for examining a single degree of swirl, namely the maximum attainable one. Following a definition used for incompressible swirling jets [32, 36], a nozzle-based geometrical swirl number S_g is defined for air as

$$S_g = \left(\frac{\pi r_o R_o}{A_t} \right) \frac{m_t}{m_a + m_t} \tag{1}$$

where $\left(\pi r_o R_o / A_t\right) = 0.68$, for the geometry of used nozzle and its tangential entries, and m_a and m_t are the axial and tangential components of airflow, respectively. Consequently, the swirling case in this study has a nozzle-based geometrical swirl number of 0.68. The term "nozzle-based" refers to nozzle operation in the absence of coaxial injection system, as it will be shown later that the presence of this system reduces the geometrical swirl number down to 0.36. This significant reduction made the examination of the effect of swirl feasible only at its maximum attainable degree.

Since the shock structure depends on air total pressure and temperature, both were kept constant at 7.91 bar and 300 K, respectively, for the non-swirling case presented in this study, which resulted in a fixed air flow rate of 175 g/s. It was noticed, however, that imparting swirl to airflow at the same nozzle reservoir pressure of 7.91 bar results in reduced mass flow rate through the nozzle. This observation agrees with the findings of many previous studies, where it was proven that imparting swirl to the airflow results in "additional choking" of the nozzle, i.e., a lower mass flow rate compared to the corresponding non-swirling conditions at the same reservoir pressure. A theoretical limit of no flow was even predicted at an infinitely large swirl number. Therefore, a higher reservoir pressure is necessary to maintain the same flow rate through the nozzle. It was found in this study that a value of 8.82 bar yields identical air flow rates of 175 g/s in the non-swirling and swirling cases. Table 1 lists the cases examined here.

V. Results and Discussion

A. Shock Structure (Non-Swirling, No Fuel Injection)

The shock structure of simple underexpanded supersonic flow is shown schematically in Figure 3. As can be seen, the structure comprises a shock-cell unit that gets repeated periodically to form a shock-cell train. This unit can be described as follows. Axial under-expanded flow undergoes an expansion fan and turns outwards. The free-jet boundary adapts accordingly and turns outwards as well. Passing again through the expansion fan, the outward flow turns back to axial. As the expansion fan meets the boundary, it reflects into a compression fan that coalesces later into the intercepting shock wave. The annular flow adjacent to boundary turns inwards through the compression fan, and the boundary again adapts by turning inwards as well. For slightly underexpanded nozzles, this intercepting shock reflects directly into a reflected shock at the centerline, forming the familiar diamond configuration. However, as the pressure ratio across the nozzle is increased, this reflection no more takes place at the centerline, and a Mach disk is formed. The reflected shock turns the inward annular flow back to the axial direction. Since the Mach disk maintains the axial direction of core flow, the entire flow is now axial again. As the reflected shock impinges on the flow free boundary, it reflects into an expansion fan, starting another shock-cell unit. The repetition of units is continued until viscous effects become predominant, and this structure is no longer observed.

In presence of a coaxial injection system, the shock structure differs significantly from the simple one described above. Figure 4 shows a Schlieren image as well as a schematic of the shock structure of free nozzle flow in the presence of a non-recessed coaxial injection system with no fuel injection. Two distinct sub-structures are

identifiable from Schlieren image and highlighted in the schematic. The first sub-structure is the simple nozzle-rim structure discussed above. A new sub-structure is generated due to the existence of coaxial injection system. It should be noted here that both sub-structures are not fully independent of each other. The presence of each affects the other. This interaction is, however, not indicated on the schematic in Figure 4, for easier understanding of the newly introduced sub-structure off injection system. Indicated here is how each structure would propagate if fully independent of the other. From this point forward, the nozzle-rim and injection-system sub-structures will be denoted “primary” and “secondary” shock structures, respectively, in this study.

The secondary structure starts with the airflow generating an inner conical boundary that completes the cone-frustum shape of fuel system tip. At the centerline, the flow collapses into itself, generating a conical shock wave that turns the flow back to parallel. This shock wave impinges on the outer flow boundaries shortly downstream of the impingement location of nozzle-rim expansion fan. The outer boundaries are altered by the impingement of that conical shock as observed from Figure 4. The shock reflects into an expansion fan that creates its own compression fan, intercepting shock, Mach disk, and reflected shock, similar to the primary structure. Both Mach disks of primary and secondary structures appear distinctly in Figure 4.

The effect of coaxial fuel injection is shown in Figure 5. Helium is used as fuel stimulant. As observed, the secondary shock structure is altered slightly. A shear layer develops in place of the former inner conical boundaries of airflow. Due to the presence of helium, the shear layer does not converge to a sharp point at the centerline. Moreover, due to the curved shape of this shear layer, the airflow undergoes gradual compression through a compression fan, which collapses later into a shock wave that generates the secondary shock sub-structure.

B. Validation of Numerical Code

Numerical simulations of the flowfield have been performed in this study, in addition to the experimental investigation, to broaden the scope of analysis of the latter and provide the desired quantification of certain flowfield parameters. For example, the Schlieren technique is incapable of visualizing the helical motion of a swirling flow or quantifying the different components of Mach number. Therefore, the numerical results are used to provide the missing data needed for examining the nozzle choking criteria, air/fuel shear layer, and propagation of swirl throughout flowfield.

Before presenting any of the numerical results, code validation is demonstrated here by comparing the experimental and numerical visualizations of shock structure side by side in Figure 6. Shown are a Schlieren image

and the corresponding numerically-obtained Mach number profile of case 1 (non-swirling airflow without fuel injection) from Table 1. The Mach number has been particularly chosen amongst other physical flow parameters, as it gives the clearest visualization of shock structure; shock waves are identifiable at regions of steep gradients of Mach number. Good agreement is observed. All flowfield details have been captured numerically with success. Moreover, the positions of shock cups and the values of jet diameter and maximum near-field Mach number agree well with the experimental findings.

Figure 7 provides another means of code validation, wherein the numerically-obtained location of first primary Mach disk (1.50 D) in case 1 is compared to the experimental findings of Adamson and Nicholls [15] (1.52 D, left) and Lewis and Carlson [16] (1.47 D, right). Recall that D is the nozzle-exit diameter. Considering the fact that the geometry investigated here comprises a coaxial fuel injection system, which does not exist in those earlier studies, it can be concluded that good agreement is observed.

Nozzle thrust was also used as means of code validation. The experimentally measured thrust values were used to validate the numerically computed ones. As will be seen later in the discussion of nozzle thrust and specific impulse, the computed and experimental thrusts differ by only 1.2 – 3.2%, which again shows good agreement.

C. Effect of Injection-System Presence

As mentioned earlier, the effect of swirl is investigated here by introducing the entire airflow through nozzle tangential inlets. Based on aforementioned definition, the resulting geometrical swirl number should be 0.68 in the absence of coaxial injection system. However, since the geometry at hand involves one, the effect of its presence on nozzle performance is analyzed first. It was shown in earlier research [26] that the presence of a coaxial needle inside nozzle affects the airflow properties. Figure 8 shows the axial variation of subsonic swirl number inside nozzle in the absence as well as presence of the coaxial injection system. Using the same conditions of case 2 in Table 1 (injection system present, no fuel injection), another case was simulated with the injection system absent. The swirl number was computed at select sections inside the nozzle using the correlation [32]

$$S = \frac{\int_{R_i}^{R_o} v_a \, v_t \, r^2 \, dr}{R_o \int_{R_i}^{R_o} v_a^2 \, r \, dr} \tag{2}$$

where v_a and v_t are the numerically-obtained axial and tangential velocity components, respectively. Multiple observations can be made from Figure 8. The most obvious and expected one is that the swirl number decreases, as

flow progresses towards nozzle throat. This agrees with the findings of Linck [34] and can be attributed to two facts: (a) v_a increases substantially due to flow expansion and acceleration, and (b) v_t was observed to decrease slightly due to viscous losses, as the flow passage narrows and boundary layers develop at the walls. It is worth noting that the swirl number can be roughly approximated as being proportional to the ratio of average tangential to axial components (neglecting the effect of nozzle geometry), which explains the trends depicted in Figure 8.

Figure 8 also reveals that the presence of injection system induces an additional reduction in swirl number throughout the entire nozzle. This is attributed mainly to the development of a second boundary layer along the injection-system walls. Close to the plane of tangential inlets, the relative reduction is small but keeps increasing as the flow progresses through nozzle. This statement is concurred by Figure 9, where the relative reduction in swirl number is plotted. While the upstream sections experience minor reductions, a 47% reduction from 0.68 to 0.36 exists at the nozzle throat due to the presence of injection system, which blocks 17% of throat area. The considerable reduction in throat swirl number is further explained graphically in Figure 10. Shown is the radial variation of tangential Mach number at $z/D = -0.1$ in the absence and presence of injection system. It can be clearly observed that a considerable percentage of angular momentum is lost, simply due to the physical existence of injection system up to r/D of 0.25. Even at $0.25 < r/D < 0.28$ some angular momentum is lost within the injection-system boundary layer.

The combination of three facts is expected to induce these common observations of Figures 8 to 10. First, the angular momentum dominates the flow at upstream sections but loses this domination to the axial momentum progressively along the nozzle. Second, the angular momentum experiences higher losses, as the ratio of boundary-layer thickness to flow-passage height increases along the axial direction. Third, the injection system blocks higher percentages of nozzle cross-sectional area at downstream locations.

D. Nozzle Choking Criteria

Another interesting observation to be made from Figures 8 and 9 is the considerable reduction in trans-throat swirl number on both absolute and relative scales. Figure 11 explains this behavior by comparing the flow sections about nozzle throat ($z/D = -0.1$) and ($z/D = +0.1$). The radial variations of axial and tangential Mach number components (M_a and M_t) are shown in Figures 11a and 11b, respectively. A significant increase in trans-throat axial momentum is observed, which incorporates both jet acceleration and expansion. Significant radial expansion occurs in the absence of the restricting walls of nozzle and injection-system. On the other hand, a reduction in the

magnitude of trans-throat M_t is observed, which agrees with the findings of Batson and Sforzini [19]. Careful inspection of Figure 11b, however, reveals that radial expansion results in an increase in angular momentum, which is undermined by the decrease associated with the reduction in magnitude of M_t. Therefore, the main conclusion to be made here is that the noticeable reduction in trans-throat swirl number (observed in Figures 8 and 9) is attributed mainly to the considerable increase in trans-throat axial momentum. Recall that the swirl number is proportional to the ratio of tangential to axial momenta.

A notable observation to be made from Figure 11a is that the trans-throat magnitudes of M_a are subsonic in the swirling flowfield. This is distinctly different from the behavior of non-swirling flow, where M_a transitions to supersonic values through the throat. Figure 11c explains such unusual behavior under swirling conditions. Shown is the radiation variation of overall trans-throat Mach number (M) within the swirling flowfield. The expected transition to supersonic propagation through nozzle throat is observed, which yields the main conclusion that both non-swirling and swirling flowfields behave similarly in terms of M, and not M_a. Such similarity exists on both the qualitative and quantitative scales, which is concurred by Figure 11d, where the radial distributions of non-swirling and swirling trans-throat Mach number are compared. The values of M within the jet ($0.26 < r/D < 0.47$) are very similar. Figure 12 further proves this fact by comparing the non-swirling and swirling sonic lines, which appear to be almost identical except at greater radii, where the sonic line is reached earlier in the swirling flowfield. This agrees with the findings of Batson and Sforzini [19], where it was reported that the flow velocity near the wall increases with swirl, due to Coriolis effects and area choking. The boundary layers are also identifiable in Figure 12 beyond the radial range $0.26 < r/D < 0.47$.

The remarkable similarity of trans-throat non-swirling and swirling flows can even be traced back to the subsonic flowfield inside nozzle. Figure 13 shows the axial variations of cross-section-averaged subsonic Mach number. It is clearly noticeable how the non-swirling and swirling behaviors are almost identical, which strengthens the findings of Figure 11d and also partially explains the aforementioned fact that the swirling value of sonic v_{air} (329 m/s) is close to the non-swirling value (323 m/s). The static temperature completes the picture, as the velocity is function of both Mach number and static temperature. Figure 14 shows the axial variations of non-swirling and swirling, total and static temperatures inside nozzle. Notice that the throat static temperature increases by about 10 degrees with the introduction of swirl, which further proves the close similarity of non-swirling and swirling

flowfields; a behavior that extends from subsonic Mach number to static temperature and consequently velocity magnitude.

It should be noted at this point that the observed throat values of static temperature are considerably higher than what would be expected in isentropic flows. The isentropic value of sonic static temperature is 250 K in airflow of 300 K total temperature. This behavior can be explained by recalling that the nozzle examined here is made of aluminum. As mentioned earlier, the high thermal conductivity of aluminum allows the nozzle to be almost isothermal at a temperature of about 280 K. The relatively warmer entrained ambient air loses heat to the external nozzle walls, which is conducted to the inner walls and convected to the flow within. The fact that the airflow inside nozzle is gaining heat energy (i.e., not isentropic) is evident in Figure 14, where it can be clearly observed that the throat total temperature is considerably higher than its 300-K inlet value. If the flow were isentropic, it would have a constant total temperature throughout.

Further careful inspection of Figure 14 reveals that the total temperature initially decreases below 300 K by about 5 degrees in the upstream sections of nozzle before recovering and increasing beyond 300 K. This peculiar behavior can be explained by observing Figure 15, where a schematic representation of heat flow and static-temperature distribution is depicted. Notice that the static temperature of nozzle flow decreases from 300 K at inlet to about 265 K at throat. Meanwhile, the stagnation temperature of ambient air is 300 K, and the temperature of nozzle walls was found experimentally to be almost constant at 280 K. It is expected to observe heat transfer from the ambient air to nozzle flow at the downstream sections. The heat flux is expected to increase as the flow approaches nozzle throat, because (a) the temperature difference between ambient air and nozzle flow increases, and (b) the thickness of nozzle wall decreases. In other words, the potential for heat transfer increases, while the resistance decreases. This explains the greater rates of total-temperature increase in Figure 14 as the throat is approached. The peculiar observation, however, is that the 280-K nozzle walls are surrounded by warmer media on both sides at the upstream sections. This allows heat to be conducted axially downstream through the walls from both the ambient air and nozzle flow. The heat lost from the latter at the upstream sections explains the initial decrease in flow total temperature below 300 K, before recovery occurs at the downstream sections.

It might be argued here that these examined conditions do not compare directly to the fundamental isentropic quasi-1D flow through nozzles, so how does the current analysis contribute to the understanding of the effect of swirl on such basic flow? The answer to this question is twofold. First, it was proven in the literature that one-

dimensional approximation cannot be applied to swirling flows without either violating some conservation equations or enforcing assumptions that are too ideal for actual flows. Three-dimensional viscous numerical simulations, on the other hand, can now be implemented to study the behavior of such actual flows. Second, non-isentropic nozzle flows with heat transfer through nozzle walls occur in a number of important practical propulsion applications, including turbofans and turbojet engines, spin-stabilized rockets, and integral rocket/ramjets. Heat transfer is essential for cooling the nozzle walls, especially near the throat section. The presented distributions of Mach number, pressure, and temperature might be specific to the examined geometry and flow conditions, which is also the case in many previous studies. Nevertheless, this study contributes significantly to the understanding of the effect of swirl on nozzle performance and flowfield, while highlighting the similarities and differences of non-swirling and swirling flows. No idealized assumptions are made, which would limit the applicability of the attained findings in engine/ nozzle design or numerical-model development.

Having observed that the throat static temperature increases by 10 K with application of swirl, the question that arises here is whether this is the actual effect of swirl or the result of the swirling flow taking a longer path through the nozzle and thus getting heated up by the relatively warmer 280-K nozzle walls. The answer to this question is discussed as follows. Consider a new case, to be called 3, which is a swirling case like 2 but has the lower reservoir pressure of case 1. All three cases have the same inlet total temperature of 300 K. A side argument might be made here that the aforementioned Mach-number similarity of non-swirling and swirling flows is attributed to the higher nozzle reservoir pressure with swirl, which leads to a common air flow rate. Figure 16, however, refutes this argument. Shown are the axial variations of Mach number inside nozzle for cases 1, 3, and 2. It is clearly evident that non-swirling and swirling flows are unconditionally similar in terms of Mach number, regardless of inlet conditions.

In terms of temperature, on the other hand, it is expected here that only cases 2 and 3 will behave identically. Both are swirling, and the airflow takes the same longer path through nozzle in both. Figure 17, however, shows that the resemblance is only qualitative. Depicted are the axial variations of total and static temperatures inside nozzle for cases 1, 3, and 2. It can be distinctly seen that case 3 is identical to neither 1 nor 2. These differences are believed to be partially attributed to an implicit effect of total pressure. It is known that pressure is a form of energy, i.e., the higher the flow pressure is, the greater is its energy potential. This extra energy can be transformed to other forms within the flow, e.g., viscous heating. If case 3 is compared to 2 from this point of view, it can be deduced that

the latter simply has more energy. Cases 1 and 3, on the other hand, start off with the same energy level (same inlet total temperature and pressure). The difference in static temperature between 1 and 3 can thus be mainly attributed to more heat gained by the latter from nozzle walls along its longer path inside nozzle. Consequently, since cases 3 and 2 share the same longer path, the difference in static temperature between them cannot be attributed to heat transfer from nozzle walls. Part of the extra pressure energy stored within the 2-flow is believed to be consumed in viscous heating, since 175 g/s of air are forced through the nozzle, whereas case 3 has a lower flow rate of only 150 g/s. Therefore, the overall increase in total temperature from case 1 to 2 incorporates both external heating through nozzle walls (≈ 60%) and internal viscous heating through the transformation of some pressure energy into heat (≈ 40%).

Having analyzed the Mach number and total and static temperatures, the discussion proceeds to analyzing the effect of swirl on the total and static pressures. Figure 18 shows the subsonic axial variations of total and static pressures for cases 1, 3, and 2. The first important observation to be made is that no significant pressure energy is consumed in additional viscous heating when case 1 is swirled to become 3. This confirms the aforementioned argument that the difference in static temperature between 1 and 3 is attributed mainly to more heat gained by the latter from nozzle walls. A fundamental question arises at this point: If the application of swirl at the same nozzle reservoir pressure (i.e., cases 1 and 3) results in very minor changes in throat static pressure and temperature, then what causes the significant reduction in flow rate with swirl? Recall that the mass flow rate is the product of throat density, cross-sectional area, and axial velocity component, i.e.,

$$\dot{m} = \left(\rho A\, v_a\right)_{throat} = \left(\frac{p}{RT} A M_a \sqrt{\gamma R T}\right)_{throat}$$

If the minor changes in throat static temperature are neglected, the above equation reduces to

$$\dot{m} \propto \left(p\, M_a\right)_{throat} \tag{3}$$

Recall from the analyses of Figures 11a, 11d, and 16 that non-swirling and swirling flows are similar in terms of overall Mach number (M) and not axial Mach number component (M_a). At the throat, $M_a = M = 1$ in non-swirling flows, but $M_a < M = 1$ in the swirling ones. Therefore, the application of swirl results in a reduction in axial Mach number component. If no measures are taken towards increasing the nozzle reservoir pressure (cases 1 and 3), the throat static pressure remains almost unchanged (Figure 18), and Equation 3 dictates that the mass flow rate will decrease. The greater reservoir pressure of case 2, on the other hand, results in a higher throat static pressure, which

compensates for the reduced axial Mach number component with swirl, and the mass flow rate can thus be kept constant at its non-swirling value. This explains the need for higher nozzle reservoir pressure with swirl to avoid reduction in mass flow rate.

The analysis of nozzle flowfield is concluded here by a remark that pertains to the tangential component of Mach number, M_t. It has been observed that the limiting Mach number in a swirling flowfield is the overall Mach number. It reaches its sonic value at the throat, independent of flow rate and inlet conditions, which means that all three components of Mach number are intrinsically subsonic. At extremely high degrees of swirl the value of tangential component approaches that of overall Mach number, which is believed to remain sonic at the throat. It should be noted here that this could not be examined experimentally in this study. No numerical simulations were conducted either in this regard, as they would not be considered a solid reference in the absence of experimental validation. Nevertheless, the current findings of this study support those of Toomre [13] and Roschke and Pivirotto [12], where it was reported that the limiting tangential Mach number is almost unity. The findings of Lewellen et al. [11] and Pinchak and Poplawski [14], who reported values of 1.2 and 1.18, respectively, are, however, questioned here but not refuted.

In light of the analysis of nozzle flowfield, the effect of swirl on nozzle thrust (F) and specific impulse (I_{sp}) can now be quantified. The former is calculated here as follows. From the integral form of momentum equation:

$$\int \rho \vec{v} \left(\vec{v} \bullet \hat{n}\right) dA \quad = \quad -\int p \hat{n} \, dA \quad + \quad \vec{F}$$

If the entire nozzle assembly is taken as the control volume, the axial component of the above equation simplifies to

$$F = \left(p A\right)_{throat} + \dot{m} v_{a,throat} \tag{4}$$

Note that the axial component of airflow enters the conditioning chamber radially. Thus, the terms $(pA)_{inlet}$ and $(\dot{m} v_a)_{inlet}$ are excluded from the axial momentum equation. The same applies for the tangential entries as well. The specific impulse is defined as

$$I_{sp} = \frac{F}{\dot{m} g} \tag{5}$$

Applying Equations 4 and 5 to cases 1, 3, and 2, the following results are obtained

Case	$p_{reservoir}$ [bar]	p_{throat} [Pa]	$\dot{m}$ [kg/s]	$v_{a,\,throat}$ [m/s]	F_{num} [N]	**F_{exp} [N]**	**I_{sp} [s]**
1	7.91	4.11×10^5	0.175	323.26	87.55	**86.5**	**50.39**
2	8.82	4.51×10^5	0.175	329.44	91.62	**89.0**	**51.84**
3	7.91	4.04×10^5	0.150	326.96	79.47	**77.0**	**52.33**

Note that wall friction losses $\left(\int \tau_w \, dA\right)$ were not accounted for in the calculation of thrust, which explains why the numerically obtained values are higher than the experimentally measured ones. Comparing cases 1 and 3 it can be clearly seen that the application of swirl at constant nozzle reservoir pressure results in loss of thrust, which is attributed to the reductions in both mass flow rate and throat static pressure. The specific impulse, on the other hand, increases, since the percentage reduction in mass flow is 1.5 times that of thrust. These findings agree with those of Carpenter and Johannesen [10], Kornblum et al. [20], and Hoffman et al. [21] in terms of thrust but not specific impulse. Partial agreement also exists with the results of Carpenter [29] who reported that high swirl levels can be achieved at the expense of a very small thrust loss.

The effect of increasing nozzle reservoir pressure from case 3 to 2 results in the expected thrust enhancement, due to the significant increases in both mass flow and throat static pressure. Nevertheless, the relative enhancement in thrust is overtaken by a greater relative increase in mass flow, and the specific impulse is thus decreased as a result of increasing the nozzle reservoir pressure. If cases 1 and 2 are finally compared, it is clearly evident that the application of swirl at constant mass flux in a fixed-geometry nozzle results in the enhancement of thrust as well as specific impulse. These results agree completely with those of Knowles [28] who examined the use of swirl to reduce screech noise in supersonic jets. Controlled mass flow rates were used, and it was reported that specific impulse can be increased with swirl.

E. Supersonic Flowfield

The above analysis of nozzle choking criteria with swirl provided answers for almost all the objective questions of this study. One question, yet to be answered, is how swirl affects the supersonic flowfield, shock strength, shock positions, and jet diameter. Before answering this question an important fact should be recalled here, pertaining to the flowfield inside nozzle. This flow is blind to the atmospheric back pressure outside, due to the sonic barrier at the throat. In other words, the subsonic flow does not adapt to the back pressure by fixing the throat static pressure at

a certain value, regardless of nozzle reservoir pressure. Figure 18 is a direct manifestation of this fact, where it is clearly evident that the higher reservoir pressure of case 2 results in a higher throat static pressure. However, once the flow exits nozzle, it is highly sensitive to the back pressure. If the flow pressure is different from that back pressure, the former has to be matched to the latter, which results in the formation of a shock structure in the supersonic flowfield outside nozzle. Convergent nozzles always generate underexpanded jets, if the back pressure is atmospheric. The super-atmospheric throat static pressure dictates how much expansion is still needed and consequently controls the geometry and strength of the formed shock structure, as explained earlier in the analysis of Figure 3.

Based on the findings of Adamson and Nicholls [15], Lewis and Carlson [16], and Crist et al. [17], the axial position of first Mach disk (relative to nozzle exit) increases with reservoir pressure. In light of the present analysis, this statement should be corrected to say that the axial position of first Mach disk is affected by both throat static pressure and degree of swirl. Figure 19 explains why this correction is necessary. Shown are the flowfield images of cases 1, 3, and 2. The horizontal white lines highlight the differences in positions of first Mach disk in cases 3 and 2 relative to case 1. It can be observed that the reservoir pressure is not the sole parameter that controls the position of first Mach disk. Although cases 1 and 3 have the same reservoir pressure, the later has an axially compact shock structure. This does not apply for cases 1 and 2, which have different reservoir pressures yet similar positions of first Mach disk. Only the comparison of cases 3 and 2 reveals the expected trend, where increasing reservoir pressure results in axial stretching of shock structure. The effect of swirl explains those unexpected behaviors. Swirling flowfields have two unique features that are absent in non-swirling ones. First, the flow is pushed radially outwards by the Coriolis effect. Second, a swirling jet has two velocity gradients (axial and tangential) across its shear layer with the ambient air, which contributes to increasing the jet diameter, as compared to a non-swirling jet with an axial velocity gradient only. The fact that swirl increases jet diameter is concurred in Figure 19, where is can be observed that the jet diameter within first shock cell is slightly larger in case 3 than it is in case 1. The larger diameter is accompanied by an axially compact shock structure, which appears to be a common feature of supersonic and subsonic swirling jets. Thus, it can be concluded here that the effects of swirl and nozzle reservoir pressure interfere destructively from the point of view of shock-structure axial compactness. Increasing reservoir pressure stretches the shock structure axially (case 3 to 2), whereas swirl shrinks it (case 1 to 3). This explains why the axial positions of first Mach disk in cases 1 and 2 are almost identical. It should be noted here that the effects of swirl and nozzle

reservoir pressure interfere constructively from the point of view of jet radial expansion. Note from Figure 19 that the flowfield of case 2 has a slightly larger diameter than that of case 3. Also note from Figure 11d that the combination of swirl and higher reservoir pressure results in the considerably greater radial expansion in case 2, compared to case 1.

To quantify the effects of swirl and nozzle reservoir pressure in more detail, Figure 20 shows the axial distributions of centerline static pressure in the supersonic flowfields of cases 1, 3, and 2. Multiple observations can be made from Figure 20. The flat segments of nearly constant static pressure immediately downstream of nozzle exit represent the confined inner region observed in Figure 19 and discussed in the analysis of Figure 3. Very low subsonic Mach numbers exist inside this region, which explains why its centerline static pressure is almost equal to the total pressure of surrounding supersonic airflow. Swirl results in axial shrinking of this region, as observed from Figure 19 as well. The presence of nozzle-rim expansion fan is noticed downstream of the inner region. Sub-atmospheric pressures are reached, as the flow passes through expansion fan twice (refer back to the analysis of Figure 3 for more details). Note that case 2 expands from 4.4 to 0.4 atm, whereas case 1 expands only from 4.0 to 0.5 atm. This confirms that the combination of swirl and higher reservoir pressure results in a greater expansion fan in case 2, which was concluded earlier in Figure 19. The considerably larger dark region observed immediately downstream of nozzle exit in the Schlieren image of case 2 is in fact a greater nozzle-rim expansion fan.

The realm of first primary and secondary shock cups is identified in Figure 20 as the region of recovery from the minimum sub-atmospheric pressure to a local maximum of super-atmospheric pressure. It can be seen that the first primary shock cup is approached at $z/D \approx 1.45$ in case 1, ≈ 1.4 in case 2, and ≈ 1.25 in case 3. This agrees with the qualitative analysis made earlier in Figure 19. The effect of swirl is evident in the upstream shift from 1.45 to 1.25, while the effect of nozzle reservoir pressure is obvious in the downstream shift from 1.25 to 1.4. Both effects interfere destructively, yielding almost the same axial compactness of shock structure in cases 1 and 2.

The strength of shock structure can also be quantified from Figure 20. While the structure of case 1 recovers 0.70 atm, that of case 3 recovers only 0.64 atm. The structure of case 2, on the other hand, recovers 0.89 atm. Thus, it can be concluded here that the application of swirl at matched nozzle reservoir pressure weakens the shock structure as expected. Both non-swirling and swirling flowfields start off with the same level of energy, but the latter dissipates more pressure energy than the former in friction losses inside nozzle. Consequently, the swirling throat flow has a smaller potential of pressure energy to dissipate through shock structure. The application of swirl at matched mass

flow, on the other hand, results in a stronger structure, because of the greater potential of pressure energy at the throat.

Having analyzed the effect of swirl on shock structure, the analysis extends now to examine the supersonic swirl number. Figure 21 shows the axial variation of supersonic swirl number within the first two shock cells of case 2. Similar to the transonic behavior (observed earlier in Figures 8 and 9), the supersonic swirl number decreases in the axial direction, which is again attributed to substantial increase in axial momentum, as the flow expands and accelerates. A minimum swirl number of 0.07 is observed at z/D of about 1.4, before the swirl number experiences a slight local increase between z/D of 1.4 and 2.7. Recall from Figure 20 that the realm of first primary and secondary shock cups in case 2 starts at z/D ≈ 1.4. To understand why the supersonic swirl number experiences a slight local increase within the shock cups, it should be noted that the axial and tangential velocity components behave very differently through shock cups. Figure 22 helps explain this statement. Depicted is a three-dimensional schematic of shock structure, showing the orientation of v_a and v_t with respect to the main features, i.e., Mach disk, intercepting, and reflected shocks. It can be easily visualized how v_a is always perpendicular to the Mach disk. Moreover, both intercepting and reflected shocks are oblique with respect to v_a. For these two reasons, the axial Mach number and momentum undergo significant reductions through shock structure. The tangential velocity component, on the other hand, is always parallel to all features of shock structure. According to the fundamentals of gas dynamics, the velocity component parallel to the plane of a shock wave is preserved through the shock and experiences no change. Combining the behaviors of v_a and v_t through shock structure, one can easily explain the small local increase in swirl number within realm of shock cups, especially when one recalls that the swirl number is proportional to the ratio of average tangential to axial momenta.

VI. Conclusions

The effects of imparting swirl to supersonic nozzle airflow on nozzle choking criteria, thrust, and specific impulse, as well as jet shock structure, have been investigated both experimentally and numerically. The analysis was conducted at matched nozzle reservoir pressure as well as matched mass flow. The following conclusions were made: (a) the throat velocity itself (and not any of its components) is choked in a swirling flowfield. Therefore, the limiting tangential Mach number is unity. Moreover, the application of swirl always results in a reduction in axial Mach number component. (b) The mass flow rate through nozzle is primarily a function of throat density and axial

Mach number. The reduction in the latter with swirl explains the observed reduction in mass flow. Greater reservoir pressures, on the other hand, result in higher throat densities, which compensates for the reduced axial Mach number, and the mass flow rate can be kept constant at its non-swirling value. (c) The distribution of subsonic Mach number (and not any of its components) in a swirling flow is solely dependent on cross-sectional area, similar to non-swirling flows, i.e., non-swirling and swirling flows have the same subsonic Mach number profile. (d) In terms of thrust and specific impulse, the application of swirl at matched nozzle reservoir pressure results in loss of thrust, which is attributed to reductions in both mass flow rate and throat static pressure. The specific impulse, on the other hand, increases, since the percentage reduction in mass flow is greater than that of thrust. At matched mass flow, however, the application of swirl results in the enhancement of both thrust and specific impulse.

Acknowledgments

This work was supported by the Space Vehicle Technology Institute, jointly funded by NASA, DoD, and USAF within the NASA Constellation University Institutes Project (CUIP), with Claudia Meyer as the Project Manager. This support is gratefully acknowledged.

The simulation package CFD-GEOM, CFD-FASTRAN, and CFD-VIEW was provided by ESI-Group and CFDRC. This support is gratefully acknowledged.

Assistance provided by Adam Kareem in data acquisition and analysis is much appreciated.

References

[1] Buckley, P. L., Craig, R. R., Davis, D. L., and Schwartzkopf, K. G., "The Design and Combustion Performance of Practical Swirlers for Integral Rocket/Ramjets," *AIAA Journal*, Vol. 21, No. 5, 1983, pp. 733-740.

[2] Mager, A., "Approximate Solution of Isentropic Swirling Flow through a Nozzle," *ARS Journal*, Vol. 31, No. 8, 1961, pp. 1140-1148.

[3] Swithenbank, J. and Sotter, G., "Vortex Generation in Solid Propellant Rockets," *AIAA Journal*, Vol. 2, No. 7, 1964, pp. 1297-1302.

[4] Glick, R. L. and Kilgore, M. S., "Effect of Specific-Heat Ratio on Mass Flow for Swirling Nozzle Flow," *Journal of Spacecraft and Rockets*, Vol. 4, No. 8, 1967, pp. 1098-1099.

[5] Bastress, E. K., "Interior Ballistics of Spinning Solid-Propellant Rockets," *Journal of Spacecraft and Rockets*, Vol. 2, No. 3, 1965, pp. 455-457.

[6] Manda, L. J., "Spin Effects on Rocket Nozzle Performance," *Journal of Spacecraft and Rockets*, Vol. 3, No. 11, 1966, pp. 1695-1696.

[7] King, M. K., Comment on "Spin Effects on Rocket Nozzle Performance," *Journal of Spacecraft and Rockets*, Vol. 3, No. 12, 1966, pp. 1812-1813.

[8] Manda, L. J., Reply by author to M. K. King, *Journal of Spacecraft and Rockets*, Vol. 3, No. 12, 1966, p. 1813.

[9] Hsu, C., "Mass Blocking of Swirling Flow in Nozzles," *Journal of Spacecraft and Rockets*, Vol. 8, No. 12, 1971, pp. 1232-1234.

[10] Carpenter, P. W. and Johannesen, N. H., "An Extension of One-Dimensional Theory to Inviscid Swirling Flow through Choked Nozzles," *Aeronautical Quarterly*, Vol. 26, May 1975, pp. 71-87.

[11] Lewellen, W. S., Burns, W. J., and Strickland, H. J., "Transonic Swirling Flow," *AIAA Journal*, Vol. 7, No. 7, July, 1969, pp. 1290-1297.

[12] Roschke, E. J. and Pivirotto, T. J., "Similarity in Confined Vortex Flows," Technical Report 32-789, 1965, Jet Propulsion Laboratory.

[13] Toomre, J., "Highly Swirling Flows Through a Convergent-Divergent Nozzle," MSc thesis, Massachusetts Institute of Technology, Cambridge, MA, June 1963.

[14] Pinchak, A. C. and Poplawski, R., "On the Attainment of Extremely High Rotational Velocities in a Confined Vortex Flow," *2nd AIAA Annual Meeting*, San Francisco, CA, July 26-29, 1965, AIAA-65-400.

[15] Adamson, T. C., Jr. and Nicholls, J. A., "On the Structure of Jets from Highly Underexpanded Nozzles into Still Air," *Journal of the Aero/Space Sciences*, Vol. 26, No. 1, January, 1959, pp. 16-24.

[16] Lewis, C. H., Jr. and Carlson, D. J., "Normal Shock Location in Underexpanded Gas and Gas-Particle Jets," Technical Note, *AIAA Journal*, Vol. 2, No. 4, April, 1964, pp. 776-777.

[17] Crist, S., Sherman, P. M., and Glass, D. R., "Study of the Highly Underexpanded Sonic Jet," *AIAA Journal*, Vol. 4, No. 1, 1966, pp. 68-71.

[18] Gostintsev, Y. A., Zelentsov, V. V., Ilyukhin, V. S., and Pokhil, P. F., "Structure of Underexpanded Supersonic Swirling Gas Jet," *Journal of Fluid Dynamics*, Vol. 4, No. 5, September, 1969, pp. 158-162.

[19] Batson, J. L. and Sforzini, R. H., "Swirling Flow through a Nozzle," *Journal of Spacecraft and Rockets*, Vol. 7, No. 2, 1970, pp. 159-163.

[20] Kornblum, B. T., Thompson, H. D., and Hoffman, J. D., "An Analytical Investigation of Swirl in Annular Propulsive Nozzles," *Journal of Propulsion and Power*, Vol. 2, No. 2, 1986, pp. 155-160.

[21] Hoffman, J. D., Thompson, H. D., and Marcum, D. L., "Analytical Study of Swirler Effects in Annular Propulsive Nozzles," *Journal of Propulsion and Power*, Vol. 3, No. 5, 1987, pp. 465-466.

[22] Naumova, I. N. and Shmyglevskii, Y. D., "Nozzle Thrust Increase by Flow Rotation," *Journal of Fluid Dynamics*, Vol. 2, No. 1, 1967, pp. 23-25.

[23] Dutton, J. C., "Swirling Supersonic Nozzle Flow," *Journal of Propulsion and Power*, Vol. 3, No. 4, 1987, pp. 342-349.

[24] Settles, G. S., "Supersonic Mixing Enhancement by Vorticity for High-Speed Propulsion," Report submitted to NASA-Langley Research Center, October 1991, NASA-CR-188920.

[25] Lee, K. H., Setoguchi, T., Matsuo, S., and Kim, H. D., "An Experimental Study of Underexpanded Sonic, Coaxial, Swirl Jets," *Proceedings of the Institution of Mechanical Engineers, Part C: Journal of Mechanical Engineering Science*, Vol. 218, No. 1, 2004, pp. 93-103.

[26] Lee, K. H., Setoguchi, T., Matsuo, S., and Kim, H. D., "Influence of the Nozzle Inlet Configuration on Underexpanded Swirling Jet," *Proceedings of the Institution of Mechanical Engineers, Part C: Journal of Mechanical Engineering Science*, Vol. 220, No. 2, 2006, pp. 155-163.

[27] Murakami, E. and Papamoschou, D., "Experiments on Mixing Enhancement in Dual-Stream Jets," *39th AIAA Aerospace Sciences Meeting & Exhibit*, Reno, NV, Jan. 8-11, 2001, AIAA-2001-0668.

[28] Knowles, K., "Combined Noise and Flow Control of Supersonic Jets Using Swirl," *14th DGLR/AIAA Aeroacoustics Conference*, Aachen, Germany, May 11-14, 1992.

[29] Carpenter, P. W., "A Linearized Theory for Swirling Supersonic Jets and its Application to Shock-Cell Noise," *AIAA Journal*, Vol. 23, No. 12, 1985, pp. 1902-1909.

[30] Yu, Y. K., Chen, R. H., and Chew, L., "Screech Tone Noise and Mode Switching in Supersonic Swirling Jets," *AIAA Journal*, Vol. 36, No. 11, 1998, pp. 1968-1974.

[31] Yu, Y. K., "An Experimental Study of Underexpanded Supersonic Swirling Jets," PhD thesis, University of Central Florida, December 1997.

[32] Gupta, A. K., Lilley, D. G., and Syred, N., "Swirl Flows," Abacus Press, UK, 1984, ISBN 0-85626-175-0.

[33] Cutler, A. D., Levey, B. S., and Kraus, D. K., "Near-Field Flow of Supersonic Swirling Jets," *AIAA Journal*, Vol. 33, No. 5, 1995, pp. 876–881.

[34] Linck, M., "Spray Flame and Exhaust Jet Characteristics of a Pressurized Swirl Combustor," PhD thesis, University of Maryland, College Park, MD, May 2006.

[35] Baldwin, B. S. and Lomax, H., "Thin Layer Approximation and Algebraic Model for Separated Turbulent Flows," *16th AIAA Aerospace Sciences Meeting*, Huntsville, Alabama, Jan. 16-18, 1978, AIAA-78-257.

[36] Claypole, T. C. and Syred, N., "The Effects of Swirl Burner Aerodynamics on NOx Formation," *Proceedings of 18th Symposium (International) on Combustion*, Combustion Institute, Pittsburgh, PA, 1981, pp. 81-89.

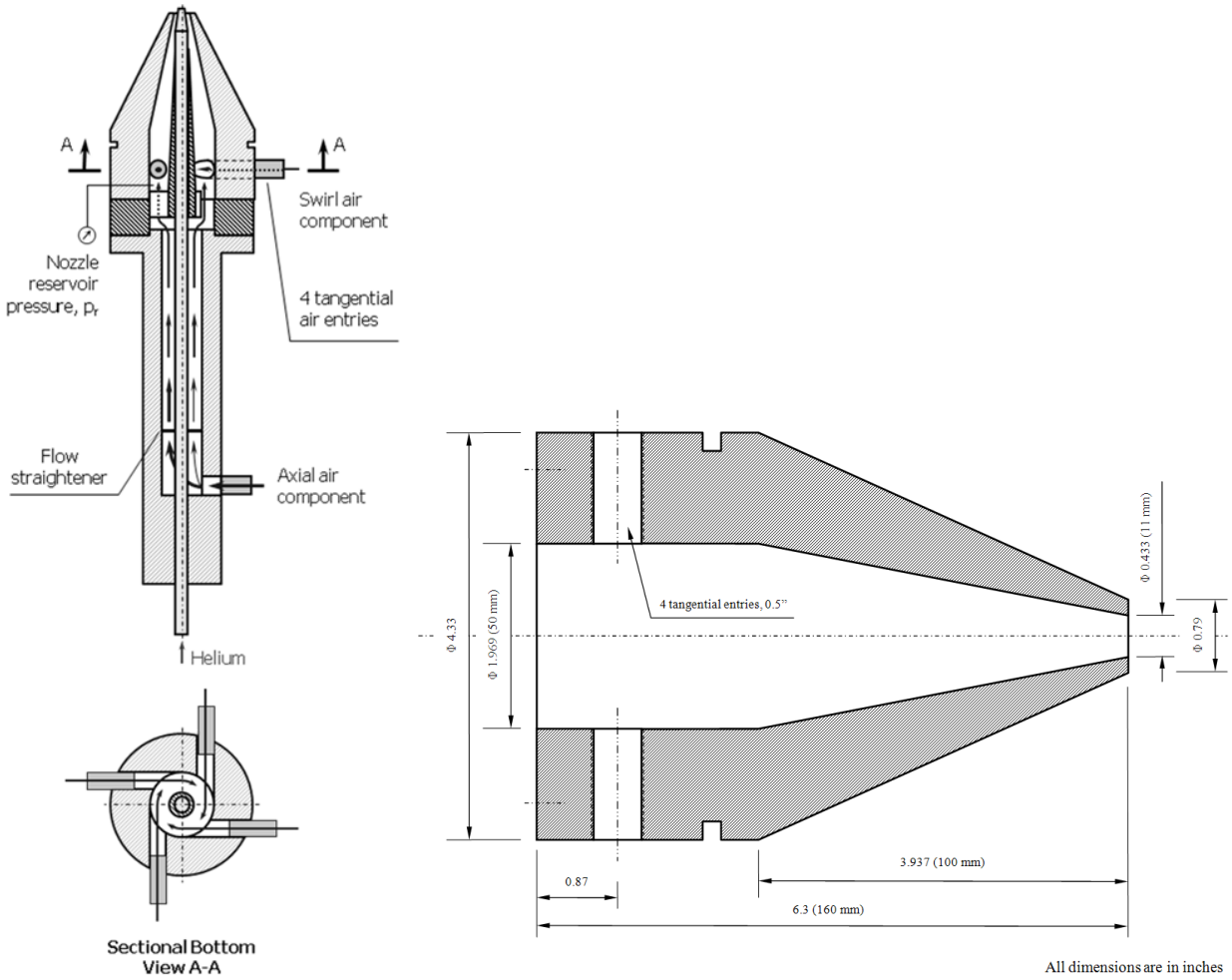

Figure 1. Schematic of UMD supersonic-nozzle assembly

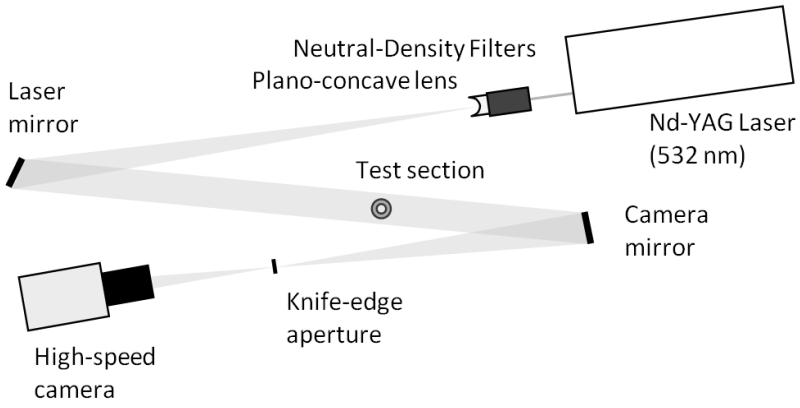

Figure 2. Schematic of nanosecond Schlieren system

Table 1. Test Matrix

Case	Reservoir pressure [bar]	Total temperature at air inlet [K]	$\dot{m}$ [kg/s]	S_g
1	7.91	300	0.175	0
2	8.82	300	0.175	0.68
3	7.91	300	0.150	0.68

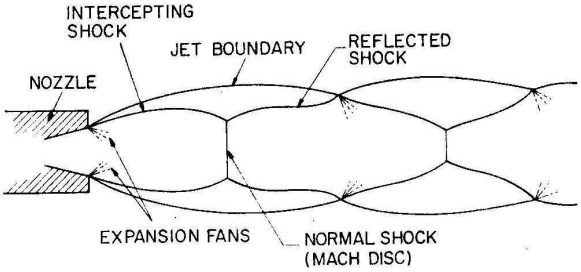

Figure 3. Schematic of shock structure of highly underexpanded nozzle flow [Ref. 15]

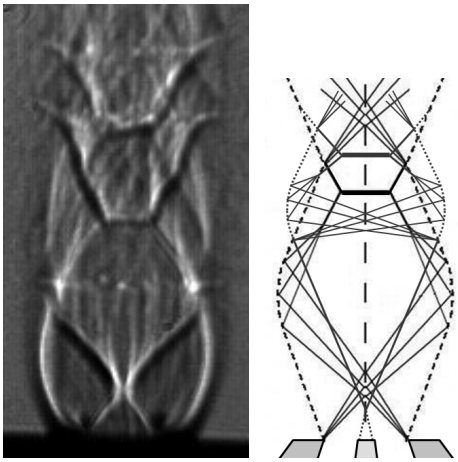

Figure 4. Shock structure of non-swirling (case 1) underexpanded nozzle airflow in presence of non-recessed coaxial injection system with no fuel injection

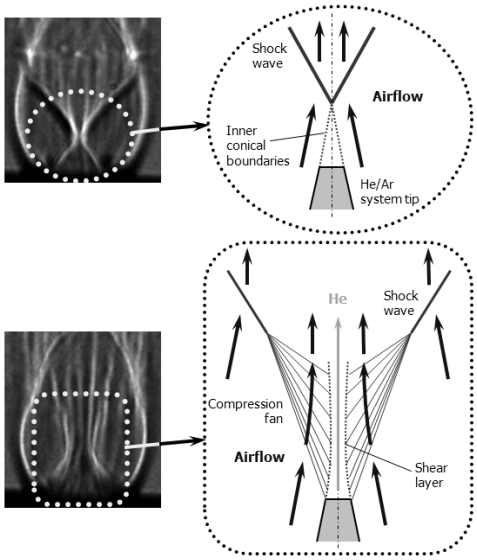

Figure 5. Effect of fuel injection on shock structure of underexpanded nozzle flow

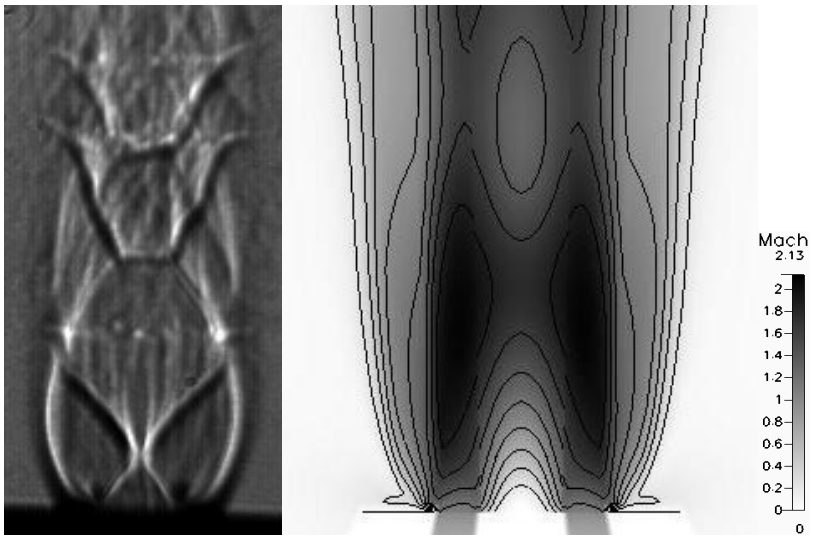

Figure 6. Comparison of experimental (Schlieren, left) and numerical (Mach number profile, right) visualizations of shock structure. Air only, no swirl (case 1)

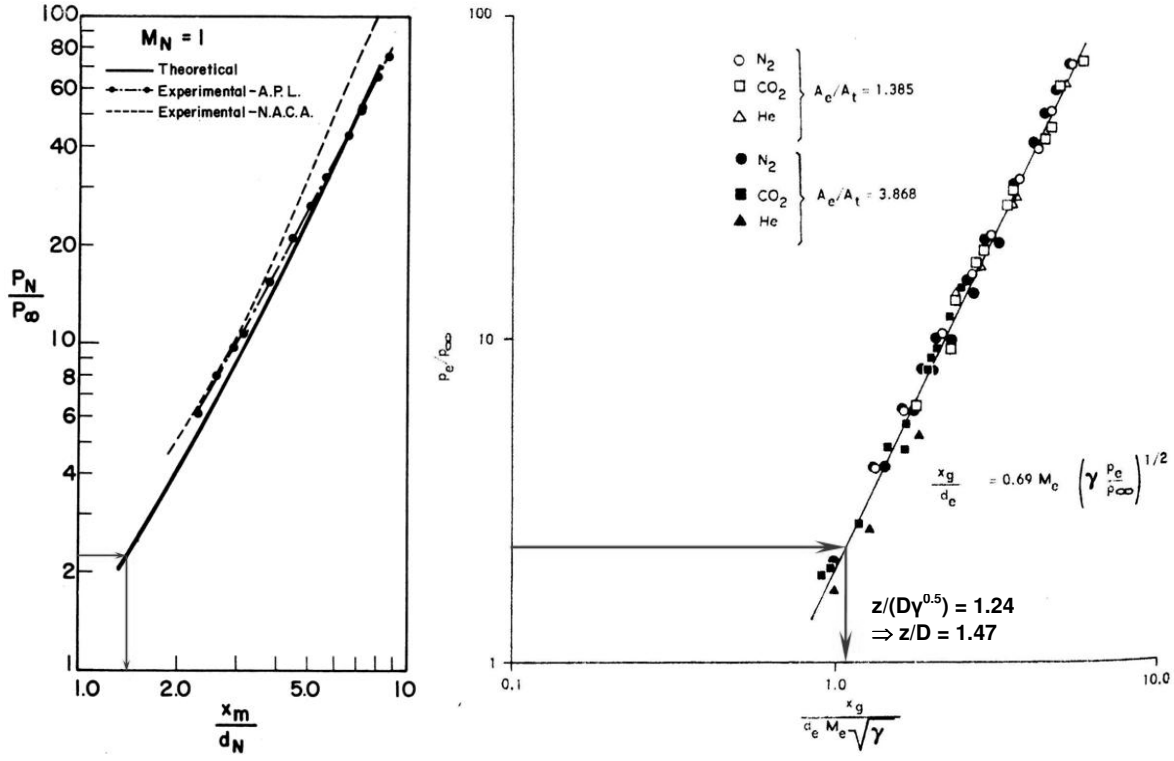

Figure 7. Axial location of first Mach disk (relative to nozzle exit plane) in non-swirling underexpanded nozzle flow. Left: Adamson and Nicholls [15]; Right: Lewis and Carlson [16]. Arrows represent findings of present study

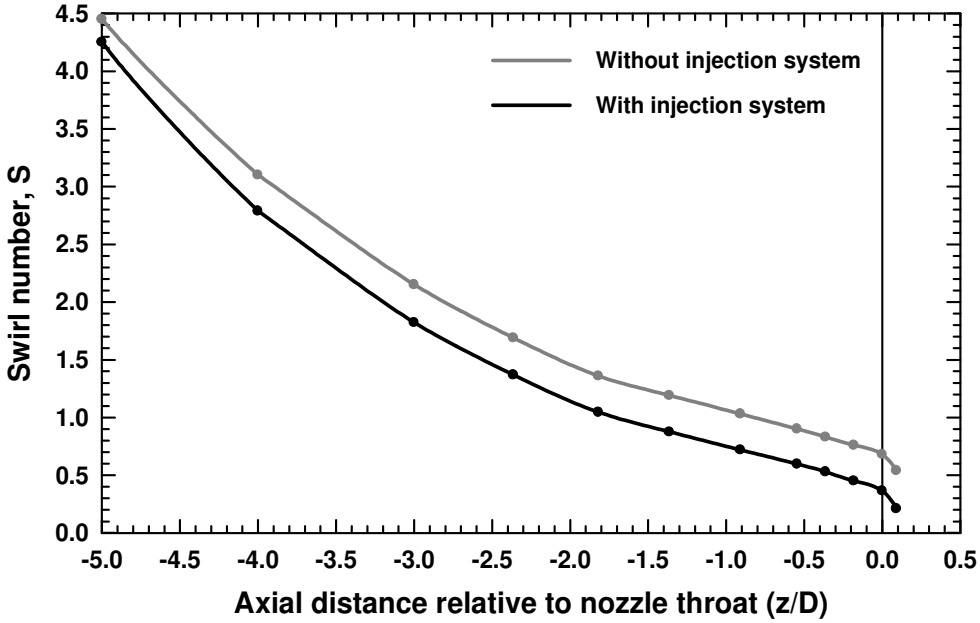

Figure 8. Axial variation of subsonic swirl number inside nozzle in the absence and presence (case 2) of coaxial injection system. Nozzle throat at z/D = 0

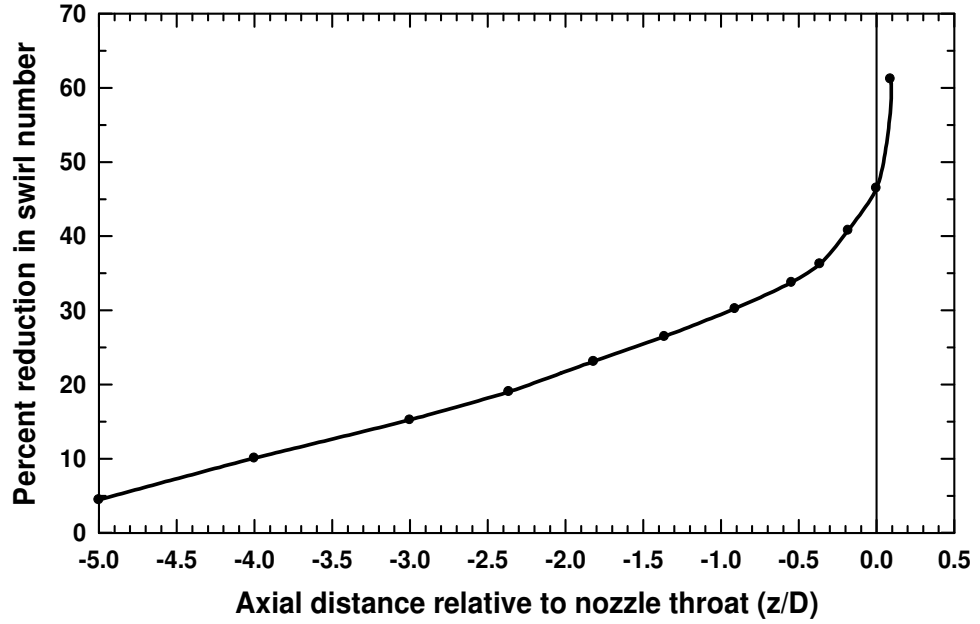

Figure 9. Axial variation of relative reduction in subsonic swirl number inside nozzle due to the presence of coaxial injection system (case 2). Nozzle throat at z/D = 0

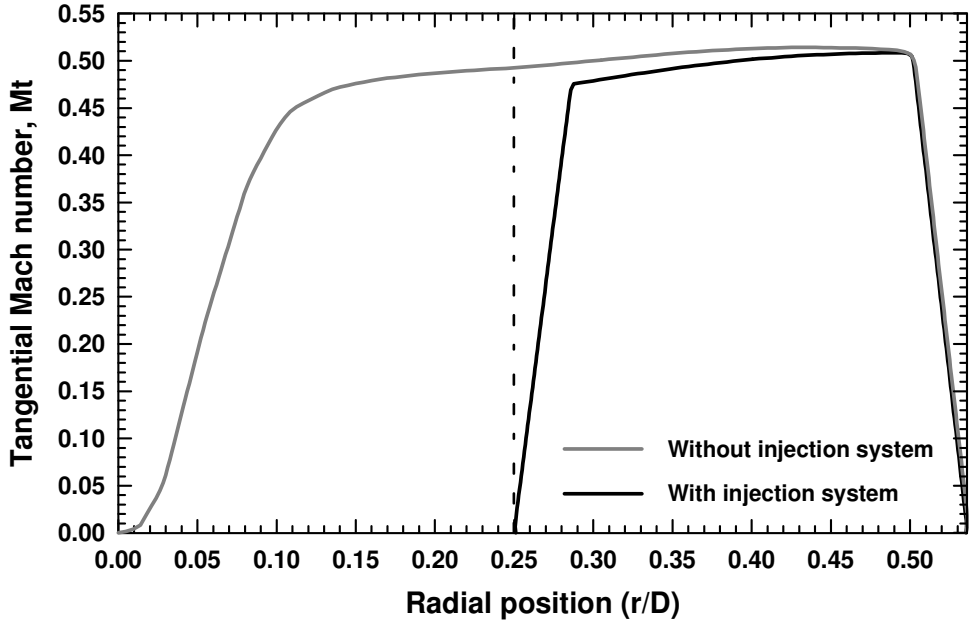

Figure 10. Radial variation of tangential Mach number at z/D = –0.1 in the absence and presence (case 2) of injection system. Dotted line at r/D = 0.25 represents radius of coaxial injection system at tip

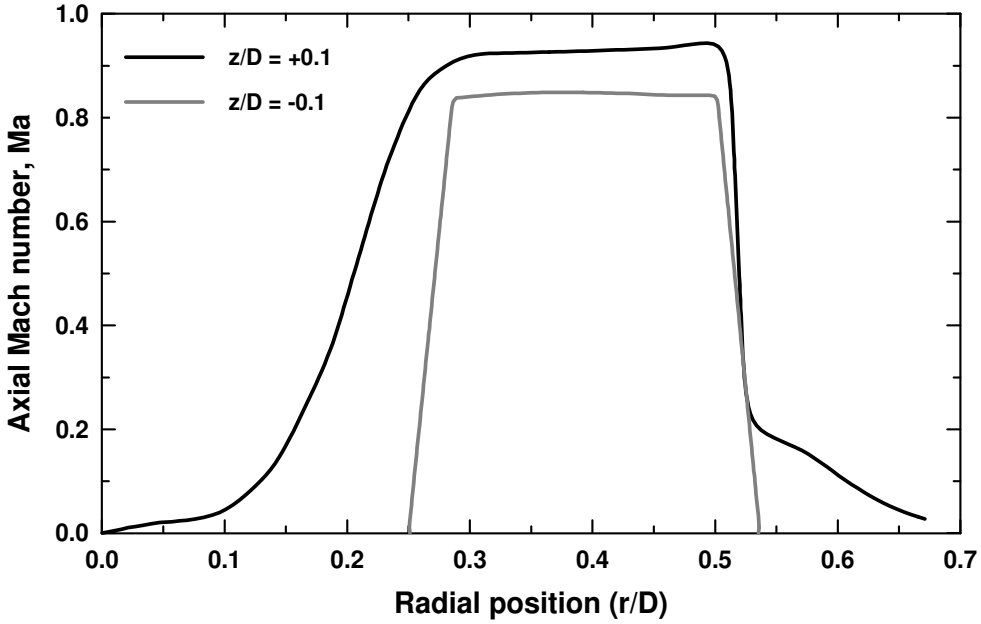

Figure 11a. Radial variation of trans-throat axial Mach-number component in case 2

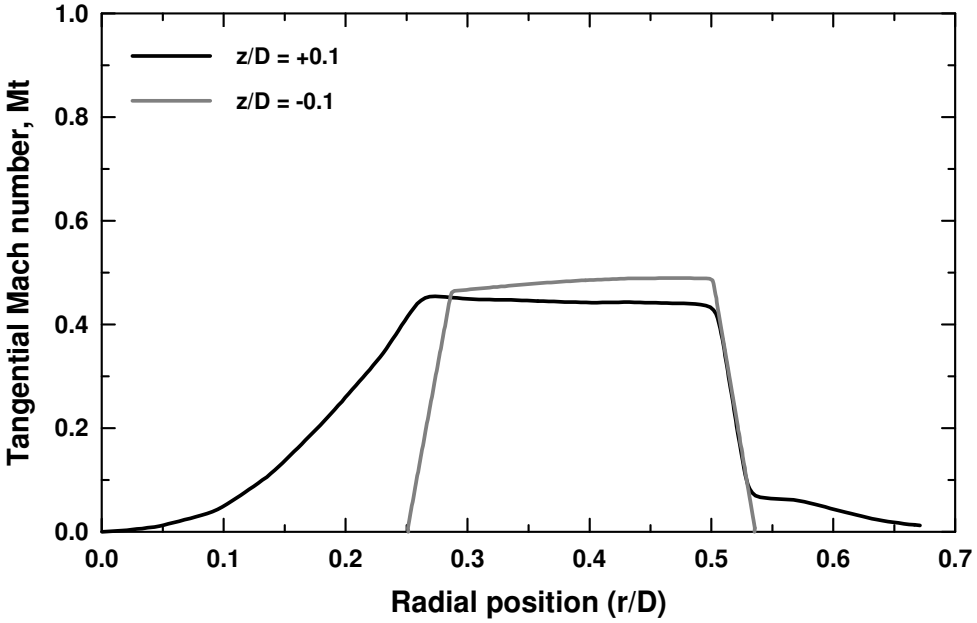

Figure 11b. Radial variation of trans-throat tangential Mach-number component in case 2

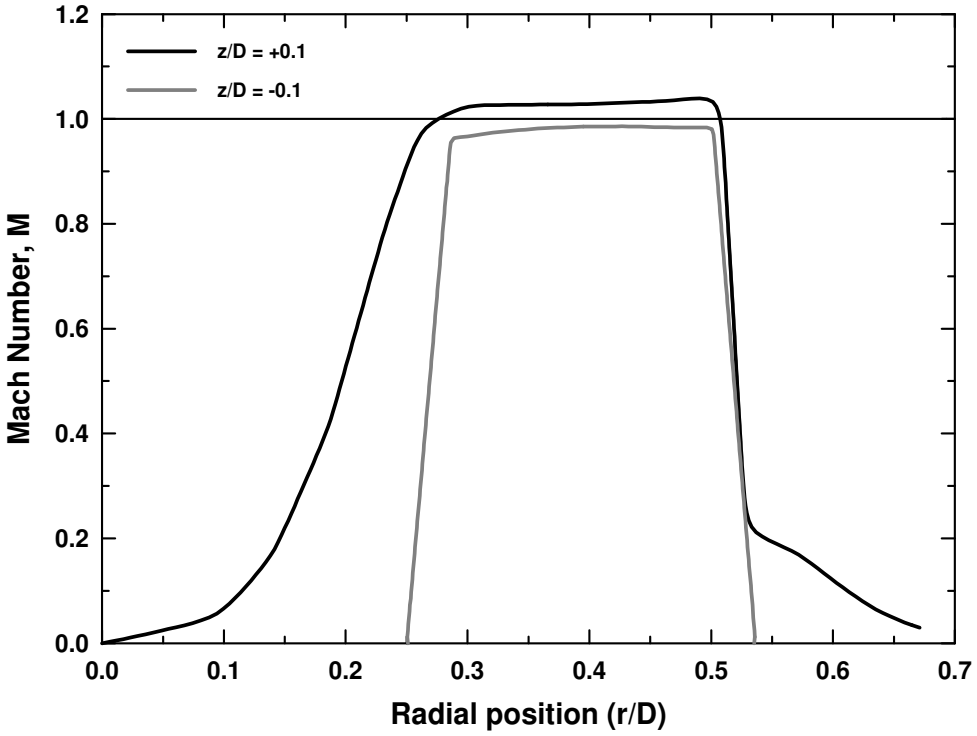

Figure 11c. Radial variation of trans-throat Mach number in case 2

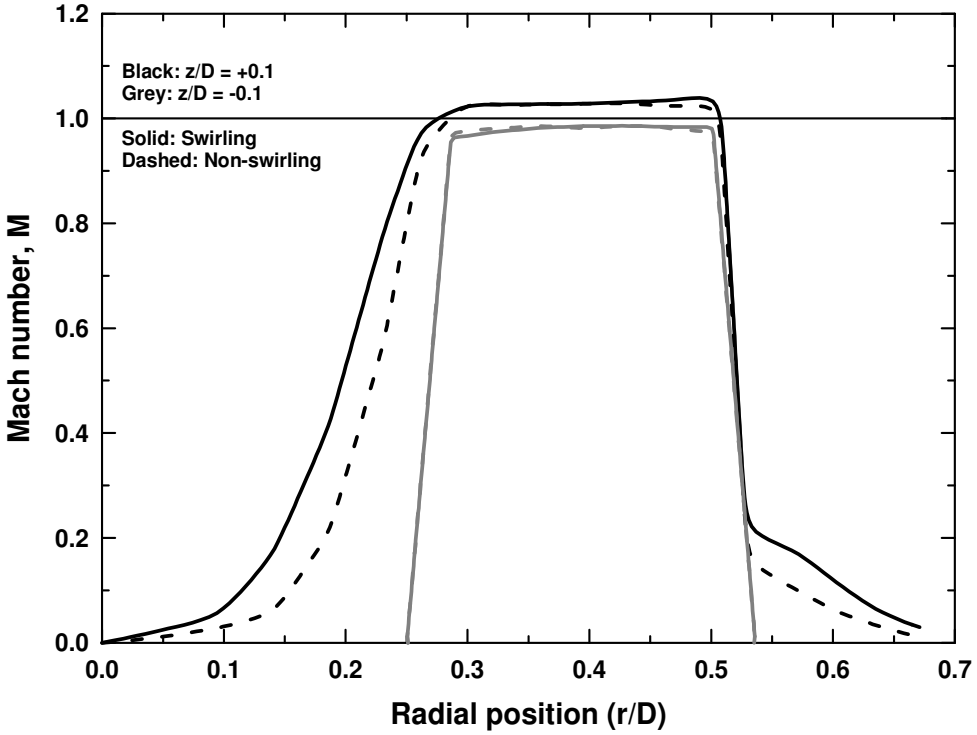

Figure 11d. Radial variation of trans-throat Mach number in cases 1 (non-swirling, dashed) and 2 (swirling, solid)

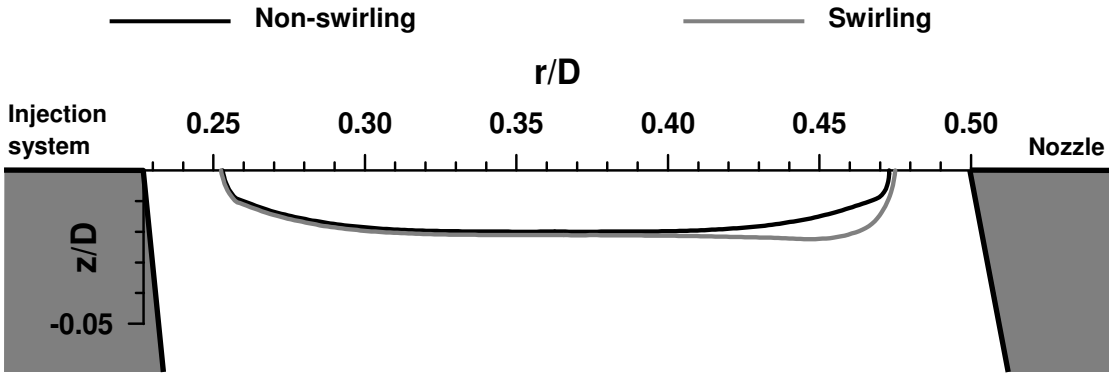

Figure 12. Sonic lines in cases 1 (non-swirling) and 2 (swirling)

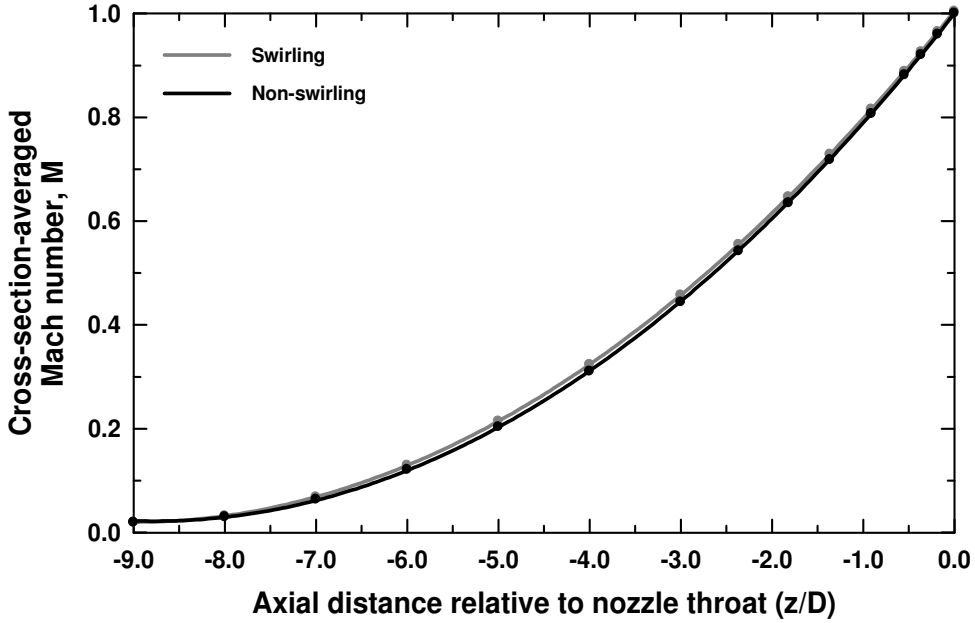

Figure 13. Axial variations of cross-section-averaged subsonic Mach number in cases 1 (non-swirling) and 2 (swirling)

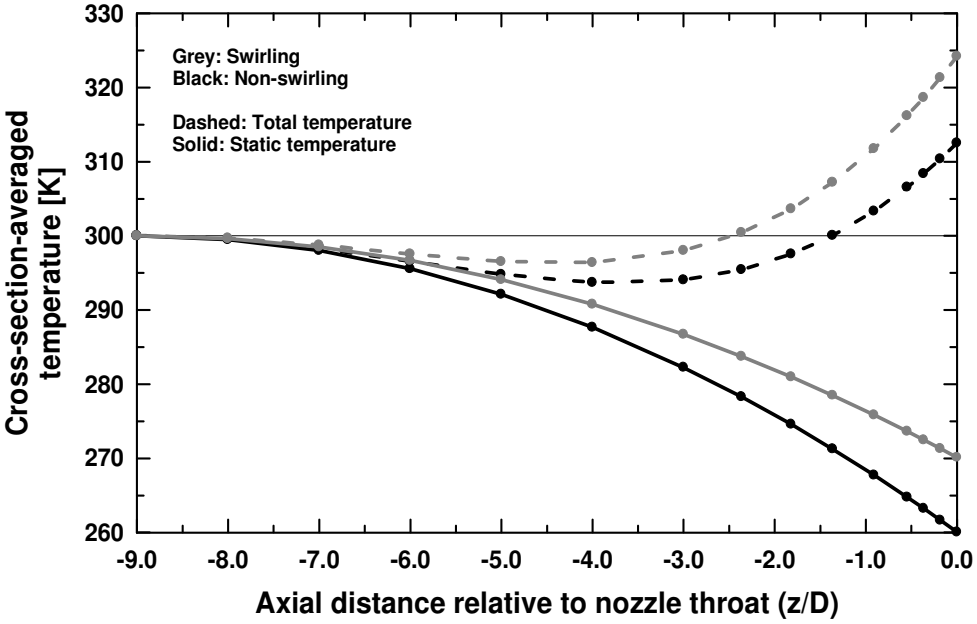

Figure 14. Axial variations of cross-section-averaged total and static temperatures inside nozzle in cases 1 (non-swirling, black) and 2 (swirling, grey)

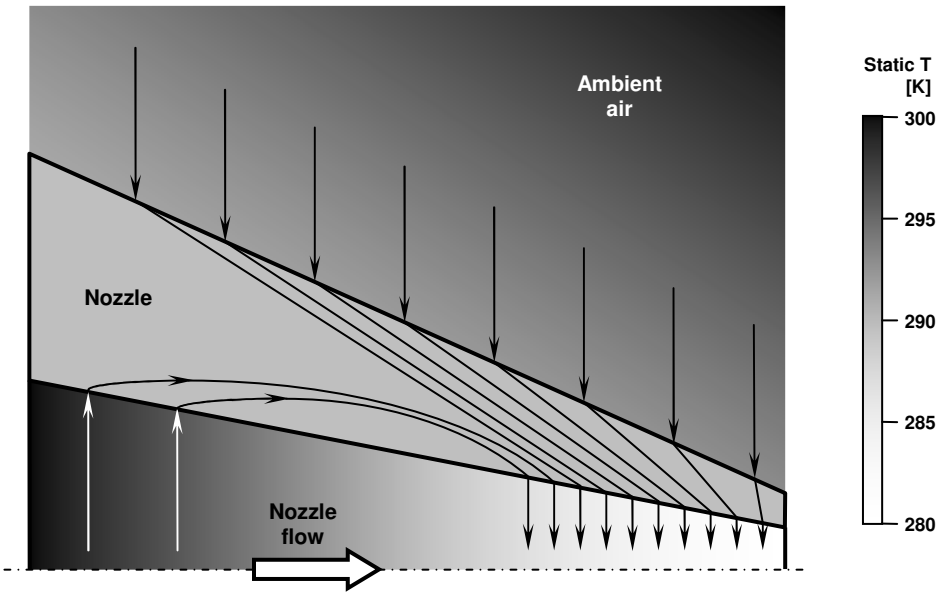

Figure 15. Schematic representation of heat flow and static-temperature distribution

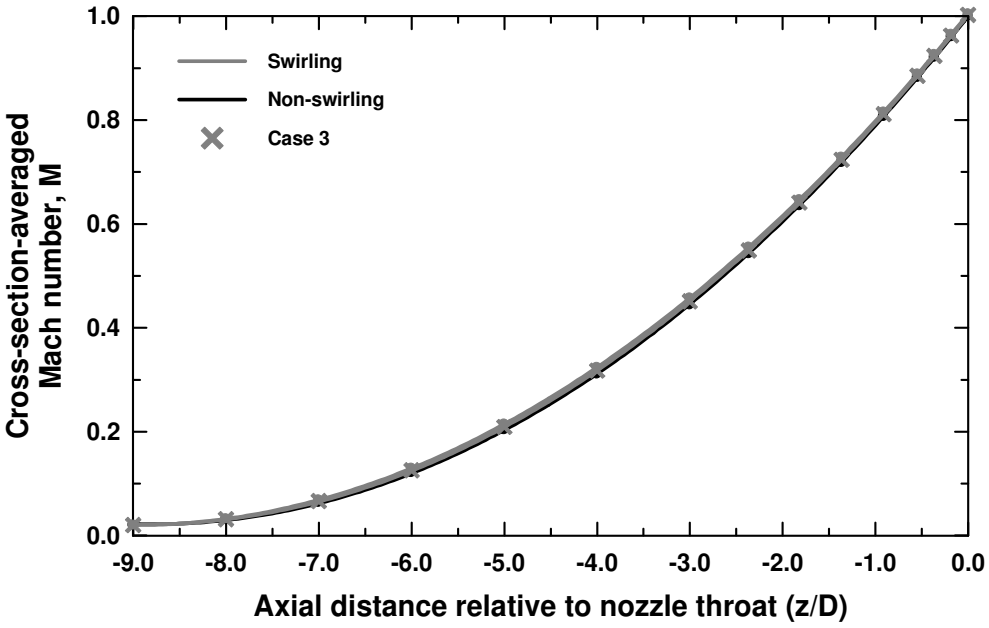

Figure 16. Axial variations of cross-section-averaged Mach number inside nozzle in cases 1 (non-swirling, reservoir pressure = 7.91 bar), 2 (swirling, reservoir pressure = 8.82 bar), and 3 (swirling, reservoir pressure = 7.91 bar)

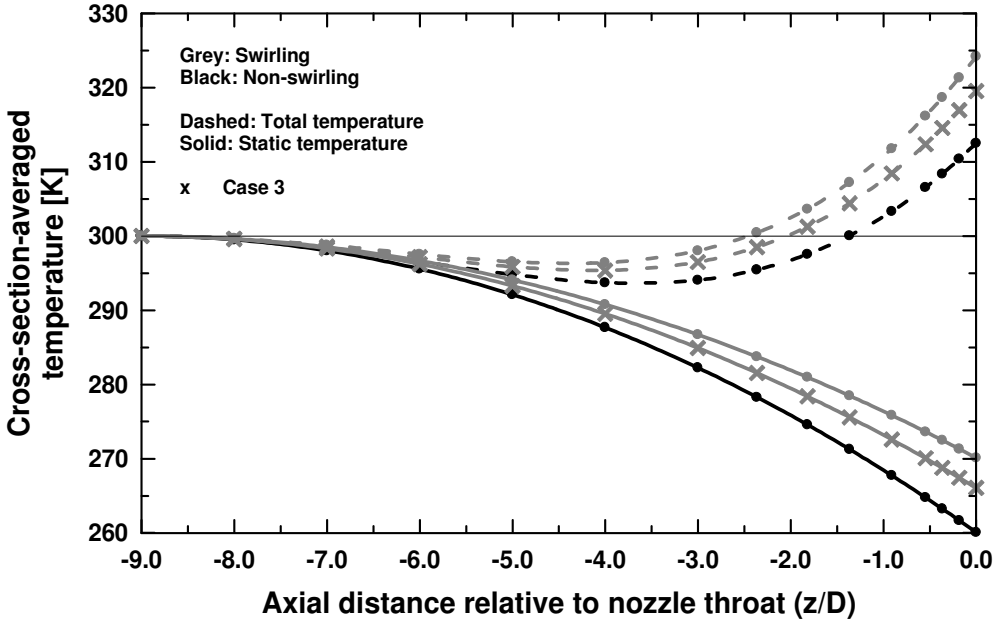

Figure 17. Axial variations of cross-section-averaged total and static temperatures inside nozzle in cases 1 (non-swirling, reservoir pressure = 7.91 bar), 2 (swirling, reservoir pressure = 8.82 bar), and 3 (swirling, reservoir pressure = 7.91 bar)

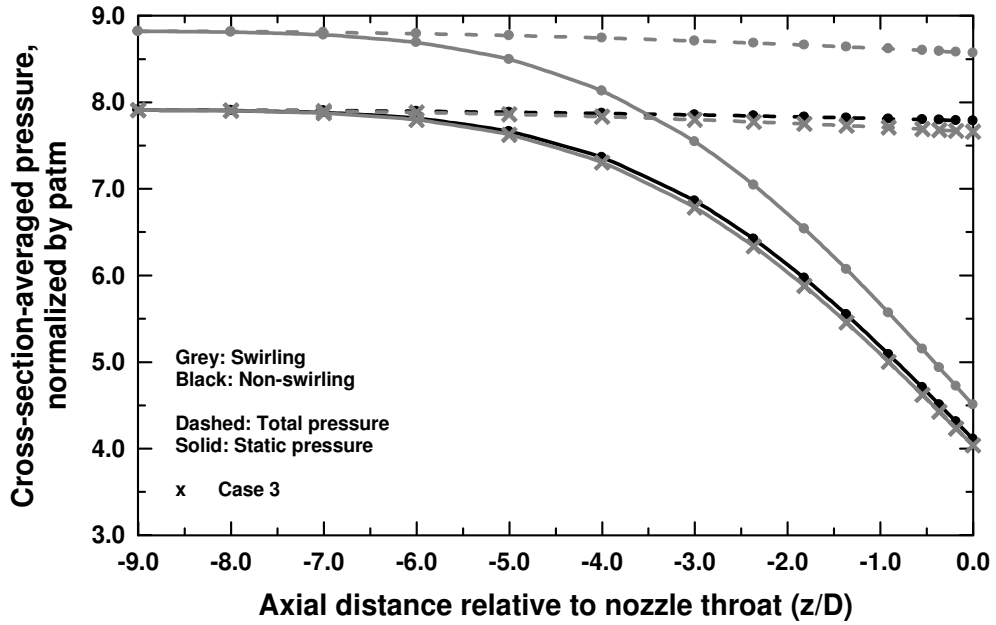

Figure 18. Axial variations of cross-section-averaged total and static pressures inside nozzle in cases 1 (non-swirling, reservoir pressure = 7.91 bar), 2 (swirling, reservoir pressure = 8.82 bar), and 3 (swirling, reservoir pressure = 7.91 bar)

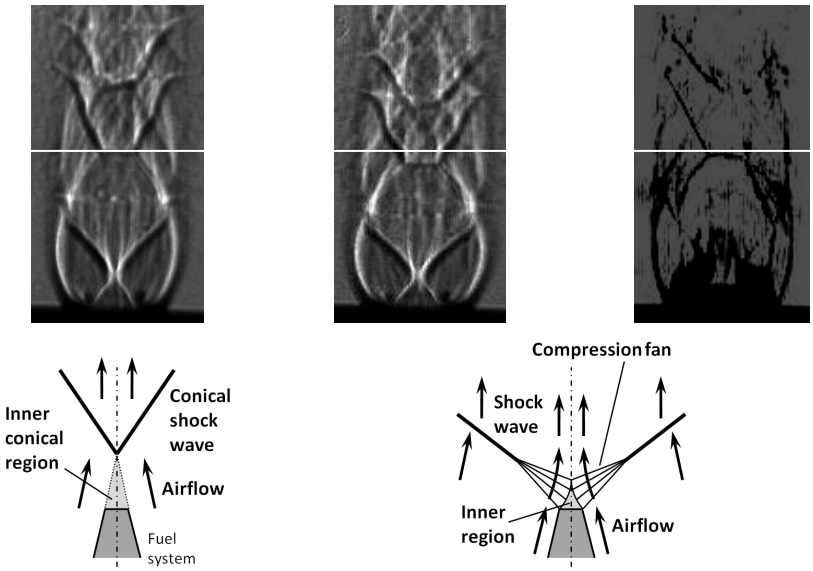

Figure 19. Images of non-swirling underexpanded nozzle airflow with no fuel injection
Left: case 1 (non-swirling, reservoir pressure = 7.91 bar);
Middle: 3 (swirling, reservoir pressure = 7.91 bar);
Right: 2 (swirling, reservoir pressure = 8.82 bar)

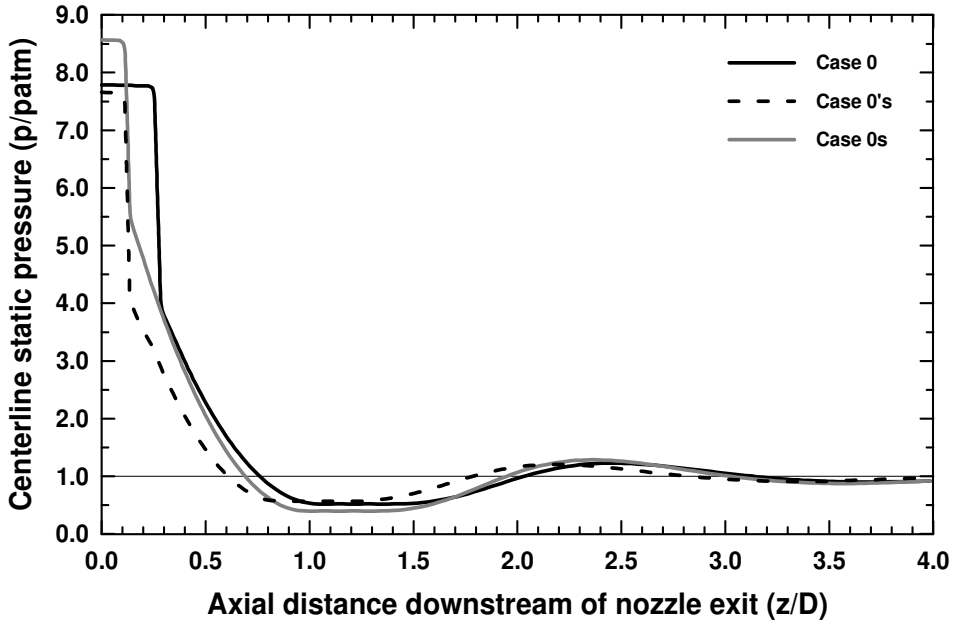

Figure 20. Axial variation of centerline static pressure within first two shock cells in cases 1 (non-swirling) and 2 (swirling)

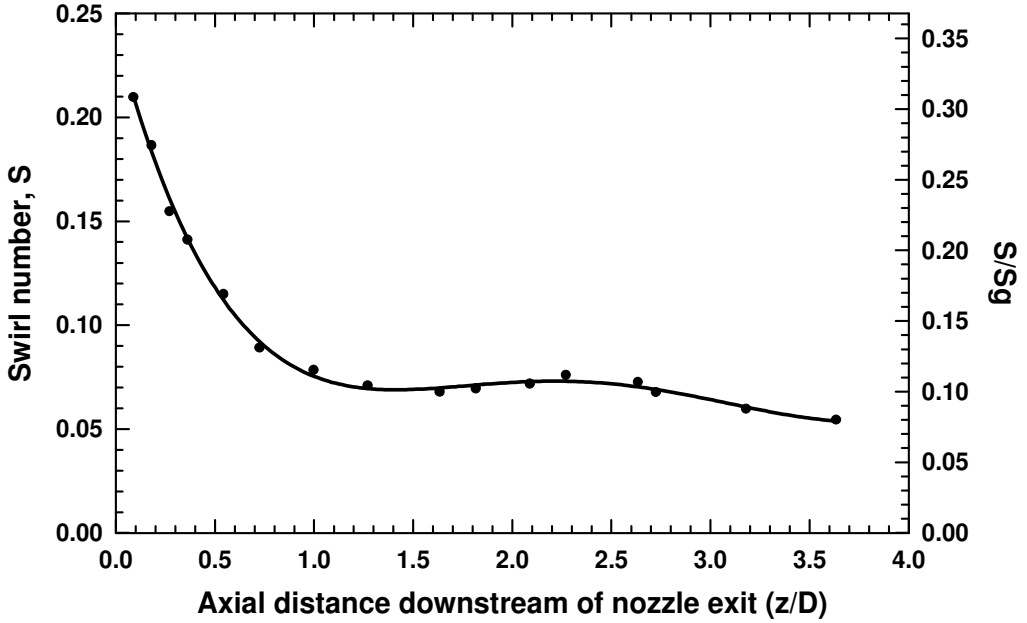

Figure 21. Axial variation of supersonic swirl number within first two shock cells in case 2

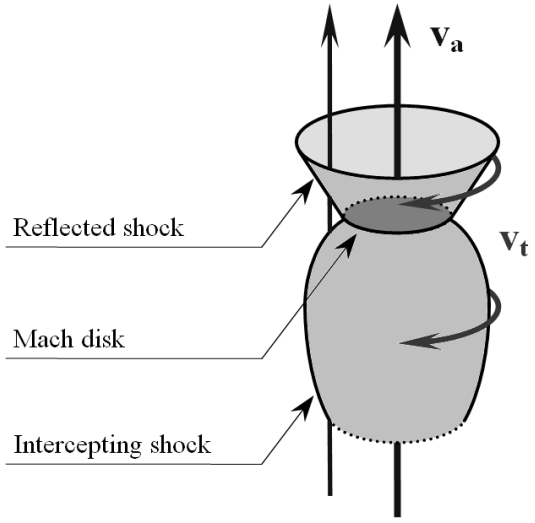

Figure 22. 3-D schematic of shock structure showing orientation of axial and tangential velocity components with respect to Mach disk and intercepting and reflected shocks

Swirling Underexpanded Supersonic Airflow, Part II: Mixing

A. Abdelhafez[1] and A. K. Gupta[2]
University of Maryland, College Park, MD 20742

This work complements the efforts of a previous study by the authors, where the effect of imparting swirl to underexpanded supersonic nozzle airflow on nozzle choking criteria, thrust, and specific impulse were examined. The effects of swirl on supersonic flowfield and mixing are examined here at matched nozzle reservoir pressure as well as matched mass flow. A convergent nozzle is used to generate the underexpanded airflow. Fuel is injected coaxially at the nozzle throat. Non-reacting conditions are considered, wherein fuel is simulated by mixtures of helium, argon, and krypton inert gases. It was found that the effects of swirl and nozzle reservoir pressure interfere destructively from the point of view of shock-structure axial compactness. Increasing reservoir pressure stretches the shock structure axially, whereas swirl shrinks it. On the other hand, constructive interference was observed from the point of view of radial jet expansion; both result in greater jet diameter. The application of swirl was found to weaken the shock structure at matched reservoir pressure but strengthen it at matched mass flow. Swirl was also found to enhance supersonic mixing significantly, which agrees with the findings of all previous studies. It was also found that fuel injected at low subsonic Mach numbers has to propagate initially with a negative shear angle, i.e., the cross-sectional area of fuel-rich core flow converges first, before this core flow reaches a throat after which it propagates supersonically. This behavior was found to be advantageous, as it results in better mixing and reduced shock-structure strength.

Nomenclature

a = speed of sound

D = nozzle-exit diameter (11 mm)

[1] Graduate Student, Dept. of Mechanical Engineering, 2181 Glenn Martin Hall, AIAA Student Member.
[2] Distinguished University Professor, Dept. of Mechanical Engineering, 2181 Glenn Martin Hall, AIAA Fellow.

DR = air-fuel density ratio at injection plane

M_c = convective Mach number

M_{rel} = air-fuel relative Mach number at injection plane

$\dot{m}$ = mass flow rate

p = pressure

S = swirl number

t = time

v = velocity

z = axial coordinate

γ = ratio of specific heats

ρ = density

$\vec{\omega}_{bc}$ = Baroclinic vorticity vector

Subscripts

a = axial

t = tangential

I. Introduction

Swirling flow in nozzles occurs in a number of important propulsion applications, including turbofans and turbojet engines, spin-stabilized rockets, and integral rocket/ramjets. In the first two cases, the tangential velocity component is induced by the motion of turbine blades and by the rocket spin, respectively. For ramjets, recent experimental studies [1] have demonstrated that swirl generated by fixed vanes located in the dump combustor inlet can lead to significantly improved combustor performance. Clearly, the generated swirl in each of those propulsion systems will persist at some level to the inlet of exhaust nozzle. Therefore, it is important to examine the effect of tangential velocity component on nozzle flowfield, so that design parameters such as thrust and mass flow rate can be accurately determined.

The structure of highly underexpanded nozzle jets was investigated experimentally and analytically by Adamson and Nicholls [2], who presented a method for calculating the position of the first Mach disk. In their calculation, the axial pressure distribution on flow centerline downstream of nozzle exit (calculated by method of characteristics) was used to define a fictitious nozzle extension. The Mach disk was then assumed to exist at the point where

atmospheric pressure would be attained upstream of the disk, i.e., the latter was assumed to exist at the end of fictitious nozzle extension. Physical arguments were employed to extend the analysis to nozzles with supersonic exit Mach numbers. An approximate method for computing the jet boundary, up to the point of maximum jet area, was also given. The analytical results compared favorably with experimental data at relatively low nozzle pressure ratios.

Lewis and Carlson [3] experimentally determined the distance from nozzle exit plane to the first Mach disc in gas-only and gas-particle jets issuing from underexpanded supersonic nozzles. An empirical correlation of the data was presented which is valid for both jet types and incorporates the effect of gas specific-heat ratio. In a relevant experimental investigation Crist et al. [4] studied the structure of underexpanded jets with stagnation pressures up to 15,000 psia, ambient pressures down to 100 μHg, and stagnation temperatures up to 4200 K. The location of first Mach disk was found to be insensitive to the ratio of specific heats, nozzle-lip geometry, and absolute pressure. For over-all pressure ratios up to about 300,000 the location of Mach disk was found to vary as the square root of overall pressure ratio. The diameters of Mach disk, jet boundary, and intercepting shock were found to increase with decrease in specific-heat ratio and to decrease at high stagnation density, where intermolecular forces become important. At high-pressure ratios, the ratio of Mach-disk diameter to Mach-disk position appeared to be constant for a given gas. It was also found that the properties along jet axis can be approximated by the properties of a flow through a hypothetical conical nozzle whose half-angle is given as a function of specific heat ratio. A simplified expression for the distribution of Mach number along the jet axis was given to good approximation as a function of specific-heat ratio.

Gostintsev et al. [5] studied an underexpanded supersonic swirling gas jet issuing from a convergent nozzle. They showed that the effect of rotation on the wave structure of axisymmetric jet is qualitatively analogous to the effect of reduction in overpressure ratio. Using formulas for spiral isentropic flow, an approximate expression was obtained for estimating the location of first Mach disc in the swirling flow downstream of nozzle exit. Batson and Sforzini [6] also studied the structure of swirling flow through a convergent nozzle with emphasis on the effect of swirl on flowfield, thrust, and mass flow produced by nozzled devices, such as jet engines and spin-stabilized rockets. It was reported that the axial velocity component increases, whereas the tangential one decreases, as the flow passes through nozzle throat.

Vortex enhancement of supersonic mixing was studied experimentally by Settles [7]. Swirl was utilized to enhance shear layer growth and mixing. It was concluded that swirl enhances compressible mixing; the degree of

enhancement increases with increasing swirl. Settles also reported that the effects of convective Mach number and density ratio on the enhancement effect of swirl are still unknown and were thus recommended for future work.

In an experimental investigation, which is very pertinent to this current study, Lee et al. [8] examined the near-field flow structure of underexpanded coaxial swirl jets. Swirl streams were issued from a secondary annular nozzle, while a primary inner nozzle provided the underexpanded free jets. The interactions between the annular swirl and the underexpanded core jets were examined, in order to quantify the effects of the former on the latter. It was shown that the presence of an annular swirl stream causes the core-flow Mach disc to move further downstream, with an increased diameter. In another pertinent study Lee et al. [9] investigated the effect of nozzle-inlet configuration on underexpanded swirling jets, which were generated by a convergent nozzle with four tangential inlets at the supply chamber. The nozzle-inlet configuration was modified by using different plugs, holes, and needles, which were also utilized for measuring the flow properties at nozzle inlet. The experimental results showed that the presence of a coaxial needle inside the nozzle supply chamber controls the properties of generated underexpanded swirling jets. The structures of these jet flows are highly dependent on the detailed configuration of nozzle supply chamber.

Murakami and Papamoschou [10] examined flow structure and mixing enhancement in 2D and axisymmetric supersonic jets surrounded by secondary annular subsonic coaxial ones. The supersonic jets were issued from a convergent-divergent nozzle operated at off-design conditions. It was shown that the mixing enhancement using secondary parallel injection (referred to as MESPI by the researchers) halves the length of potential core in both round and 2D jets. A short distance past the potential core, mixing enhancement caused a reduction in centerline Mach number by 30% in round jets and 20% in 2D ones. The corresponding reduction in peak molar concentration of a scalar injected in the primary flow was 65% in round jets and around 40% in 2D ones.

Carpenter [11] developed a linearized theory for underexpanded inviscid supersonic jets with arbitrary initial swirl. Estimates were made of the effect of swirl on the total radiated sound power of shock-associated noise. It was found that this noise can be greatly reduced, or even eliminated, at sufficiently high swirl levels, which can be achieved at the expense of a very small thrust loss. Noise elimination was believed to be due to enhanced mixing that leads to the disappearance of some initial shock cells.

In another study more pertinent to mixing in free supersonic flows Yu et al. [12] experimentally examined mode-switching phenomena of supersonic jets with swirl. They observed that the shock-cell spacing of swirling jets is smaller than that of non-swirling ones, which suggests enhanced mixing. In non-swirling compressible jets, the

typical two-dimensional vortex roll-up is believed to be suppressed, and mixing and entrainment are reduced, as compared to incompressible jets. Therefore, to counter the adverse effects of compressibility on mixing, adding swirl to a supersonic jet is favorable. The enhanced entrainment and mixing in swirling supersonic jets is thought to be due to the inherent three-dimensionality associated with the axial component of turbulent vorticity in swirling jets. Yu [13] studied underexpanded supersonic jets to determine the effect of swirl on mixing efficiency. The screech tones, which result from the interaction of shock waves with unstable jet boundaries, were examined at different degrees of swirl for their effect on mixing. Implication of enhanced mixing was discussed. It was also reported that swirl did not eliminate shock cells, nor did it affect their quasi-periodic nature, in spite of the generation of a recirculation zone in strongly swirling jets.

Increased molecular mixing between fuel and oxidizer is essential for efficient combustion, which can be accomplished by increasing the turbulent mixing. It is now well known that large-scale coherent structures play an important role in incompressible turbulent mixing layers [14]. These structures engulf surrounding unmixed fluid and carry it into the mixing layer. Furthermore, it is possible that two adjacent vortical structures roll up upon one another, creating one larger structure, which leads to spreading of the mixing layer [15]. These two processes are believed to be fundamental for turbulent mixing in incompressible mixing layers.

Studies of compressible shear layers have shown that large-scale structures are similarity important in compressible turbulent mixing, changing its nature with convective Mach number [16 – 19]. It was found that the visual growth rate of a compressible shear layer with almost unity convective Mach number was only one-fourth the growth rate of an incompressible mixing layer having the same freestream velocity and density ratios, regardless of the values of these ratios [16]. Moreover, it is known that supersonic shear layers are highly stable [20], limiting the desired mixing of fuel and oxidizer. It was predicted that a supersonic shear layer will be completely stable, if the Mach number based on the relative speed exceeds 2.83, assuming an infinitely thin vortex sheet. This predicted stable nature of supersonic mixing layers has been later observed both in experiments [16, 21] and in numerical simulations [22].

The flow of supersonic swirling jets in a stagnant atmosphere was further investigated by Cutler et al. [23], Cutler and Levey [24], and Levey [25]. The swirling jets were created by tangential injection into a swirl chamber and accelerated through a convergent-divergent nozzle. The researchers observed higher peak helix angles than previous studies, as well as lower densities and pressures along the jet axis. They found that the growth rates of

mixing layer increased considerably with swirl. Moreover, when the swirling jets were operated overexpanded, unstable shock interactions produced vortex breakdown.

This work complements the efforts of a previous study by the authors, where the effect of imparting swirl to underexpanded supersonic nozzle airflow on nozzle choking criteria, thrust, and specific impulse were examined. The effects of swirl on supersonic flowfield and mixing are examined here experimentally and numerically at matched nozzle reservoir pressure as well as matched mass flow. Such effect has not been fully quantified in the literature yet, due to the inherent three-dimensionality of the problem.

II. Experimental Setup

The experimental investigation of this present work has been performed on the UMD supersonic facility. The utilized supersonic-nozzle assembly is shown schematically in Figure 1. A convergent nozzle of inlet-to-exit area ratio of 25 is used to generate an underexpanded supersonic airflow. Reservoir pressures of up to about 9 atm (abs) are available, yielding near-field Mach numbers of up to 2.2 under non-swirling conditions. The nozzle has swirling capabilities, wherein the axial-tangential-entry technique with four tangential inlets is utilized to accurately control the degree of swirl imparted to airflow. This technique has been proven in previous research to be an efficient method for generating supersonic swirling jets [26 – 28]. Thermal flow meters/controllers are used to meter the flow rates of axial and tangential air components with an accuracy of ±1.5% full-scale.

The nozzle was machined out of a single aluminum rod. Aluminum was preferred to stainless steel because the former has higher thermal conductivity, which prevents overheating of nozzle walls during combustion experiments. The higher conductivity allows radiated heat to be dissipated effectively through the thick nozzle walls. The dissipated heat is removed by forced convection of the entrained ambient cold air through the large surface area of nozzle external walls. The thickness of nozzle lip was optimized to allow for significant entrainment of ambient air while having adequate rigidity for machining the exit section to the desired surface finish and dimensional tolerance.

A coaxial fuel-injection system can be used to inject fuel along the axis of air nozzle. A support flange upstream of nozzle ensures and maintains concentricity of the fuel injection system with respect to air nozzle, especially under swirling conditions. This flange comprises a conical sleeve that embraces the injection system. The sleeve wall-thickness decreases in the direction of flow to provide streamlined performance and prevent any blockage close to the nozzle exit. The sleeve is held in place by three spokes extending to the support flange. Their thickness has been

optimized to provide rigidity with minimum blockage to incoming axial component of airflow. It should be noted here that those spokes are located physically upstream of air tangential inlets and do not affect the flowfield of tangential air component. Some wakes are expected to exist in axial-component flowfield behind the spokes, but the supersonic flow exiting the nozzle was found to be fully axisymmetric with and without swirl.

The nanosecond Schlieren diagnostic technique was used to visualize the shock-structure in this study. Schlieren imaging yields the first derivative of refractive index in the test region, thus giving an estimate of the density gradients within flowfield. The intensity of captured light can be further processed using image-processing techniques to obtain more quantitative information of the shock structure. Figure 2 shows a schematic of the utilized setup. The light source is a 532-nm Q-switched Nd:YAG laser with pulse duration of only 5 ns, which explains the term "nanosecond Schlieren" and makes this setup unique, compared to conventional Schlieren setups. The nanosecond light duration allows for capturing instantaneous images of the flowfield. No fluctuations are thus accumulated or averaged on the image, which allows for accurate visualization of shock structure.

Due to the fact that the intensity of laser light is too high for safe camera operation, the laser was equipped with neutral-density filters that reduce its light intensity. The divergence of the collimated beam is then increased by means of a plano-concave lens. The divergent beam fully illuminates a concave mirror, which reflects the light in a collimated fashion through the test section. This is essential for avoiding skewed perspective of flowfield. After penetrating the flow, the light is focused by another concave mirror. A knife-edge aperture intercepts the light at the focal point of second mirror to fulfill the Schlieren principles. The resulting images are then captured at a resolution of 1024 x 1024 pixels using a high-speed camera that is synchronized with the laser.

Since Schlieren is incapable of providing solid direct quantification of the variation of mixedness within the flowfield, a nanosecond condensate-seeded Mie-scattering diagnostic technique was developed and utilized to achieve this goal. The basic principle of this technique is to saturate either the air or fuel flow with the vapor of a volatile material upstream of nozzle. As the temperature decreases during expansion, some vapor has to condensate back to form a fog or mist of submicron seed particles that are small enough to follow the flow faithfully. When illuminated, these particles emit a Mie-scattering signal that is used for mixedness quantification.

Diethyl ether was selected as condensate-seeding material in this study. See Figure 3 for a schematic of the nanosecond Mie-scattering setup. Two metered streams of liquid diethyl ether (one for each air component) are solid-atomized, and the resulting spray jets are injected into the lines of high-pressure airflow supplied to nozzle.

The spray droplets evaporate rapidly upon injection, and the vapor mixes thoroughly with air saturating it. Controlled flow rates are injected, in order to provide adequate visualization of flowfield while preventing over-saturation of airflow, which can result in the formation of a liquid diethyl-ether film on the internal walls of nozzle or air delivery system.

The supersonic flowfield is illuminated along a centerline plane using the same 532-nm Q-switched pulse laser of Schlieren setup. The nanosecond light duration prevents the seeding particles from creating light streaks on the captured images. The Mie-scattering signal is captured using a Princeton Instruments PI-MAX2:1003 UNIGEN2 digital ICCD camera operated in synchronization with the laser and aligned at right angles to the light sheet. Although the right-angle alignment does not allow for capturing the greater intensity of forward scattering, it was used to provide a non-skewed perspective of flowfield. A resolution of 1024 x 1024 pixels and a gain of 125 were set for all images presented here. This value of gain was found sufficient for boosting the intensity of scattering signal while avoiding magnification of background noise. The intensity distribution on captured images was used to highlight the mixedness distribution, shock structure, shear layers, and slip lines within the flowfield.

III. Numerical Simulation Type and Assumptions

The ESI-Group CFD-FASTRAN 2008 LES-based code was used for all the simulations conducted in this study. A variable-size grid was generated for the examined geometry. Tighter meshing was implemented near and at the critical geometry locations, e.g., the exits of nozzle and fuel-injection system. Special emphasis was placed on the level of cell skewness. The geometry was sub-divided into individual volumes, each meshed separately, in order to keep the skewness level of the most skewed cell below 0.5. Mesh dependence was carefully examined through testing multiple levels of mesh tightness. A total of 7,166,860 nodes were found sufficient. Higher tightness levels did not yield any significant changes in the obtained profiles and were thus not considered, in order to optimize the computational time.

The Baldwin-Lomax turbulence model was implemented [29]. Calculation of viscosity and conductivity was based on the kinetic theory of gases. The mass diffusivity was calculated based on Fick's law with a Schmidt number of 0.5. A turbulent Prandtl number of 0.9 was used for calculating the turbulent conductivity. Similar to the experimental conditions, the total temperature at air inlets was kept fixed at 300 K, while the total pressure was maintained at 7.91 bar for the non-swirling case and 8.82 bar for the swirling one. The 8.82-bar value was carefully

chosen to ensure a common air flow rate of 175 g/s. (The need for higher nozzle reservoir pressure with swirl is explained in detail in the 'Results and Discussion' section.) The total pressure and temperature at air inlets were preserved throughout the iteration process in each examined case until convergence was attained. Owing to the relatively large cross-sectional areas of the air inlets, the entrance velocity of air was only 9.7 m/s, resulting in almost identical inlet stagnation and static conditions.

The nozzle walls were set to be isothermal at 280 K, based on multiple temperature measurements of the nozzle interior and exterior walls. This is attributed to the aforementioned fact that the nozzle is made of aluminum, which has a high thermal conductivity and thus allows the nozzle to act as a near-isothermal body. The walls of fuel-injection system, on the other hand, were set to be adiabatic, because the injection system is immersed almost totally into the nozzle and conditioning chamber, which allows for negligible amounts of heat to be conducted axially upstream through the thin walls of fuel system. Moreover, it is made of stainless steel that has a much lower thermal conductivity (relative to aluminum).

Since the simulation involves a free supersonic flow, special emphasis was placed on the choice of boundary conditions that represent the flow surroundings. The entire nozzle assembly was surrounded by a cylindrical enclosure of (40 D) diameter and (70 D) length, where D is the nozzle exit diameter (11 mm) — a good representative of jet size. The 40-D enclosure diameter assures that the side boundaries are far enough from the jet, in order to eliminate any interference of both and to maintain constant near-stagnation atmospheric properties at the boundaries. Consequently, the bottom and side enclosure surfaces were assigned the fixed-pressure boundary condition, which matches the constant actual atmospheric ambient pressure. The top side of enclosure, on the other hand, is an outlet located 55 D away from the nozzle exit (≈ 78% of the 70-D enclosure length). This guarantees that the flow leaves the simulated geometry shock-wave-free, since it was observed experimentally that complete transition to subsonic speeds occurs about 30 D downstream of nozzle exit.

The initial conditions of simulation were set for all cases at 1-atm static pressure, 300-K static temperature, 9.7-m/s axial velocity, and zero radial and tangential velocities. Consequently, the simulation incorporated the transient flow behavior as the high-pressure air expands and "marches" from geometry inlet to exit. An initial CFL number of 0.1 was chosen that increases to unity as convergence is approached. Time integration is implicit, where the Point Jacobi (fully implicit) scheme was used. Backward Euler discretization was implemented. Each iteration included 20 sub-iterations. Convergence was usually attained after 18500 – 19500 iterations.

IV. Test Matrix

The effect of swirl is investigated here by forwarding the entire airflow to nozzle tangential entries. This allows for examining a single degree of swirl, namely the maximum attainable one. Following a definition used for incompressible swirling jets [26, 30], a nozzle-based geometrical swirl number S_g is defined for air as

$$S_g = \left(\frac{\pi r_o R_o}{A_t} \right) \frac{m_t}{m_a + m_t} \tag{1}$$

where $(\pi r_o R_o / A_t) = 0.68$, for the geometry of used nozzle and its tangential entries, and m_a and m_t are the axial and tangential components of airflow, respectively. Consequently, all swirling cases of this study have a common nozzle-based geometrical swirl number of 0.68. The term "nozzle-based" refers to nozzle operation in the absence of coaxial injection system, as it will be shown later that the presence of this system reduces the geometrical swirl number down to 0.36. This significant reduction made the examination of the effect of swirl feasible only at its maximum attainable degree.

In addition to an extensive examination of the effect of swirl on shock structure and mixing, the effects of two flow parameters are investigated here under both non-swirling and swirling conditions, namely the relative Mach number (M_{rel}) and air-fuel density ratio (DR). The former is defined here as:

$$M_{rel} = \frac{v_{air} - v_{fuel}}{0.5(a_{air} + a_{fuel})} \tag{2}$$

This definition relates the difference in freestream velocities between fuel and air to the average speed of sound. It should be noted that the fuel simulant is injected here at velocities smaller than those of transonic airflow in most examined cases. Therefore, v_{fuel} is subtracted from v_{air} in the above definition, in order for M_{rel} to have positive values. Nevertheless, in a few extreme cases the fuel simulant is injected at velocities greater than those of airflow, and the corresponding values of M_{rel} are indicated here without neglecting their negative signs, in order to highlight the unique nature of those cases, i.e., $v_{fuel} > v_{air}$.

Each examined case in this study has a nominal value of M_{rel} that describes the injection conditions within that case. Since all cases to be presented here utilize no recess, i.e., fuel is injected at the throat of air nozzle, the nominal value of M_{rel} was calculated for each case using the fuel injection velocity and the sonic (throat) value of v_{air}. A comparison based on nominal M_{rel} thus allows for examining the effect of fuel-injection conditions on the global features of flowfield, including shock structure and mixing. Such analysis should not be confused with the shear-

layer-specific analysis of the effect of convective Mach number (M_c) on shear-layer properties (to be conducted in this study as well). Under non-swirling conditions, sonic v_{air} was found to be 323 m/s, based on isentropic ideal-gas relations. No similar simple calculations of v_{air} could be carried out for the swirling cases, due to the intrinsic three-dimensionality of swirling flows. Nevertheless, the results of numerical simulations revealed that the magnitude of sonic v_{air} is 329 m/s with swirl, which is almost equal to the non-swirling value. This fact allowed for examining the same nominal values of M_{rel} under both non-swirling and swirling conditions in this study.

The shock structure and all properties of airflow, including the aforementioned values of v_{air}, depend on air total pressure and temperature. Both were kept constant at 7.91 bar and 300 K, respectively, for all non-swirling cases presented in this study, which resulted in a fixed air flow rate of 175 g/s. It was noticed, however, that imparting swirl to airflow at the same nozzle reservoir pressure of 7.91 bar results in reduced mass flow rate through the nozzle. This observation agrees with the findings of many previous studies, where it was proven that imparting swirl to the airflow results in "additional choking" of the nozzle, i.e., a lower mass flow rate compared to the corresponding non-swirling conditions at the same reservoir pressure. A theoretical limit of no flow was even predicted at an infinitely large swirl number. Therefore, a higher reservoir pressure is necessary to maintain the same flow rate through the nozzle. It was found in this study that a value of 8.82 bar yields identical air flow rates of 175 g/s in the non-swirling and swirling cases.

Table 1 lists the test matrix for the results presented here. A total of 48 cases are examined (24 non-swirling cases plus their swirling counterparts). Case pair 0 utilizes no fuel injection and serves for quantifying the effect of swirl on supersonic flowfield, shock strength, shock positions, and jet diameter. Case pairs 1 – 13 study the effect of M_{rel}, wherein the injectant is helium. The injection velocity of helium is changed to induce different values of nominal M_{rel}. The effect of DR is studied through case pairs 14 – 23, wherein the injectant comprises different inert-gas mixtures. The mixture composition is varied to change mixture density and consequently DR. In order to maintain constant M_{rel} throughout the DR analysis, the injection velocity was adjusted to account for the changes in a_{fuel} due to the varying injectant composition. The values to be examined in both analyses of M_{rel} and DR were carefully selected according to the following criteria:

- The experimentally attainable ranges are spanned with narrow intervals, in order to quantify the examined effects accurately. For example, M_{rel} is examined over the range 0.44 – 0.26 with 8 intervals, while DR is covered in the range 12.68 – 4.33 with 6 intervals

- The numerical simulations span the experimental ranges with wide intervals, i.e., one simulation at the beginning of range, one in the middle, and one at the end. Case pairs 1, 5, and 9 within the M_{rel} analysis, for example, were examined both experimentally and numerically. The same applies for case pairs 15, 18, and 21 within the DR analysis. The duplicate examination of a few case pairs provides means of code validation through direct comparison of the experimental and numerical results. It should be noted, however, that only the experimental data were considered when quantifying the effects of M_{rel} and DR on flowfield parameters, since the experimental results require no further validation, unlike the numerical ones
- The numerical simulations extend beyond the experimental ranges to broaden the scope of analysis and qualitatively examine how accurate the experimental trends would be when extrapolated beyond the ranges they were obtained in. No accurate assessments of the extrapolation errors could be made, since the extended numerical simulations involve some error themselves and thus cannot be considered as accurate reference for the extrapolated experimental trends. Nevertheless, good agreement was observed, and estimates of the extrapolation errors are given here, which will support the findings of future studies

Note that case pairs 10 and 14 (highlighted in *italics* in Table 1) are identical, as they have the same fuel simulant (helium), M_{rel}, and DR. These two case pairs link the analyses of M_{rel} and DR. Also note that a letter "s" next to a case number denotes a swirling case.

V. Results and Discussion

A. Shock Structure (Non-Swirling, No Fuel Injection)

The shock structure of simple underexpanded supersonic flow is shown schematically in Figure 4. As can be seen, the structure comprises a shock-cell unit that gets repeated periodically to form a shock-cell train. This unit can be described as follows. Axial under-expanded flow undergoes an expansion fan and turns outwards. The free-jet boundary adapts accordingly and turns outwards as well. Passing again through the expansion fan, the outward flow turns back to axial. As the expansion fan meets the boundary, it reflects into a compression fan that coalesces later into the intercepting shock wave. The annular flow adjacent to boundary turns inwards through the compression fan, and the boundary again adapts by turning inwards as well. For slightly underexpanded nozzles, this intercepting shock reflects directly into a reflected shock at the centerline, forming the familiar diamond configuration. However, as the pressure ratio across the nozzle is increased, this reflection no more takes place at the centerline, and a Mach

disk is formed. The reflected shock turns the inward annular flow back to the axial direction. Since the Mach disk maintains the axial direction of core flow, the entire flow is now axial again. As the reflected shock impinges on the flow free boundary, it reflects into an expansion fan, starting another shock-cell unit. The repetition of units is continued until viscous effects become predominant, and this structure is no longer observed.

In presence of a coaxial injection system, the shock structure differs significantly from the simple one described above. Figure 5 shows a Schlieren image as well as a schematic of the shock structure of free nozzle flow in the presence of a non-recessed coaxial injection system with no fuel injection. Two distinct sub-structures are identifiable from Schlieren image and highlighted in the schematic. The first sub-structure is the simple nozzle-rim structure discussed above. A new sub-structure is generated due to the existence of coaxial injection system. It should be noted here that both sub-structures are not fully independent of each other. The presence of each affects the other. This interaction is, however, not indicated on the schematic in Figure 5, for easier understanding of the newly introduced sub-structure off injection system. Indicated here is how each structure would propagate if fully independent of the other. From this point forward, the nozzle-rim and injection-system sub-structures will be denoted “primary” and “secondary” shock structures, respectively, in this study.

The secondary structure starts with the airflow generating an inner conical boundary that completes the cone-frustum shape of fuel system tip. At the centerline, the flow collapses into itself, generating a conical shock wave that turns the flow back to parallel. This shock wave impinges on the outer flow boundaries shortly downstream of the impingement location of nozzle-rim expansion fan. The outer boundaries are altered by the impingement of that conical shock as observed from Figure 5. The shock reflects into an expansion fan that creates its own compression fan, intercepting shock, Mach disk, and reflected shock, similar to the primary structure. Both Mach disks of primary and secondary structures appear distinctly in Figure 5.

The effect of coaxial fuel injection is shown in Figure 6. Helium is used as fuel stimulant. As observed, the secondary shock structure is altered slightly. A shear layer develops in place of the former inner conical boundaries of airflow. Due to the presence of helium, the shear layer does not converge to a sharp point at the centerline. Moreover, due to the curved shape of this shear layer, the airflow undergoes gradual compression through a compression fan, which collapses later into a shock wave that generates the secondary shock sub-structure.

B. Validation of Numerical Code

Numerical simulations of the flowfield have been performed in this study, in addition to the experimental investigation, to broaden the scope of analysis of the latter and provide the desired quantification of certain flowfield parameters. For example, the Schlieren technique is incapable of visualizing the helical motion of a swirling flow or quantifying the different components of Mach number. Therefore, the numerical results are used to provide the missing data needed for examining the air/fuel shear layer and propagation of swirl throughout flowfield.

Before presenting any of the numerical results, code validation is demonstrated here by comparing the experimental and numerical visualizations of shock structure side by side in Figure 7. Shown are a Schlieren image and the corresponding numerically-obtained Mach number profile of case 1 (non-swirling airflow without fuel injection) from Table 1. The Mach number has been particularly chosen amongst other physical flow parameters, as it gives the clearest visualization of shock structure; shock waves are identifiable at regions of steep gradients of Mach number. Good agreement is observed. All flowfield details have been captured numerically with success. Moreover, the positions of shock cups and the values of jet diameter and maximum near-field Mach number agree well with the experimental findings.

Figure 8 provides another means of code validation, wherein the numerically-obtained location of first primary Mach disk (1.50 D) in case 1 is compared to the experimental findings of Adamson and Nicholls [2] (1.52 D, left) and Lewis and Carlson [3] (1.47 D, right). Recall that D is the nozzle-exit diameter. Considering the fact that the geometry investigated here comprises a coaxial fuel injection system, which does not exist in those earlier studies, it can be concluded that good agreement is observed.

C. Conclusions of Our Study of Nozzle Choking Criteria

Some conclusions of our study of nozzle choking criteria are summarized here, due to their importance to the current analysis. The throat velocity itself (and not any of its components) was found to be choked in a swirling flowfield. Therefore, the limiting tangential Mach number is unity. Moreover, the application of swirl always results in a reduction in axial Mach number component. The mass flow rate through nozzle was found to be primarily a function of throat static pressure and axial Mach number. The reduction in the latter with swirl explains the observed reduction in mass flow. Greater reservoir pressures, on the other hand, result in higher throat static pressures, which compensates for the reduced axial Mach number, and the mass flow rate can be kept constant at its non-swirling value. It was also found that the distribution of subsonic Mach number (and not any of its components) in a swirling

flow is solely dependent on cross-sectional area, similar to non-swirling flows, i.e., non-swirling and swirling flows have the same subsonic Mach number profile.

D. Supersonic Flowfield

The main objective of this current study is to analyze how swirl affects the supersonic flowfield, shock strength, shock positions, and jet diameter. Before beginning the analysis an important fact should be recalled here, pertaining to the subsonic flowfield inside nozzle. This flow is blind to the atmospheric back pressure outside, due to the sonic barrier at the throat. In other words, the subsonic flow does not adapt to the back pressure by fixing the throat static pressure at a certain value, regardless of nozzle reservoir pressure. However, once the flow exits nozzle, it is highly sensitive to the back pressure. If the flow pressure is different from that back pressure, the former has to be matched to the latter, which results in the formation of a shock structure in the supersonic flowfield outside nozzle. Convergent nozzles always generate underexpanded jets, if the back pressure is atmospheric. The super-atmospheric throat static pressure dictates how much expansion is still needed and consequently controls the geometry and strength of the formed shock structure, as explained earlier in the analysis of Figure 4.

Based on the findings of Adamson and Nicholls [2], Lewis and Carlson [3], and Crist et al. [4], the axial position of first Mach disk (relative to nozzle exit) increases with reservoir pressure. In light of the present study, this statement should be corrected to say that the axial position of first Mach disk is affected by both throat static pressure and degree of swirl. Before explaining why this correction is necessary, consider a new case, to be called 0's, which is a swirling case like 0s but has the lower reservoir pressure of case 0. All three cases have the same inlet total temperature of 300 K. Figure 9 shows the flowfield images of cases 0, 0's, and 0s. The horizontal white lines highlight the differences in positions of first Mach disk in cases 0's and 0s relative to case 0. It can be observed that the reservoir pressure is not the sole parameter that controls the position of first Mach disk. Although cases 0 and 0's have the same reservoir pressure, the later has an axially compact shock structure. This does not apply for cases 0 and 0s, which have different reservoir pressures yet similar positions of first Mach disk. Only the comparison of cases 0's and 0s reveals the expected trend, where increasing reservoir pressure results in axial stretching of shock structure. The effect of swirl explains those unexpected behaviors. Swirling flowfields have two unique features that are absent in non-swirling ones. First, the flow is pushed radially outwards by the Coriolis effect. Second, a swirling jet has two velocity gradients (axial and tangential) across its shear layer with the ambient air, which contributes to increasing the jet diameter, as compared to a non-swirling jet with an axial velocity gradient only. The fact that swirl

increases jet diameter is concurred in Figure 9, where is can be observed that the jet diameter within first shock cell is slightly larger in case 0's than it is in case 0. The larger diameter is accompanied by an axially compact shock structure, which appears to be a common feature of supersonic and subsonic swirling jets. Thus, it can be concluded here that the effects of swirl and nozzle reservoir pressure interfere destructively from the point of view of shock-structure axial compactness. Increasing reservoir pressure stretches the shock structure axially (case 0's to 0s), whereas swirl shrinks it (case 0 to 0's). This explains why the axial positions of first Mach disk in cases 0 and 0s are almost identical. It should be noted here that the effects of swirl and nozzle reservoir pressure interfere constructively from the point of view of jet radial expansion. Note from Figure 9 that the flowfield of case 0s has a slightly larger diameter than that of case 0's.

To quantify the effects of swirl and nozzle reservoir pressure in more detail, Figure 10 shows the axial distributions of centerline static pressure in the supersonic flowfields of cases 0, 0's, and 0s. Multiple observations can be made from Figure 10. The flat segments of nearly constant static pressure immediately downstream of nozzle exit represent the confined inner region observed in Figure 9 and discussed in the analysis of Figure 4. Very low subsonic Mach numbers exist inside this region, which explains why its centerline static pressure is almost equal to the total pressure of surrounding supersonic airflow. Swirl results in axial shrinking of this region, as observed from Figure 9 as well. The presence of nozzle-rim expansion fan is noticed downstream of the inner region. Sub-atmospheric pressures are reached, as the flow passes through expansion fan twice (refer back to the analysis of Figure 4 for more details). Note that case 0s expands from 4.4 to 0.4 atm, whereas case 0 expands only from 4.0 to 0.5 atm. This confirms that the combination of swirl and higher reservoir pressure results in a greater expansion fan in case 0s, which was concluded earlier in Figure 9. The considerably larger dark region observed immediately downstream of nozzle exit in the Schlieren image of case 0s is in fact a greater nozzle-rim expansion fan.

The realm of first primary and secondary shock cups is identified in Figure 10 as the region of recovery from the minimum sub-atmospheric pressure to a local maximum of super-atmospheric pressure. It can be seen that the first primary shock cup is approached at $z/D \approx 1.45$ in case 0, ≈ 1.4 in case 0s, and ≈ 1.25 in case 0's. This agrees with the qualitative analysis made earlier in Figure 9. The effect of swirl is evident in the upstream shift from 1.45 to 1.25, while the effect of nozzle reservoir pressure is obvious in the downstream shift from 1.25 to 1.4. Both effects interfere destructively, yielding almost the same axial compactness of shock structure in cases 0 and 0s.

The strength of shock structure can also be quantified from Figure 10. While the structure of case 0 recovers 0.70 atm, that of case 0's recovers only 0.64 atm. The structure of case 0s, on the other hand, recovers 0.89 atm. Thus, it can be concluded here that the application of swirl at matched nozzle reservoir pressure weakens the shock structure as expected. Both non-swirling and swirling flowfields start off with the same level of energy, but the latter dissipates more pressure energy than the former in friction losses inside nozzle. Consequently, the swirling throat flow has a smaller potential of pressure energy to dissipate through shock structure. The application of swirl at matched mass flow, on the other hand, results in a stronger structure, because of the greater potential of pressure energy at the throat.

Having analyzed the effect of swirl on shock structure, the analysis extends now to examine the supersonic swirl number. Figure 11 shows the axial variation of supersonic swirl number within the first two shock cells of case 0s. The swirl number was computed at select sections inside the nozzle using the correlation [26]

$$S = \frac{\int_{R_i}^{R_o} v_a \, v_t \, r^2 \, dr}{R_o \int_{R_i}^{R_o} v_a^2 \, r \, dr} \tag{3}$$

where v_a and v_t are the numerically-obtained axial and tangential velocity components, respectively. It can be observed that the supersonic swirl number decreases in the axial direction. This is attributed to substantial increase in axial momentum, as the flow expands and accelerates. A minimum swirl number of 0.07 is observed at z/D of about 1.4, before the swirl number experiences a slight local increase between z/D of 1.4 and 2.7. Recall from Figure 10 that the realm of first primary and secondary shock cups in case 0s starts at z/D ≈ 1.4. To understand why the supersonic swirl number experiences a slight local increase within the shock cups, it should be noted that the axial and tangential velocity components behave very differently through shock cups. Figure 12 helps explain this statement. Depicted is a three-dimensional schematic of shock structure, showing the orientation of v_a and v_t with respect to the main features, i.e., Mach disk, intercepting, and reflected shocks. It can be easily visualized how v_a is always perpendicular to the Mach disk. Moreover, both intercepting and reflected shocks are oblique with respect to v_a. For these two reasons, the axial Mach number and momentum undergo significant reductions through shock structure. The tangential velocity component, on the other hand, is always parallel to all features of shock structure. According to the fundamentals of gas dynamics, the velocity component parallel to the plane of a shock wave is preserved through the shock and experiences no change. Combining the behaviors of v_a and v_t through shock

structure, one can easily explain the small local increase in swirl number within realm of shock cups, especially when one recalls that the swirl number is proportional to the ratio of average tangential to axial momenta.

In terms of mixing, several important observations can be made from the Mie-scattering images of cases 0, 0's, and 0s in Figure 9. First, the dark core region downstream of nozzle exit has almost no diethyl-ether seeding particles, hence its dark appearance. It is believed to comprise toroidal vortices of subsonic flow, where kinetic energy is dissipated in viscous heating. Moreover, the static pressure and temperature within this region are equal to the corresponding stagnation values of the surrounding supersonic flow. Diethyl ether particles are thus heated up and re-evaporated, which explains the dark appearance of the core region. It should be noticed here that swirl strongly affects the size of this region. It is forced by the greater nozzle-rim expansion fan of swirling flowfield to take a smaller size with curved boundaries, which explains the schematic to the right in Figure 9.

The conical shock wave of secondary shock structure is also identifiable in the Mie-scattering images; so are all the other major shocks of flowfield, such as intercepting shock, Mach disk, and reflected shock. The second important observation to be made here is that the intensity of Mie-scattered light increases after the flow passes through each shock. This is attributed to flow compression. The dense fog of seeding particles downstream of a shock wave scatters more light. Based on this observation it can be concluded which shocks are stronger than others. The intercepting shock, for example, is distinctly stronger than the reflected one. The Mach disk is an exception of this rule. Being a normal shock, it decelerates the incoming core flow to subsonic speeds, thus raising its temperature significantly. The higher temperature is believed to cause re-evaporation of the liquid diethyl-ether seeding particles. Their absence explains the dark appearance of subsonic core flow downstream of Mach disk. This subsonic core is separated by slip lines from supersonic annular flow. The considerably lower temperature of this annular flow preserves the existence of liquid seeding particles.

The most remarkable observation to be made from the Mie-scattering images in Figure 9 is that swirl enhances mixing significantly, which agrees with the findings of all studies in the aforementioned literature review. A clear proof is evident in the smeared slip lines and narrower subsonic core downstream of first primary Mach disk in the swirling flowfield. Enhanced mixing occurs between the supersonic and subsonic sides of slip lines, which is absent across the sharp slip lines of non-swirling flowfield. Note that the presence of visible seeding particles inside the warmer subsonic core means that (a) the annular supersonic flow is the source of these particles, and (b) swirl-

induced vortices stir up the core and annular flows across slip lines, thus lowering the temperature of core flow down to the level where it can sustain the presence of liquid seeding particles.

It should be noted here that the analysis of Mie-scattering images cannot be extended to a quantitative level, i.e., the intensity scale of scattered light cannot be converted to a mixture fraction scale, even when fuel is injected into the airflow. This is attributed to the nature of condensate seeding, where the local temperature and pressure strongly affect the size, concentration, and even presence of seeding particles. The obtained light-intensity scale is thus a complicated function of pressure, temperature, and air mixture fraction. Decoupling the three individual effects is a very intricate process.

E. Effect of Relative Mach Number (M_{rel})

Having attained thorough understanding of the effect of swirl on supersonic flowfield, the analysis proceeds to examine the effect of fuel injection at different relative Mach numbers. Recall that M_{rel} is defined here as the ratio of $(v_{air} - v_{fuel})$ to the average speed of sound, where v_{air} is the throat velocity of air, and v_{fuel} is the injection velocity of fuel, since fuel is injected coaxially at nozzle throat (i.e., no recess) in all the following analyses. Also recall that the close values of sonic air velocity under non-swirling and swirling conditions allowed for examining the same values of relative Mach number and air-fuel density ratio (DR) with and without swirl. Another very important detail to be pointed out here is that swirl is imparted to air at matched mass flow from this point forward, i.e., all swirling cases have the same mass flow rate of the non-swirling ones (175 g/s). This implies that the swirling cases have the elevated nozzle reservoir pressure of 8.82 bar. Matching of air mass flow ensures a fair comparison between the different case-pairs based on mixture fractions and mixedness.

The effect of M_{rel} is examined in case-pairs 1 – 13 given in Table 1. Case-pairs 1 – 9 span the M_{rel} range 0.44 – 0.26 experimentally. Case-pairs 1 (range begin), 5 (range middle), and 9 (range end) were selected to be examined both experimentally and numerically, in order to optimize the parameters of numerical code for best agreement with the experimental results. It should be noted, however, that only the experimental data was considered when quantifying the effects of M_{rel} and DR on flowfield parameters, since it requires no further validation. The experimental range is extended numerically to -0.48 in case-pairs 10 – 13. Case-pair 11 represents a unique condition, where fuel is injected at the throat velocity of air, resulting in M_{rel} of zero. Case-pairs 12 and 13 represent the extreme situations, where fuel is injected at velocities higher than the throat velocity of air. The corresponding

values of M_{rel} are indicated here without neglecting their negative signs, in order to highlight the unique nature of those two case-pairs.

Keeping all airflow properties constant, the flow rate of fuel (simulated by helium) was changed to induce different fuel velocities and thus multiple values of M_{rel}. The injection Mach number of helium was kept below 0.3 (except in case-pairs 12 and 13), in order to maintain a constant helium density and to avoid compressibility effects on the helium-side of air/helium shear layer. The resulting DR was about 35.5 for most cases. The supply pressure of helium was carefully selected for each case-pair to match the total pressures of helium and air at injection.

Figure 13 shows the effect of M_{rel} at constant DR. The experimental results, i.e., Schlieren and Mie-scattering images, are depicted in Figures 13a and 13b, respectively, while Figure 13c shows the numerical results in form of Mach number and fuel mixture fraction profiles. The non-swirling cases are depicted in the top row of each figure, while the bottom one contains the swirling cases. The values of M_{rel} and injection Mach number of each case-pair are indicated at the top of its column.

The most remarkable observation to be made from the Schlieren and Mie-scattering images, as well as the fuel mass fraction profiles, in Figure 13 is that the air/fuel shear layer initiates with a negative angle that transforms later to positive. In other words, the cross-sectional area of core flow converges initially to a minimum value before propagating divergently as expected. Figure 14 helps explain this observation. Shown are the axial variations of computed centerline Mach number and fuel mass fraction for different values of M_{rel} under non-swirling conditions. Note that subsonic injection is implemented throughout the analysis of M_{rel}. However, the centerline Mach numbers are observed to increase from the subsonic injection values to supersonic maxima of 1.75 – 2.10. The only possible way for the subsonic core flow to expand to supersonic speeds is to resemble a convergent-divergent nozzle. This can only be achieved if the cross-sectional area of core flow initially converges to a throat before diverging again. The creation of a throat allows the core flow to transition from subsonic to supersonic speeds. To attain further understanding of the location of core-flow throat within flowfield, Figure 15 shows how the axial position of this throat varies with M_{rel}. Notice that at high M_{rel} (i.e., low injection velocities) the core flow propagates axially for about 0.5 D with a negative shear angle. The throat of core flow, however, approaches nozzle exit at low M_{rel} (high injection velocities), and negative-shear-angle propagation is confined to an axial distance of 0.25 D only.

Another important observation to be made from Figure 14 is that the initial mixing rate up to z/D of about 0.2 is observed to be affected significantly by the compressibility of fuel injection. Note that incompressible injection is

implemented up to M_{rel} of 0.21, whereas case-pairs 11 – 13 (0.00 to -0.48) utilize compressible injection. Higher M_{rel} demonstrate superior mixing. The mixture fraction of fuel drops to centerline values as low as 0.13, which demonstrates how short the potential core of fuel is at high M_{rel}.

Combining the analyses of core-flow throat and initial mixing rate, it can be concluded here that fuel injected at low subsonic Mach numbers (high M_{rel}) has to propagate for longer axial distances with a negative shear angle, before the fuel-rich core flow reaches a throat after which it propagates supersonically. This is advantageous from two aspects. First, increasing the distance between core throat and injection point allows for more mixing to take place across a supersonic/subsonic shear layer, which is significantly more effective than the fully supersonic one downstream of core throat. This is evident in the rates of decay in centerline fuel mass fraction in Figure 14. Notice that the decay rates are significantly higher upstream of core throat, which indicates better mixing quality. The second advantage of low injection Mach numbers is that a negative-angled shear layer propagates with a radially inwards component, which allows it to confine the fuel-rich core flow more effectively. This core is thus consumed more rapidly by the growing shear layer, which results in superior mixing at high M_{rel}. The Mie-scattering images in Figure 13b confirm this discussion. It can be clearly observed that the high M_{rel} of case-pair 1 results in near-complete mixing of the helium jet with surrounding airflow. Mixing deteriorates gradually as M_{rel} is decreased, which is evidenced in the increasing darkness and size of the unseeded helium-rich core flow.

Another notable advantage of the presence of a negative shear angle downstream of injection point can be observed in the strength of shock structure. As shown schematically in Figure 16, the inner conical boundaries and conical shock wave, which initiate the secondary shock sub-structure in the absence of fuel injection, are replaced by a compression fan that is generated off the curved profile of a negative shear angle at subsonic injection Mach numbers. This fan allows for gradual compression of the airflow. Although the fan eventually collapses into a shock wave, the strength of this wave is significantly lower than the conical one at no fuel injection. If M_{rel} is decreased (by increasing injection Mach number), the throat of core flow approaches the injection point, as mentioned earlier. Consequently, the negative shear angle and its compression fan diminish gradually. At the extreme of sonic injection a positive shear angle exists right from the start, accompanied by a strong shock at the injection point. This results in a stronger shock structure. Figure 13c confirms this discussion. Notice that the average Mach number within second shock cell is significantly reduced, as the injection Mach number increases and M_{rel} decreases.

One last observation to be made from Figure 14 is that the axial position of first primary Mach disk is almost constant for the range of examined M_{rel}. Note that the location of this Mach disk is identified on the curve of centerline Mach number by the point of zero slope (*dM/dz*) after the initial expansion. It can be clearly observed that the axial position (z/D) of first primary Mach disk is about 1.32 – 1.39 for the broad range of examined relative Mach numbers. The Schlieren and Mie-scattering images of Figure 13 confirm this finding, where it can be observed that the first primary Mach disk is located at almost the same axial position, regardless of M_{rel}. Note that the depicted images are instantaneous. The fluctuation of shock structure within flowfield dictated the analysis of multiple images for each case, in order to attain good-accuracy experimental quantification of the axial positions of Mach disks. Fifty Schlieren images were used per case. The positions of Mach disks were determined from each image, and the results of all fifty images were averaged to give the values that represent this case. Figure 17a shows the effect of M_{rel} on the axial positions of first primary and secondary Mach disks. Note that only experimental results are plotted in the M_{rel} range 0.44 – 0.26. Also note that the included trend lines were fitted from the experimental data points only. Multiple observations can be made here. First, the experimental values show good agreement with the numerical results of Figure 14. This has been expected, since the parametric assumptions of numerical simulations were optimized to yield best agreement over the experimental range. Outside this range it can be noticed, however, that the simulations always underestimate the positions of Mach disks with a maximum error of about 4%. It should be noted though that this error is based on the extrapolated trend lines of experimental data. Nevertheless, it can be concluded here that good qualitative agreement is observed.

Another observation to be made from Figure 17a is that M_{rel} has little effect on the axial position of first primary Mach disk, as concluded earlier. An asymptotic behavior is noticed at very low M_{rel}. On the other hand, the effect of M_{rel} on the position of secondary Mach disk is significant at high values of M_{rel} but approaches an asymptote at very low M_{rel} as well. The behavior of primary Mach disk is mainly attributed to the fact that airflow properties were kept constant throughout the M_{rel} analysis, while those of fuel flow were changed. Since the primary shock structure starts by the nozzle-rim expansion fan, it is expected to be least affected by any changes in fuel flow. The secondary structure, on the other hand, initiates at the tip of injection system and is strongly dependent on the shape and curvature of air/fuel shear layer, which explains why the position of secondary Mach disk is so susceptible to changes in M_{rel}. Recall here from the analysis of Figure 16 that decreasing M_{rel} results in the gradual diminishing of compression fan at the base of secondary structure. It can thus be imagined that the founding shock wave of

secondary structure is shifted axially upstream in this process. Consequently, the location of impingement of this shock on the free boundaries of flow is shifted axially upstream as well. The immediate result of these shifts is that the secondary Mach disk approaches the nozzle, which explains the trends observed in Figure 17a.

Along the same line of examining the effect of M_{rel} on shock structure, Figure 17b shows how the maximum jet diameter is affected within first shock cell. Notice that decreasing M_{rel} results in greater jet diameters, which is primarily attributed to the aforementioned dependence of secondary shock structure on M_{rel}. It should be recalled here that both sub-structures of the flowfield are not fully independent of one another, i.e., the fact that coaxial injection is implemented here does not mean that changes in injection conditions are confined to the core-flow region. The entire flowfield is affected.

The analysis of M_{rel} is concluded here by highlighting the effect of swirl. The first outcome of applying swirl is significant mixing enhancement. This has been expected and can be clearly observed from the Mie-scattering images in Figure 13b. Notice that the unseeded core flow in all swirling cases has considerably brighter shades and smaller sizes. Enhanced mixing with the surrounding supersonic airflow explains the presence of seeding particles inside the core flow of swirling cases, whereas the helium-rich core flows of non-swirling cases are particle-free. Another outcome of swirl is an overall axial shrinkage in shock structure accompanied by an increased jet diameter. Notice from Figure 17a that the primary and secondary Mach disks are shifted upstream as a result of swirl. Also notice from Figure 17b that the jet diameter increases with swirl. Both observations are in agreement with the aforementioned discussion on the effect of swirl on shock structure. It should be finally noted that this effect fades out as M_{rel} is decreased (higher injection Mach number), since the injected fuel is non-swirling in this study.

F. Effect of Air-Fuel Density Ratio (DR)

Having analyzed the effect of relative Mach number, the analysis proceeds to examine the effect of air-fuel density ratio (DR) at constant M_{rel}. DR is defined here as the ratio of throat density of air to injection density of fuel. Also recall that the close values of sonic air velocity under non-swirling and swirling conditions allowed for examining the same values of DR with and without swirl. Another very important detail to be pointed out again here is that swirl is imparted to air at matched mass flow, i.e., all swirling cases have the same mass flow rate of the non-swirling ones (175 g/s). This implies that the swirling cases have the elevated nozzle reservoir pressure of 8.82 bar. Matching of air mass flow ensures a fair comparison between the different case-pairs based on mixture fractions and mixedness.

The effect of DR is examined in case-pairs 14 – 23 given in Table 1. Case-pairs 15 – 21 span the DR range 12.68 – 4.33 experimentally. Case-pairs 15 (range begin), 18 (range middle), and 21 (range end) were selected to be examined both experimentally and numerically, in order to optimize the parameters of numerical code for best agreement with the experimental results. It should be noted again here that only the experimental data was considered when quantifying the effect of DR on flowfield parameters, since it requires no further validation. The experimental range is extended numerically from both sides. Case 14 examines a DR of 35.5, while case-pairs 22 and 23 have DR of 3.24 and 2.29, respectively. Note that case pairs 10 (from M_{rel} analysis) and 14 are identical, as they have the same fuel simulant (helium), M_{rel}, and DR.

Keeping all airflow properties constant, fuel was simulated by different inert-gas mixtures (helium, argon, and krypton). The mixture composition is varied to change mixture density and consequently DR. In order to maintain a constant M_{rel} of 0.21 throughout this analysis, the injection velocity was adjusted to account for the changes in a_{fuel} due to the varying injectant composition. The supply pressure of fuel was carefully selected for each case-pair to match the total pressures of fuel and air at injection. Compressible injection is utilized throughout this analysis, except for case-pair 14, which is copied over from M_{rel} analysis. Case-pair 23 represents the extreme conditions, where fuel is injected at its sonic velocity, i.e., the injection system is choked.

Figure 18 shows the effect of DR at constant M_{rel}. The experimental results, i.e., Schlieren and Mie-scattering images, are depicted in Figures 18a and 18b, respectively, while Figure 18c shows the numerical results in form of Mach number and fuel mixture fraction profiles. The non-swirling cases are depicted in the top row of each figure, while the bottom one contains the swirling cases. The values of DR and injection Mach number of each case-pair are indicated at the top of its column, together with the composition of fuel simulant.

In light of the comprehensive M_{rel} analysis, the effect of DR will be analyzed here in a concise fashion. It can be observed from the Schlieren and Mie-scattering images, as well as the fuel mass fraction profiles, in Figure 18 that the air/fuel shear layer again initiates with a negative angle that transforms later to positive. Consequently, the cross-sectional area of core flow converges initially to a throat before propagating divergently. This allows the core flow to accelerate from the subsonic Mach numbers of injection to supersonic maxima of 1.84 – 2.13 in Figure 19. The variation of axial position of core throat with DR is shown in Figure 20. Notice that at high DR the core flow propagates axially for about 0.5 D with a negative shear angle. However, at a DR of 2.29 the throat of core flow is exactly at the nozzle exit, and negative-shear-angle propagation is completely absent. Also notice from the rate of

decay in centerline fuel mass fraction in Figure 19 that a fully supersonic, positive-angled shear layer (DR = 2.29) yields deteriorated mixedness, compared to the supersonic/subsonic negative-angled shear layer at DR = 35.50. The findings of Figures 19 and 20 are confirmed in the Mie-scattering images of Figure 18, where mixing is observed to deteriorate gradually as DR is decreased, as evidenced in the increasing size of unseeded fuel-rich core flow.

The effect of DR on shock-structure strength is observed in Figure 18c. Notice again that the transition from negative to positive shear angles results in stronger shock structure at low DR, as evidenced in the decreasing average Mach number within second shock cell. The axial position of first primary Mach disk is observed to be once more almost constant (1.32 – 1.46) for the range of examined DR in Figure 19, which is confirmed in the Schlieren and Mie-scattering images of Figure 18. This finding is concurred in Figure 21a, where the effect of DR on axial positions of first primary and secondary Mach disks is quantified under non-swirling and swirling conditions. The solid fit lines again represent purely experimental trends. Notice that DR has little effect on both primary and secondary Mach disks, except for DR below 4. However, since the extreme case-pairs 22 and 23 have not been validated experimentally, this DR region was fitted (separately from the experimental trends) by dashed lines in Figure 21a.

Figure 21b shows how the maximum jet diameter is affected within first shock cell. Notice that decreasing DR results in greater jet diameters, which is once more primarily attributed to the aforementioned dependence of secondary shock structure on the angle of air-fuel shear layer. It should be noticed here, however, that the effect of DR on jet diameter is less pronounced than that of M_{rel}. The analysis of DR is concluded here by highlighting the effect of swirl. The first outcome of applying swirl is again significant mixing enhancement, which can be clearly observed from the Mie-scattering images in Figure 18b. Notice that the unseeded core flow in all swirling cases has considerably brighter shades and smaller sizes. Enhanced mixing with the surrounding supersonic airflow explains the presence of seeding particles inside the core flow of swirling cases, whereas the fuel-rich core flows of non-swirling cases are particle-free. Another outcome of swirl is an overall axial shrinkage in shock structure accompanied by an increased jet diameter. Notice from Figure 21a that the primary and secondary Mach disks are shifted upstream as a result of swirl. Also notice from Figure 21b that the jet diameter increases with swirl. Both observations are once more in agreement with the aforementioned discussion on the effect of swirl on shock structure. This effect, however, fades out as DR is decreased, since the injected fuel is non-swirling in this study.

G. Shear-Layer Growth

The analyses of M_{rel} and DR revealed how the angle of air/fuel shear layer critically affects both shock structure and mixing. The following analysis is thus dedicated to attaining better understanding of shear-layer growth, which is another very important parameter. An analysis of shear-layer thickness is conducted here, following the same roadmap of Papamoschou and Roshko [16]. They defined a convective frame of reference that incorporates the effect of flow compressibility and accounts for different speeds of sound on both sides of the shear layer. Figure 22 compares this convective frame of reference to the stationary (traditional) one. Notice that the former moves with the flow at the convective wave velocity (v_c). The mainstream Mach numbers on both sides of shear layer transform to this new frame of reference as follows

$$M_{c_{air}} = \frac{v_{air} - v_c}{a_{air}} \quad \text{and} \quad M_{c_{fuel}} = \frac{v_c - v_{fuel}}{a_{fuel}} \tag{4}$$

where M_c stands for convective Mach number. Both values are considerably close, and they always have the same sign, since v_c always lies somewhere between v_{air} and v_{fuel}. If a streamline is traced across the shear layer, as seen in Figure 22, a point has to be met, where the local velocity is v_c on an absolute scale but zero (stagnation) on the convective one. This stagnation point forces the equilibrium of total pressures on both sides of shear layer, i.e.,

$$p_{air}\left(1+\frac{\gamma_{air}-1}{2}M_{c_{air}}^2\right)^{\frac{\gamma_{air}}{\gamma_{air}-1}} = p_{fuel}\left(1+\frac{\gamma_{fuel}-1}{2}M_{c_{fuel}}^2\right)^{\frac{\gamma_{fuel}}{\gamma_{fuel}-1}} \tag{5}$$

Substituting from Equation 4 into 5, the convective wave velocity can be solved for by trial and error. Back-substitution in Equation 4 then yields the individual convective Mach numbers of air and fuel. The effect of convective Mach number on shear-layer thickness can thus be quantified, which is a direct indication of how the degrees of compressibility of mainstreams on both sides of the shear layer affect its growth rate. Shear-layer thickness is determined as follows. Consider the shear layer shown schematically in Figure 23. A *Pitot thickness*, δ_{pit}, is defined after Papamoschou and Roshko [16] as the width of total-pressure profile from 5% to 95% of the difference of mainstream values. The parameters (p, γ, v, and a) of air and fuel mainstreams are thus calculated at the end points of δ_{pit}.

The analysis of shear-layer thickness is carried out here on all the numerical cases given in Table 1, since their simulations contain all the necessary data. The axial positions z/D = 0.1 and 1.0 were selected in each case. Before constructing the final plot of δ_{pit} versus M_c, twenty-four additional simulations were conducted to replicate the 12

numerical case-pairs of Table 1 under incompressible conditions, while maintaining their individual velocity and density ratios. The analysis of shear-layer thickness was applied to the attained incompressible flowfields at z/D = 0.1 and 1.0 as well. The ratio of compressible to incompressible shear-layer thicknesses was finally calculated for all the 24 numerical cases at hand. Figure 24 is the fruit of this effort. The normalized Pitot thickness of shear layer is plotted versus air convective Mach number. All data points fall in the Mach-number range 0.25 – 0.83. The findings of Papamoschou and Roshko [16] are also included. Good qualitative agreement is observed, since most data points of this current study fall within the dashed lines that represent bounding envelopes of the results of Papamoschou and Roshko. A very important conclusion to be made from Figure 24 is that the normalized shear-layer Pitot thickness decreases with the application of swirl. It should be noted, however, that this reduction occurs in the normalized thickness and not the absolute one. As a matter of fact, it was noticed throughout the computations of Figure 24 that the absolute value of shear-layer thickness increases slightly with swirl, which agrees with findings of Cutler et al. [23], Cutler and Levey [24], and Levey [25]. The controversy is caused here by the fact that the thickness of an incompressible shear layer was found to increase more with swirl than that of a compressible shear layer.

VI. Conclusions

This work complements the efforts of a previous study by the authors, where the effect of imparting swirl to underexpanded supersonic nozzle airflow on nozzle choking criteria, thrust, and specific impulse were examined. The effects of swirl on supersonic flowfield and mixing are examined here at matched nozzle reservoir pressure as well as matched mass flow. The following conclusions were made: (a) The effects of swirl and nozzle reservoir pressure interfere destructively from the point of view of shock-structure axial compactness. Increasing reservoir pressure stretches the shock structure axially, whereas swirl shrinks it. On the other hand, both effects interfere constructively from the point of view of radial jet expansion; both result in greater jet diameter. (b) The application of swirl at matched reservoir pressure weakens the shock structure as expected. Both non-swirling and swirling flowfields start off with the same total pressure, but the latter dissipates more pressure energy than the former in friction losses inside nozzle. Consequently, the swirling throat flow has a smaller potential of pressure energy to dissipate through shock structure. The application of swirl at matched mass flow, on the other hand, results in a stronger structure, because of the greater potential of pressure energy at the throat. (c) Swirl was found to enhance

supersonic mixing significantly, which agrees with the findings of all previous studies. (d) Fuel injected at low subsonic Mach numbers has to propagate initially with a negative shear angle. In other words, the cross-sectional area of fuel-rich core flow converges first, before this core flow reaches a throat after which it propagates supersonically. This behavior is advantageous, as it results in better mixing and reduced shock-structure strength.

Acknowledgments

This work was supported by the Space Vehicle Technology Institute, jointly funded by NASA, DoD, and USAF within the NASA Constellation University Institutes Project (CUIP), with Claudia Meyer as the Project Manager. This support is gratefully acknowledged.

The simulation package CFD-GEOM, CFD-FASTRAN, and CFD-VIEW was provided by ESI-Group and CFDRC. This support is gratefully acknowledged.

Assistance provided by Adam Kareem in data acquisition and analysis is much appreciated.

References

[1] Buckley, P. L., Craig, R. R., Davis, D. L., and Schwartzkopf, K. G., "The Design and Combustion Performance of Practical Swirlers for Integral Rocket/Ramjets," *AIAA Journal*, Vol. 21, No. 5, 1983, pp. 733-740.

[2] Adamson, T. C., Jr. and Nicholls, J. A., "On the Structure of Jets from Highly Underexpanded Nozzles into Still Air," *Journal of the Aero/Space Sciences*, Vol. 26, No. 1, January, 1959, pp. 16-24.

[3] Lewis, C. H., Jr. and Carlson, D. J., "Normal Shock Location in Underexpanded Gas and Gas-Particle Jets," Technical Note, *AIAA Journal*, Vol. 2, No. 4, April, 1964, pp. 776-777.

[4] Crist, S., Sherman, P. M., and Glass, D. R., "Study of the Highly Underexpanded Sonic Jet," *AIAA Journal*, Vol. 4, No. 1, 1966, pp. 68-71.

[5] Gostintsev, Y. A., Zelentsov, V. V., Ilyukhin, V. S., and Pokhil, P. F., "Structure of Underexpanded Supersonic Swirling Gas Jet," *Journal of Fluid Dynamics*, Vol. 4, No. 5, September, 1969, pp. 158-162.

[6] Batson, J. L. and Sforzini, R. H., "Swirling Flow through a Nozzle," *Journal of Spacecraft and Rockets*, Vol. 7, No. 2, 1970, pp. 159-163.

[7] Settles, G. S., "Supersonic Mixing Enhancement by Vorticity for High-Speed Propulsion," Report submitted to NASA-Langley Research Center, October 1991, NASA-CR-188920.

[8] Lee, K. H., Setoguchi, T., Matsuo, S., and Kim, H. D., "An Experimental Study of Underexpanded Sonic, Coaxial, Swirl Jets," *Proceedings of the Institution of Mechanical Engineers, Part C: Journal of Mechanical Engineering Science*, Vol. 218, No. 1, 2004, pp. 93-103.

[9] Lee, K. H., Setoguchi, T., Matsuo, S., and Kim, H. D., "Influence of the Nozzle Inlet Configuration on Underexpanded Swirling Jet," *Proceedings of the Institution of Mechanical Engineers, Part C: Journal of Mechanical Engineering Science*, Vol. 220, No. 2, 2006, pp. 155-163.

[10] Murakami, E. and Papamoschou, D., "Experiments on Mixing Enhancement in Dual-Stream Jets," *39th AIAA Aerospace Sciences Meeting & Exhibit*, Reno, NV, Jan. 8-11, 2001, AIAA-2001-0668.

[11] Carpenter, P. W., "A Linearized Theory for Swirling Supersonic Jets and its Application to Shock-Cell Noise," *AIAA Journal*, Vol. 23, No. 12, 1985, pp. 1902-1909.

[12] Yu, Y. K., Chen, R. H., and Chew, L., "Screech Tone Noise and Mode Switching in Supersonic Swirling Jets," *AIAA Journal*, Vol. 36, No. 11, 1998, pp. 1968-1974.

[13] Yu, Y. K., "An Experimental Study of Underexpanded Supersonic Swirling Jets," PhD thesis, University of Central Florida, December 1997.

[14] Brown, G. L. and Roshko, A., "On Density Effects and Large Structure in Turbulent Mixing Layers," *Journal of Fluid Mechanics*, Vol. 64, No. 4, 1974, pp. 775-816.

[15] Winant, C. D. and Browand, F. K., "Vortex Pairing: The Mechanism of Turbulent Mixing-Layer Growth at Moderate Reynolds Number," *Journal of Fluid Mechanics*, Vol. 63, No. 2, 1974, pp. 237-255.

[16] Papamoschou, D. and Roshko, A., "The Compressible Turbulent Shear Layer: An Experimental Study," *Journal of Fluid Mechanics*, Vol. 197, 1988, pp. 453-477.

[17] Clemens, N. T. and Mungal, M. G., "Two- and Three-Dimensional Effects in the Supersonic Mixing Layer," *26th AIAA/SAE/ASME/ASEE Joint Propulsion Conference*, Orlando, FL, July 16-18, 1990, AIAA-90-1978.

[18] Hermanson, J. C. and Winter, M., "Imaging of a Transverse Sonic Jet in Supersonic Flow", *27th AIAA/SAE/ASME/ASEE Joint Propulsion Conference*, Sacramento, CA, June 24-26, 1991.

[19] Hall, J. L., Dimotakis, P. E., and Rosemann, H., "Experiments in Non-Reacting Compressible Shear Layers," *29th AIAA Aerospace Sciences Meeting*, Reno, NV, Jan. 7-10, 1991.

[20] Miles, J. W., "On the Disturbed Motion of a Plane Vortex Sheet," *Journal of Fluid Mechanics*, Vol. 4, No. 5, 1958, pp. 538-552.

[21] Chinzei, N., Masuya, G., Komura, T., Mukrami, A., and Kudou, K., "Spreading of Two-Stream Supersonic Turbulent Mixing Layers," *Physics of Fluids*, Vol. 29, No. 5, 1986, pp. 1345-1347.

[22] Menon, S., "Numerical Simulations of Supersonic Flows Past Generic SCRAMJET Flameholders," Final Report under Contract No. F33615-87-C-2782 to US Air Force, Wright Patterson AFB, Report No. 434, 1988.

[23] Cutler, A. D., Levey, B. S., and Kraus, D. K., "An Experimental Investigation of Supersonic Swirling Jets," *24th AIAA Fluid Dynamics Conference*, Orlando, FL, July 6-9, 1993, AIAA-93-2922.

[24] Cutler, A. D. and Levey, B. S., "Vortex Breakdown in a Supersonic Jet," AIAA Paper 91-1815, June 1991.

[25] Levey, B. S., "An Experimental Investigation of Supersonic Vortical Flow," M.S. Thesis, School of Engineering and Applied Science, The George Washington University, September 1991.

[26] Gupta, A. K., Lilley, D. G., and Syred, N., "Swirl Flows," Abacus Press, UK, 1984, ISBN 0-85626-175-0.

[27] Cutler, A. D., Levey, B. S., and Kraus, D. K., "Near-Field Flow of Supersonic Swirling Jets," *AIAA Journal*, Vol. 33, No. 5, 1995, pp. 876–881.

[28] Linck, M., "Spray Flame and Exhaust Jet Characteristics of a Pressurized Swirl Combustor," PhD thesis, University of Maryland, College Park, MD, May 2006.

[29] Baldwin, B. S. and Lomax, H., "Thin Layer Approximation and Algebraic Model for Separated Turbulent Flows," *16th AIAA Aerospace Sciences Meeting*, Huntsville, Alabama, Jan. 16-18, 1978, AIAA-78-257.

[30] Claypole, T. C. and Syred, N., "The Effects of Swirl Burner Aerodynamics on NOx Formation," *Proceedings of 18th Symposium (International) on Combustion*, Combustion Institute, Pittsburgh, PA, 1981, pp. 81-89.

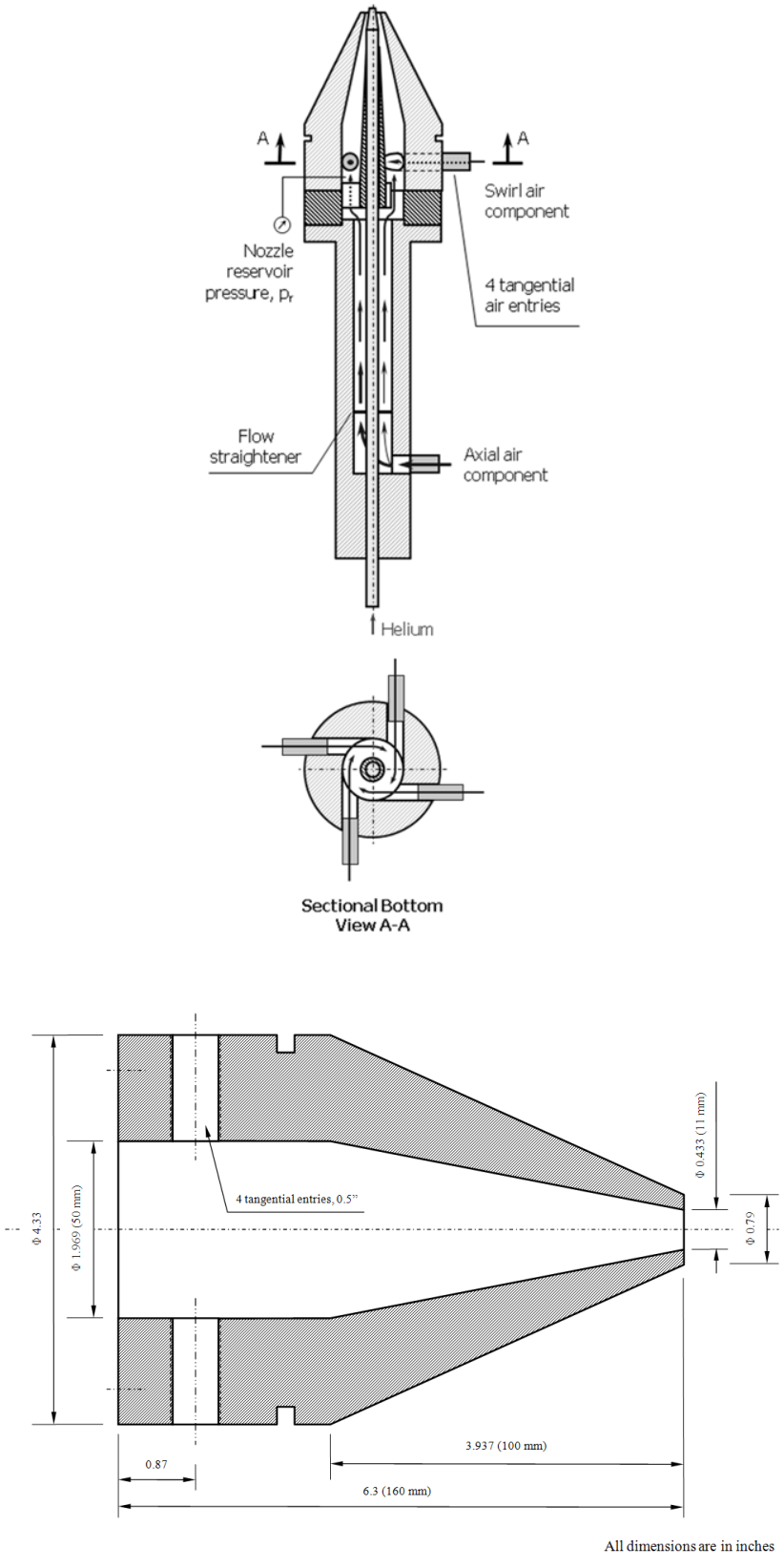

Figure 1. Schematic of UMD supersonic-nozzle assembly

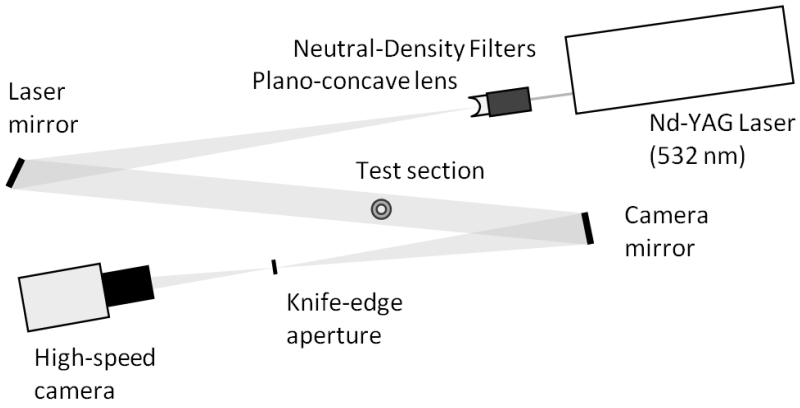

Figure 2. Schematic of nanosecond Schlieren system

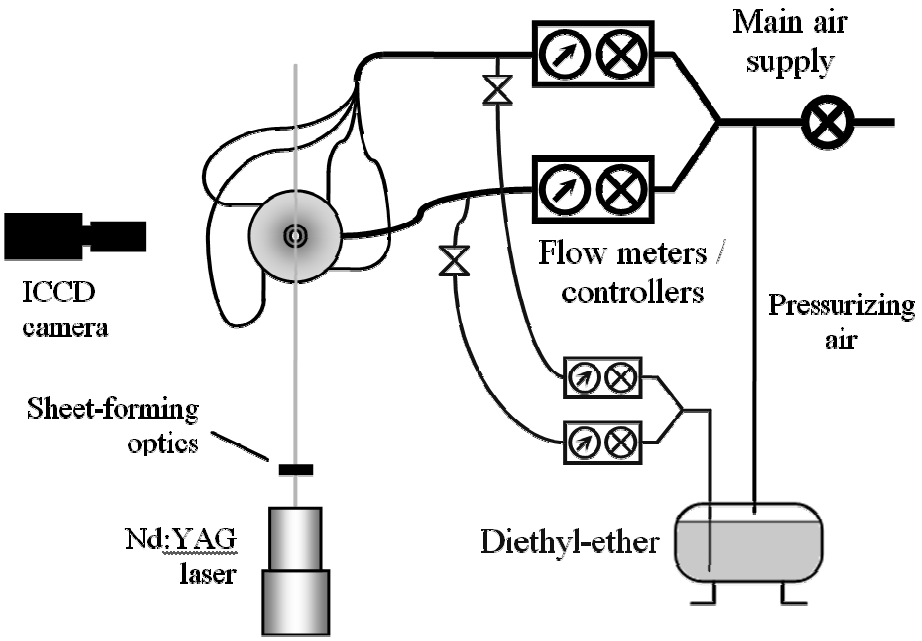

Figure 3. Schematic of condensate-seeded Mie-scattering setup

Table 1. Test Matrix

Constant parameters:
Air total temperature at inlet = 300 K
Nozzle reservoir pressure = 7.91 bar (non-swirling), 8.82 bar (swirling)
Geometrical swirl number for swirling cases, $S_g = 0.68$

Case	Injected Gas	M_{rel}	DR	Experimental	Numerical
0 & 0s	Air only; no fuel injection				
Effect of Relative Mach Number					
1 & 1s	Helium	0.44	35.50	✓	✓
2 & 2s		0.41		✓	
3 & 3s		0.39		✓	
4 & 4s		0.37		✓	
5 & 5s		0.35		✓	✓
6 & 6s		0.32		✓	
7 & 7s		0.30		✓	
8 & 8s		0.28		✓	
9 & 9s		0.26		✓	✓
10 & 10s		*0.21*			✓
11 & 11s		0.00			✓
12 & 12s		-0.21*			✓
13 & 13s		-0.48*			✓
Effect of Density Ratio					
14 & 14s	*100% Helium*	0.21	*35.50*		✓
15 & 15s	80% Helium / 20% Argon		12.68	✓	✓
16 & 16s	70% Helium / 30% Argon		9.60	✓	
17 & 17s	60% Helium / 40% Argon		7.72	✓	
18 & 18s	50% Helium / 50% Argon		6.46	✓	✓
19 & 19s	40% Helium / 60% Argon		5.55	✓	
20 & 20s	30% Helium / 70% Argon		4.86	✓	
21 & 21s	20% Helium / 80% Argon		4.33	✓	✓
22 & 22s	50% Helium / 50% Krypton		3.24		✓
23 & 23s	50% Argon / 50% Krypton		2.29		✓

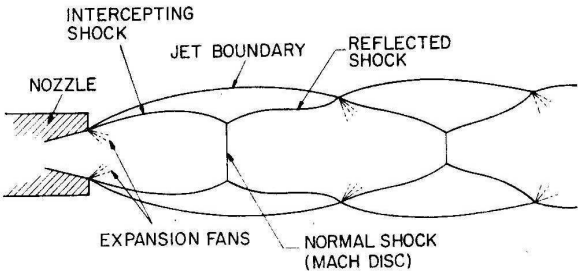

Figure 4. Schematic of shock structure of highly underexpanded nozzle flow [Ref. 2]

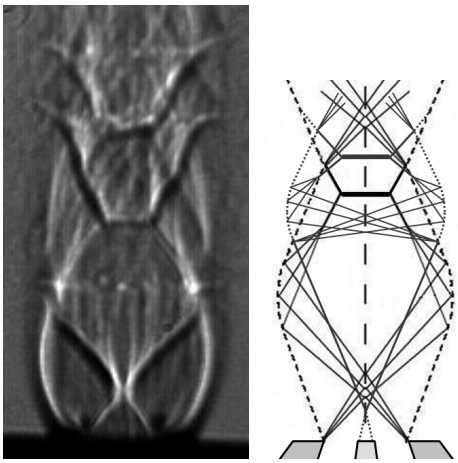

Figure 5. Shock structure of non-swirling (case 1) underexpanded nozzle airflow in presence of non-recessed coaxial injection system with no fuel injection

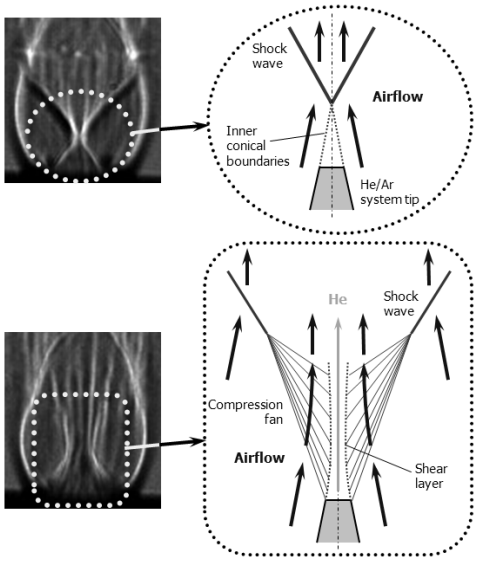

Figure 6. Effect of fuel injection on shock structure of underexpanded nozzle flow

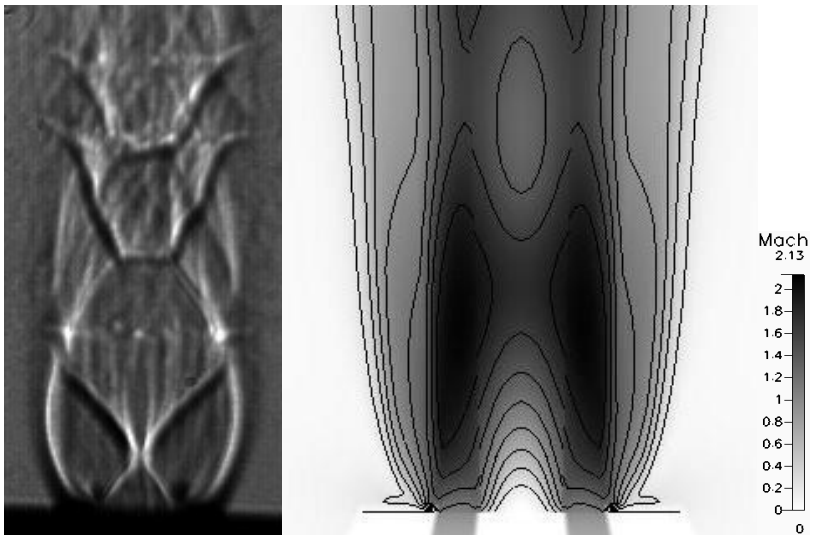

Figure 7. Comparison of experimental (Schlieren, left) and numerical (Mach number profile, right) visualizations of shock structure. Air only, no swirl (case 1)

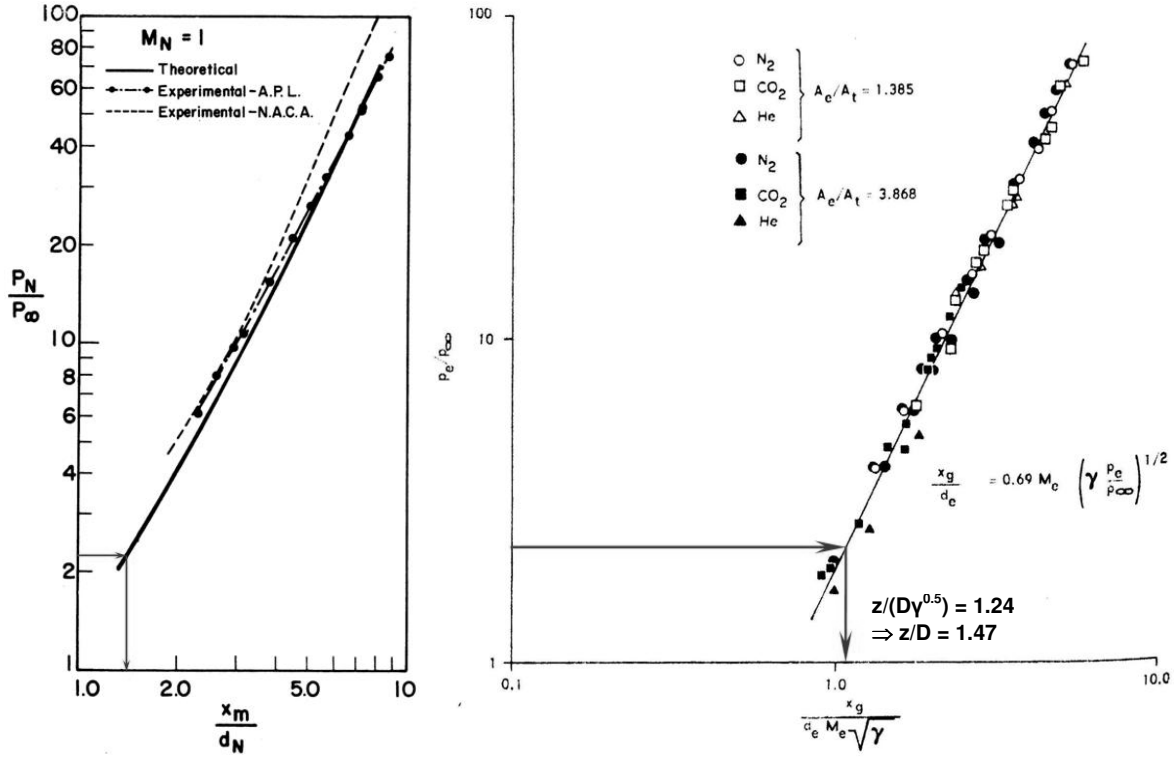

Figure 8. Axial location of first Mach disk (relative to nozzle exit plane) in non-swirling underexpanded nozzle flow. Left: Adamson and Nicholls [2]; Right: Lewis and Carlson [3]. Arrows represent findings of present study

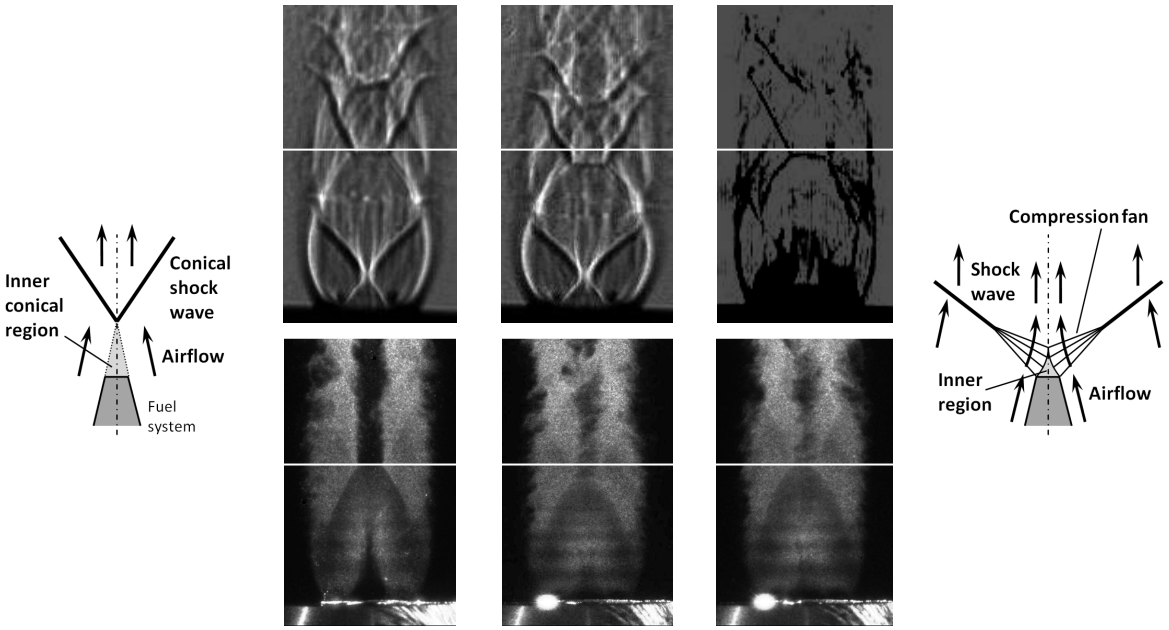

Figure 9. Images of non-swirling underexpanded nozzle airflow with no fuel injection.
Top: Schlieren; Bottom: Mie-scattering.
Left: case 0 (non-swirling, reservoir pressure = 7.91 bar);
Middle: 0's (swirling, reservoir pressure = 7.91 bar);
Right: 0s (swirling, reservoir pressure = 8.82 bar)

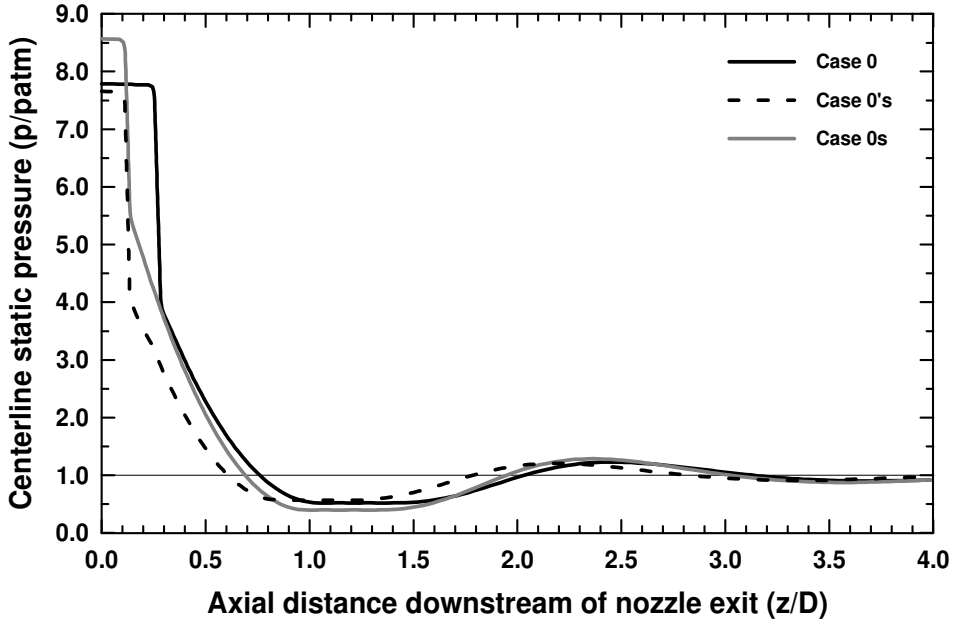

Figure 10. Axial variation of centerline static pressure within first two shock cells in cases 0 (non-swirling) and 0s (swirling)

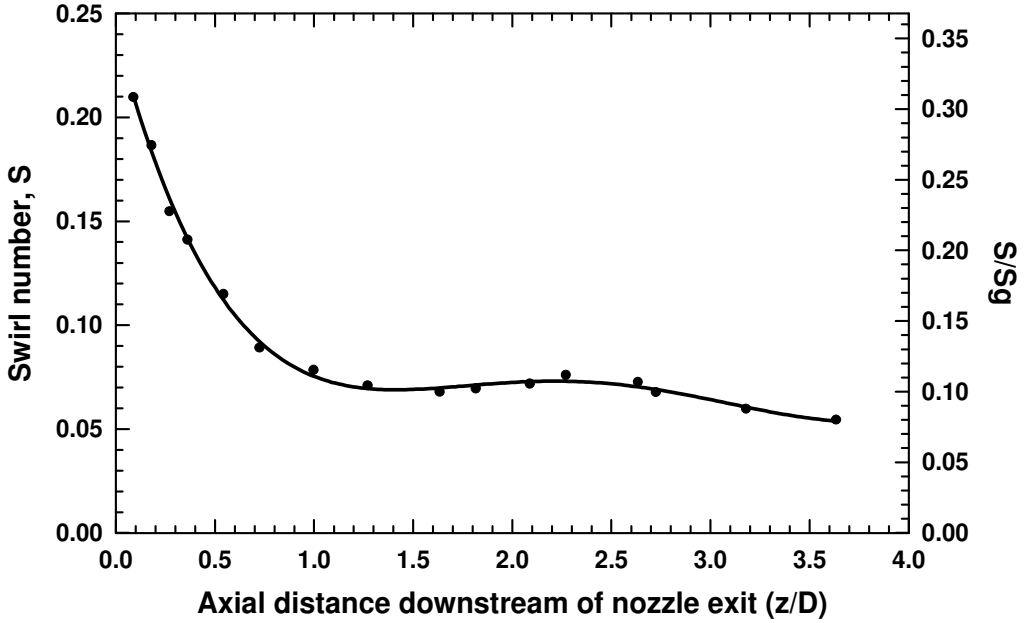

Figure 11. Axial variation of supersonic swirl number within first two shock cells in case 0s

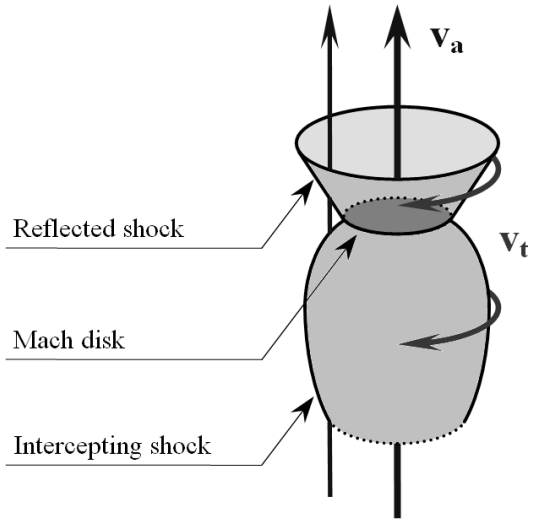

Figure 12. 3-D schematic of shock structure showing orientation of axial and tangential velocity components with respect to Mach disk and intercepting and reflected shocks

M_{rel}	**0.44**	**0.41**	**0.39**	**0.37**	**0.35**	**0.32**	**0.30**	**0.28**	**0.26**
M_{He}	0.03	0.04	0.06	0.07	0.09	0.10	0.12	0.13	0.15

Non-Swirling

Case	**(1)**	**(2)**	**(3)**	**(4)**	**(5)**	**(6)**	**(7)**	**(8)**	**(9)**

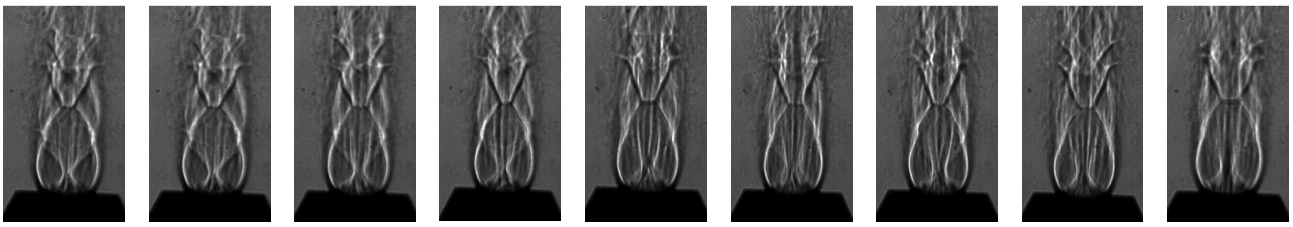

Swirling

Case	**(1s)**	**(2s)**	**(3s)**	**(4s)**	**(5s)**	**(6s)**	**(7s)**	**(8s)**	**(9s)**

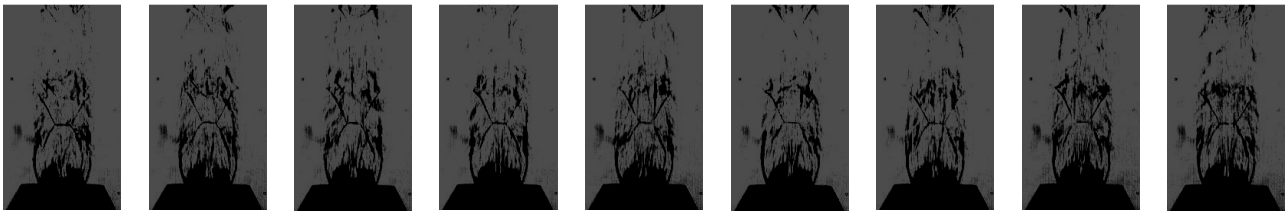

Figure 13a. Effect of M_{rel}; Schlieren images (constant DR = 35.50)

M_{rel}	**1.91**	**1.81**	**1.72**	**1.63**	**1.53**
M_{fuel}	M_{He} = 0.03	M_{He} = 0.06	M_{He} = 0.09	M_{He} = 0.12	M_{He} = 0.15

Non-Swirling

Case	**(1)**	**(3)**	**(5)**	**(7)**	**(9)**

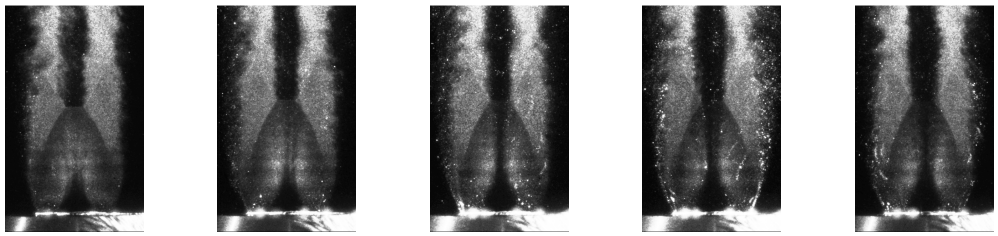

Swirling

Case	**(1s)**	**(3s)**	**(5s)**	**(7s)**	**(9s)**

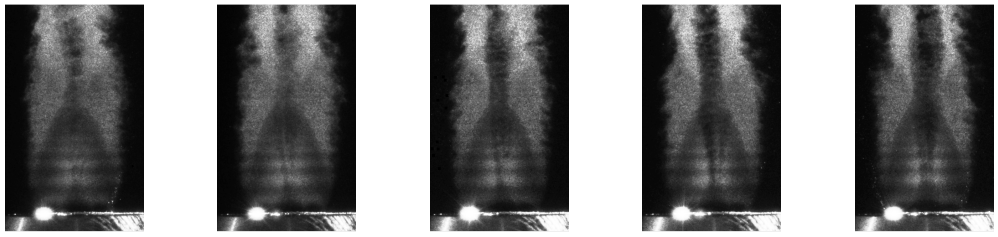

Figure 13b. Effect of M_{rel}; Mie-scattering images (constant DR = 35.50)

M_{rel}	**0.44**	**0.35**	**0.26**	**0.21**	**0.00**	**-0.21**	**-0.48**
M_{fuel}	M_{He} = 0.03	M_{He} = 0.09	M_{He} = 0.15	M_{He} = 0.18	M_{He} = 0.32	M_{He} = 0.46	M_{He} = 0.63

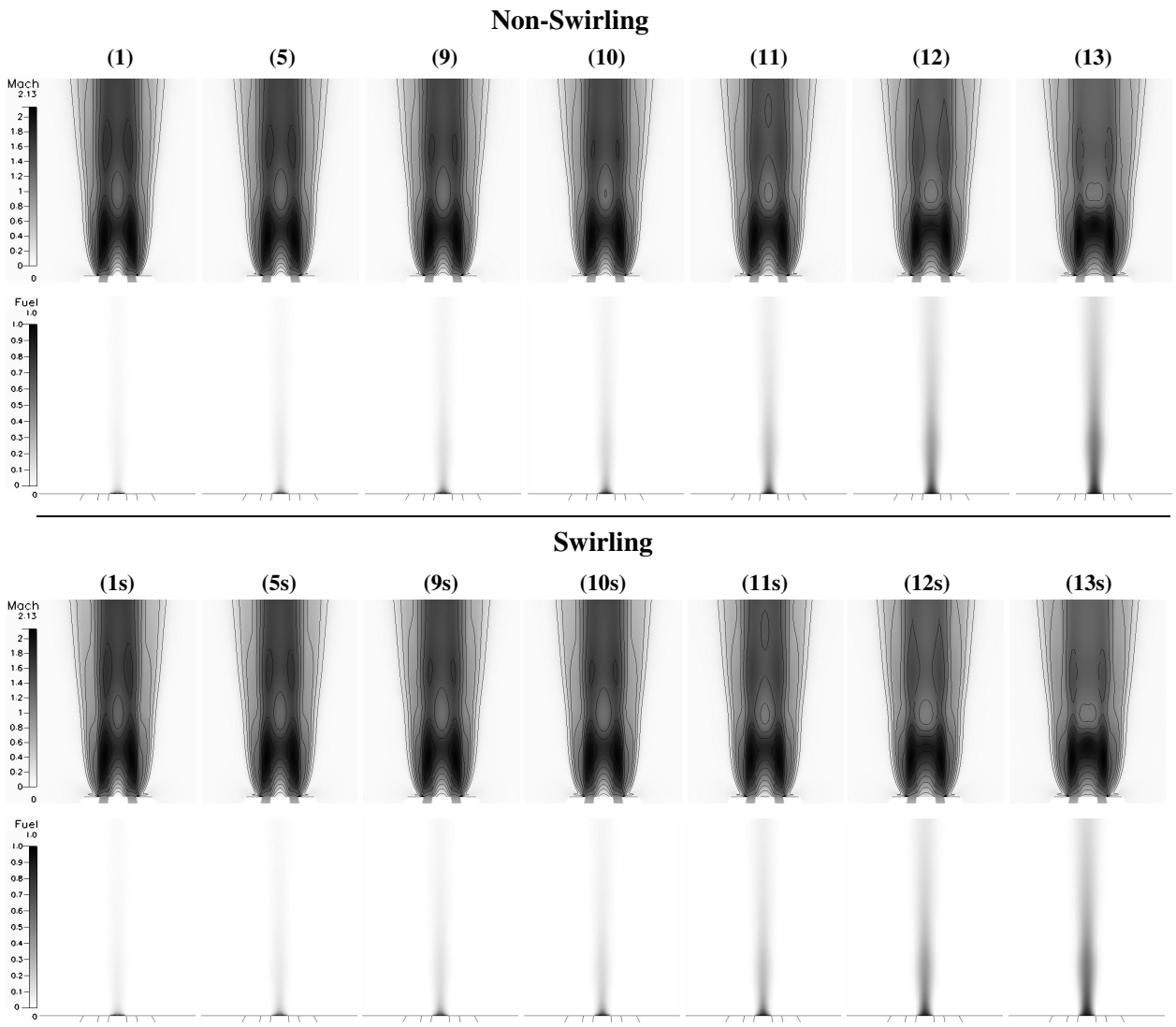

Figure 13c. Effect of M_{rel}; numerical results (constant DR = 35.50)
Mach number and fuel mass fraction profiles

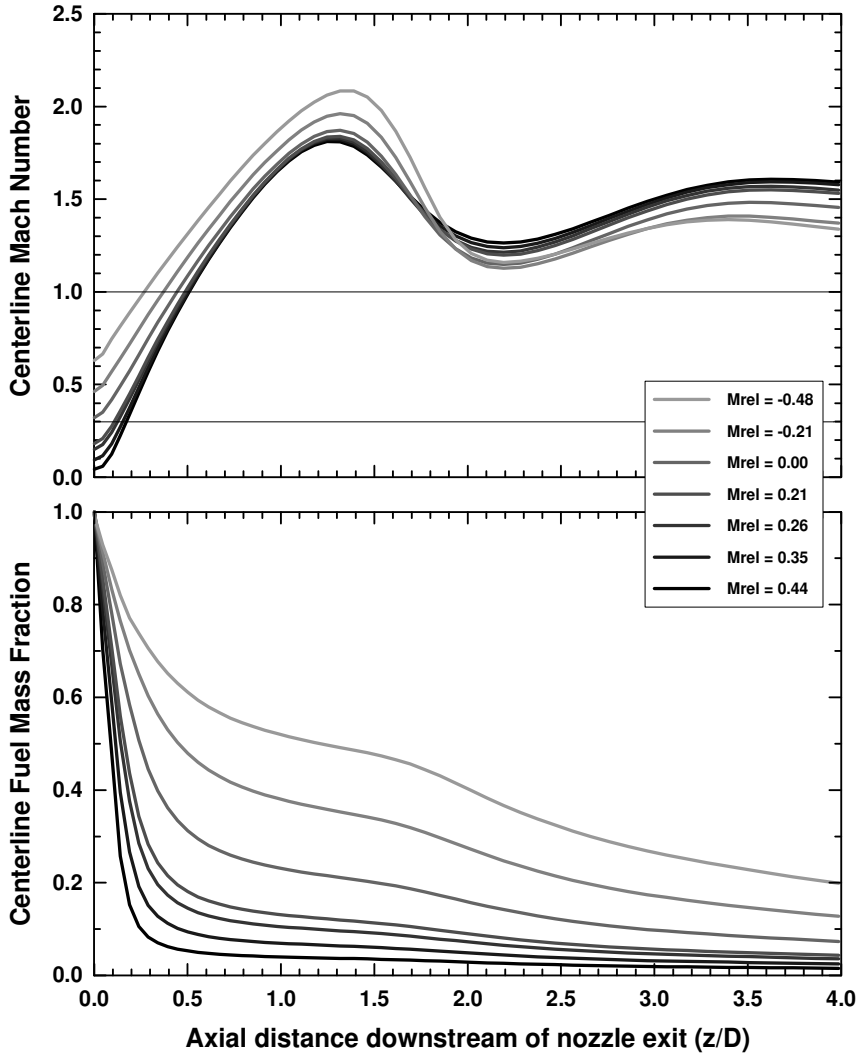

Figure 14. Axial variations of centerline Mach number and fuel mass fraction for different values of M_{rel} under non-swirling conditions

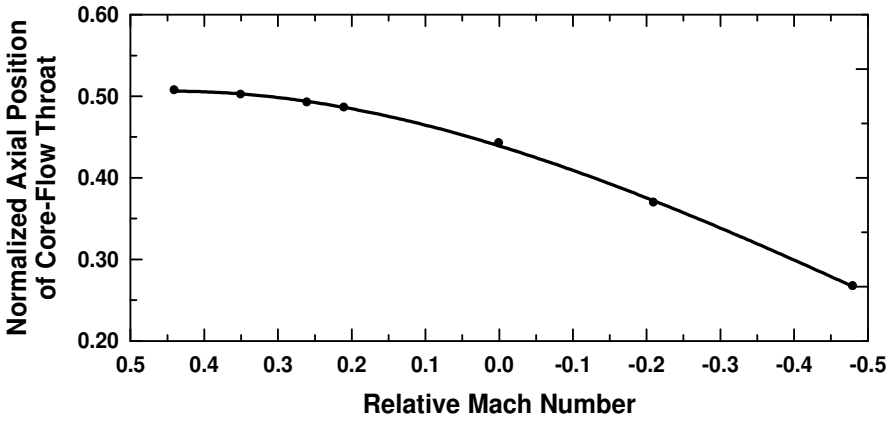

Figure 15. Variation of axial position of core-flow throat with M_{rel}

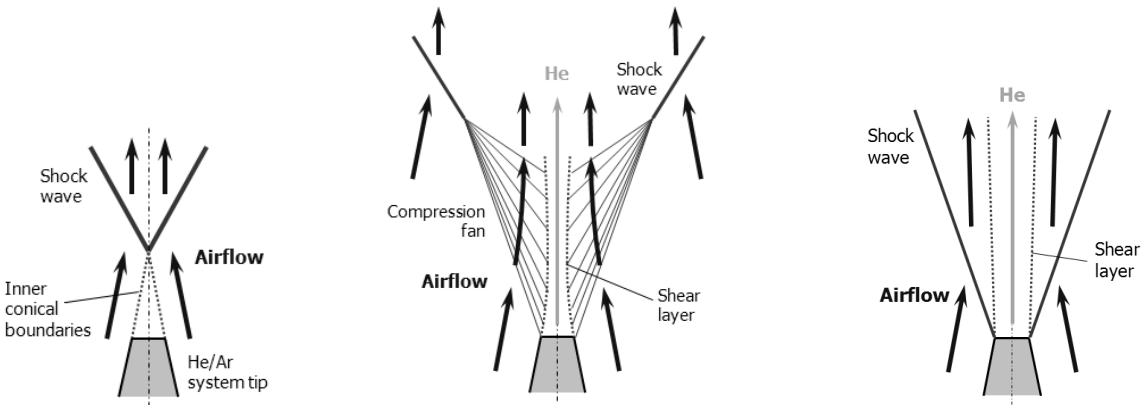

Figure 16. Schematic presentation of how the secondary shock sub-structure initiates. Left: no fuel injection; Middle: high M_{rel}; Right: Low M_{rel}

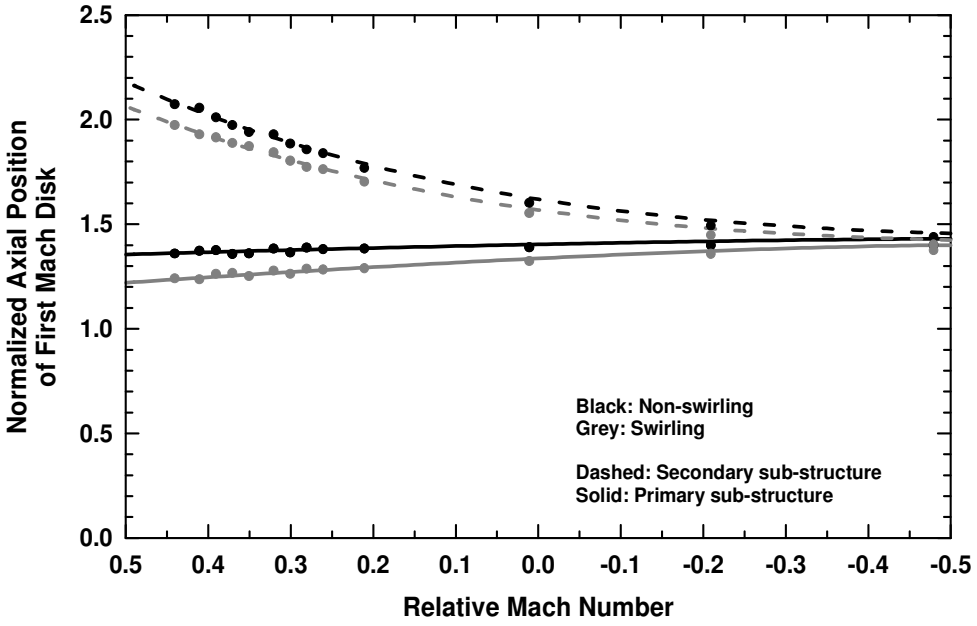

Figure 17a. Effect of M_{rel} on axial positions of first primary and secondary Mach disks under non-swirling and swirling conditions

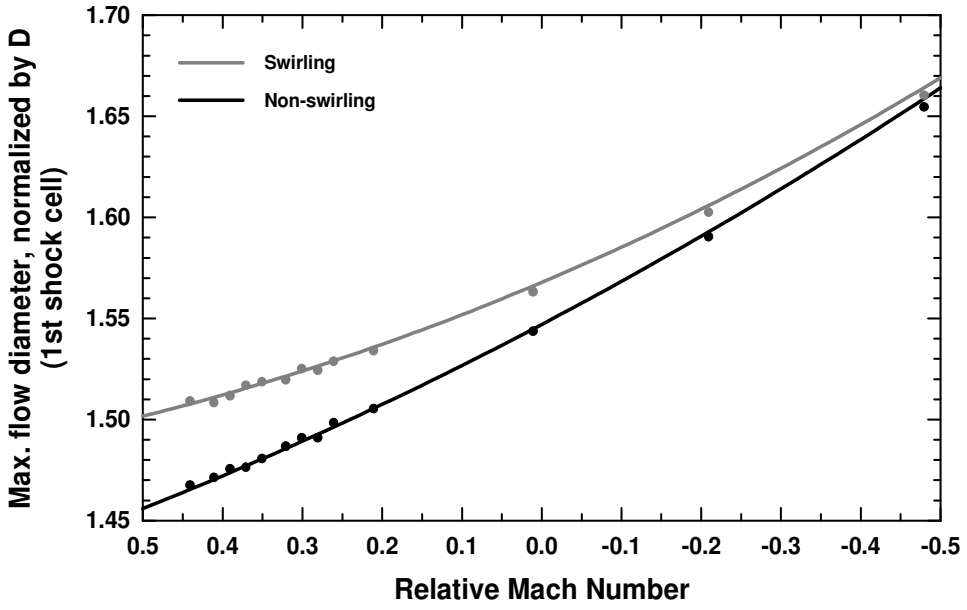

Figure 17b. Effect of M_{rel} on maximum jet diameter within first shock cell under non-swirling and swirling conditions

DR	12.68	9.60	7.72	6.46	5.55	4.86	4.33
M_{fuel}	0.37	0.44	0.50	0.56	0.61	0.66	0.70
	80% He / 20% Ar	70% He / 30% Ar	60% He / 40% Ar	50% He / 50% Ar	40% He / 60% Ar	30% He / 70% Ar	20% He / 80% Ar
Non-Swirling							
Case	**(15)**	**(16)**	**(17)**	**(18)**	**(19)**	**(20)**	**(21)**
	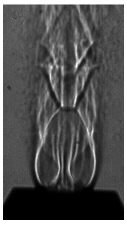	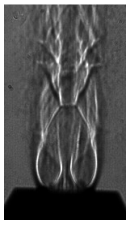		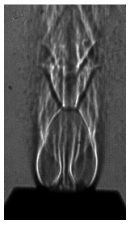	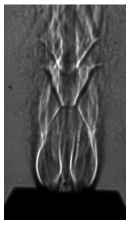	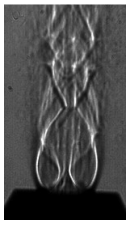	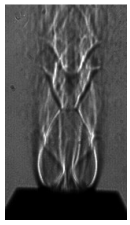
Swirling							
Case	**(15s)**	**(16s)**	**(17s)**	**(18s)**	**(19s)**	**(20s)**	**(21s)**
			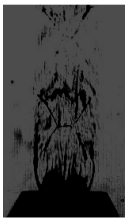				

Figure 18a. Effect of DR; Schlieren images (constant M_{rel} = 0.21)

DR	12.68	7.72	5.55	4.33
M_{fuel}	0.37	0.50	0.61	0.70
	80% He / 20% Ar	60% He / 40% Ar	40% He / 60% Ar	20% He / 80% Ar
Non-Swirling				
Case	**(15)**	**(17)**	**(19)**	**(21)**
	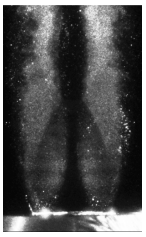	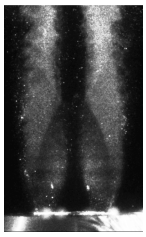	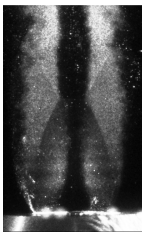	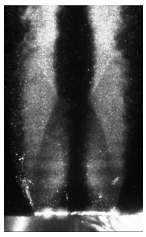
Swirling				
Case	**(15s)**	**(17s)**	**(19s)**	**(21s)**
	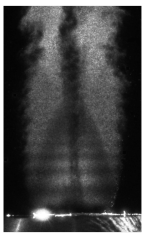	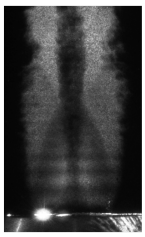	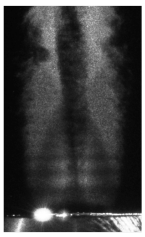	

Figure 18b. Effect of DR; Mie-scattering images (constant M_{rel} = 0.21)

DR	**35.50**	**12.68**	**6.46**	**4.33**	**3.24**	**2.29**
M_{fuel}	0.18	0.37	0.56	0.70	0.83	1.00
	100% He	80% He / 20% Ar	50% He / 50% Ar	20% He / 80% Ar	50% He / 50% Kr	50% Ar / 50% Kr

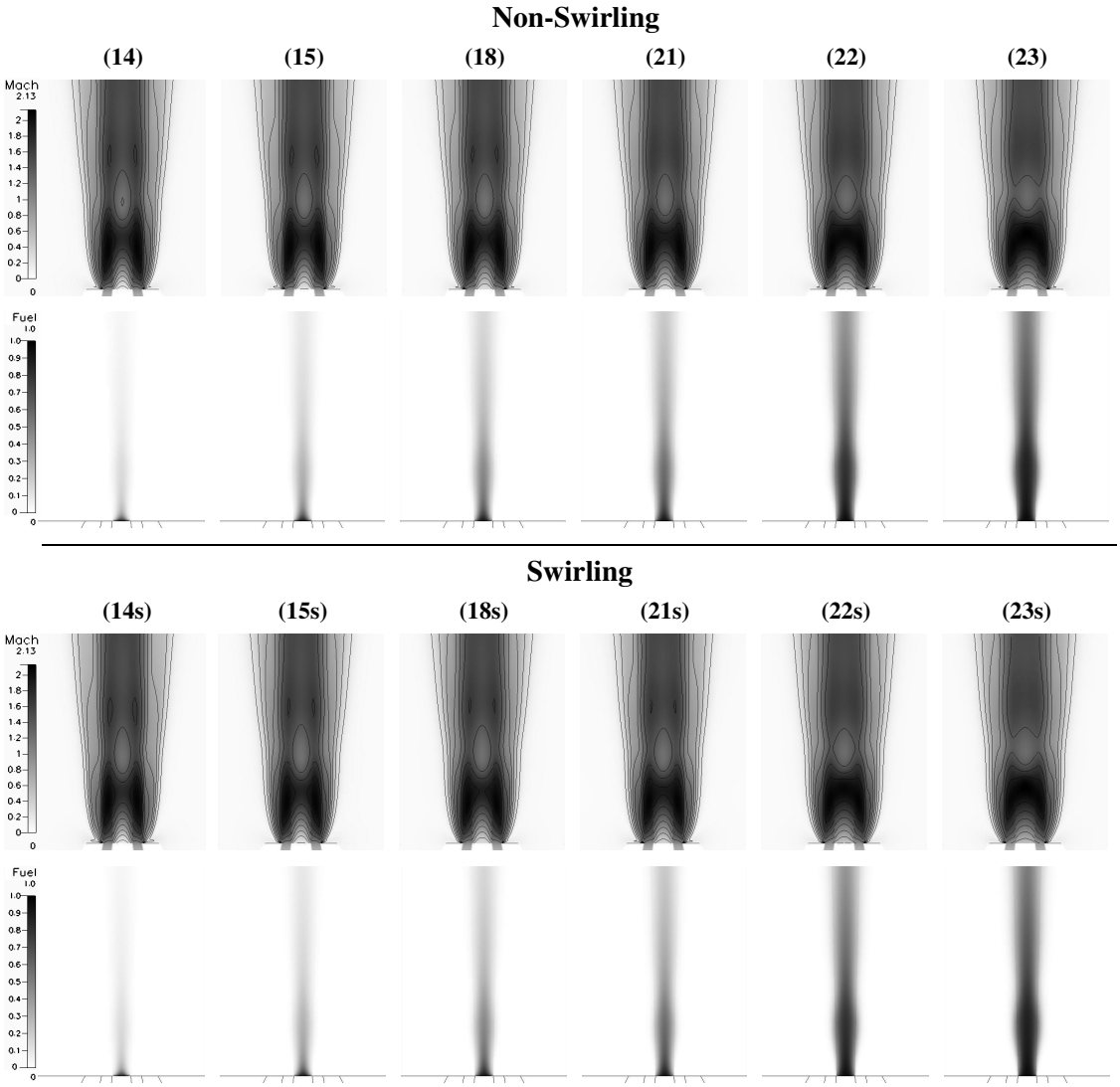

Figure 18c. Effect of DR; numerical results (constant M_{rel} = 0.21)
Mach number and fuel mass fraction profiles

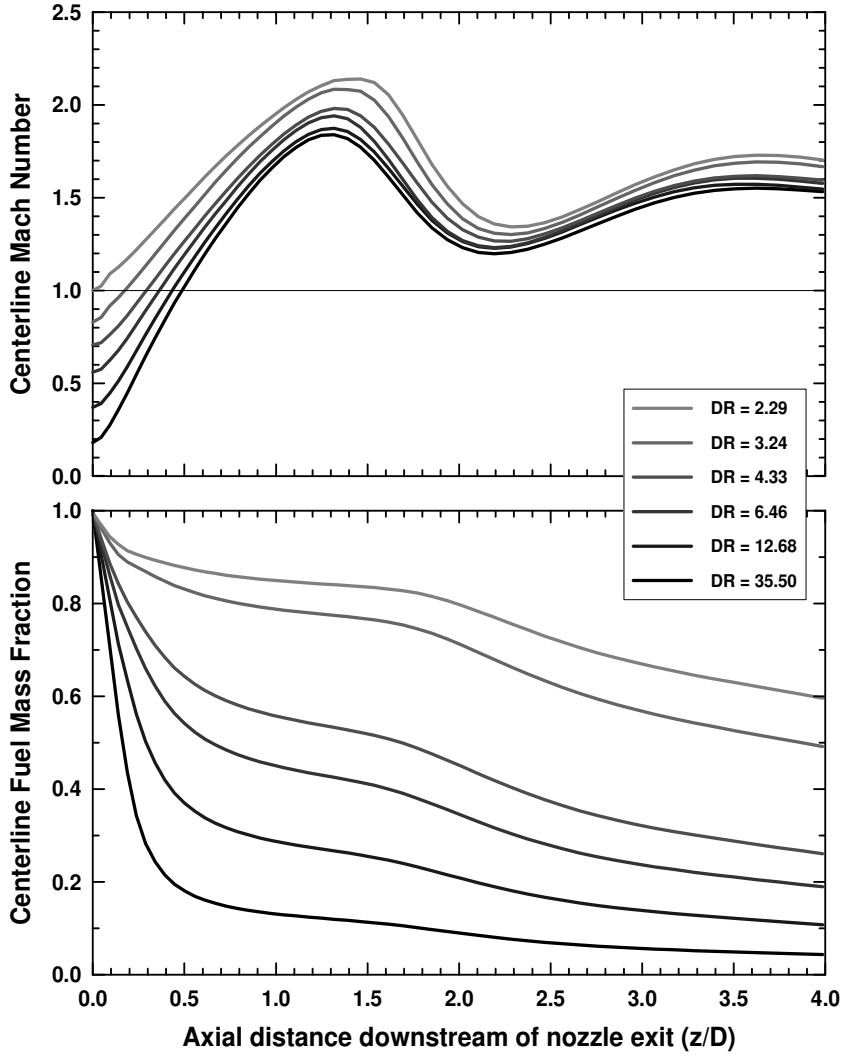

Figure 19. Axial variations of centerline Mach number and fuel mass fraction for different values of DR under non-swirling conditions

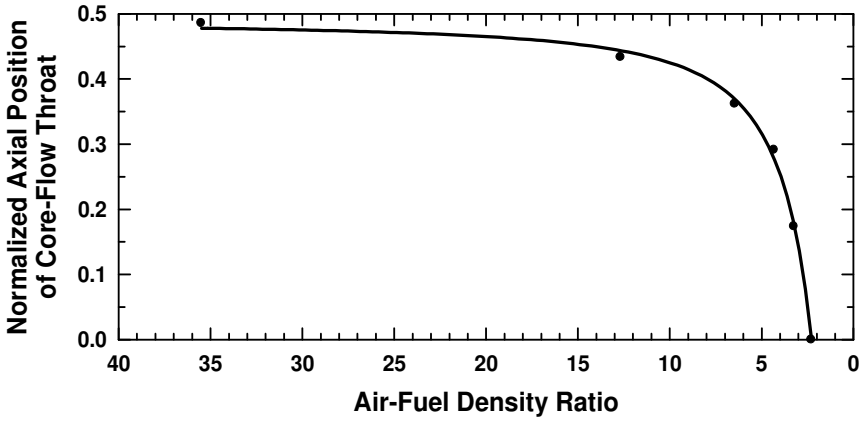

Figure 20. Variation of axial position of core-flow throat with DR

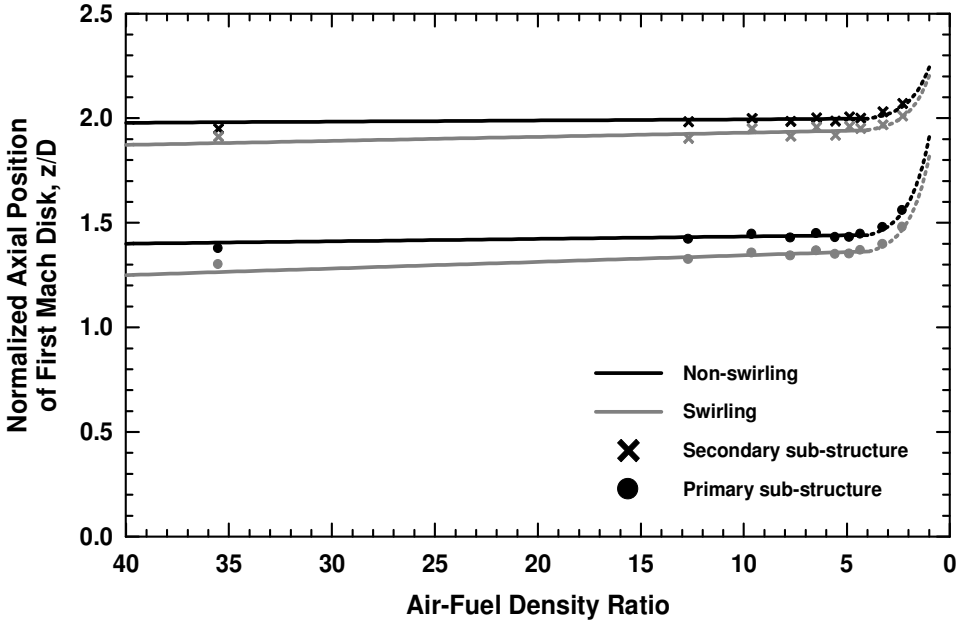

Figure 21a. Effect of DR on axial positions of first primary and secondary Mach disks under non-swirling and swirling conditions

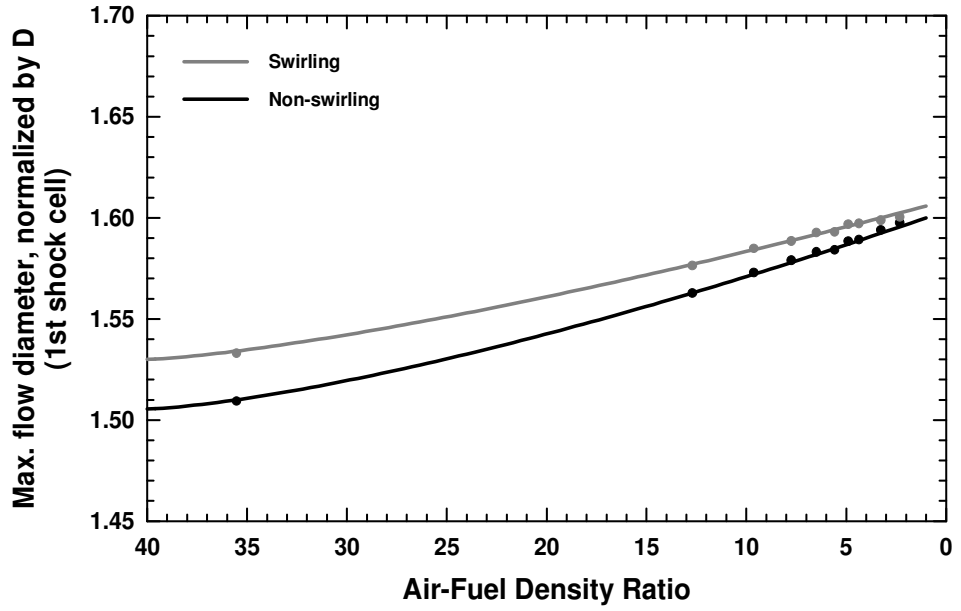

Figure 21b. Effect of DR on maximum jet diameter within first shock cell under non-swirling and swirling conditions

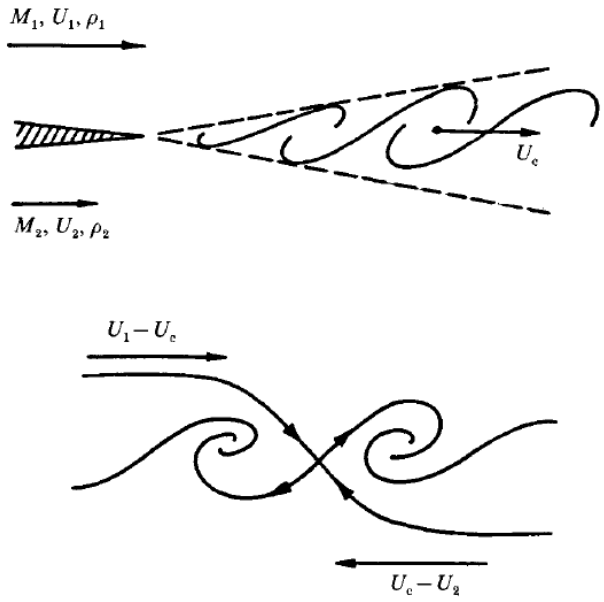

Figure 22. Schematic presentation of the stationary (top) and convective (bottom) frames of reference with sketches of streamlines; Papamoschou and Roshko [16]

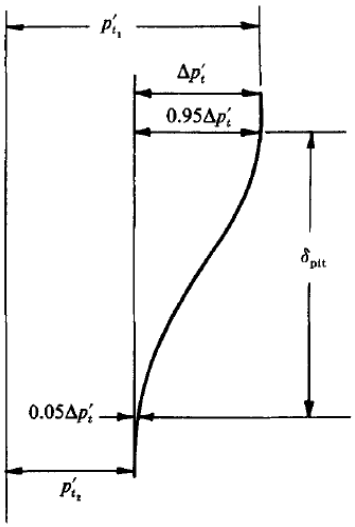

Figure 23. Definition of shear-layer Pitot thickness; Papamoschou and Roshko [16]

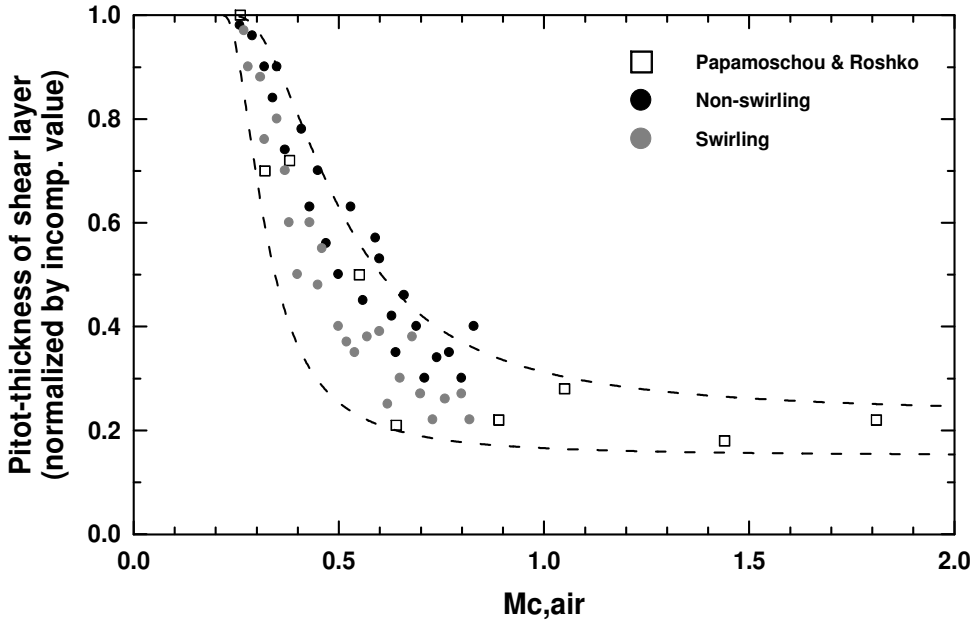

Figure 24. Normalized Pitot thickness of shear layer versus $M_{c,air}$

REFERENCES

Abdelhafez, A. and Gupta, A. K., "Numerical Investigation of Oblique Fuel Injection in Supersonic Combustors," 46th AIAA Aerospace Sciences Meeting and Exhibit, Reno, NV, Jan. 7-10, 2008, AIAA-2008-0068.

Abdelhafez, A., Gupta, A. K., Balar, R., and Yu, K., "Evaluation of Oblique and Traverse Fuel Injection in a Supersonic Combustor," 43rd AIAA/ASME/SAE/ASEE Joint Propulsion Conference & Exhibit, Cincinnati, OH, July 8-11, 2007, AIAA-2007-5026.

Adamson, T. C., Jr. and Nicholls, J. A., "On the Structure of Jets from Highly Underexpanded Nozzles into Still Air," Journal of the Aero/Space Sciences, Vol. 26, No. 1, January, 1959, pp. 16-24.

Baldwin, B. S. and Lomax, H., "Thin Layer Approximation and Algebraic Model for Separated Turbulent Flows," 16th AIAA Aerospace Sciences Meeting, Huntsville, Alabama, Jan. 16-18, 1978, AIAA-78-257.

Bastress, E. K., "Interior Ballistics of Spinning Solid-Propellant Rockets," Journal of Spacecraft and Rockets, Vol. 2, No. 3, 1965, pp. 455-457.

Batson, J. L. and Sforzini, R. H., "Swirling Flow through a Nozzle," Journal of Spacecraft and Rockets, Vol. 7, No. 2, 1970, pp. 159-163.

Ben-Yakar, A., "Experimental Investigation of Transverse Jets in Supersonic Cross-flows," Ph.D. Dissertation, Dept. of Mechanical Engineering, Stanford Univ., Stanford, CA, 2000.

Brown, G. L. and Roshko, A., "On Density Effects and Large Structure in Turbulent Mixing Layers," Journal of Fluid Mechanics, Vol. 64, No. 4, 1974, pp. 775-816.

Brummund, U. and Nuding, J. R., "Interaction of a Compressible Shear Layer with Shock Waves - An Experimental Study," 35th AIAA Aerospace Sciences Meeting & Exhibit, Reno, NV, Jan. 6-9, 1997, AIAA-97-0392.

Brummund, U. and Mesnier, B., "A Comparative Study of Planar Mie and Rayleigh Scattering for Supersonic Flowfield Diagnostics," Proceedings of the 18th International Congress on Instrumentation in Aerospace Simulation Facilities (ICIASF), Toulouse, France, June 14-17, 1999, ISBN 0-7803-5715-9, pp. 42.1 – 42.10.

Buckley, P. L., Craig, R. R., Davis, D. L., and Schwartzkopf, K. G., "The Design and Combustion Performance of Practical Swirlers for Integral Rocket/Ramjets," AIAA Journal, Vol. 21, No. 5, 1983, pp. 733-740.

Bushnell, D. M., "Hypervelocity Scramjet Mixing Enhancement," Journal of Propulsion and Power, Vol. 11, No. 5, 1995, pp. 1088-1090.

Carpenter, P. W. and Johannesen, N. H., "An Extension of One-Dimensional Theory to Inviscid Swirling Flow through Choked Nozzles," Aeronautical Quarterly, Vol. 26, May 1975, pp. 71-87.

Carpenter, P. W., "A Linearized Theory for Swirling Supersonic Jets and its Application to Shock-Cell Noise," AIAA Journal, Vol. 23, No. 12, 1985, pp. 1902-1909.

Chinzei, N., Masuya, G., Komura, T., Mukrami, A., and Kudou, K., "Spreading of Two-Stream Supersonic Turbulent Mixing Layers," Physics of Fluids, Vol. 29, No. 5, 1986, pp. 1345-1347.

Claypole, T. C. and Syred, N., "The Effects of Swirl Burner Aerodynamics on NOx Formation," Proceedings of 18th Symposium (International) on Combustion, Combustion Institute, Pittsburgh, PA, 1981, pp. 81-89.

Clemens, N. T. and Mungal, M. G., "Two- and Three-Dimensional Effects in the Supersonic Mixing Layer," 26th AIAA/SAE/ASME/ASEE Joint Propulsion Conference, Orlando, FL, July 16-18, 1990, AIAA-90-1978.

Cohen, H., Rogers, C. F. C., and Saravanamuttoo, H. I. H., "Gas Turbine Theory," 4th Edition, Longman, Burnt Mill, Harlow, Essex, UK, 1996, ISBN 058230539X.

Crist, S., Sherman, P. M., and Glass, D. R., "Study of the Highly Underexpanded Sonic Jet," AIAA Journal, Vol. 4, No. 1, 1966, pp. 68-71.

Cutler, A. D., Levey, B. S., and Kraus, D. K., "An Experimental Investigation of Supersonic Swirling Jets," 24th AIAA Fluid Dynamics Conference, Orlando, FL, July 6-9, 1993, AIAA-93-2922.

Cutler, A. D., Levey, B. S., and Kraus, D. K., "Near-Field Flow of Supersonic Swirling Jets," AIAA Journal, Vol. 33, No. 5, 1995, pp. 876-881.

Cutler, A. D. and Levey, B. S., "Vortex Breakdown in a Supersonic Jet," AIAA Paper 91-1815, June 1991.

Davis, N. T. and Samuelsen, G. S., "Optimization of Gas Turbine Combustor Performance Throughout the Duty Cycle," Proceedings of the 26th Symposium (International) on Combustion, The Combustion Institute, 1996, pp. 2819-2825.

Dutton, J. C., "Swirling Supersonic Nozzle Flow," Journal of Propulsion and Power, Vol. 3, No. 4, 1987, pp. 342-349.

Glick, R. L. and Kilgore, M. S., "Effect of Specific-Heat Ratio on Mass Flow for Swirling Nozzle Flow," Journal of Spacecraft and Rockets, Vol. 4, No. 8, 1967, pp. 1098-1099.

Gostintsev, Y. A., Zelentsov, V. V., Ilyukhin, V. S., and Pokhil, P. F., "Structure of Underexpanded Supersonic Swirling Gas Jet," Journal of Fluid Dynamics, Vol. 4, No. 5, September, 1969, pp. 158-162.

Gupta, A. K., Lilley, D. G., and Syred, N., "Swirl Flows," Abacus Press, Tunbridge Wells, Kent, UK, 1984, ISBN 0-85626-175-0.

Gupta, A. K., Lourenco, L., Linck, M., and Archer, S., "A New Method to Measure Flowfield in Luminous Spray Flames," Journal of Propulsion and Power, Vol. 20, No. 2, 2004, pp. 369-372.

Hall, J. L., Dimotakis, P. E., and Rosemann, H., "Experiments in Non-Reacting Compressible Shear Layers," 29th AIAA Aerospace Sciences Meeting, Reno, NV, Jan. 7-10, 1991.

Heiser, W. H. and Pratt, D. T., "Hypersonic Airbreathing Propulsion," AIAA Education Series, AIAA, Inc., Washington, D.C., 1994, ISBN 1-56347-035-7.

Hermanson, J. C. and Winter, M., "Imaging of a Transverse Sonic Jet in Supersonic Flow", 27th AIAA/SAE/ASME/ASEE Joint Propulsion Conference, Sacramento, CA, June 24-26, 1991.

Hersch, M. and Povinelli, L. A., "Effect of Interacting Vortices on Jet Penetration into a Supersonic Stream," NASA TM-X-2134, Nov. 1970.

Hoffman, J. D., Thompson, H. D., and Marcum, D. L., "Analytical Study of Swirler Effects in Annular Propulsive Nozzles," Journal of Propulsion and Power, Vol. 3, No. 5, 1987, pp. 465-466.

Hsu, C., "Mass Blocking of Swirling Flow in Nozzles," Journal of Spacecraft and Rockets, Vol. 8, No. 12, 1971, pp. 1232-1234.

Huh, H. and Driscoll, J. F., "Measured Effects of Shock Waves on Supersonic Hydrogen-Air Flames," 32nd Joint Propulsion Conference and Exhibit, Lake Buena Vista, FL, July, 1996a, AIAA-96-3035.

Huh, H. and Driscoll, J. F., "Shock-Wave-Enhancement of the Mixing and the Stability Limits of Supersonic Hydrogen-Air Jet Flames," 26th Symposium (International) on Combustion, Combustion Inst., Pittsburgh, PA, 1996b, pp. 2933-2939.

Johnson, C., "Applications of Streamwise Vorticity in Enhancement of Injectant Mixing and Penetration in a Supersonic Flow," M.S. Thesis, School of Engineering and Applied Science, The George Washington University, May 1996.

King, M. K., Comment on "Spin Effects on Rocket Nozzle Performance," Journal of Spacecraft and Rockets, Vol. 3, No. 12, 1966, pp. 1812-1813.

Knowles, K., "Combined Noise and Flow Control of Supersonic Jets Using Swirl," 14th DGLR/AIAA Aeroacoustics Conference, Aachen, Germany, May 11-14, 1992.

Kornblum, B. T., Thompson, H. D., and Hoffman, J. D., "An Analytical Investigation of Swirl in Annular Propulsive Nozzles," Journal of Propulsion and Power, Vol. 2, No. 2, 1986, pp. 155-160.

Kraus, D. K. and Cutler, A. D., "Mixing Enhancement by Use of Supersonic Swirling Jets," AIAA Paper 93-3126, July 1993.

Kraus, D. K. and Cutler, A. D., "Mixing of Swirling Jets in a Supersonic Duct Flow," Journal of Propulsion and Power, Vol. 12, No. 1, 1995, pp. 170-177.

Kraus, D. K., "An Experimental Investigation of Mixing Enhancement in a Simulated Scramjet Combustor by Use of Swirling Jets," M.S. Thesis, School of Engineering and Applied Science, The George Washington University, August 1993.

Lee, K. H., Setoguchi, T., Matsuo, S., and Kim, H. D., "An Experimental Study of Underexpanded Sonic, Coaxial, Swirl Jets," Proceedings of the Institution of Mechanical Engineers, Part C: Journal of Mechanical Engineering Science, Vol. 218, No. 1, 2004, pp. 93-103.

Lee, K. H., Setoguchi, T., Matsuo, S., and Kim, H. D., "Influence of the Nozzle Inlet Configuration on Underexpanded Swirling Jet," Proceedings of the Institution of Mechanical Engineers, Part C: Journal of Mechanical Engineering Science, Vol. 220, No. 2, 2006, pp. 155-163.

Lefebvre, A. H., "Gas Turbine Combustion," 2nd Edition, CRC Press, 1998, ISBN 1560326735.

Levey, B. S., "An Experimental Investigation of Supersonic Vortical Flow," M.S. Thesis, School of Engineering and Applied Science, The George Washington University, September 1991.

Lewellen, W. S., Burns, W. J., and Strickland, H. J., "Transonic Swirling Flow," AIAA Journal, Vol. 7, No. 7, July, 1969, pp. 1290-1297.

Lewis, C. H., Jr. and Carlson, D. J., "Normal Shock Location in Underexpanded Gas and Gas-Particle Jets," Technical Note, AIAA Journal, Vol. 2, No. 4, April, 1964, pp. 776-777.

Li, J. and Acharya, S., "Velocity Measurements in a Combustor Undergoing Limit-Cycle Pressure Oscillations," Combustion Science and Technology, Vol. 162, No. 1, 2001, pp. 147-173.

Linck, M. and Gupta, A. K., "Effect of Swirl and Combustion on Flow Dynamics in Luminous Kerosene Spray Flames," 41st AIAA Aerospace Sciences Meeting, Reno, NV, Jan. 6-9, 2003, AIAA-2003-1345.

Linck, M., "Spray Flame and Exhaust Jet Characteristics of a Pressurized Swirl Combustor," PhD thesis, University of Maryland, College Park, MD, May 2006.

Lu, P. J. and Wu, K. C., "On the Shock Enhancement of Confined Supersonic Mixing Flows," Physics of Fluids, part A: Fluid Dynamics, Vol. 3, No. 12, Dec. 1991, pp. 3046-3062.

Mager, A., "Approximate Solution of Isentropic Swirling Flow through a Nozzle," ARS Journal, Vol. 31, No. 8, 1961, pp. 1140-1148.

Manda, L. J., “Spin Effects on Rocket Nozzle Performance,” Journal of Spacecraft and Rockets, Vol. 3, No. 11, 1966a, pp. 1695-1696.

Manda, L. J., Reply by author to M. K. King, Journal of Spacecraft and Rockets, Vol. 3, No. 12, 1966b, p. 1813.

Marble, F. E., Zukoski, E. E., Jacobs, J., Hendricks, G., and Waitz, I., “Shock Enhancement and Control of Hypersonic Mixing and Combustion,” 26th AIAA/SAE/ASME/ASEE Joint Propulsion Conference, Orlando, FL, July 16-18, 1990, AIAA-90-1981.

Menon, S., “Numerical Simulations of Supersonic Flows Past Generic SCRAMJET Flameholders,” Final Report under Contract No. F33615-87-C-2782 to US Air Force, Wright Patterson AFB, Report No. 434, 1988.

Menon, S., “Shock-wave-induced mixing enhancement in scramjet combustors,” 27th AIAA Aerospace Sciences Meeting, Reno, NV, Jan. 1989, AIAA-89-0104.

Miles, J. W., “On the Disturbed Motion of a Plane Vortex Sheet,” Journal of Fluid Mechanics, Vol. 4, No. 5, 1958, pp. 538-552.

Murakami, E. and Papamoschou, D., “Experiments on Mixing Enhancement in Dual-Stream Jets,” 39th AIAA Aerospace Sciences Meeting & Exhibit, Reno, NV, Jan. 8-11, 2001, AIAA-2001-0668.

Murugappan, S., Gutmark, E., Carter, C., Donbar, J., Gruber, M., and Hsu, K., “Control of a Transverse Supersonic Jet Injection into a Supersonic Cross-Stream,” 42nd AIAA Aerospace Sciences Meeting and Exhibit, Reno, NV, Jan. 5-8, 2004, AIAA-2004-1204.

Murugappan, S., Gutmark, E., Carter, C., Donbar, J., Gruber, M., and Hsu, K., “Transverse Supersonic Controlled Swirling Jet in a Supersonic Cross Stream,” AIAA Journal, Vol. 44, No. 2, 2006, pp. 290-300.

Murugappan, S. and Gutmark, E., “A Novel Swirling Injector for Improving Mixing in High Speed Flows,” 39th AIAA/ASME/SAE/ASEE Joint Propulsion Conference and Exhibit, Huntsville, AL, July 20-23, 2003, AIAA-2003-4785.

Naughton, J. W., Cattafesta, L. N., and Settles, G. S., “An Experimental Study of the Effect of Streamwise Vorticity on Supersonic Mixing Enhancement,” 25th AIAA/ASME/SAE/ ASEE Joint Propulsion Conference, Monterey, CA, July 10-12, 1989, AIAA-89-2456.

Naumova, I. N. and Shmyglevskii, Y. D., "Nozzle Thrust Increase by Flow Rotation," Journal of Fluid Dynamics, Vol. 2, No. 1, 1967, pp. 23-25.

Papamoschou, D. and Roshko, A., "The Compressible Turbulent Shear Layer: An Experimental Study," Journal of Fluid Mechanics, Vol. 197, 1988, pp. 453-477.

Pinchak, A. C. and Poplawski, R., "On the Attainment of Extremely High Rotational Velocities in a Confined Vortex Flow," 2nd AIAA Annual Meeting, San Francisco, CA, July 26-29, 1965, AIAA-65-400.

Povinelli, L. A., Povinelli, F. P., and Hersch, M., "A Study of Helium Penetration and Spreading in a Mach-2 Airstream Using a Delta Wing Injector," NASA TN D-5322, July 1969.

Povinelli, L. A. and Ehlers, R. C., "Swirling Base Injection for Supersonic Combustion Ramjets," AIAA Journal, Vol. 10, No. 9, 1972, pp. 1243-1244.

Rayleigh, J. W. S., "The Theory of Sound," Vol. 2, Dover Publications, New York, NY, 1945, pp. 170-235, ISBN 0486602931.

Roschke, E. J. and Pivirotto, T. J., "Similarity in Confined Vortex Flows," Technical Report 32-789, 1965, Jet Propulsion Laboratory.

Roy, C. J. and Edwards, J. R., "Numerical Simulation of a Three-Dimensional Flame/Shock Wave Interaction," AIAA Journal, Vol. 38, No. 5, May 2000, pp. 745-754.

Schetz, J. A. and Swanson, R. C., "Turbulent Jet Mixing at High Supersonic Speeds," Zeitschrift fuer Flugwissenschaften, Vol. 21, No. 5, 1973, pp. 166-173.

Settles, G. S., "Supersonic Mixing Enhancement by Vorticity for High-Speed Propulsion," Report submitted to NASA-Langley Research Center, October 1991, NASA-CR-188920.

Swithenbank, J. and Chigier, N. A., "Vortex Mixing for Supersonic Combustion," 12th Symposium (International) on Combustion, The Combustion Institute, Pittsburgh, PA, 1968, pp. 1153-1162.

Swithenbank, J. and Sotter, G., "Vortex Generation in Solid Propellant Rockets," AIAA Journal, Vol. 2, No. 7, 1964, pp. 1297-1302.

Tillman, T. G., Patrick, W. P., and Paterson, R. W., "Enhanced Mixing of Supersonic Jets," Journal of Propulsion and Power, Vol. 7, No. 6, 1991, pp. 1006-1014.

Toomre, J., “Highly Swirling Flows Through a Convergent-Divergent Nozzle,” MSc thesis, Massachusetts Institute of Technology, Cambridge, MA, June 1963.

Waltrup, P. J., “Liquid Fueled Supersonic Combustion Ramjets - A Research Perspective of the Past, Present and Future,” 24th Aerospace Sciences Meeting, Reno, NV, Jan. 6-9, 1986, AIAA-1986-158.

Winant, C. D. and Browand, F. K., “Vortex Pairing: The Mechanism of Turbulent Mixing-Layer Growth at Moderate Reynolds Number,” Journal of Fluid Mechanics, Vol. 63, No. 2, 1974, pp. 237-255.

Yang, J., Kubota, T., and Zukoski, E. E., “Applications of Shock-Induced Mixing to Supersonic Combustion,” AIAA Journal, Vol. 31, No. 5, 1993, pp. 854-862.

Yu, Y. K., Chen, R. H., and Chew, L., “Screech Tone Noise and Mode Switching in Supersonic Swirling Jets,” AIAA Journal, Vol. 36, No. 11, 1998, pp. 1968-1974.

Yu, Y. K., “An Experimental Study of Underexpanded Supersonic Swirling Jets,” PhD thesis, University of Central Florida, December 1997.